Noncontact
Temperature
Measurement

Noncontact Temperature Measurement

Mark C. Lee, *Editor*
NASA Office of Space Science and Applications
Washington, D.C.

NASA

National Aeronautics
and Space Administration

Scientific and Technical
Information Division

1988

Noncontact Temperature Measurement Instrument has been identified as one of the eight Advanced Technology Development (ATD) areas to support the Microgravity Science and Applications Division's effort in developing the six Space Station Flight Experiment Facilities. The other seven ATD's are High Resolution/High Rate Video Technology, Microgravity Fluid Diagnostics, Laser Light Scattering Instrument, Vibration Isolation Technology, High Temperature Furnace Technology, High Temperature Material Technology and Interface Measurement. Those ATD areas are defined as generic areas of technology advancement that will enhance the scientific integrity and quality of flight experiments. These technologies shall not be in the critical path of on-going programs or near-term facility development programs.

This two-day workshop at NASA Headquarters, Washington, D.C. was intended as an opportunity for all the six disiplines in the microgravity program to present their requirements on Noncontact Temperature Measurement; equally important, the state-of-the-art technology on noncontact measurement for each discipline area was reviewed and assessed. A preliminary survey of this report reveals that at least three categories of experiments demand immediate attention in noncontact temperature measurement: experiments involving levitated samples and samples falling in a drop tube;crystal growth processes and gaseous and fluid flows experiments. This workshop only represents an initial effort for developing a critical technology which is definitely required in the Space Station era. More areas needing noncontact temperature measurements will certainly become apparent as this task progresses.

The participants of this workshop cover NASA Centers, other national agencies, academia, industries and commercial organizations. The Chairman would like to take this opportunity to thank them all for their enthusiasm and support of the workshop, and also wishes to acknowledge the logistic support of Ms. Elizabeth Pentecost, USRA, Dr. James Beebe and Mrs. June Meeks, Bionetics and Mr. Michael Price, Code EN, NASA Headquarters.

The Chairman particularly, apppreciates the support and encouragement of Ms. Kathryn Schmoll, Dr. Roger Crouch and the entire Code EN staff, NASA Headquarters.

Mark C. Lee, Chairman
Senior Scientist
Microgravity Science and
  Applications Division
NASA Headquarters

I

CONTENTS

PRECEDING PAGE BLANK NOT FILMED

OVERVIEW

RADIATION THERMOMETRY - THE MEASUREMENT PROBLEM*

G.D. Nutter

Instrumentation Systems Center

University of Wisconsin - Madison

RADIATION THERMOMETRY - THE MEASUREMENT PROBLEM

INTRODUCTION

Radiation thermometry is the measurement of the temperature of an object by radiometric methods. A radiation thermometer is a radiometer calibrated to indicate the temperature of a blackbody having the same apparent radiance as the "target, the specific surface area over which the temperature is to be measured. An idealized radiation thermometer is illustrated in Fig. 1.

This method of temperature measurement is used when contact with the heated object - such as by a thermocouple - is undesirable or impossible, e.g., when the target is in motion, is inaccessible or would be damaged by contact, when the target temperature might be perturbed by a contact device, or when the target temperature is so high that the intense heat would degrade or destroy a contact temperature sensor. Radiometric methods are particularly important in industrial processes and in laboratory applications.

Radiation thermometry can be separated into three parts: the radiator (the target), the environment between the target and the radiation thermometer, and the radiation thermometer
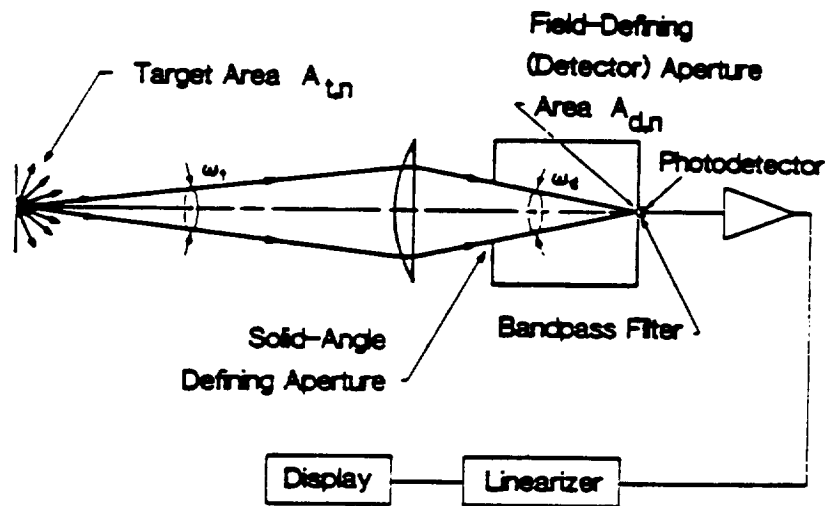
Fig. 1. Idealized Radiation Thermometer
The radiometer output signal is directly proportional
to spectral radiance, which is exponentially related
to temperature through Planck's radiation law.

itself. We begin by considering blackbody radiation, which forms the theoretical basis for radiation thermometry.

THERMAL RADIATORS

BLACKBODIES

A blackbody is a surface that absorbs all electromagnetic radiation incident on it, reflecting nothing. At room temperature, such a surface would appear to be absolutely black, but at sufficiently elevated temperatures it would glow somewhat more brightly than the surface of any real material at the same temperature. The <u>spectral radiance</u> of a blackbody is given as a function of temperature T and wavelength λ by the Planck radiation distribution (Fig. 2):

$$L_{\lambda,b}(\lambda,T) = \frac{c_1}{\lambda^5 \cdot (e^{c_2/\lambda \cdot T} - 1)} \qquad (1)$$

where

$$c_1 = 2 \cdot c^2 \cdot h = 1.191062 \times 10^8 \quad [W \cdot \mu m^4 \cdot sr^{-1} \cdot m^{-2}] \ ; \qquad (2)$$
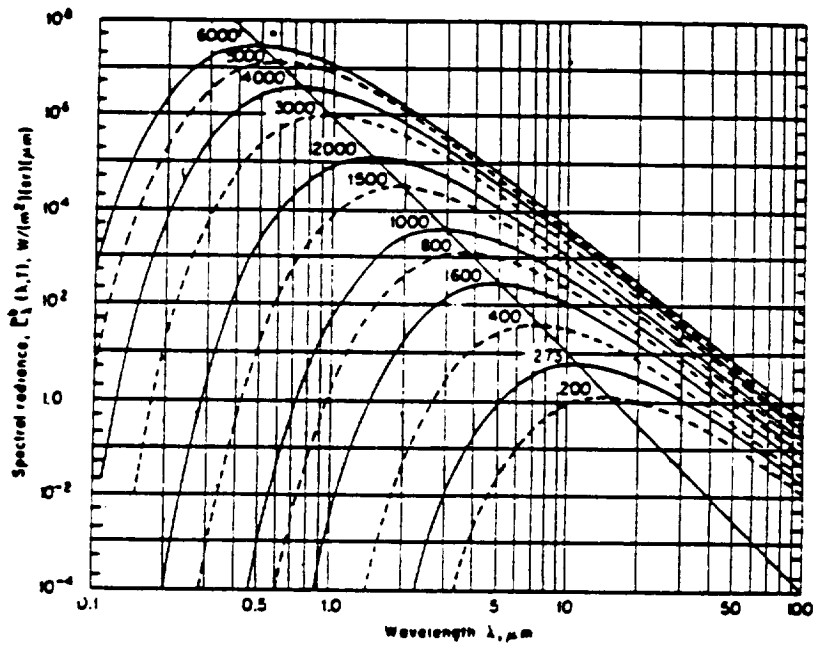
Fig. 2. Spectral radiance of a blackbody, from Planck's radiation law. Temperature in kelvins is shown for each curve.

7

$$c_2 = c \cdot h/k = 1.438786 \times 10^4 \; [\mu m \cdot K] \; ; \tag{3}$$

c is the velocity of light ;

h is Planck's constant ;

k is the Boltzmann constant

The spectral radiance of a surface (Fig. 3) is defined as

$$L_\lambda(\lambda) = \frac{\partial^3 \phi(\lambda)}{\partial A \cdot \cos\theta \cdot \partial\omega \cdot \partial\lambda} \tag{4}$$

where $\partial^3\phi(\lambda)$ is the electromagnetic radiant flux (watts) in the spectral band $\partial\lambda$ at wavelength λ radiating into the elemental solid angle $\partial\omega$ from the elemental area ∂A having its normal at an angle θ with the elemental beam. The spectral radiance of a surface can be recognized as corresponding closely to the quantity perceived by the eye as brightness, and has the very important property of being invariant along a ray. This invariance is the basis for the usefulness of spectral radiance in radiometry

A blackbody surface is, strictly speaking, a purely hypothetical entity. No such material surface exists in practice, but blackbody radiation does exist. An opaque isothermal cavity is filled with blackbody radiation characteristic of
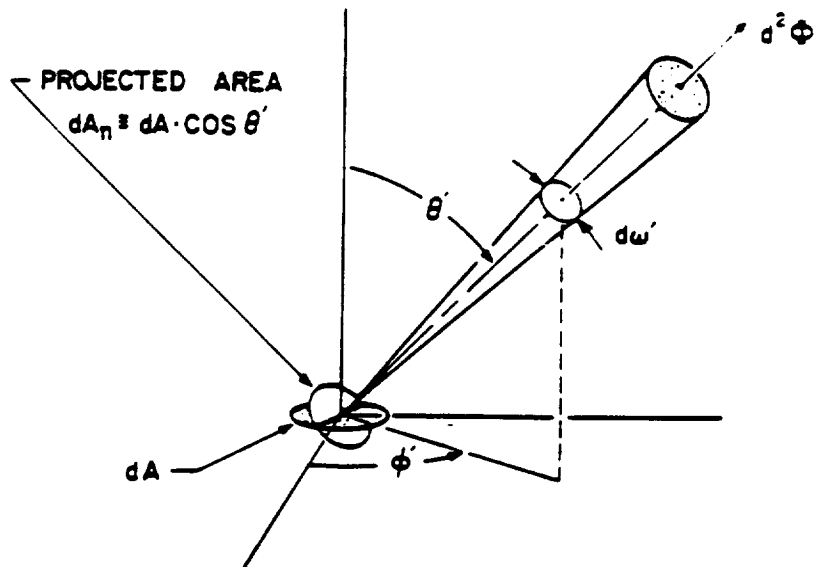
Fig. 3.   Geometric aspects of spectral radiance,
defined to be the derivative of radiance
with respect to wavelength.

9

the temperature of the cavity wall; such radiation is isotropic and "unpolarized." If a small aperture is made through the wall, the escaping radiation very closely approximates that of a blackbody. Because of the invariance of the spectral radiance along a ray, the spectral radiance of the aperture is equal to that of the inner wall of the blackbody opposite the aperture as viewed along the ray. Such cavity radiators have long been used to simulate blackbodies experimentally and can be made to do so with high accuracy. This provides the experimental basis for calibrating a radiometer in terms of blackbody temperature.

NON-BLACKBODIES

All real materials at temperatures above absolute zero also emit thermal radiation, but always less than a blackbody at the same temperature. The treatment of non-blackbody radiation is usually based on a rigorous but somewhat abstract thermodynamic argument that tends to obscure the physical processes giving rise to the observed effects. We consider here an alternative somewhat simplistic but otherwise very helpful model, in which it is shown that an opaque isothermal material can be considered to be filled with blackbody radiation that is continually being absorbed and re-radiated. The outbound radiant flux that originates in a layer just beneath the surface is partially internally

reflected at the surface, in the case of optically homogeneous semi-transparent materials, or from scattering sites just beneath the surface, in the case of strongly scattering dielectrics. The fraction that penetrates the surface and is emitted is defined to be the spectral emissivity, $\varepsilon(\lambda)$, and the fraction that is internally reflected and re-absorbed can be recognized as the spectral reflectance, $\rho(\lambda)$.

As an example, we consider the combined effects of volume absorption and emission, together with surface reflection, on radiation from a thin elemental isothermal slab (Fig. 4) lying a short distance x beneath and parallel to the surface of a thick optically homogeneous semi-transparent semi-infinite solid. For simplicity, we consider only radiation normal to the surface; this does not lead to an error. By Kirchhoff's law, we know that the spectral emissivity of the slab must be equal to its spectral absorptivity:

$$\varepsilon(\lambda) = \alpha(\lambda) = a(\lambda) \cdot dx \qquad\qquad (5)$$

where $a(\lambda)$ is the spectral linear absorption coefficient, the fraction of radiation absorbed per unit path length. The radiance emitted by the elemental slab $[a(\lambda) \cdot dx] \cdot L_{\lambda,b}(\lambda,T)$ in the direction of the surface and normal to it is reduced by absorption by a factor $e^{-a(\lambda) \cdot x}$ and is then

11

dL(λ) a(λ)·dx·L$_{λ,b}$(λ,T)

x dx
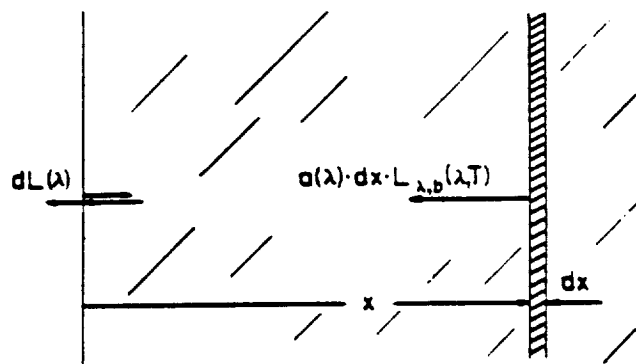
Fig. 4.

further reduced by surface reflection by a factor $1 - \rho(\lambda)$. Thus the contribution to the surface spectral radiance by the elemental slab is

$$dL(\lambda) = [1 - \rho(\lambda)] \cdot e^{-a(\lambda) \cdot x} \cdot [a(\lambda) \cdot dx] \cdot L_{\lambda,b}(\lambda,T) \qquad (6)$$

For a semi-infinite solid slab of thickness x great enough that radiation reflected from the back surface can be neglected,

$$L(\lambda) = [1 - \rho(\lambda)] \cdot L_{\lambda,b}(\lambda,T) \int_{0}^{x} e^{-a(\lambda) \cdot x} \cdot a(\lambda) \cdot dx \qquad (7)$$

Upon integration, this yields

$$L(\lambda) = [1 - \rho(\lambda)] \cdot [1 - e^{-a(\lambda) \cdot x}] \, L_{\lambda,b}(\lambda,T) \qquad (8)$$

From the formal definition of spectral emissivity,

$$L_{\lambda}(\lambda) \equiv \varepsilon(\lambda) \cdot L_{\lambda,b}(\lambda,T) \quad ; \qquad (9)$$

it follows that

$$\varepsilon(\lambda) = [1 - \rho(\lambda)] \cdot [1 - e^{-a(\lambda) \cdot x}] \qquad (10)$$

13

If the material is thick enough that $e^{-a(\lambda) \cdot x}$ is negligible compared to unity, the material is said to be <u>opaque</u>. Under these conditions,

$$\varepsilon(\lambda) = 1 - \rho(\lambda) . \qquad (11)$$

An opaque isothermal body is thus seen to behave as if it were filled with blackbody radiation, part of which is internally reflected by the surface and re-absorbed in the interior of the body; the remainder penetrates the surface and is emitted. It follows that the emissivity of an opaque isothermal body can be described in terms of its reflectivity.

The spectral absorption coefficient varies with wavelength, sometimes markedly; a material specimen such as glass may therefore be opaque at some wavelengths and transparent or semi-transparent at others, whereas metals of appreciable thickness tend to be opaque at all wavelengths. Eq.(10) applies in all cases, but only in spectral regions in which an isothermal body is opaque does it behave as if it were filled with blackbody radiation.

SURFACE ROUGHNESS

The effects of surface roughness are difficult to predict quantitatively, largely because there is presently no fully satisfactory method of characterizing surface topography. Statistical descriptions have been used successfully in some applications. One of the more useful parameters is the optical roughness, σ/λ , where σ is the root mean square of the depth of the surface irregularities. When $\sigma/\lambda > 1$, the reflective behavior is determined by geometrical optics, but when $\sigma/\lambda \ll 1$, the reflective properties depend on diffraction. (DeWitt [2] gives $\sigma/\lambda = 0.15$ as the upper limit of the diffraction range.) Between these two regions, the reflective properties depend on the wavelength and the character of the surface topography [3] and are not well understood.

We know from Kirchhoff's law that, for any given direction from the surface and for any given component of polarization, the spectral absorptivity of a surface is equal to its spectral emissivity, i.e.,

$$\alpha(\lambda) = \epsilon(\lambda) \ . \tag{12}$$

This allows us to explain the fact that a roughened surface always has a higher emissivity than a smooth surface of

the same material (Fig. 5 and 6). If one considers radiation incident on a surface for which $\sigma/\lambda > 1$, where geometrical optics applies, a ray striking a smooth flat surface can reflect only once before leaving the surface, whereas a ray striking a pit may be reflected more than once before leaving the pit. The deeper the pit relative to its width, the greater the probable number of reflections that will occur before that radiant flux leaves the pit. Since some energy is absorbed at each reflection, a larger fraction of incident radiation is absorbed by a pit, on the average, than by a smooth surface. Since the absorptivity of the pitted surface is therefore higher than that of the smooth surface, so must be its emissivity, in accordance with Kirchhoff's law. The effects of surface roughness in the case of aluminum can be seen in Fig. 5 and 6.

For the case in which $\sigma/\lambda << 1$, diffraction dominates the directional distribution of reflected radiation. Assuming a Gaussian distribution of σ, Bennett and Porteus [7] extended earlier work done by Davies [8] and Chinmayanandam [9], based on diffraction theory, to obtain the following expression for the special case of normally incident irradiation:

$$\frac{\rho}{\rho_0} = e^{-(4\pi\cdot\sigma/\lambda)^2} + 32\cdot\pi^4\cdot(\sigma/\lambda)^4\cdot(\Delta\theta)^2/m^2 \qquad (13)$$
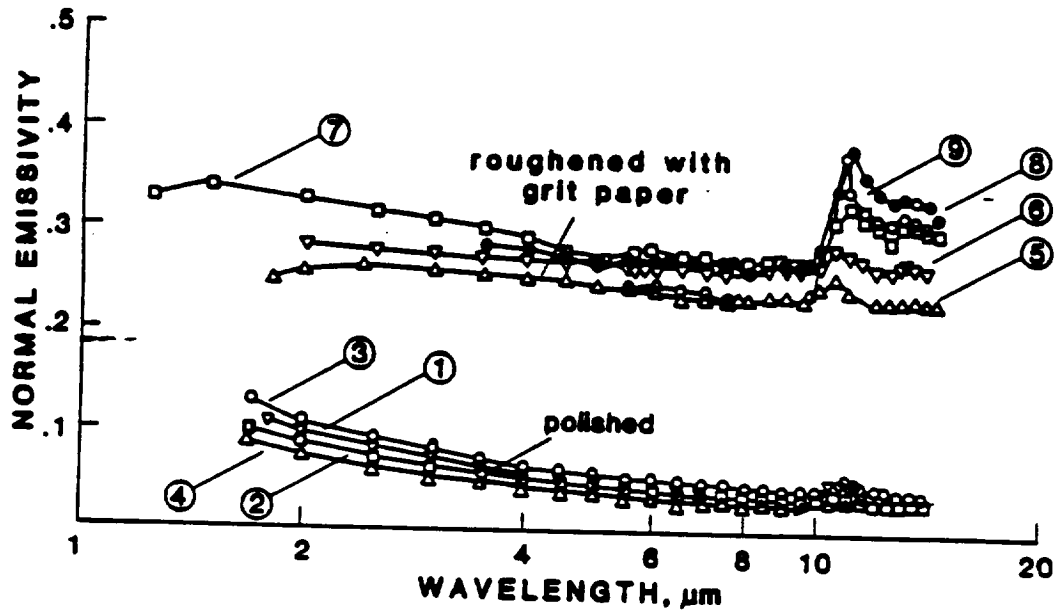
Fig. 5. Normal spectral emissivity of aluminum 11XX series. See Table 1 for experimental details.
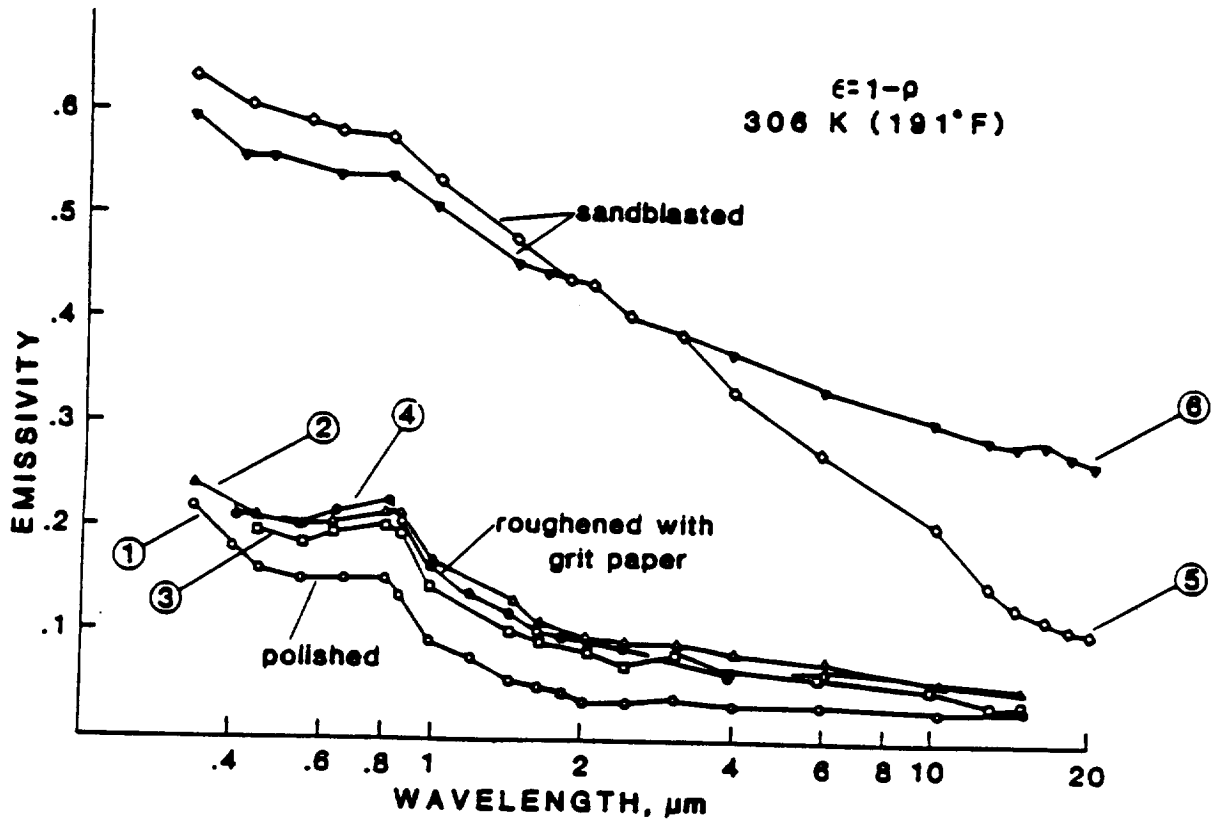
Fig. 6. Angular spectral emissivity of alloy 7075 (aluminum + Zn 7.5% + Mg 2.5% + Cu 1.6%) measured at 25° to the normal. See Table 2 for experimental details.

TABLE 1

Sample description and conditions for normal spectral emissivity of aluminum, 11XX series shown in Fig. 5 [4].

Curve No.	Temperature K	Reported Error, %	Composition (Weight Percent), Specification and Remarks
1	599	±20	99.7 Al, 0.11 Si, 0.01 Cu, 0.01 Mg, <0.01 Mn, Ni and Zn; cylindrical tube; heated at 467K for 15 hrs; polished with Carnu on Selvyt cloth; surface roughness 0.08 μm (center line average); data extracted from smooth curve; error given in the wavelength range 2 to 10 μm.
2	697	±20	Above specimen and conditions except heated at 697K for 20 hrs before measurement.
3	805	±20	Above specimen and conditions except heated at 805K for 15 hrs before measurement.
4	599	±20	Above specimen and conditions.
5	462	±10	99.7 Al, 0.11 Fe, 0.11 Si, 0.01 Cu, 0.01 Mg, <0.01 Mn, Ni and Zn; tube; heated for 25 hrs at 462K; roughened and knurled with grade 180 silicon carbide paper, surface roughness 2.9 μm (center line average); data extracted from a smooth curve; error given over the wavelength range 2 to 10 μm.
6	599	±10	Above specimen and conditions except heated at 598K for 22 hrs before measurement.
7	715	±10	Above specimen and conditions except heated at 715K for 27 hrs before measurement.
8	803	±10	Above specimen and conditions except heated at 787K for 17 hrs before measurement.
9	461	±10	Above specimen and conditions.

NOTE: Original publication is reference [5].

18

TABLE 2

Sample description and conditions for angular spectral emissivity of 7075-T6 alloy shown in Fig. 6 [4].

Curve No.	Temperature K	Composition (Weight Percent), Specification and Remarks
1	306	Aluminum 7075-T6; nominal composition: 5.6 Zn, 2.5 Mg, 1.6 Cu, 0.30 Cr, and Al balance, polished surface roughness .08 μm (RMS); authors assumed ε=α=1-ρ (25°, 2π).
2	306	Aluminum 7075-T6; nominal composition: 5.6 Zn, 2.5 Mg, 1.6 Cu, 0.30 Cr, and Al balance; sanded with 150 grit paper (grit sieve opening 104 μm); RMS surface roughness in microinches; in line 0.3 μm, across 2 μm; authors assumed ε=α=1-ρ(25°,2π).
3	306	Aluminum 7075-T6; nominal composition: 5.6 An, 2.5 Mg, 1.6 Cu, 0.30 Cr and Al balance; sanded with 80 grit paper (grit sieve opening 175 μm); RMS surface roughness in microinches; in line 1 μm, across 4 μm; authors assumed ε=α=1-ρ(25°,2π).
4	306	Aluminum 7075-T6; nominal composition: 5.6 Zn, 2.5 Mg, 1.6 Cu, 0.30 Cr and Al balance; sanded with 40 grit paper (grit sieve opening 42 μm); RMS surface roughness in microinches; in line 1.9 μm, across 7.3 μm; authors assumed ε=α=1-ρ(25°,2π).
5	306	Aluminum 7075-T6; nominal composition: 5.6 Zn, 2.5 Mg, 1.6 Cu, 0.30 Cr and Al balance; sandblasted with 250 mesh silicon carbide (mesh opening 60 μm); RMS surface roughness .3 μm; authors assumed ε=α=1-ρ(25°,2π).
6	306	Aluminum 7075-T6; nominal composition: 5.6 Zn, 2.5 Mg, 1.6 Cu, 0.30 Cr and Al balance; sandblasted with 60 mesh silicon carbide (mesh opening 250 μm); RMS surface roughness 7 μm; authors assumed ε=α= 1-ρ(25°, 2π).

NOTE: Original publication is reference [6].

where ρ is the reflectance of the roughened surface for normally incident radiation, ρ_0 is the corresponding reflectance of an ideally smooth surface, $\Delta\theta$ is the half angle of the field of view and m is the rms slope of the pitted surface. This expression was experimentally verified for aluminized ground glass surfaces, with good accuracy. The first term on the right corresponds to specular (coherent) reflection and the second to diffuse reflection. Note that specular reflection dominates at long wavelengths and diffuse reflection dominates at short wavelengths. A more complete treatment of the scattering of electromagnetic waves from rough surfaces can be found in reference [10].

OXIDATION

Oxidation can also have a major effect on the emissivity of metal surfaces [1]. We consider aluminum as an example. A tightly bound oxide barrier layer is formed on an initially unoxidized surface, impeding the rate of subsequent oxidation. A porous oxide layer then grows more gradually on top of the barrier layer. In the case of relatively pure aluminum (Fig. 7), these layers have only a small effect on the emissivity, but alloys containing magnesium are much more strongly affected. For all aluminum alloys containing significant amounts of magnesium, heating at a fixed temperature above 317 deg C (603 deg F) causes emissivity to

20
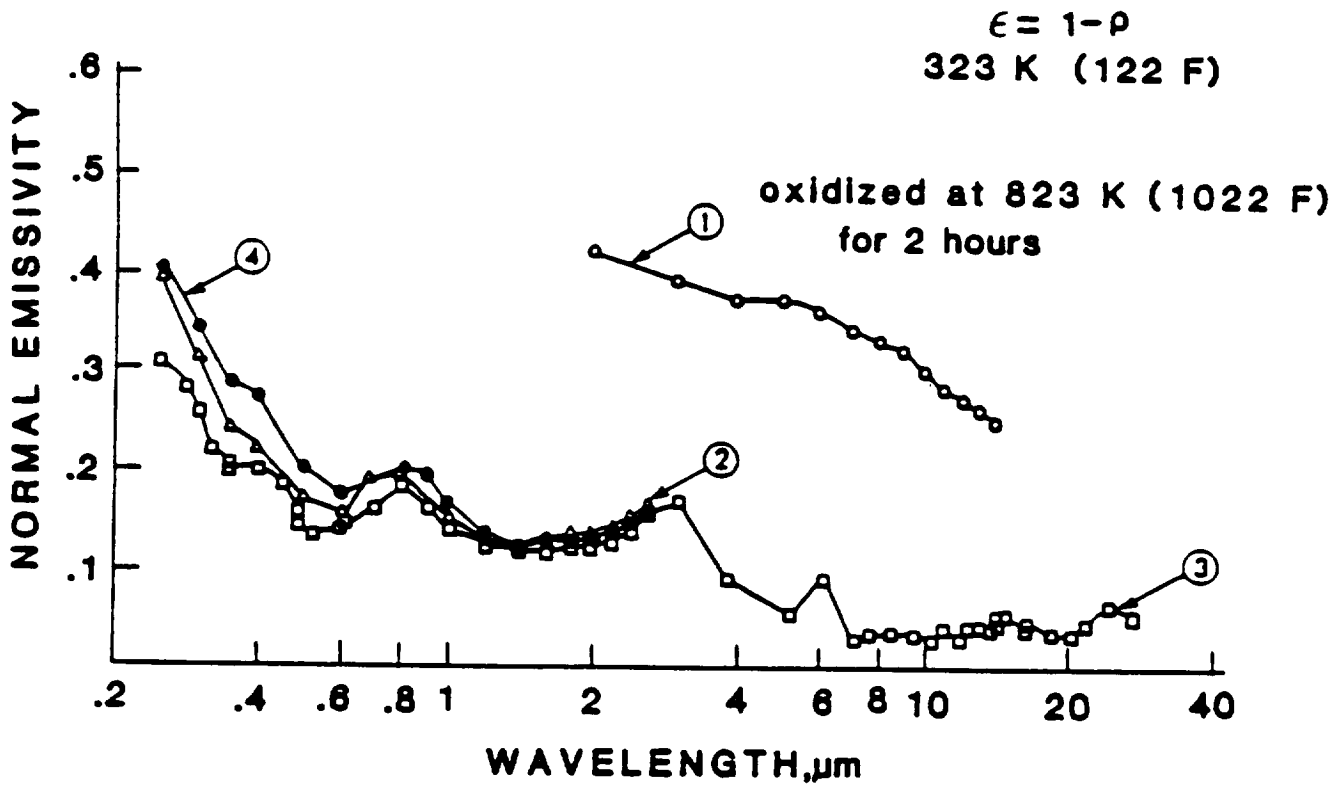
Fig. 7. Normal spectral emissivity of alloy 2024 (Aluminum + Cu 4.4% + Mg 1.5% + Mn 0.6%). See Table 3 for experimental details.

TABLE 3

Sample description and conditions for normal spectral emissivity of 2024 alloy shown in Fig. 7 [4].

Curve No.	Temperature K	Composition (Weight Percent), Specifications and Remarks
1	823	Aluminum alloy 2024; nominal composition; 4.5 Cu, 1.5 Mg, 0.6 Mn, Al balance; oxidized in air for 2 hrs; measured in air.
2	323	Aluminum alloy 2024; nominal composition; 4.5 Cu, 1.5 Mg, 0.6 Mn, Al balance; surface roughness 0.04 μm (center line average); measured in nitrogen; computed by $\varepsilon = 1 - \rho(2\pi, 5°)$, [Author's designation Specimen 1].
3	323	Different sample, same as above specimen and conditions except surface roughness 0.2 μm (center line average); [Author's designation: Specimen 3].
4	323	Different angle, same as above specimen and conditions except surface roughness 0.08 μm (center line average); [Author's designation: Specimen 4].

NOTE: Original publication is reference [4] for curve 1 and reference [12] for curves 2, 3 and 4.

increase at a rate that is a function of the magnesium concentration, nearly independently of other factors. This effect has its roots in the relatively high vapor pressure of magnesium, which causes the magnesium to migrate to the surface where it either evaporates or oxidizes. This causes roughening of the interface between the alloy and the oxide, thus increasing the emissivity. The outward migration of magnesium also causes dislodged microscopic aluminum be trapped in the oxide layer, further increasing the emissivity due to optical scattering effects. The effects of oxidation are illustrated in Fig. 7. Haugh [1] found oxidation to be "the most serious obstacle for applying radiation thermometry to aluminum alloys." This problem could be largely eliminated if a satisfactory method could be found for measuring the emissivity of aluminum alloys during the manufacturing process.

Emissivity effects for opaque surfaces can thus be accounted for in terms of reflection effects, and a knowledge of the reflective properties of such a surface forms much of the basis for an understanding of its emissivity. For a closer look at reflectance effects, we now consider some well-known conclusions from electromagnetic field theory.

FRESNEL REFLECTION

The Fresnel formulas, which can be derived from Maxwell's equations, are expressions for the reflectivity of an ideally smooth (specular) and optically homogeneous plane material surface for incident electromagnetic radiation. The polarized components of reflectivity are expressed in terms of the optical "constants" n (the refractive index) and κ (the extinction coefficient) of the surface material, and θ, the angles of incidence and reflection. These are given below for two orthogonal components of polarization:

$$\rho_{\lambda \parallel}(\lambda, \theta) = \frac{a^2 + b^2 - 2 \cdot a \cdot \sin \theta \cdot \tan \theta + \sin^2\theta \cdot \tan^2\theta}{a^2 + b^2 + 2 \cdot a \cdot \sin \theta \cdot \tan \theta + \sin^2\theta \cdot \tan^2} \rho_{\lambda \perp}(\lambda, \theta) \quad (14)$$

$$\rho_{\lambda \perp}(\lambda, \theta) = \frac{a^2 + b^2 - 2 \cdot a \cdot \cos \theta + \cos^2 \theta}{a^2 + b^2 + 2 \cdot a \cdot \cos \theta + \cos^2 \theta} \quad (15)$$

where

$$2 \cdot a^2 = [(n^2 - \kappa^2 - \sin^2\theta)^2 + 4 \cdot n^2 \cdot \kappa^2]^{1/2} + n^2 - \kappa^2 - \sin^2\theta \quad (16)$$

and

$$2 \cdot b^2 = [(n^2 - \kappa^2 - \sin^2\theta)^2 + 4 \cdot n^2 \cdot \kappa^2]^{1/2} - (n^2 - \kappa^2 - \sin^2\theta) \quad (17)$$

where $\rho_\perp$ is the reflectivity for plane polarized incident radiation with the direction of vibration of the electric vector perpendicular to the plane of incidence and $\rho_\parallel$ is the reflectivity when the direction of vibration of the electric vector is parallel to the plane of incidence. Note that the refractive index n and extinction coefficient κ properties of the material, are both dependent on wavelength and, at least to some extent, on temperature, and are therefore not truly constants.

Since an incident plane polarized wave of any orientation can always be resolved into two orthogonal components, one perpendicular and one parallel to the plane of incidence, the above expressions are sufficient to cover all cases of specular reflectance.

It can be shown that eq.(11) holds for each of the polarized components:

$$\varepsilon_\perp(\lambda) + \rho_\perp(\lambda) = 1 \qquad (18)$$

and

$$\varepsilon_\parallel(\lambda) + \rho_\parallel(\lambda) = 1 \qquad (19)$$

and that for unpolarized incident radiation,

$$\rho(\lambda) = \frac{1}{2} \cdot [\rho_\perp(\lambda) + \rho_\parallel(\lambda)]$$ (20)

Plots of the reflectivities corresponding to eq. (14), (15), and (20) are given in Fig. 8 for a range of values of n and κ, and for angles of incidence up to 90 degrees. The extinction coefficient, and therefore the reflectivity, is characteristically low in materials classified as dielectrics, is characteristically high in materials classified as electrical conductors, and is very high in the case of resonance absorption. For dielectrics, typically 1.3 < n < 3, and κ < 1. Values of n and κ for a number of metals are given in Table 4, for a few selected wavelengths.

Changes in the phase angle of an incident wave occur during the reflection process, giving rise to additional polarization effects. As a result, thermal radiation from a smooth metallic surface viewed off-normal is elliptically polarized. In the case of a rough surface, on the other hand, the angle of incidence of a beam of radiation depends on the surface micro-topography and varies across the width of the beam. The reflected radiation thus contains many different components of polarization, the net effect of which is difficult to characterize in practice. An understanding of these and other such effects is likely to be important to future

Reflectance, %

k₁ = 3.3

k₁ = 2.3

k₁ = 1.3

k₁ = 0.3

k₁ = 0

Angle of incidence, deg

n₁/n₀ = 0.3   0.8   1.3   1.8   2.3
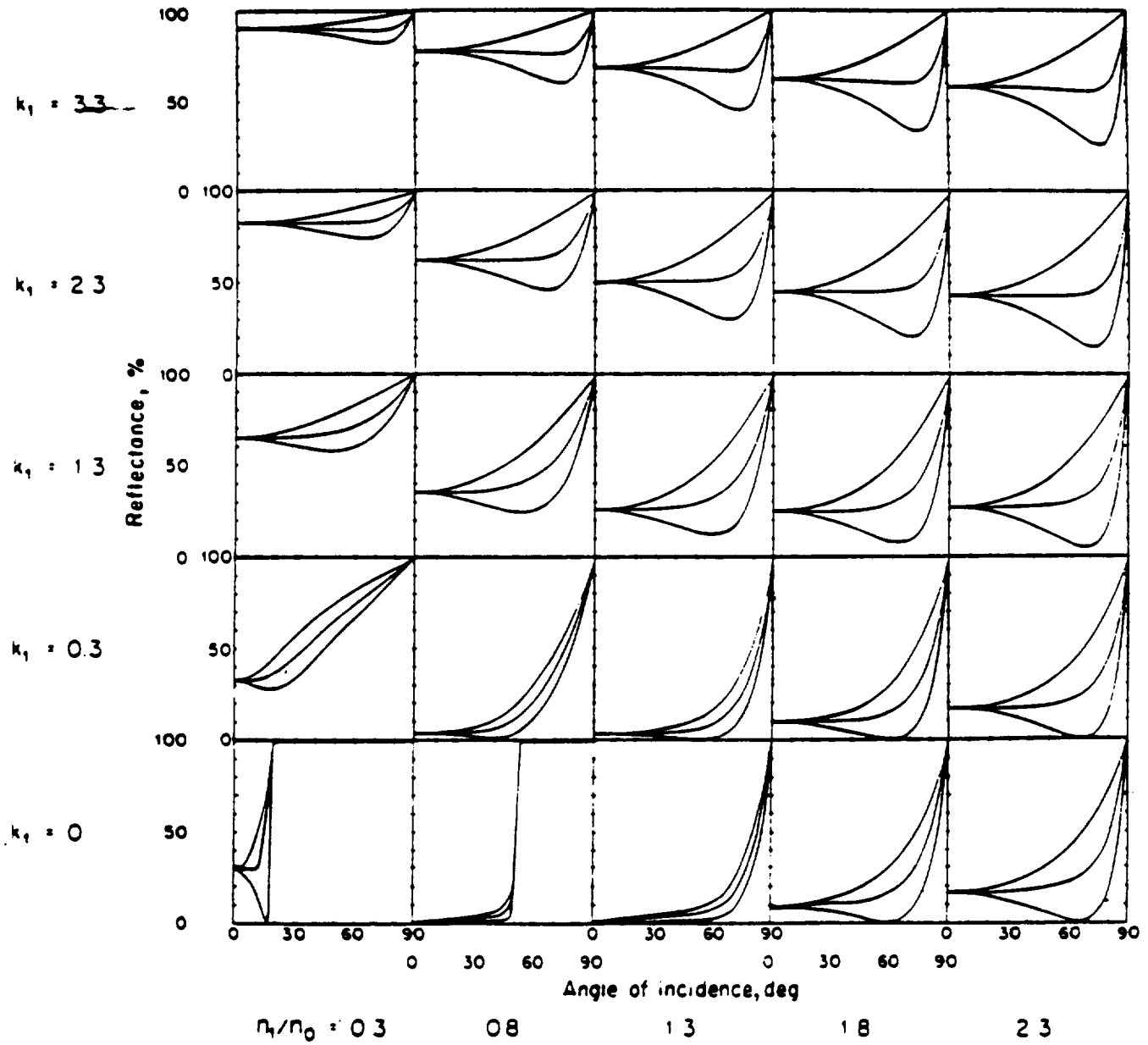
Fig. 8. $\rho_\perp$ (upper curves), $\rho_{||}$ (lower curves), and $\rho_{av} = (\rho_\perp + \rho_{||})/2$ as a function of angle of incidence for various values of the refractive index ratio n_1/n_0 and κ_1 . The incident medium, having refractive index n , is assumed to be non-absorbing. Adapted from J.M. & H.E. Bennett, Handbook of Optics [13].

TABLE 4

Optical Constants of Selected Metals

	λ	n	κ
Aluminum	12 μm	33.6	76.4
Cobalt	0.589	2.120	1.900
Copper	0.650	0.44	3.26
	2.25	1.03	11.7
	4.00	1.87	21.3
	4.20	1.92	22.8
	5.50	3.16	28.4
Gold	0.589	0.47	2.83
	2.00	0.47	12.5
	5.00	1.81	32.8
Iron	0.589	1.51	1.63
Magnesium	0.589	0.37	4.42
Nickel	0.589	1.79	3.33
	2.25	3.95	9.20
Platinum	5.00	11.5	15.7
Silver	0.589	0.18	3.64
	2.25	0.77	15.4
	4.37	4.34	32.6
	4.50	4.49	33.3
Sodium	0.589	0.005	522
Steel	0.589	2.485	1.381

NOTE: There are often significant differences between values for optical
constants determined by different investigators. Those given above
are typical.

28

developments in radiation thermometry, since consideration of the polarized components of radiation taken separately offers significant potential advantages over the consideration only of unpolarized radiation. As an example, consider the reflectivities illustrated in Fig. 8 It is clear that $\rho_\parallel$ is much smaller than $\rho_\perp$ in certain angular regions off-normal, and therefore that $\varepsilon_\parallel$ is much larger than $\varepsilon_\perp$ at those angles. Similarly, $\varepsilon_\parallel$ is substantially larger than the unpolarized emissivity in those regions. The existence of polarized components of reflectivity and emissivity also creates the possibility of other useful relationships, such as Abele's condition [14]. For a further discussion of polarization effects, the reader is referred to standard texts on optics [15,16].

The Fresnel formulas are reliable to the extent that surface conditions approach the ideal and the correct values of the optical constants are known. In practice, surface conditions are often far from ideal and optical constants can be strongly affected by the presence of impurities and inhomogeneities. When allowances are made for non-ideal surface conditions such as roughness, impurities, inhomogeneities and coatings, however, the Fresnel formulas provide a sound basis for understanding emissivity effects.

The values of the optical constants can be determined experimentally by a sophisticated experimental procedure known as ellipsometry [13]. This requires very nearly ideal optically smooth homogeneous surfaces of the material under consideration. In the case of pure aluminum, such surfaces can be prepared by vacuum vapor-deposition on an optically flat glass plate. When values of n and κ determined by ellipsometry for vapor deposited aluminum are substituted into the Fresnel equations, the computed values of spectral reflectance compare very favorably with experimentally determined values [1], as can be seen in Fig. 9.

Expressions for n and κ can also be deduced from quantum theory and expressed in terms of atomic constants and wavelength, so it is possible in principle to determine emissivity from physical theory. Since the appropriate physical constants are not all sufficiently well known in practical situations, however, emissivities are determined experimentally in practice. The theory is used primarily to correlate emissivity values obtained experimentally under one set of conditions with the corresponding values to be expected under a different set of conditions, most commonly at different temperatures.

Free electron theory, which allows predictions of emissivity as a function of electrical resistivity and wavelength, is

30
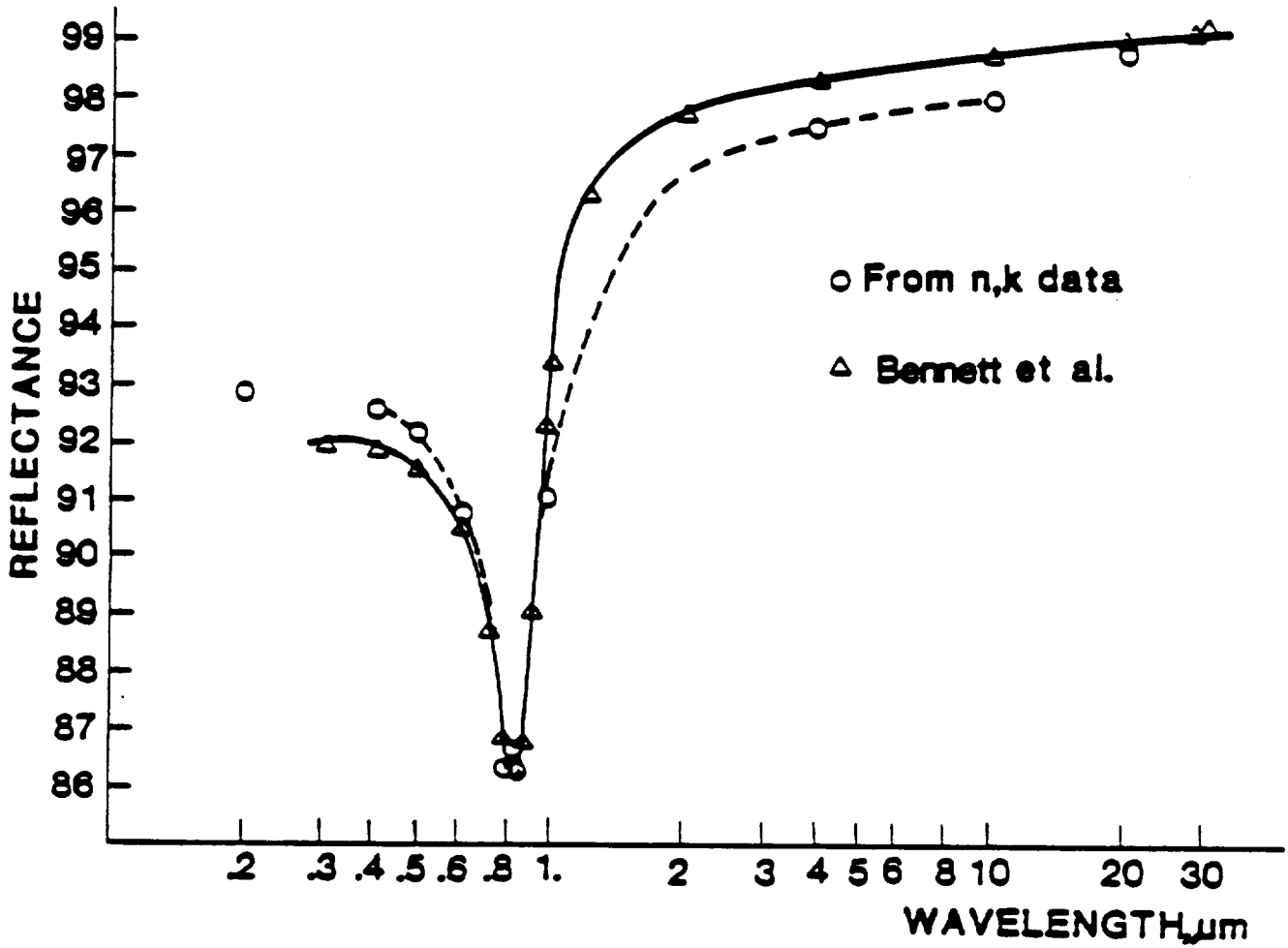
Fig. 9. Experimental values for spectral reflectivity of aluminum vacuum evaporated on optical plate. See Table 5 for numerical values.

TABLE 5

Experimentally Determined Reflectance for
Aluminum Vacuum Evaporated on Optical Plate

λ mu	1	2	3
		Reflectance	
.2	.928		
.4	.926		.919
.65	.907		.906
.8	.864		.868
.95	.912		.924
1.0			.940
1.2			.964
1.5			.974
2.	.968		.978
4.	.975		.983
6.	.978		.986
8.	.979		.987
10.	.980	.978	.988
12.	.982		.988
14.		.984	
16.		.988	.989
18.		.989	.990
20.		.989	.990
22.			.991
24.			.991
26.			.992
28.			.992
30.			.993

1. Hess[17], Schultz [18]; from n and κ values.

2. Lenhan [21]; from n and κ values.

3. Bennett [22]; direct measurement.

accurate only at wavelengths longer than those ordinarily used for radiation thermometry. Discussions of free electron theory as it applies to predicting emissivity can be found in reference [4], with examples in the case of aluminum in reference [1].

SUBSURFACE EFFECTS IN DIELECTRICS

The depth to which radiation penetrates is much greater in dielectrics than in electrical conductors, and the reflectivity of the air-dielectric interface is much lower. Emission from dielectrics, being primarily a volume effect, therefore tends to be diffuse. Since reflection by the air-dielectric interface is a relatively small effect, surface roughness plays only a minor role.

The decrease in emissivity for angles approaching the tangent of optically smooth and homogeneous materials is caused by refraction and internal reflection of internally emitted radiation. In the case of dielectrics (Fig. 10), total internal reflection occurs for off-normal angles beyond the critical angle, which is determined by the refractive index. This is not true of conductors, which tend to have their maximum emissivity at around 75-85 degrees off normal (for ideally smooth surfaces), with the emissivity dropping to zero along the tangent as in the case
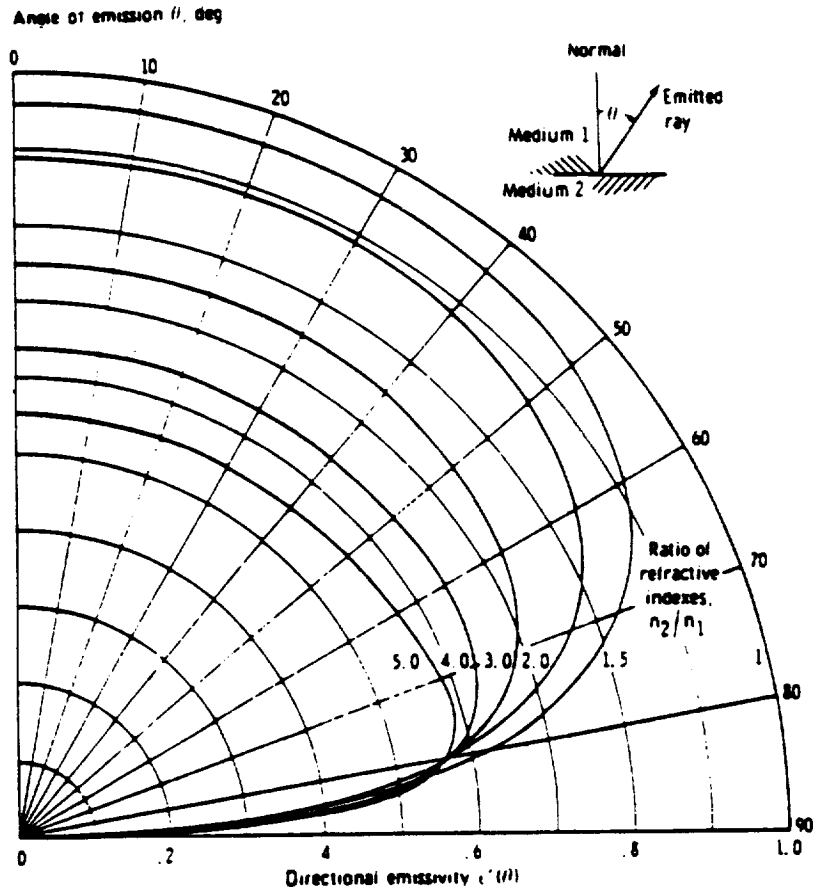
Fig. 10. Directional emissivity of an optically smooth opaque dielectric, as predicted from electromagnetic theory [23], for unpolarized radiation.

of dielectrics. The maximum in the emissivity of conductors is caused by the minimum in the reflectivity at those angles, as seen in Fig. 8. The tendency for diffuse emission by dielectrics is further enhanced when the material is optically inhomogeneous, as in the case of polycrystalline dielectrics, where reflection by subsurface scattering from grain boundaries, pores and inclusions dominates both the reflectance and the emissivity. Thus we see that there is a characteristic difference between the emissivity of dielectrics (high and diffuse) and that of metals (low and substantially more directional).

COMPLEMENTARITY

Eq.(11) provides us with an indirect but commonly used way to determine the spectral emissivity of opaque surfaces, that is, by measuring spectral reflectance. Care must be taken, however, to assure that the kind of spectral reflectance measured is complementary to the kind of spectral emissivity desired. In radiation thermometry, one ordinarily wants directional rather than hemispheric spectral emissivity, and the complementary quantity is the directionally incident-hemispherically reflected spectral reflectance. This can be seen by considering a ray incident on a surface, which may be either diffuse or specular, from direction i. A fraction $\alpha_i(\lambda)$, the spectral directional absorptivity, is

35

absorbed and the remaining fraction $\rho_{ih}(\lambda)$, the spectral directional-hemispherical reflectance, is reflected into the hemisphere above the surface. From the conservation of energy, we therefore have

$$\alpha_i(\lambda) + \rho_{ih}(\lambda) = 1 \quad .\tag{21}$$

It follows directly from Kirchhoff's law that

$$\varepsilon_i(\lambda) + \rho_{ih}(\lambda) = 1\tag{22}$$

This implies that the reflectance must be that corresponding to directionally incident radiation reflected into the hemisphere above the surface, where the direction of incidence is the opposite of that in which the emissivity is desired. From the Helmholtz reciprocity theorem [24], it is known that the reflectance for hemispherically incident-directionally reflected radiation is the same as that for directionally incident-hemispherically reflected radiation. Helmholtz reciprocity applies in the vast majority of cases encountered in radiation thermometry. Measurements are usually made with hemispherically-incident radiation, for which appropriate measurement techniques have been developed [25]. Note also that if such measurements are made at one temperature, such as room temperature, the actual values of spectral reflectance and spectral emissivity will be somewhat

different at other temperatures because of at least some
degree of temperature dependence in the optical constants.

ENVIRONMENTAL EFFECTS

ATMOSPHERIC EFFECTS

The optical medium between the thermally radiating target and
the radiation thermometer includes atmospheric gases, vapors,
dust and any windows that might be in the sight path. The
atmosphere in most cases is composed of gaseous nitrogen,
oxygen, water and carbon dioxide, with other gases also
present to a significant extent in a variety of industrial
processes. These gases, vapors and dust particles absorb,
emit and scatter radiation, and their effects on radiometric
measurements range from negligible to severe. By Kirchhoff's
law, emission is proportional to absorption. If the concen-
tration and temperature of a vapor-free atmosphere were
uniform, it would radiate in accordance with eq.(8), with
$\alpha(\lambda) = 0$; in practice, however, the concentration and
temperature of these atmospheric constituents tend to be
highly variable with time and position, and vapors are
frequently present.

37

Although the physics of the absorption, emission and scatter-
ing processes is generally understood, the conditions under
which it applies are highly variable and seldom well enough
known quantitatively to allow for practical corrections to
be determined and applied. Once recognized, however, this
need not be a serious problem in most cases (gaseous absorp-
tion and emission), since there are spectral regions - known
as atmospheric windows - in which the atmosphere does not
absorb and therefore does not emit radiation. These spectral
regions are clearly evident in Fig. 11. If radiometric
measurements are confined to those spectral regions, atmos-
pheric interference - in the absence of particulate scatter-
ing - is entirely negligible. When scattering effects are
strong, however, as in the case of suspended particulates
(dust), steam clouds or sooty flames, the use of an atmos-
pheric window alone does not correct the problem. It is then
common practice for the radiometer to view through a tube
purged with a clean dry (transparent) gas, using a filter to
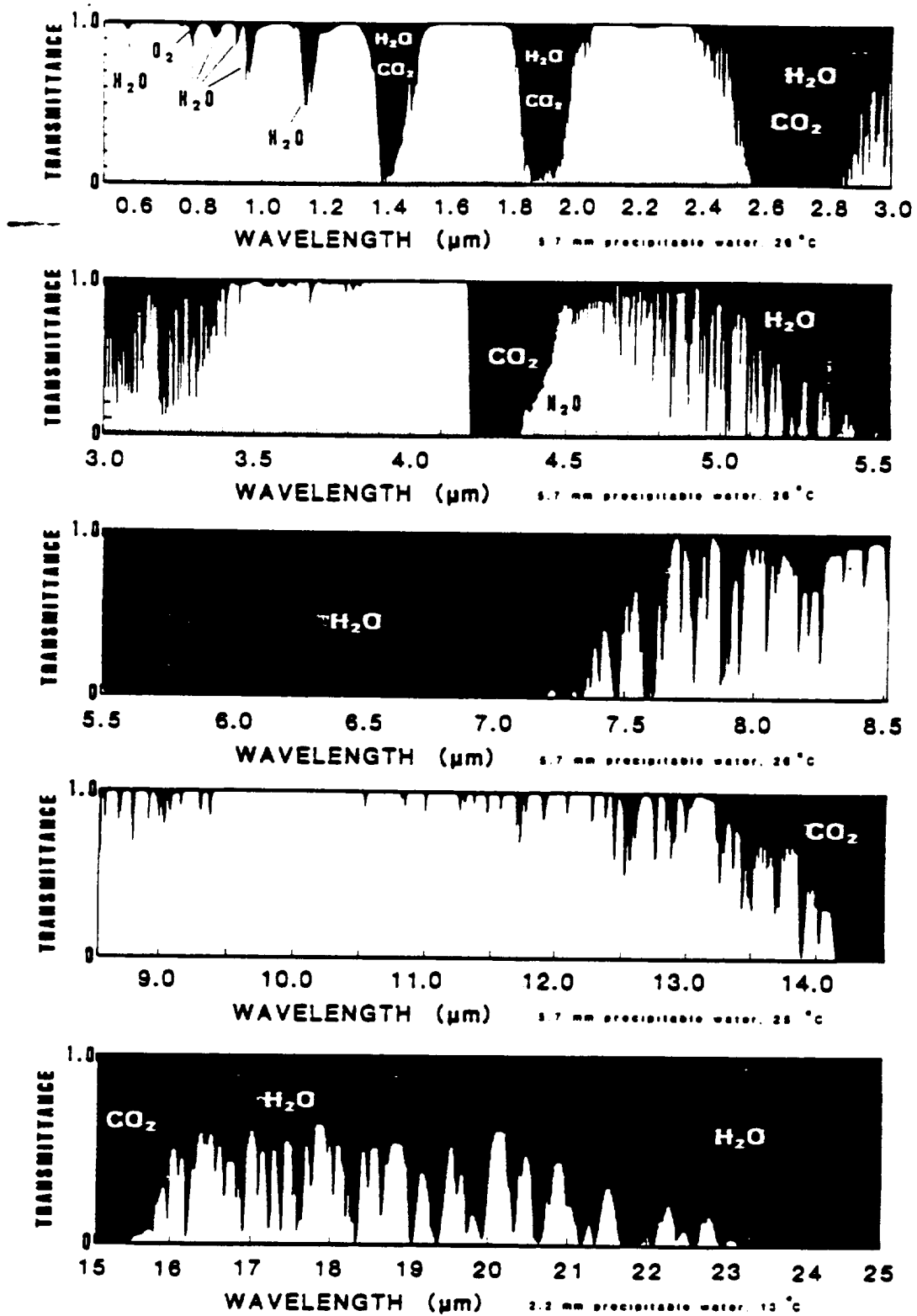limit the radiometer passband to an atmospheric window.

Fig. 11. Atmospheric transmission at sea level over a 300 meter path.
From NRL report 5453 by H. W. Yates and J. H. Taylor, 1960
[26]. Adapted by G. D. Nutter

REFLECTED RADIATION

Radiation originating from extraneous sources and reflecting from a target surface increases its spectral radiance and causes errors in radiometric temperature measurements:

$$L_\lambda(\lambda)_{observed} = L_\lambda(\lambda)_{emitted} + L_\lambda(\lambda)_{reflected} \tag{23}$$

The magnitude of the reflected spectral radiance depends on the spectral radiance of the extraneous source, the solid angle subtended by it from the target area, and the bidirectional spectral reflectance distribution function of the target. When the magnitude of the reflected radiance is comparable to or larger than that of the emitted radiance, errors in temperature measurement tend to be large. This is most likely to occur when target temperatures are not greatly different from ambient temperature, and the problem intensifies as target temperatures decrease. At target temperatures below about 100-150 deg C, reflected radiation is usually the dominant source of error in radiation thermometry.

The target can often be successfully shielded from the extraneous radiation by a suitably placed screen. It is also sometimes possible to measure the reflected component separately with the aid of a relatively cool auxiliary reflector of known reflectance located near the target and

subjected to the same irradiance, and to then subtract that component from the observed spectral radiance (eq.(23)). The trend in recent years has been toward trying to develop techniques for dealing with reflected radiation, some of which have met with a significant degree of success [27].

SEVERE AMBIENT TEMPERATURE AND DUST ENVIRONMENTS

It is frequently necessary to use radiation thermometers in severe environments such as those commonly found in industry, where the high temperatures would destroy an unprotected instrument. Cooling is satisfactorily accomplished by the use of air or water flowing through tubes provided in the instrument housing to regulate its temperature. Air or some other dry gas to purge dust from the sight path and lens is also usually supplied through tubes in the instrument housing.

WINDOWS

Radiation thermometers must often view targets through windows, thus reducing the spectral radiance by a factor equal to the (external) spectral transmittance $\tau(\lambda)$ of the window:

$$\frac{L_\lambda(\lambda,T)_{apparent}}{L_\lambda(\lambda,T)} = \tau(\lambda) \qquad (24)$$

A simple expression for the difference between the (true) temperature and the apparent temperature of the target viewed through the window can be obtained by substituting the expression for $L_{\lambda,b}(\lambda,T)$ from Wien's law into eq.(24):

$$\frac{1}{T} = \frac{1}{T_{apparent}} + \frac{\lambda}{c_2} \cdot \ln \tau(\lambda) \quad , \qquad (25)$$

where τ can be either the mean effective wavelength of the instrument or, if the spectral bandwidth is sufficiently narrow, the reference wavelength, which can be determined more accurately. The theory of effective and reference wavelengths is very important in high accuracy applications, such as in realizing the temperature scale, and has been highly developed [28,29,30]. The mean effective wavelength is an appropriately averaged wavelength that accounts for the spectral response characteristics of the radiometer and is found to be a function of T and $T_{apparent}$. The reference wavelength, on the other hand, is determined primarily by the filter characteristics and is independent of T and $T_{apparent}$.

For sufficiently narrow bandwidths, λ is only very weakly dependent on T and $T_{apparent}$, and we then define the "A-value" of the window such that

42

$$\frac{1}{T_{apparent}} - \frac{1}{T} \equiv A \quad . \tag{26}$$

In ordinary applications the A-value of the window is treated as a constant; once determined for any pair of temperatures, it can be used to relate any other pair of temperatures. The International Practical Temperature Scale above the gold point is generated in this manner from a single known temperature (a blackbody at the freezing temperature of gold, 1064.43 deg C) using a set of filters of known transmittance and a known spectral band, except that the Planck distribution is used instead of Wien's law in eq.(24). This technique can also be used to extrapolate from any given temperature on one range of a radiation thermometer to a temperature on a higher range by viewing a target through a gray filter having a known A-value, thus calibrating the upper range in terms of the lower range as in the case of the disappearing-filament optical pyrometer.

THE RADIATION THERMOMETER

THE RADIOMETER MEASUREMENT EQUATION

The elemental radiant flux input to the radiometer (Fig. 1) from the target area A_t into the solid angle ω_t is obtained from eq.(4):

$$\partial^3\phi = L_\lambda(\lambda) \cdot \partial A_t \cdot \cos\theta \cdot \partial\omega_t \cdot \partial\lambda \tag{27}$$

The radiant flux is attenuated by $\tau(\lambda)$, the spectral transmittance of the optical system, as determined primarily by a bandpass filter, and is then incident on the photodetector having a spectral responsivity $R(\lambda)$; the photodetector generates an elemental output signal

$$\partial^3 S = R(\lambda) \cdot \tau(\lambda) \cdot \partial^3\phi = R(\lambda) \cdot \tau(\lambda) \cdot L_\lambda(\lambda) \cdot \partial A_t \cdot \cos\theta \cdot \partial\omega_t \cdot \partial\lambda \tag{28}$$

from which we have the radiometer measurement equation:

$$S = \iiint_{\lambda\ \omega\ A_t} R(\lambda) \cdot \tau(\lambda) \cdot L_\lambda(\lambda) \cdot \partial A_t \cdot \cos\theta \cdot \partial\omega_t \partial\lambda \tag{29}$$

44

From the Lagrange Invariant, $A_t \cdot \cos\theta \omega_t = A_{n,d} \cdot \omega_d$, where $A_{n,d}$ is the projection of the field-defining aperture area normal to the optical axis and ω_d is the solid angle of radiant flux incident on that aperture. Where $L_\lambda(\lambda)$ varies only slowly with direction, we therefore have

$$S = A_{n,d} \cdot \omega_d \cdot \int_0^\infty R(\lambda) \cdot \tau(\lambda) \cdot L_\lambda(\lambda) \cdot d\lambda \qquad (30)$$

If the spectral band $\delta\lambda$ centered about λ is sufficiently narrow, the radiometer measurement equation can be simplified to the form

$$S = K(\lambda_c) \cdot L_\lambda(\lambda_c) \qquad (31)$$

where

$$K(\lambda_c) = A_{n,d} \cdot \omega_d \cdot R(\lambda_c) \cdot \tau(\lambda_c) \cdot \delta\lambda \qquad (32)$$

Thus we see that the output signal of an ideal radiometer is directly proportional to the spectral radiance of the target.

The three dimensional form of the Lagrange Invariant is also known as the <u>throughput</u>, the <u>geometric extent</u>, or as the <u>etendue</u> of the beam.

This simplified form of the radiometer measurement equation, when used with an appropriately defined correction factor, can be used for high accuracy radiation thermometry with relative spectral bandwidths ($\delta\lambda/\lambda$) up to about 10 %, using the reference wavelength [29]. For larger relative bandwidths, it is customary to use the mean effective wavelength [30]. For less accurate work, eq.(31) is commonly used - without the correction factor - because of its simplicity. For wide spectral bands, eq.(30) must be used.

THE OPTICAL SYSTEM

The optical systems of most radiation thermometers used in industry are similar to that illustrated in Fig. 1, although many instruments also include a visual viewing system for alignment purposes. More sophisticated research laboratory instruments often have additional optical elements behind the field-defining aperture.

Some instruments use a mirror objective in place of the objective lens, ordinarily for the purpose of viewing low temperature targets where a very wide spectral band is required. Mirror objectives have the advantage of being fully achromatic, i.e., their focal length is independent of

wavelength. While reflective (mirror) and refractive (lens) objectives each have their advantages and disadvantages, single-element lenses are more widely used than mirror objectives in industrial radiation thermometers except for low temperature measurements.

Materials suitable for use in infrared optics are relatively few in number, and are much more costly than those used in the visible spectrum. Finding a material with the desired combination of properties is often difficult and sometimes impossible. The spectral transmittance of several of the most commonly used infrared optical materials are shown in Fig. 12. The spectral range of greatest interest in industrial applications is from about 1.5 to about 4 μm, with some applications out to 14 μm. The visible spectrum is from 400 to 780 nm (0.4-0.8 μm).

There are several other properties of optical materials that must also be taken into account. Many infrared optical materials tend to be hygroscopic, sharply limiting their usefulness in industrial radiation thermometers; those shown in Fig. 12 are non-hygroscopic.

The refractive index of any optical material varies systematically with wavelength. Since the focal length of the lens is a function of the refractive index, the focal length also
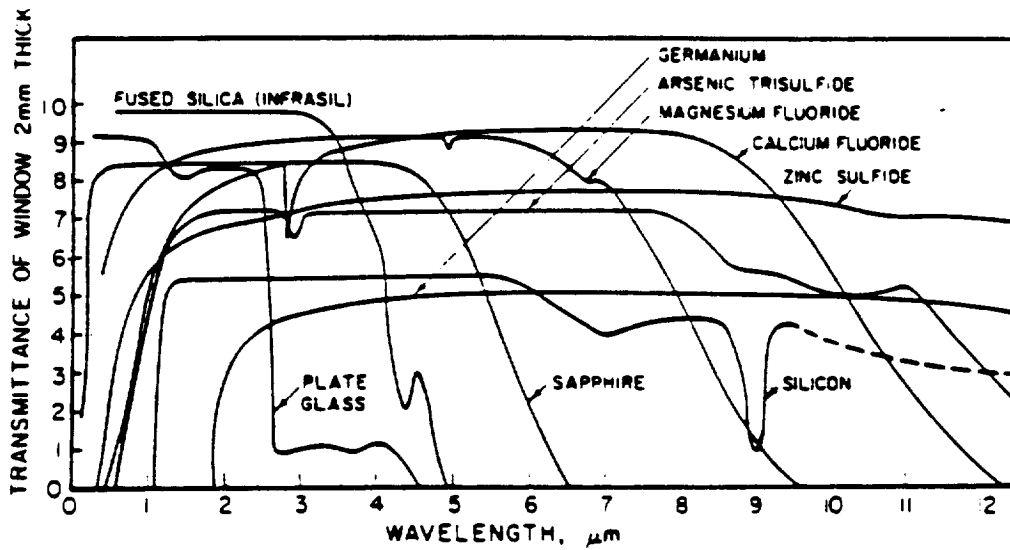
Fig. 12. Commonly used infrared optical materials.

diffraction limited even as a single element lens; however,
it is opaque in the visible spectrum. Those, such as zinc
sulfide, that have a high refractive index, transmit in the
visible spectrum, and have other desirable properties,
are very limited in number, and are expensive. Lenses having
a low refractive index, such as fused silica and calcium
fluoride, have a large amount of spheric aberration, making
them unable to focus sharply on small targets and causing the
target area to be larger than expected because of the
blurred image.

PHOTODETECTION

Photodetectors (Fig. 13) are classed as _quantum_ detectors if
they convert photons to charge carriers, or _thermal_ detectors
if they sense the heating effect of absorbed radiation. Both
types are used in radiation thermometry   Linearity of
photodetector response is particularly useful in radiometry,
as is stability of responsivity with time and temperature. A
large variety of photodetectors is now commercially avail-
able. Those most widely used in radiation thermometry at
present include PbS, PbSe, Si, InAr, InSb, thermopiles and
pyroelectrics. Some of these exhibit linear response to
radiant power input over dynamic ranges up to about nine
orders of magnitude; others are linear only over much smaller
ranges.

varies with wavelength (longitudinal chromatic aberration).
An optical system with a simple objective lens designed to
work at one wavelength is therefore likely to be unsuitable
for simultaneous use at a substantially different wavelength,
since it focuses at a different target distance for one
wavelength than for the other. This can be a serious problem
in instruments intended for spectral radiance measurements at
more than one wavelength, particularly when the target is
small. This also limits the extent to which an objective
lens that is intended to transmit radiant power to the
photodetector can also be used for visually aiming the
instrument. The problem can sometimes be largely eliminated
by achromatizing the lens. This is seldom done in industrial
instruments, however, since it greatly increases the cost of
an already expensive infrared lens, and often does not
produce an otherwise high quality image except on or very
near the optical axis. Mirror objectives are often used to
eliminate chromatic aberration, since they are fully achro-
matic.

Spheric aberration is the only other significant lens
aberration affecting the performance of "spot-type" radiation
thermometers, and it can be controlled or eliminated by
choosing a lens material that has a sufficiently large
refractive index. There are several materials that work
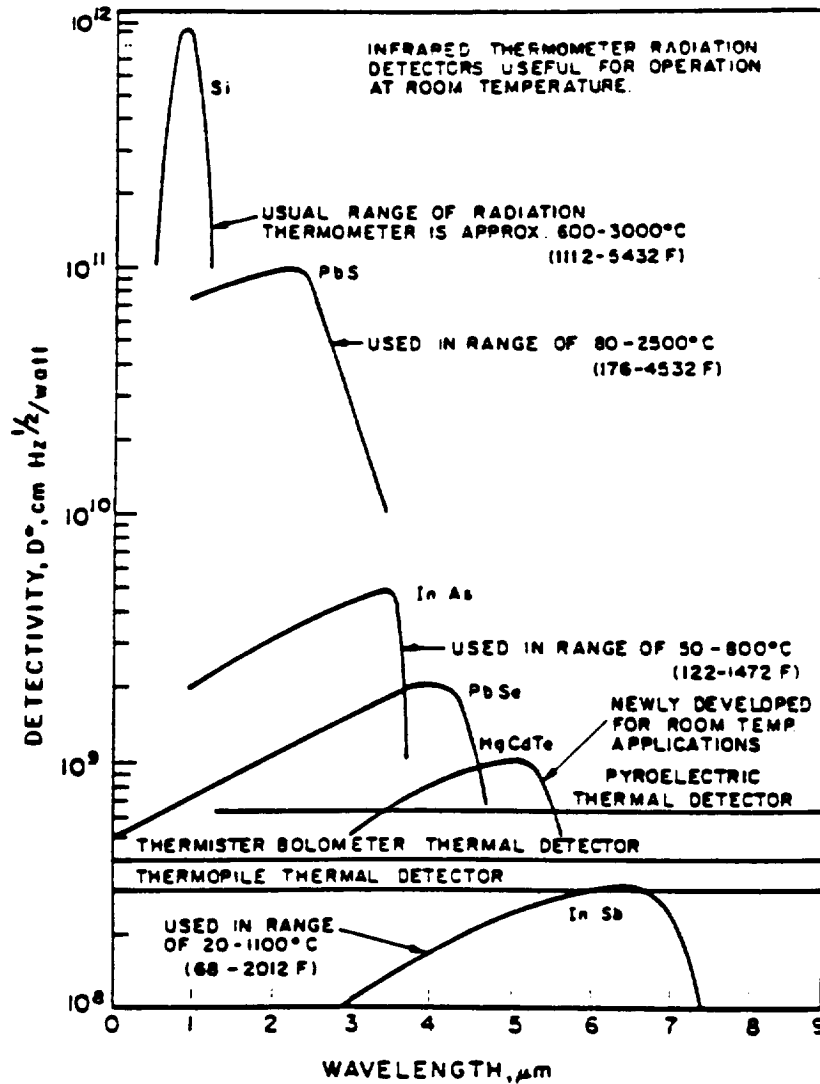well for this purpose. The best is germanium, which can be

Fig. 13. Photodetectors commonly used in radiation thermometry, for room temperature operation.

The spectral responsivity of most quantum photodetectors is strongly temperature-dependent, requiring extensive use of temperature compensation techniques. Silicon photodiodes, used for the target temperature range above about 500 deg C, are especially noteworthy in that they have a highly linear response (over eight decades in many cases), their responsivity is nearly independent of temperature over a significantly wide spectral range, and special techniques have recently been developed for their accurate "self-calibration" [31].

Those detectors that perform best in the spectral range best suited to radiation thermometry in the metals industries (about 1.5 to 2.5 μm) tend to need a substantial amount of ambient temperature compensation. The responsivity of lead sulfide, for example, changes by about 3% per degree C change in ambient temperature. This is an area in which present day industrial radiation thermometers are in need of improvement if they are to meet the tightest tolerances required by industry. Suitable technology presently exists to do this, primarily through the use of temperature-regulated thermoelectric coolers to cool and regulate the temperature of the photodetectors. Some industrial radiation thermometers already use thermoelectric cooling, but most are not sufficiently well temperature regulated, holding the detector temperature constant only to within about 1 degree

C. The principal disadvantage to this approach is the
increased cost of the instrumentation.

Radiation thermometry is frequently concerned with very
low-level signals, where noise is a significant factor.
Noise is present in the photon stream due to the statistics
of photon emission. Noise also originates in the detector
itself, where it is described in terms of the specific
spectral detectivity, $D^*(\lambda)$, of the detector, and finally,
noise is introduced in the amplification process. The
use of modulated - or "chopped" - radiation permits the use
of ac amplification; this introduces less noise than dc
amplification and serves to eliminate much of the signal
component due to unwanted "background" radiation. The
effects of noise are controlled by filtering, in combination
with the selection of various optical system parameters in
the measurement equation. Noise ultimately sets the limit
to temperature resolution in radiation thermometry.

Long-term changes in the spectral responsivity of photodetec-
tors or their temperature compensation are often accommodated
by the use of some form of internal reference standard such
as an incandescent or solid state lamp. The internal
reference standard in such cases has been determined to be
much more repeatable over an extended period of time than is
the responsivity of the photodetector. In some instruments

using highly sensitive but unstable detectors (e.g., PbS), the reference source is used continuously in a radiation null-balancing system. The disappearing-filament optical pyrometer is an early example of such a system; automated versions of that and other null-balancing instruments now exist.

HIGH POWER OF T

Much of the behavior characteristic of narrow-band radiation thermometers can be understood by expressing thermally emitted spectral radiance in terms of a power of the temperature , i.e.,

$$L \propto T^n \tag{33}$$

Where Wien's law is a suitable approximation, it can be shown that

$$n = \frac{c_2}{\lambda \cdot T} \tag{34}$$

It follows that

$$\frac{dT}{T} = \frac{1}{n} \cdot \frac{dL_\lambda}{L_\lambda} \tag{35}$$

The typical range of values for n is approximately $5 < n < 20$. The relative error in the measurement of emitted spectral radiance is thus seen to be reduced by a factor of $1/n$ in its effect on the relative error in the temperature. It is apparent that such errors can be minimized by maximizing n. This usually means using the shortest feasible wavelength, as in the case of window or emissivity effects, although there are circumstances (e.g., in the presence of reflected radiation) in which the opposite is true.

CORRECTIONS FOR EMISSIVITY EFFECTS

If the emissivity is known and is essentially independent of wavelength across the radiometer passband, its effects can be compensated for by increasing the radiometer amplifier gain by a factor equal to the reciprocal of the emissivity. When the gain cannot be adjusted, as in the case of a disappearing-filament optical pyrometer or a null-balancing radiometer, a correction can be computed by substituting Wien's law into eq.(9), from which we obtain

$$\frac{1}{T} - \frac{1}{T_{apparent}} = \frac{\lambda}{c_2} \cdot \ln \varepsilon(\lambda) \qquad (36)$$

where λ is the mean effective wavelength, discussed earlier. When the emissivity changes appreciably across the passband, we must use a different approach that is more direct but more

difficult to implement. The radiometer responds with the same signal that it would have if it were viewing a blackbody at the temperature $T_{apparent}$ From eq. (30)

$$A_{n,d} \cdot \omega_d \cdot \int_0^\infty R(\lambda) \cdot \tau(\lambda) \cdot \epsilon(\lambda) \cdot L_{\lambda,b}(\lambda,T) \cdot d\lambda = A_{n,d} \cdot \omega_d \cdot \int_0^\infty R(\lambda) \cdot \tau(\lambda) \cdot L_{\lambda,b}(\lambda,T_{apparent}) \cdot d \quad (37)$$

The true temperature T is determined from the indicated temperature $T_{apparent}$ by numerical integration of the above expression. This requires numerical descriptions of $\epsilon(\lambda)$, $\tau(\lambda)$ and $R(\lambda)$. Prior to the advent of computers, this method - although exact in principle - required so much labor that it was seldom used. This no longer is true, although other methods may still be preferable in many cases, particularly for narrow passbands or where fast response is needed.

RATIO THERMOMETERS

A ratio thermometer can be used to compensate for emissivity effects when the emissivity ratio $\epsilon(\lambda_1)/\epsilon(\lambda_2)$ is known. Such an instrument can be thought of as two nearly monochromatic radiometers operating at known wavelengths, λ_1 and λ_2 respectively, viewing the same target. From eq. (31),

$$S_1(T) = K_1 \cdot \epsilon(\lambda_1) \cdot L_{\lambda,b}(\lambda_1,T) \quad (38)$$

56

and

$$S_2(T) = K_2 \cdot \epsilon(\lambda_2) \cdot L_{\lambda,b}(\lambda_2, T) \qquad (39)$$

where K_1 and K_2, or their ratio, are determined by
calibration in terms of a blackbody or graybody From the
ratio of the measured signals, and by substituting from
Wien's law for $L_{\lambda,b}(\lambda, T)$, we have

$$R(T) = \frac{S_1(T)}{S_2(T)} = \frac{K_1}{K_2} \cdot \frac{\epsilon(\lambda_1)}{\epsilon \lambda_2} \cdot e^{-\frac{c_2}{T}\left(\frac{1}{\lambda_1} - \frac{1}{\lambda_2}\right)} \qquad (40)$$

which can be solved for the temperature, since all other
quantities are known. This type of radiation thermometer is
most frequently applied where graybody conditions have been
shown to exist, i.e., where $\epsilon(\lambda_1) = \epsilon(\lambda_2)$, such as is often
the case in the steel industry. Thus far, it has not proven
satisfactory in aluminum industry applications because the
spectral emissivity ratio at any two suitable wavelengths is
too variable from one alloy to another. Ratio thermometers
are also useful where only part of the target lies in the
field of view, such as when dust obscures the target,
or where the target is a hot wire passing through the field
of view. It is only necessary that the same fraction of the
field of view be used at each of the two wavelengths.

FUTURE DEVELOPMENTS

Radiometric methods of temperature measurement have advanced
to the point where commercially available radiometers
operating in a number of spectral regions are widely used in
industry, especially in process control and monitoring
applications. While radiometer performance is presently
satisfactory for most industrial applications, however,
repeatability and noise levels often fall short of the mark
required for research and development applications. The
performance of a number of custom-built research radiometers,
on the other hand, suggests that existing technology can
support higher performance radiometry than is currently
practiced in industrial radiation thermometry.

The effects of unknown emissivity and reflected extraneous
radiation remain as the major hurdles for applied radiation
thermometry, but the new hybrid methods are making serious
inroads into these problem areas, and hold promise for much
more progress. The development of hybrid methods was made
possible, in turn, by the improved engineering understanding
of the physics of thermal radiation from the surfaces of real
materials and the development of related analytical techni-
ques. The possibility of the widespread application of
hybrid methods in the form of practical radiation thermometry

has been made likely to become reality by the recent advent of microprocessors.

These advances hold high promise for the development of methods and instrumentation that will greatly improve the accuracy and extend the range of application of radiometric methods. Future developments are likely to require a greater familiarity with the theory of radiometry and a detailed understanding of the radiative properties of surfaces.

REFERENCES

1. Haugh, M.J., "Infrared Thermometry in the Aluminum Industry," Chapter 14 of "Theory and Practice of Radiation Thermometry," DeWitt, D.P., and Nutter, G.D., Editors, in publication.

2. DeWitt, D.P., "Thermal Radiative Properties - Metallic Elements and Alloys," Vol. 7, p. 28a, IFI Plenum, New York, 1970.

3. Porteus, J.O., "Relation Between the Height Distribution of a Rough Surface and the Reflectances at Normal Incidence," J. Opt. Soc. Am. 53, 1934-1402, 1963.

4. Touloukian, Y.S., and DeWitt, D.P., Ed., Thermophysical Properties of Matter, Vol. 7: "Thermal Radiative Properties, Metallic Elements and Alloys," Plenum Publishing Corp., New York (1970).

5. Reynolds, P.M., Brit. J. Appl. Physics, 12, 111-114 (1961).

6. Edwards, D.K., and Catton, I., from "Advances in Thermophysical Properties at Extreme Temperatures and Pressures," 3rd ASME Symposium on Thermophysical Properties, West Lafayette, Ind., 188-199 (1965).

7. Bennett, H.E., and Porteus, J.O., "Relationship Between Surface Roughness and Specular Reflectance at Normal Incidence," J. Opt. Soc. Am. 51, No. 2, 123-129, Feb., 1961.

8. Davies, H., "The Reflection of Electromagnetic Waves From a Rough Surface," Proc. Inst. Elec. Engrs. 101, 209-213, 1954.

9. Chinmayanandam, T.K., "On the Specular Reflection From Rough Surfaces," Phys. Rev. Vol. 13, 1919, p. 96.

10. Beckmann, P., and Spizzichino, A., "The Scattering of Electromagnetic Waves from Rough Surfaces," Macmillan, New York, 1963.

11. Blau, H.H. Jr., Marich, J.B., Martin, W.S., Jaspers, J.R., and Chafee, E., AFCRL-TR-60-416, 1-78, 1960 [AD 248276].

12. Research Projects Division, G.C. Marshall Space Flight Center, Huntsville, Ala., NASA-TN-D-1523, NASA-N63-14272, 1-253 (1963).

13. Bennet, J.M, and Bennett, H.E., "Polarization," Section 10 of *Handbook of Optics*, Driscoll, W.G., and Vaughan, W., (Ed.), McGraw Hill, New York, 1978.

14. Tingwald, C.P., and Magdeburg, H., "A New Optical Method for the Determination of Thermodynamic Temperatures of Glowing Metals, *"Temperature, Its Measurement and Control in Science and Industry*," Vol. 3, 483-486, Reinhold Publishing Corporation, New York, 1962.

15. Jenkins, F.A., and White, H.E., *Fundamentals of Optics*, Fourth Ed., McGraw Hill, New York, 1976.

16. Born, M., and Wolfe, E., *Principles of Optics*, Macmillan, New York, 1964.

17. Hess, G. and Waylonis, J.E., J. Opt. Soc. Am. 50, 1133 (TB15) (1960).

18. Schulz, L.G., "The Optical Constants of Silver, Gold, Copper and Aluminum. I. The Absorption Coefficient k." J. Opt. Soc. Am. 44, 357 (1954). L.G. Schultz and F.R. Tangherlini, "Optical Constants of Silver, Gold, Copper and Aluminum. II. The Index of Refraction n". J. Opt. Soc. Am. 44 (1954).

19. Beattie, J.R., "The Anomalous Skin Effect and the Infrared Properties of Silver and Aluminum," Physica 23,

898 (1957). J. R. Beattie and G.K.T. Conn, Phil. Mag. 46, 989 (1955).

20. Gray, Dwight D., Ed., "American Institute of Physics Handbook," 3rd Edition, McGraw-Hill Book Co., New York (1972).

21. Lenham, A.P. and Treherne, D.M., "Optical Constants of Single Crystals of Mg, Zn, Cd, Al, Ga, In and White Sn," J. Opt. Soc. Am. 56, 752 (1966).

22. Bennett, H.E. and Bennett, J.M., "Validity of the Drude Theory for Silver, Gold, and Aluminum in the Infrared," in "Optical Properties and Electronic Structure of Metals and Alloys," F. Ables, Ed., p. 176. No. Holland Pub. (1966).

23. Siegel, R., and Howell, J.R., Thermal Radiation Heat Transfer, Second Ed., p. 104, Hemisphere Publishing Corp., McGraw Hill, New York, 1981.

24. Helmholtz, H. von, Handbuch der Physiologischen Optik, Third edition (Hamburg and Leipzig: Leopold Voss) pp 189-199 (1909).

25. Ref. [2], p. 32a.

26. Yates, H.W., and Taylor, J.H., "Infrared Transmission of the Atmosphere," U.S. Naval Research Laboratory, Washington, DC, NRL Report 5453, 1960.

27. Iuchi, T., and Kusaka, R., "Two methods for simultaneous measurement of temperature and emittance using multiple reflection and specular reflection, and their applica-

tions to industrial processes," <u>Temperature, Its Measurement and Control in Science and Industry</u>, Vol. 5, p. 491-503, American Institute of Physics, New York, 1982.

28. Kostkowski, H.J., and Lee, R.D., "Theory and Methods of Optical Pyrometry," <u>Temperature, Its Measurement and Control in Science and Industry</u>, Vol. 3, p. 449-481, Reinhold Publishing Corporation, New YHork, 1962.

29. Coates, P.B., "Wavelength Specifications in Optical and Photoelectric Pyrometry," Metrologia 13, 1-5, 1977.

30. Nutter, G.D., "Radiation Thermometers - Design Principles and Operating Characteristics," Chapter 4 of <u>Theory and Practice of Radiation Thermometry</u>," DeWitt, D.P., and Nutter, G.D., Editors, National Bureau of Standards, Washington, DC, in publication.

31. Zalewski, E.F., and Geist, J., "Silicon photodiode absolute spectral response self-calibration," Applied Optics, Vol. 19, No. 8, pp. 1214-1216, 15 Apr. 1980.

The NBS Scale of Radiance Temperature

William R. Waters, James H. Walker, and Albert T. Hattenburg

Center for Radiance Research,
National Bureau of Standards National Measurement Laboratory

The paper describes the measurement methods and instrumentation used in
the realization and transfer of the International Practical Temperature
Scale (IPTS-68) above the temperature of freezing gold. The determination
of the ratios of spectral radiance of tungsten-strip lamps to a gold-point
blackbody at a wavelength of 654.6 nm is detailed. The response
linearity, spectral responsivity, scattering error, and polarization
properties of the instrumentation are described. The analysis of
sources of error and estimates of uncertainty are presented. The
assigned uncertainties (three standard deviations) in radiance
temperature range from ± 2 K at 2573 K to ± 0.5 K at 1073 K.

MICROGRAVITY SCIENCE AND APPLICATIONS DIVISION
DISCIPLINE REQUIREMENTS

I

Non-Contact Temperature Measurement Requirements for

Electronic Materials Processing

S.L. Lehoczky and F.R. Szofran

Space Science Laboratory

NASA/Marshall Space Flight Center

Huntsville, AL 35812

ABSTRACT

The requirements for non-contact temperature measurement capabilities for electronic materials processing in space are assessed. Non-contact methods are probably incapable of sufficient accuracy for the actual absolute measurement of temperatures in most such applications but would be useful for imaging in some applications.

PRECEDING PAGE BLANK NOT FILMED

1. Introduction

In a terrestrial environment the crystal growth of electronic and electro-optical materials are significantly effected by gravitational forces. In particular, free-convection caused by density gradients resulting from thermal and compositional gradients in the fluid phase can alter the compositional distribution of components, increase the probability of incorporation of impurities leached from the container walls, and cause growth rate fluctuations that lead to an increase in the densities of intrinsic crystal defects.

It is generally believed that the reduction or elimination in space of gravity-induced, convective flows and hydrostatic pressure related phenomena will result in materials with improved electrical and optical properties due to concomitant improvements in compositional homogeneity and reductions in crystal defect density. Additionally, the elimination of the need for confinement for some of the solidification processes is expected to lead to a reduction in impurity concentrations and in the densities of stress-induced defects such as dislocations.

The materials of interest include inorganic semiconductors (Si, Ge, GeAs, CdTe, HgCdTe, PbSnTe, etc.), organic and inorganic non-linear materials, various conducting and insulating oxides and

|

selected magnetic and piezoelectric materials. The preparation
methods include solidification from molten and vapor phases,
crystallization from saturated solutions, and various solid-state
compaction and crystallization processes. The latter are not expected
to be effected by reduced gravity; thus, only the processes that
involve solidification from a fluid phase will be considered further.

In general, the various solidification methods used do not
depend on a precise knowledge of the material surface temperatures,
and thus, usually do not employ non-contact temperature measurement
data for process control and implementation. Nonetheless, some of the
methods, e.g., Czochralski and float-zone, frequently use similar
optical measurement techniques to assist crystal diameter measurement
and control. In the near term, of the commonly used melt growth
methods (Czochralski, Bridgman, Bridgman-Stockbarger, float-zone,
traveling heater-zone, etc.) only the Czochralski and float-zone
growth processes are expected to benefit significantly from advances
in non-contact temperature measurement technology. Thus, the
remainder of the paper will primarily address issues associated with
these two melt growth methods.

Section two of the paper gives a brief description of the two
processes. Section three gives an example of the use of an infrared
television system for thermal imaging and diameter control for a

Czochralski-type crystal growth process. Finally in section four details of the specific requirements for future non-contact temperature measurements are discussed.

2. Crystal Growth Methods and Related Non-Contact Temperature Measurement Problems

. The Czochralski and float-zone crystal growth processes are briefly described below. In the Czochralski growth process the source material is placed in an inert crucible and melted by using RF or resistive heating methods. A seed crystal is inserted into the melt and crystal growth proceeds by controlled withdrawal of the crystal from the melt. The crystallographic orientation of the growing crystal is determined by the orientation of the seed and its diameter is determined by the temperature distribution in the growth system, which is controlled by the power input into the heaters.

In the classical float zone method a molten zone is established at the juncture of a mono-crystalline seed and the source material. The zone width is controlled by the amount of heat input into the zone region. Similarly to the Czochralski method either RF or resistive heating techniques are used to establish and maintain the desired temperature distribution in the zone region. Additional process control can be derived from provisions for the rotation and relative axial displacement of the seed and source materials. Usually, for both growth processes, the particular vapor pressures of the materials at the growth temperatures are large and thus evaporation from the melts can result in deposition of the materials on the container walls

71

and the "viewing-port" windows. For some of the smaller vapor pressure electronic materials, e.g. Si, Ge, etc., the evaporation rate can be significantly reduced by the introduction of an inert gas into the process chamber. The processing of the higher vapor pressure materials, e.g., compound semiconductors, usually requires both large inert gas pressures (up to 100 atm.) and the use of liquid encapsulants, e.g., B_2O_3. Changes in either the window or encapsulant spectral transmissivities with time are expected to significantly impact the accuracy of temperature values derived from the measured intensity of the thermal radiation from the surface region of interest. Additional errors may result from the lack of knowledge of the pertinent emissivities as well as of their temperature, wavelength and composition dependences. A related problem is the potential for time-dependent changes in the surface compositions caused by either preferential surface segregation of minority components, e.g., impurities and dopants, or by preferential evaporation and thus surface depletion of some of the major components caused by differences in component chemical potentials at the phase boundaries. Finally, as the crystal grows, the relative volumes of the crystal and melt will change. Related changes in surface geometries will result in changes in the various geometrical view-factors leading to further temperature determination errors.

The extreme sensitivity of device yield and performance to variations in material properties necessitates a high degree of reproducibility in the material processing variables, in particular, thermal conditions. Because of the potential sources of error described above, we believe that in most cases, contact temperature measurements cannot provide accurate enough data to assure routine reproduction of the desired temperature values. Nonetheless, data provided by such measurements can be very useful for determining relative variations in surface temperatures and thus thermal gradients. Such data can be useful in establishing thermal boundary conditions for process modeling and optimization.

3. System for Thermal Imaging and Crystal Diameter Control

Non-contact measurement systems have been in use for diameter control in Czochralski growth systems for more than 20 years.[1] By 1972 non-contact imaging systems had already reached the fundamental physical limits discussed in Section 2. Improvements since that time have, therefore, been limited to faster processing and better graphical display of the information. The improved graphics capabilities are due in part to faster computers and in part to improvements in detector technology, especially detector arrays. For example, the earlier use of ordinary photovoltaic diode arrays has more recently given way to the significant use of charge coupled arrays. CCDs have higher sensitivity and inherent integration capability for noise filtering. The 1972 system of Kwap et al. [2] is described below. A current system for non-contact temperature measurements in a Czochralski system was described by Wargo at this Workshop.

The system of Kwap, et al. used an infrared TV camera to determine relative temperatures of the melt surface and growing crystal. The diode array in the camera had a range of 0.55 to $1.15\mu m$ with peak sensitivity near 0.83 μm. By computer analysis of the TV data, crystal diameter measurements were made and the power to the crystal puller was controlled by computer to regulate the diameter.

This system was used to grow oxides near 1400°C. The system could measure diameter to 0.1 mm and data were taken from the camera at the rate of 30 scans per second. By changing filters at 300°C intervals, the system could measure temperatures from 300°C to 1500°C. The output voltage sensitivity ranged from 4 to 12 mV/$^\circ$C so that temperature resolution for most applications would not be a problem. The limitations on temperature measurement accuracy were primarily due to the laws of nature and the lack of knowledge of the emissivities, as discussed in Section 2. These limitations remain unchanged.

4. Thermal and Optical Imaging Requirements

In summary, requirements exists for thermal and optical imaging of free or liquid encapsulated melt/crystal surfaces for the Czochralski-type and float-zone type crystal growth. The temperature range of interest is from 200 to 1600°C. Requirements also exist for thermal mapping of growth interfaces and real-time monitoring of solidification rates during vapor crystal growth. The shape/temperature/growth-rate data can be used for feedback control of thermal fields, crystal growth rates and crystal/ingot diameters.

The crystal growth of electronic materials, in most cases, requires the precise knowledge of the absolute values of the temperatures at selected locations on the sample/growth-system surfaces. Usually the desired absolute temperature measurement accuracies range from: 1) $\pm 1.5^{\circ}$C for the 200 to 700°C range, 2) $\pm 2.5^{\circ}$C for the 700°C to 1100°C range, 3) $\pm 3.5^{\circ}$C for the 1100 to 1350°C and $\pm 5^{\circ}$C for the highest temperatures. Sampling rates of up to 5 samples per second are required. We believe that these accuracy requirements very likely cannot be met in most cases using non-contact temperature measurement techniques because of (1) the errors resulting from the lack of precise knowledge of some of the required thermophysical properties, e.g., emissivities, and (2) the various

inherent process-imposed limitations described in some detail in Section 2.

The requirements for temperature resolution measurements range from about $0.2^{\circ}C$ to about $4^{\circ}C$. For imaging purposes the required sampling rates are of the order of 30 samples/second. The spatial resolution requirements range from about 0.1 to 1 mm. In contrast to the absolute temperature accuracies, for most cases, especially for the higher temperature ranges ($>700^{\circ}C$), these imaging requirements probably can be met by using the combination of judiciously designed imaging optics and commercially available photovoltaic or CCD array cameras. The most stringent requirements will probably require the use of special cryogenically cooled detector arrays or scanning detector systems.

5. <u>References</u>

1. E.J. Patzner, R.G. Dessauer, and M.R. Poponiak, Solid State Technology, October 1967, p. 25.

2. T.W. Kwap, D.F. O'Kane, and L. Gulitz, in <u>Temperature, It's Measurement and Control in Science and Industry</u>, Vol. 4, Part 1, Instrument Soc. of America, Pittsburgh (1972) p. 541, and D.F. O'Kane, T.W. Kwap, L. Gulitz, and A.L. Bednowitz, J. Crystal Growth <u>13/14</u> (1972) 624.

Noncontact Temperature Measurement - Requirements and Applications for Metals and Alloys Research

J. H. Perepezko

University of Wisconsin-Madison

Department of Metallurgical and Mineral Engineering

Madison, WI 53706

Temperature measurement is an essential capability for almost all areas of metals and alloys research. In the microgravity environment many of the science priorities that have been identified for metals and alloys also require noncontact temperature measurement capability. For example, in order to exploit the full potential of containerless processing, it is critical to have available a suitable noncontact temperature measurement system. This system is needed to track continuously the thermal history, including melt undercooling and rapid recalescence, of relatively small metal spheres during free-fall motion in drop tube systems. During containerless processing with levitation - based equipment, accurate noncontact temperature measurement is required to monitor one or more quasi-static samples with sufficient spatial and thermal resolution to follow the progress of solidification fronts originating in undercooled melts. In crystal growth, thermal migration, coarsening and other experiments high resolution thermal maps would be a valuable asset in the understanding and modeling of solidification processes, fluid flows and microstructure development. The science and applications requirements place several constraints on the spatial resolution, response time and accuracy of suitable instrumentation.

Introduction

Melts and alloys constitute a critically important category of engineering materials. Many of the applications of metals frequently depend on structure sensitive properties which reflect the microstructural details and processing history of an alloy. The processing of most metals and alloys usually involves a solidification step, during which a gravitational field may have dramatic effects on microstructure and on those properties influenced by microstructure. There are several well established examples of microstructural influences of gravity in the areas of solidification, crystal growth, containerless processing and supercooling of metallic melts. Gravity has a direct bearing on buoyancy induced convection and on the resulting chemical segregation levels produced by solidification. An important component in the progress that has been achieved in controlling solidification processing has resulted from a closer study of the relationships between the liquid transport and the solidification interface. This understanding has resulted from the ability to quantify the conditions at the solidification interface in terms of the relevant compositions of liquid and solid and the interface temperature.

In the microgravity environment there are new opportunities for controlling the solidification process. One of the most important is the minimization of convective flows to allow better control of melt temperature and composition. Similarly, sedimentation types of effects can be reduced considerably. There are also new possibilities for melt processing including containerless processing to avoid the affects of crucible induced contamination of reactive liquids. However, to optimize the advantages and

I

to realize the new opportunities for processing it is vital to have accurate temperature measurements which because of the new processing routes are also required to be of a non-contact nature.

Non-Contact Temperature Measurement Requirements

Metals and Alloys

In addressing the science priority needs in the metals and alloys discipline a Metals and Alloys Discipline Working Group has been active for the past several years in formulating plans (1). A summary of the key science areas that have been identified by the members of the Discipline Working Group for microgravity processing is presented in Table 1. For the most part, the key science areas relate to liquid processing or the treatment of liquid-solid mixtures and the microstructural consequences of solidification. An important addition refers to measurements of thermophysical properties which are critical to the effective development and testing of solidification models. It should also be emphasized that the science priority areas are continually being examined for revision and updating.

In order to illustrate the non-contact temperature needs in the metals and alloys discipline a full discussion of all the science areas in Table 1 is not required. Instead a few areas will be highlighted to demonstrate the requirements.

Dendritic Microstructures

The phenomena of dendrite coarsening is important in determining the overall solidification microstructure with regard to the microstructural scale. The typical effects involved in coarsening are illustrated in Fig. 1 which comes from the work of Voorhees and Glicksman (2). A series of secondary dendrite arms is illustrated with a distribution in sizes that has
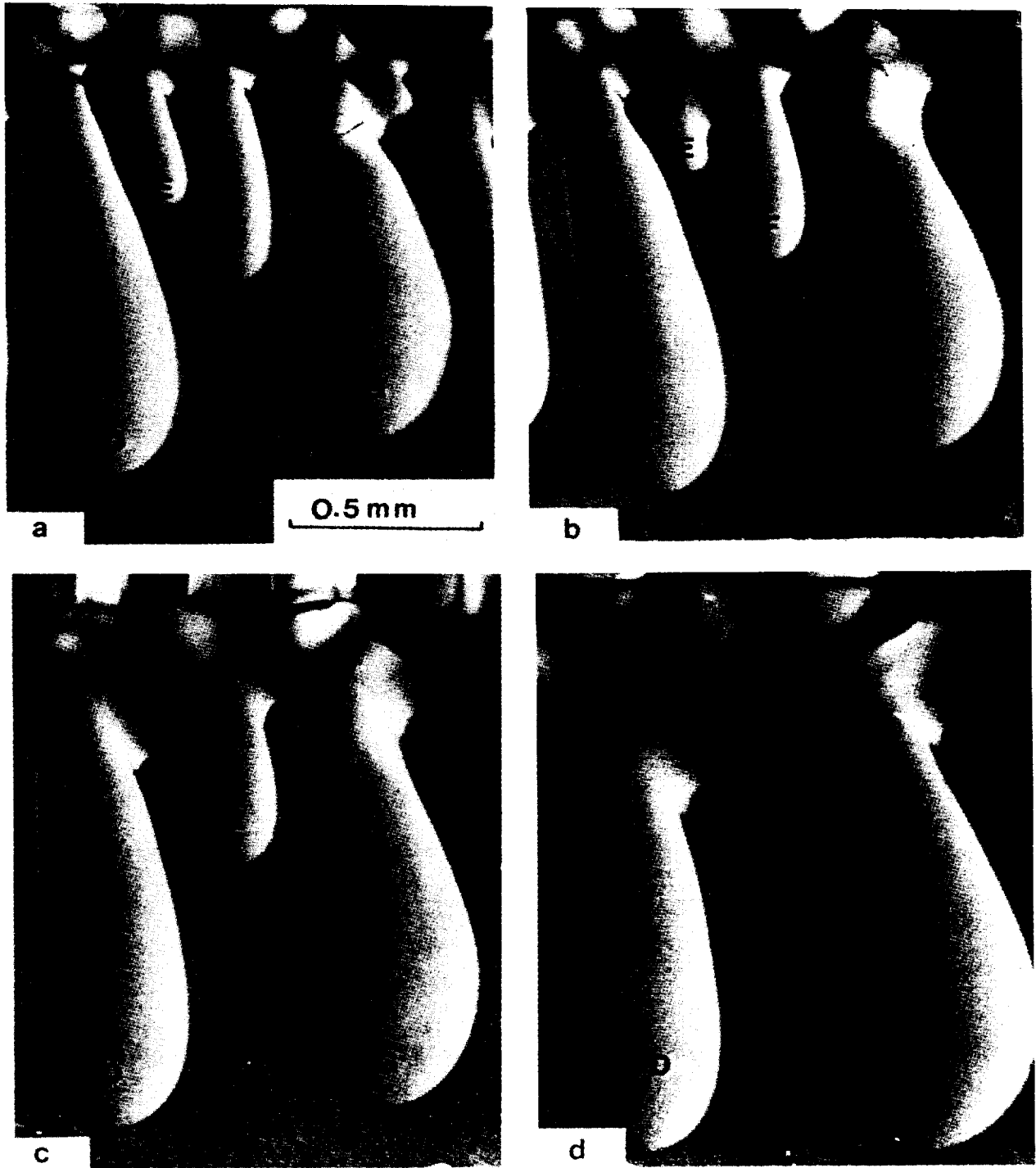
Fig. 1 Sequence of photomicrographs showing dendritic side branches evolving in time (a-d) under nearly isothermal conditions (from ref. 1).

developed as a result of competitive growth due to melting point differences produced by differences in local radius of curvature. To characterize the thermal distribution within such a microstructure is necessary to have the resolution of measurement be of the order of the scale of the microstructural features i.e., secondary dendrite arm spacing. Although in the situation shown in Fig. 1 this scale is rather large, at the early stages of dendritic growth the scale becomes much finer as illustrated in Fig. 2. Furthermore, the sequence of dendritic growth events illustrated in Fig. 2 demonstrate very rapid growth associated with dendrite microstructures. This rapid growth is also related to the fineness of the microstructural scale and exhibits a steep dependence on temperature. In fact, at much larger values of supercooling of the order of 10-100°C, dendrite growth volocities of the order of tens of meters per sec have been recorded (3). Thus, in dendrite coarsening a high spatial and thermal resolution is required due to the microstructural scale and the relatively small temperature differences involved. On the other hand, in the case of dendritic growth, a very rapid temperature response and accurate temperature measurement is required in order to resolve the dependence of dendrite velocity upon undercooling.

Containerless Processing

Containerless processing involves the thermal treatment of a volume of material usually as a liquid in a suspended state free from a supporting vessel. During containerless processing potential contaminants originating from a crucible and possible heterogeneous sites for nucleation catalysis of the liquid that can be associated with a crucible may be avoided. A high purity melt can be maintained even with reactive materials at elevated temperatures. This can allow for the reliable measurement of thermophysical properties and for the study of chemical reactions in liquids which are
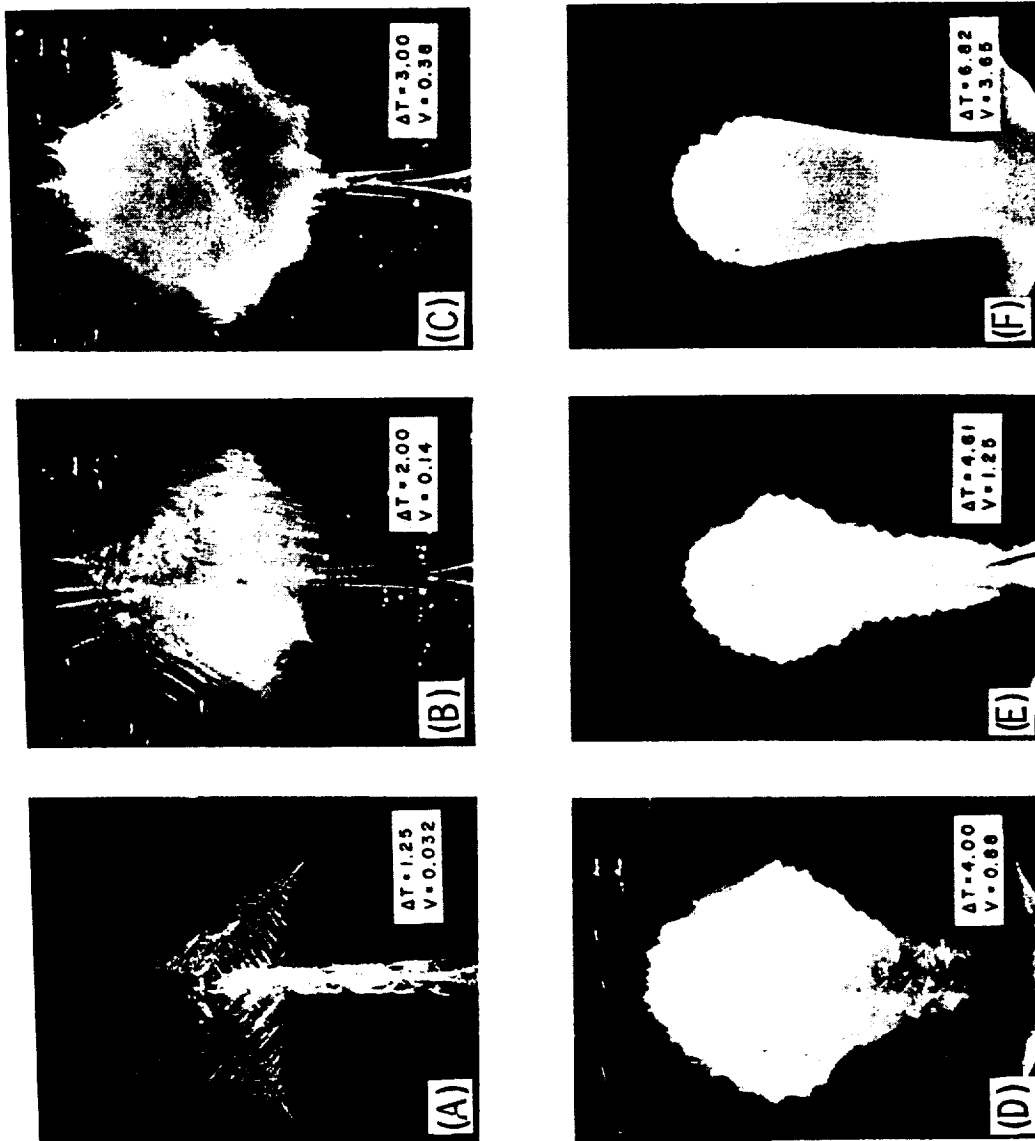
83

Fig. 2 Sequence of photographs showing dendritic growth at various levels of melt supercooling and steady state growth rates, V.

84

usually difficult to handle due to their reactivity. The elimination of crucible induced nucleation can lead to large supercooling, to the development of novel solidification microstructures, and to the formation of metastable phases. A microgravity environment facilitates the application of containerless processing and with externally applied positioning fields allows for the treatment of much larger volumes than are possible during ground based processing.

A variety of containerless processing techniques have been developed as illustrated in Fig. 3. In each case a crucible is not used. Instead, either a free fall environment or an environment in which a molten sample is held in position through some externally applied force is used. The containerless processing approach illustrates many of the specific needs of non-contact temperature measurement in the metals and alloys discipline. These requirements can be illustrated by highlighting the conditions involved in drop tube processing. Drop tube processing is a containerless technique in which solidification occurs as a molten sample undergoes free fall through a chamber. While elimination of crucible induced nucleation can encourage liquid supercooling during processing, the presence of catalytic sites associated with internal impurities or the particle coating may limit the level of supercooling obtained during the falling period. With fine droplets nucleation sites may be isolated, allowing most of the particles to supercool more deeply (4). The coating may be modified to alter the catalytic potency of surface nucleation sites through the control of the gas environment during processing. The gas environment also influences the thermal conductivity and the resultant cooling behavior during solidification. High cooling rates can promote alternate microstructure formation during solidification under a
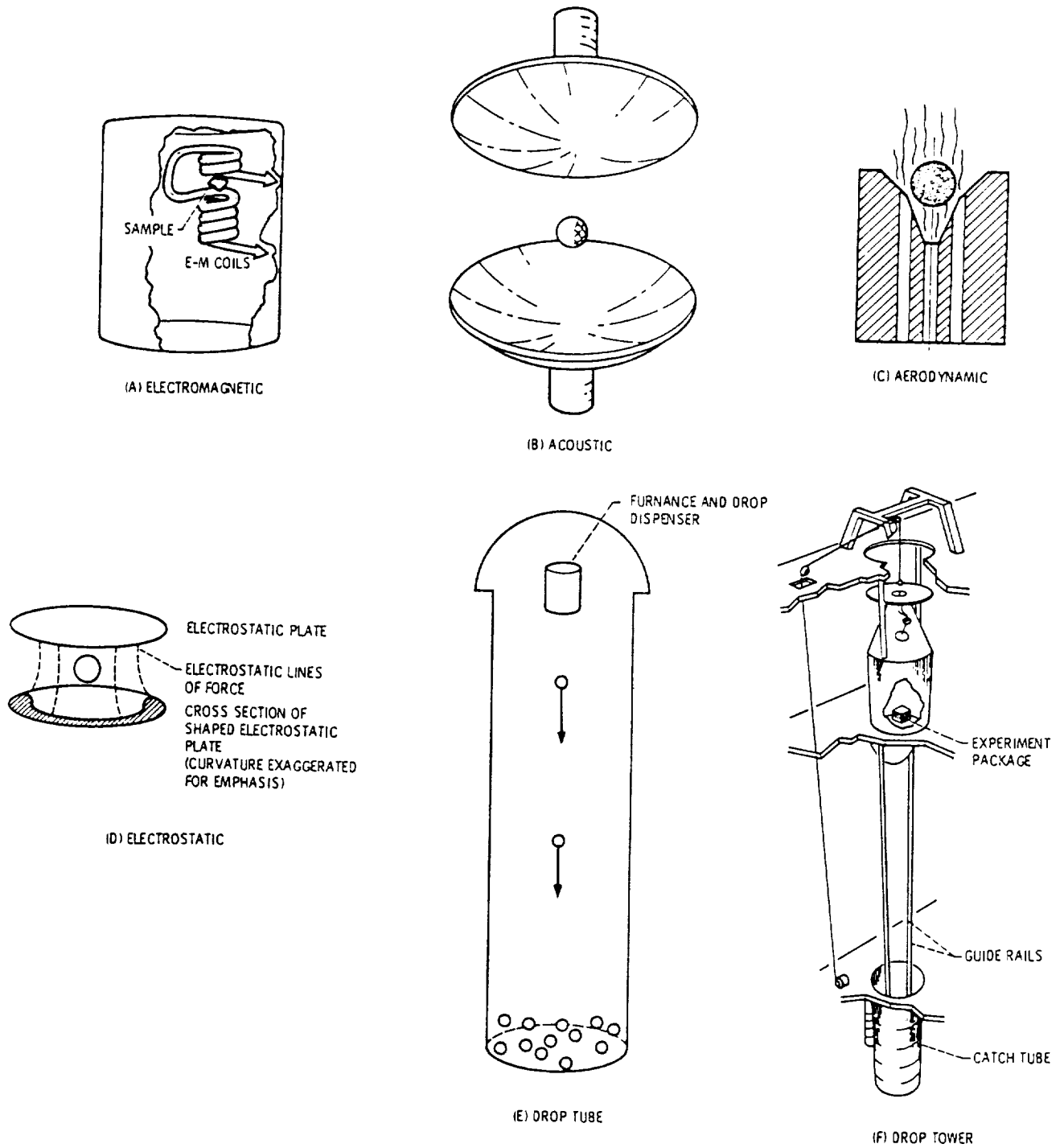
(A) ELECTROMAGNETIC

SAMPLE

E-M COILS

(B) ACOUSTIC

(C) AERODYNAMIC

ELECTROSTATIC PLATE

ELECTROSTATIC LINES OF FORCE

CROSS SECTION OF SHAPED ELECTROSTATIC PLATE (CURVATURE EXAGGERATED FOR EMPHASIS)

(D) ELECTROSTATIC

FURNANCE AND DROP DISPENSER

(E) DROP TUBE

EXPERIMENT PACKAGE

GUIDE RAILS

CATCH TUBE

(F) DROP TOWER

Fig. 3 Illustration of the variety of containerless processing techniques that are available.

containerless condition. Therefore, drop tube processing allows for the study of solidification under conditions of high supercooling during the free fall period which simulates the conditions of the microgravity environment.

While long drop tubes of the order of 100 m allow for the processing of sample diameters in the order of 1 cm, laboratory drop tubes of the order of 3-5 m in length are restricted to smaller diameters of the order of 100-300 microns. In each case however, the temperature requirements are similar in that one would like to measure the temperature continuously during the free fall period. At present, continuous recording of the temperature of a falling particle is not possible. In order to address the problem of temperature measurement, a variety of alternate approaches have been tried and are continually to be developed further. These developments are equally applicable to other forms of containerless processing and have been centered along three main areas. These areas include: the use of internal droplet microstructural information to calibrate the temperature changes during solidification, the application of heat flow analysis combined with droplet structure information to infer some of the thermal history of a sample and the application of some instrumentation combined with heat flow calculations to arrive at an estimate of the thermal history.

Microstructural Evaluation of Thermal History

A useful technique for determining the thermal history of a particle during drop tube processing is to relate the scale of the microstructure to the temperature of the droplet during solidification. A eutectic alloy solidification that results in the formation of a normal type cooperative solidification product is most useful for this purpose. This allows a correlation to be made between eutectic spacing and the undercooling at nucleation. Using thermal analysis of powders, control over the size and

cooling rate allows for different levels of undercooling to be achieved below the eutectic temperature as illustrated in Fig. 4 for a InSb-Sb eutectic alloy (5). Through quantative image analysis, the onset eutectic spacing can then be determined for each undercooling level as summarized in Fig. 5. In agreement with eutectic growth theory, the eutectic spacing, λ, values are related to the initial undercooling ΔT by the following relation;

$$\ell n\ (\lambda) = -3.48 - 1.56\ (\ln\ \Delta T) \tag{1}$$

Using this expression the undercooling level for samples processed in a drop tube can be assessed. Furthermore, based upon directional solidification data a model was derived to relate the eutectic spacing to the solidification rate and can also be applied to both the thermal analysis and drop tube processed samples. For the InSb-Sb system an increase in undercooling from 0.1-0.2 T_e resulted in a decrease in the onset eutectic spacing from 275-93 nm and a corresponding increase in the initial growth rate 0.23-2.2 cm/sec.

Microstructural examination of the undercooled eutectic powder revealed two well defined morphological regions as illustrated in Fig. 6. A rod type eutectic structure forms upon nucleation at the droplet surface and is maintained with a increase in rod spacing as a re-heating or recalescence occurs due to the release of the heat of fusion during solidification. As growth slows with continued recalescence, external cooling begins to assist in removal of the latent heat and a transition from a rod to lamellar growth occurs which allows for most efficient heat flow. The eutectic spacing for the rod morphology is determined by the initial undercooling and thermal conditions during droplet recalescence, while the lamellar spacing is controlled by heat transfer to the surroundings. The microstructures
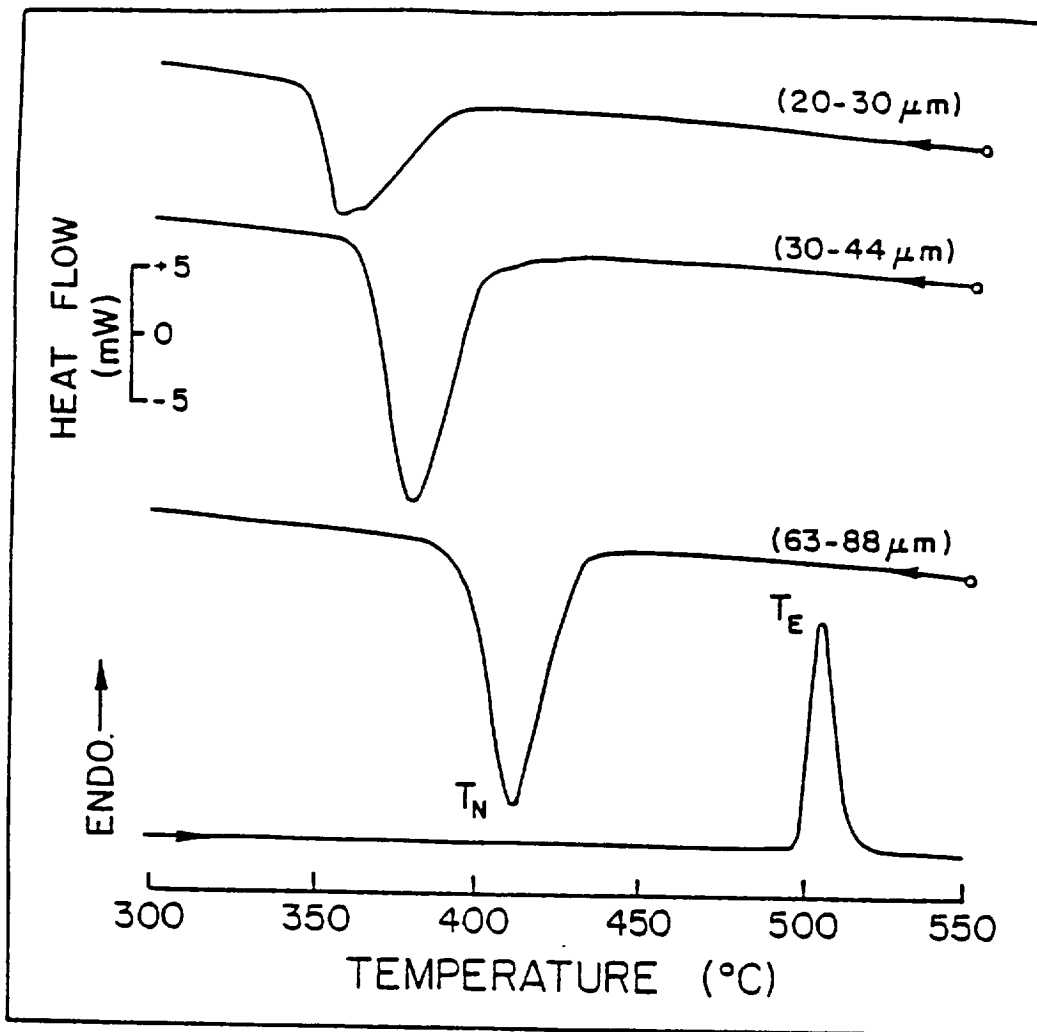
Fig. 4   DTA thermograms indicating the dependence of undercooling on droplet size for a InSb-Sb eutectic alloy.
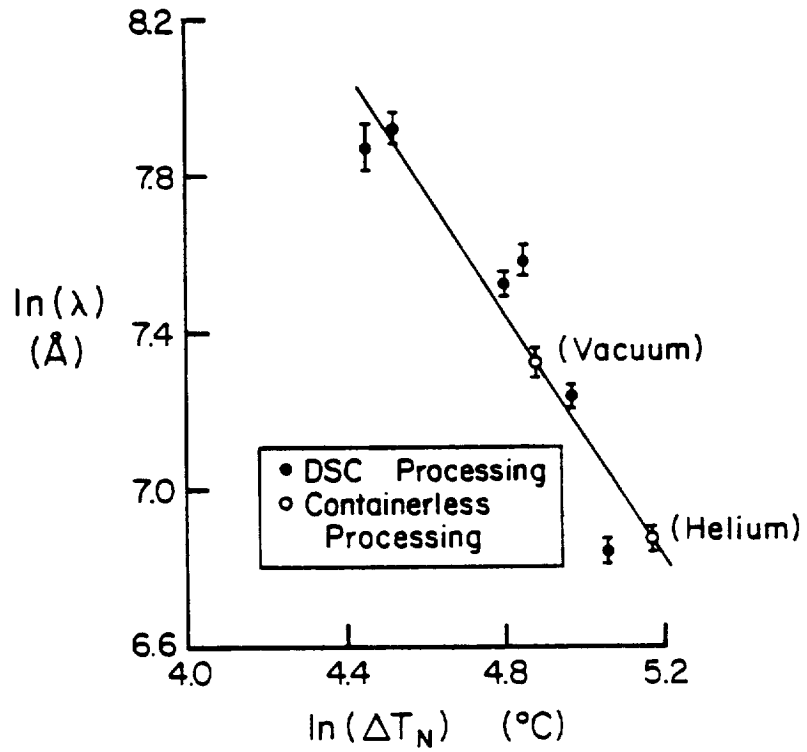
Fig. 5. Variation in onset eutectic spacing with undercooling at nucleation for InSb-Sb eutectic powder.
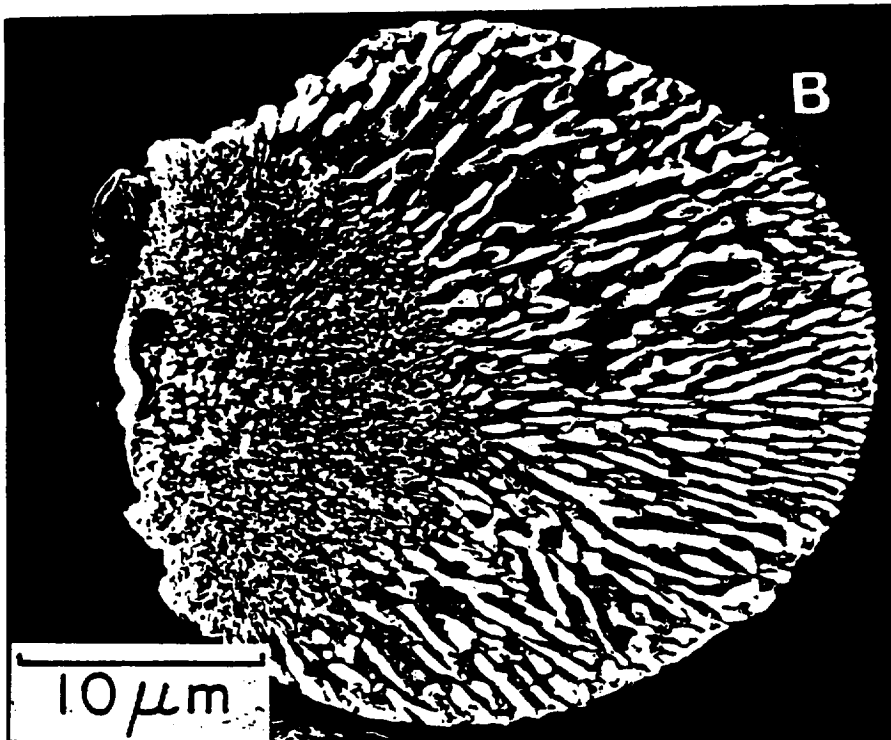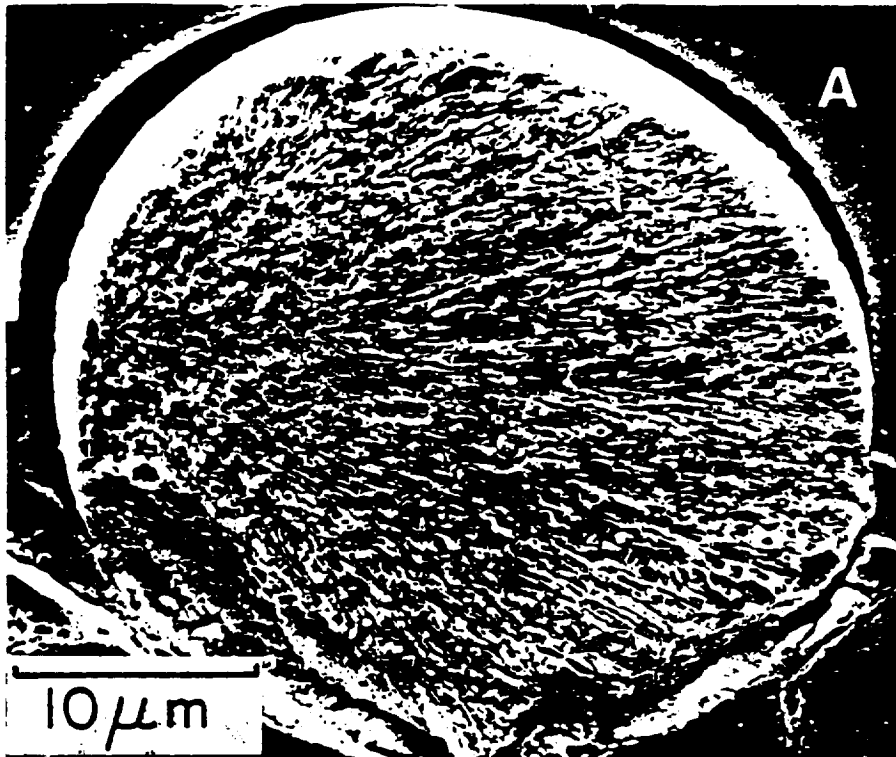
Fig. 6. SEM micrographs illustrating the eutectic structure developed in undercooled InSb-Sb powder, drop tube processed under (a) He gas and (b) vacuum conditions.

C-2

developed in similar size powders by drop tube processing under helium and vacuum conditions are compared in Fig. 6. The rod spacing is much finer for the helium processed sample reflecting an increased level of undercooling and a higher cooling rate. Furthermore, the application of the relation in Eq. 1 to detailed microstructural information on the progress of solidification across the drop allows for the interface temperature to be inferred at different stages of solidification so that a more complete thermal history for the sample may be evaluated. While this approach is quite effective and relies upon a eutectic solidification reaction, the occurrence of eutectics is fairly widespread and represents one of the most interesting solidification type reactions.

Heat Flow Analysis

During drop tube processing the cooling of a liquid droplet is due partially to radiator heat transfer and also to convective heat transfer. The temperature history of a liquid droplet during drop tube processing may be described by the following governing equation (6) as:

$$\frac{dT}{dt} = -\frac{\epsilon A \sigma}{mc} (T^4 - T_w^4) - \frac{hA}{mc} (T - T_a) \qquad (2)$$

where T_a is the gas film temperature, approximately $(T + T_g)/2$, T_g is the gas temperature, T_w is room temperature, t is the time, ϵ is the emissivity of the liquid, A is the surface area of the droplet, σ is the Stefan-Boltzmann constant, m is the mass of the droplet, c is the specific heat of the liquid and h is the heat transfer coefficient.

I

A finite difference method can be applied to eq. 2 to calculate the liquid droplet temperature as a function of falling distance in the drop tube and is illustrated for an Fe-Ni alloy in Fig. 7. In order to access the undercooling an experimental approach was developed to determine where the falling drop solidifies in the drop tube. A copper substrate was held at fixed distance from the initial drop point. If the drop was molten upon impacting the platform, the shape would be a splat, while if solidification had started before impact a spherical or hemispherical particle would result. By varying the platform height, the position at which solidification occurred could be determined and used with the calculation summarized in Fig. 7 to estimate the undercooling. For the case of an Fe-30 w/o Ni alloy an undercooling of about 120°C below the stable liquidus was attained in a 2 mm drop (Fig. 7). Similar experiments were conducted on Fe-10, 20 and 25 w/o Ni alloys. The undercooling results coupled with the Fe-Ni phase diagram are shown in Fig. 8. For the alloys with 10 and 20 w/o Ni a metastable BCC phase formed, while for alloys of 25 and 30 w/o Ni the stable FCC phase was produced. These results agree well with the calculated metastable phase boundaries. Therefore, the formation of the metastable BCC phase provides a measurement of the minimum undercooling. The consistency between the minimum undercooling estimate, the solidification free fall distance measurement and the heat flow calculation provides support for this approach to the analysis of the thermal history during drop tube processing.

Thermal Measurements

Another example of an attempt to judge the thermal history during drop tube processing has been developed for use with the NASA/MSFC 105 m drop tube (6). As illustrated in Fig. 9, a two color pyrometer is used for initial temperature determination of the sample at the top of the drop tube prior to
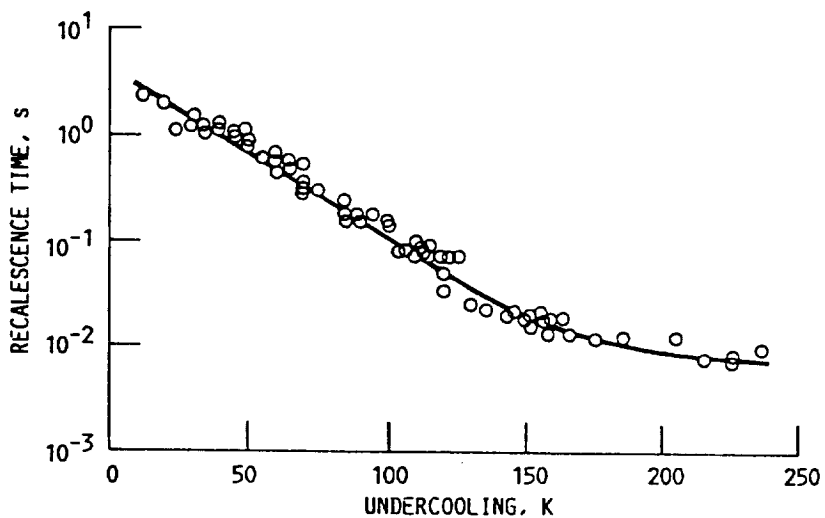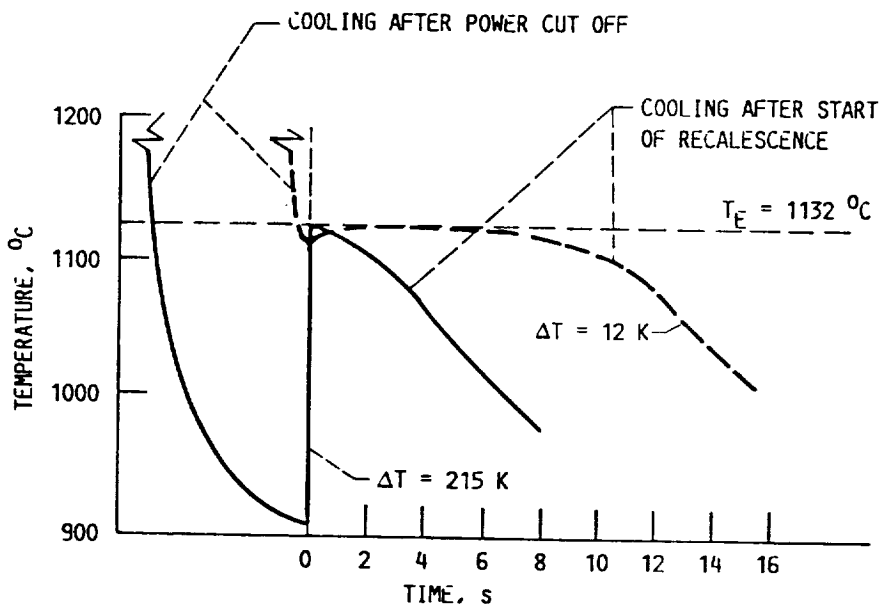
Fig. 12 a) Cooling curves for a eutectic Ni-Sn alloy at two levels
of undercooling. b) Recalescence time and initial
undercooling for a Ni-Sn eutectic sample. (From ref. 7).

100

A finite difference method can be applied to eq. 2 to calculate the liquid droplet temperature as a function of falling distance in the drop tube and is illustrated for an Fe-Ni alloy in Fig. 7. In order to access the undercooling an experimental approach was developed to determine where the falling drop solidifies in the drop tube. A copper substrate was held at fixed distance from the initial drop point. If the drop was molten upon impacting the platform, the shape would be a splat, while if solidification had started before impact a spherical or hemispherical particle would result. By varying the platform height, the position at which solidification occurred could be determined and used with the calculation summarized in Fig. 7 to estimate the undercooling. For the case of an Fe-30 w/o Ni alloy an undercooling of about 120°C below the stable liquidus was attained in a 2 mm drop (Fig. 7). Similar experiments were conducted on Fe-10, 20 and 25 w/o Ni alloys. The undercooling results coupled with the Fe-Ni phase diagram are shown in Fig. 8. For the alloys with 10 and 20 w/o Ni a metastable BCC phase formed, while for alloys of 25 and 30 w/o Ni the stable FCC phase was produced. These results agree well with the calculated metastable phase boundaries. Therefore, the formation of the metastable BCC phase provides a measurement of the minimum undercooling. The consistency between the minimum undercooling estimate, the solidification free fall distance measurement and the heat flow calculation provides support for this approach to the analysis of the thermal history during drop tube processing.

Thermal Measurements

Another example of an attempt to judge the thermal history during drop tube processing has been developed for use with the NASA/MSFC 105 m drop tube (6). As illustrated in Fig. 9, a two color pyrometer is used for initial temperature determination of the sample at the top of the drop tube prior to
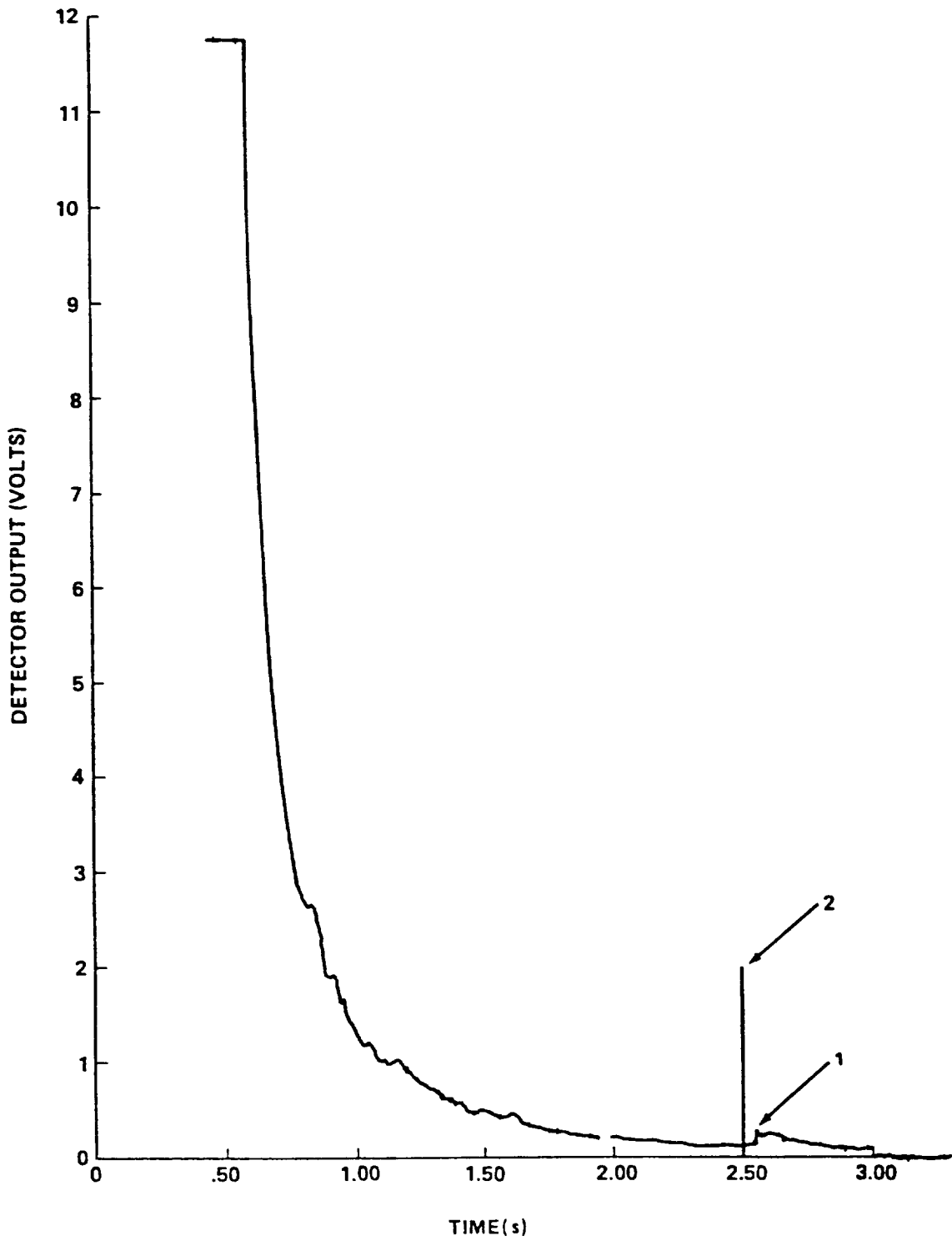
Fig. 7   Schematic illustration of the main components in the NASA/MSFC
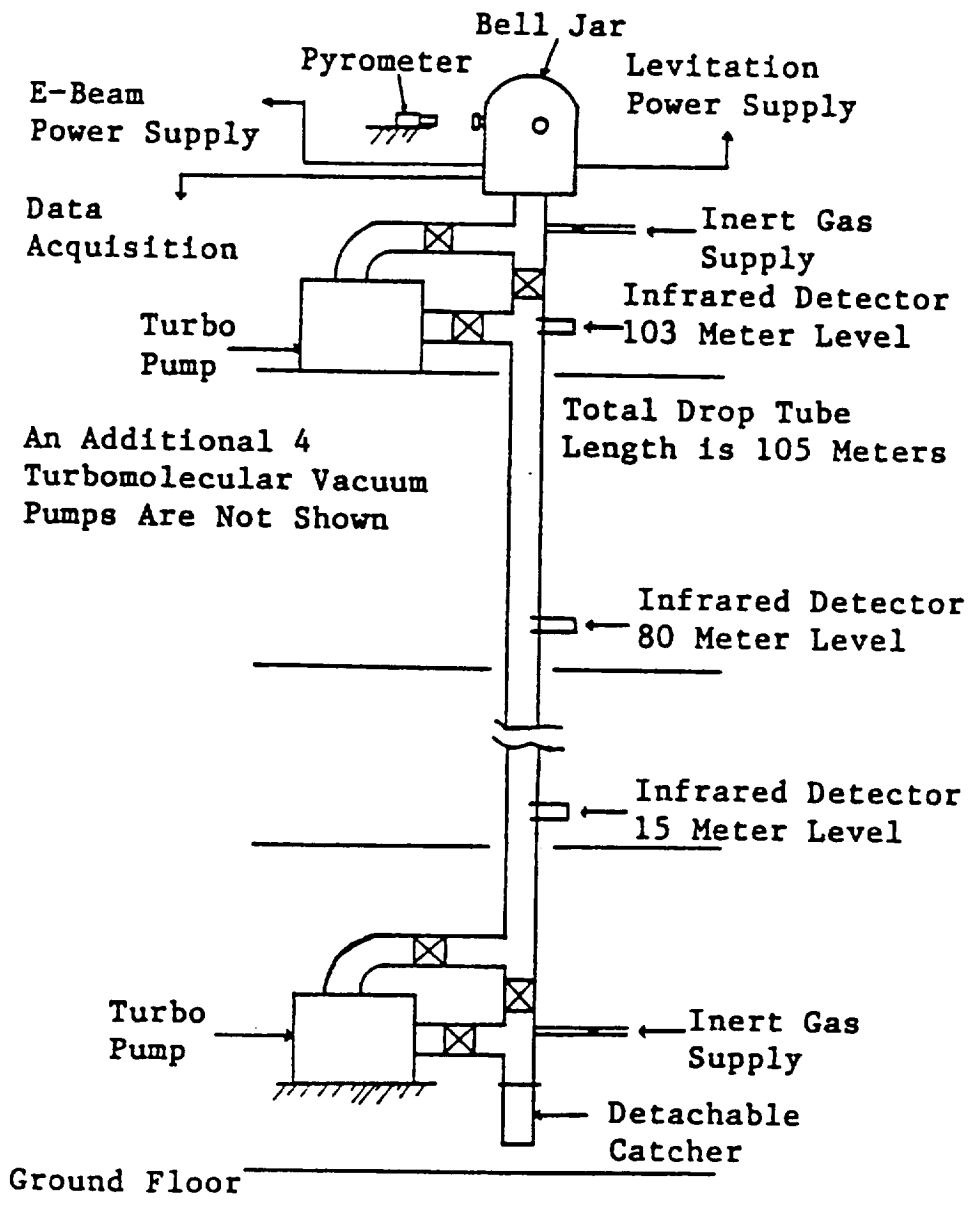105 m drop tube.   (From ref. 6).

94

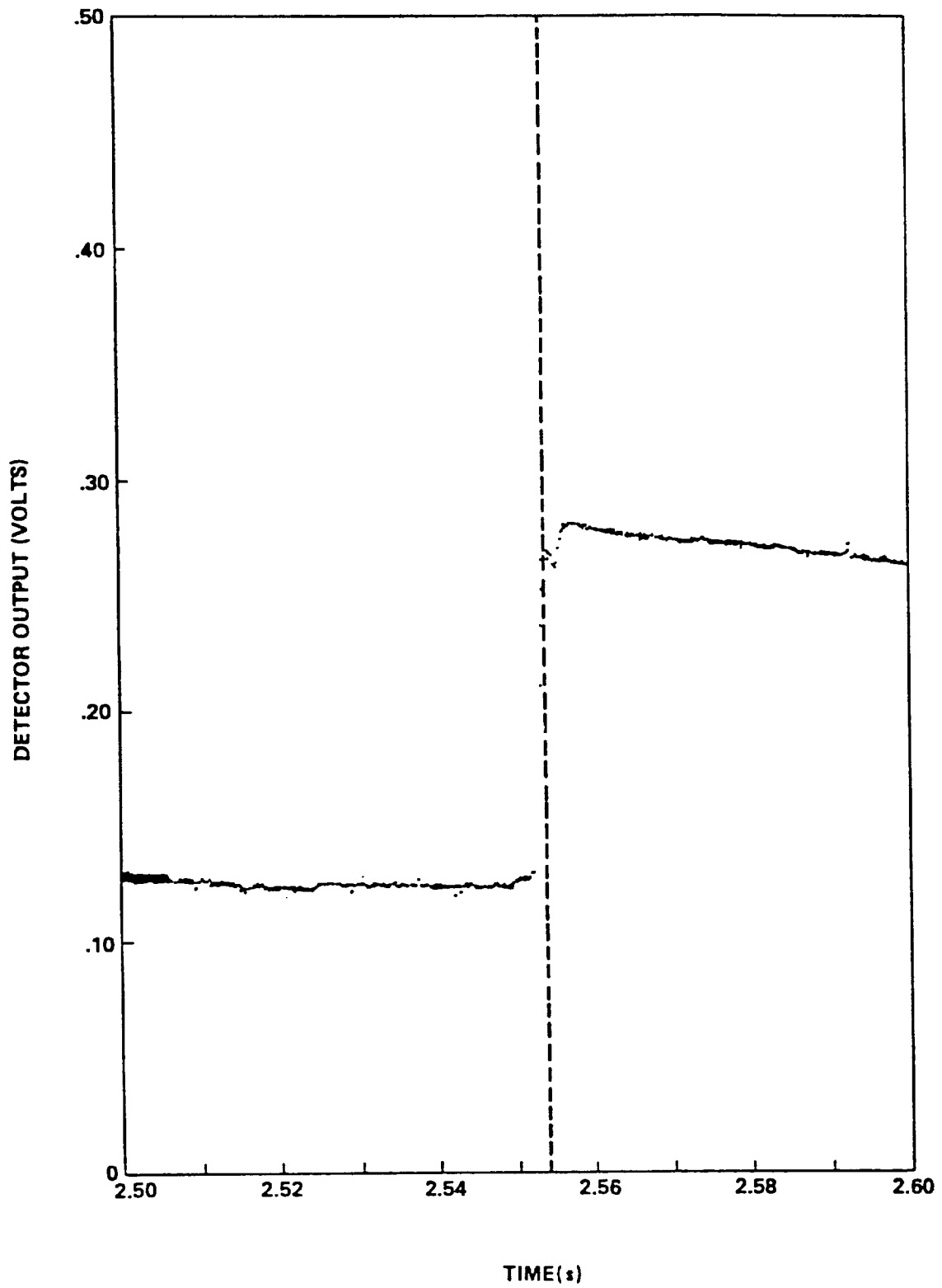Fig. 8 Computer-stored infrared detector signal for a Nb-Ge alloy drop. (From ref. 6).

Fig. 9 Expanded recalescence peak for a Nb-Ge alloy drop. (From ref. 6).

release. The samples are allowed to free-fall the entire length of the drop tube. During the fall the recalescence event associated with the nucleation is detected by a series of infrared sensors. With a knowledge of the release temperature at the top of the tube and the cooling time to recalescence which is measured by the infared sensors, the undercooling can be calculated from a heat flow analysis. The uncertainty in the calculations of undercooling for samples processed in this manner is of the order of ± 50°C. Part of the uncertainty in temperature determination is due to incomplete knowledge of the thermophysical properties of liquid metals such as the specific heat. With this approach significant undercooling levels of about 23% of the melting temperature have been obtained for a number of high melting temperature metals and alloys. The example shown in Fig. 10 is for a Nb-Ge alloy drop. In an expanded view shown in Fig. 11, the details of the recalescence event are apparent. The recalescence behavior is an important component of the microstructural development because it relates to the period of rapid crystal growth following nucleation from a highly undercooled state. The details of this process are more clearly illustrated in Fig. 12 which represents results from a Ni-Sn eutectic alloy that was processed with an electromagnetic levitation system (7). The measured time periods for the duration of the recalescence portion of solidification approach milliseconds for this particular alloy and illustrate the high speed response required. When it is considered that only one such recalescence event will occur over the entire length of a long drop tube, the demands on the instrumentation become clear. Perhaps this is the reason that a fully instrumented approach to drop tube processing is not yet available, but certainly is urgently needed for all aspects of research and development in containerless processing.

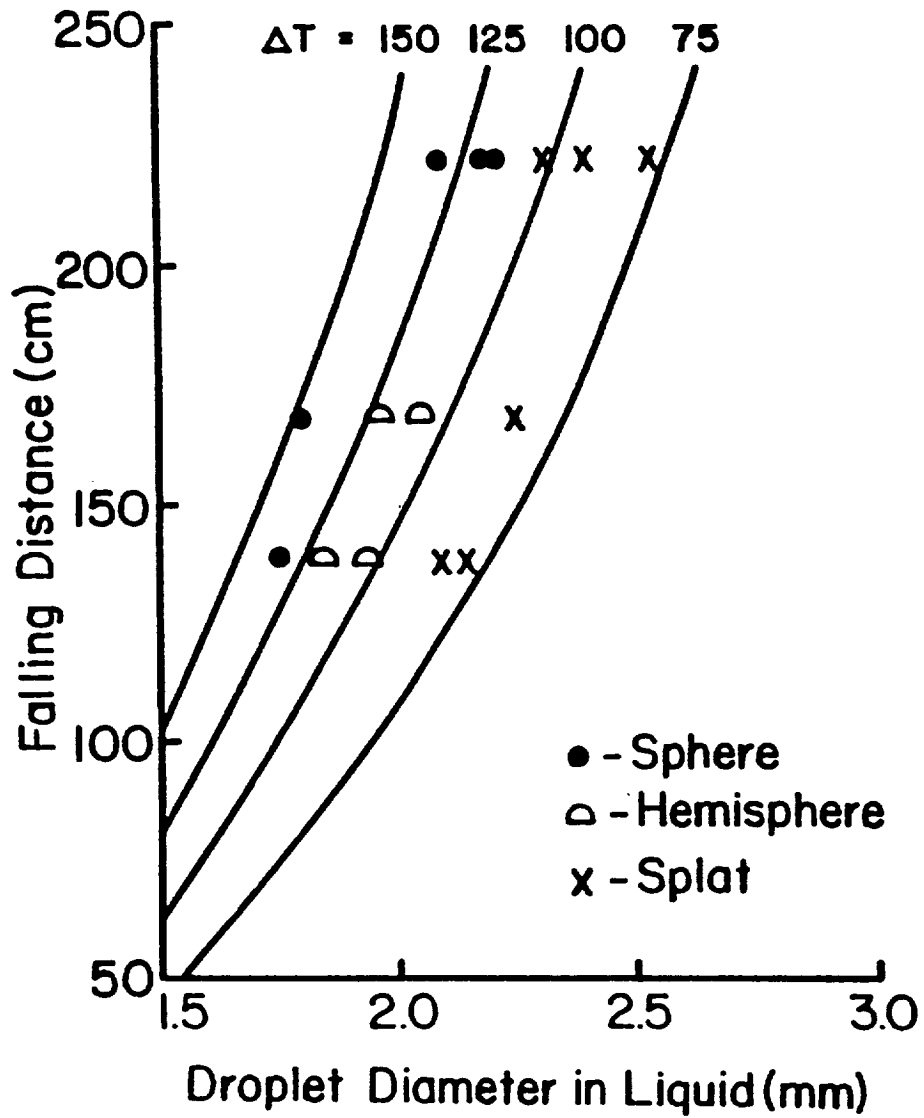Fig. 10 The calculated undercooling curves during free fall, with droplet shape observation summary (superheat of 200°C).
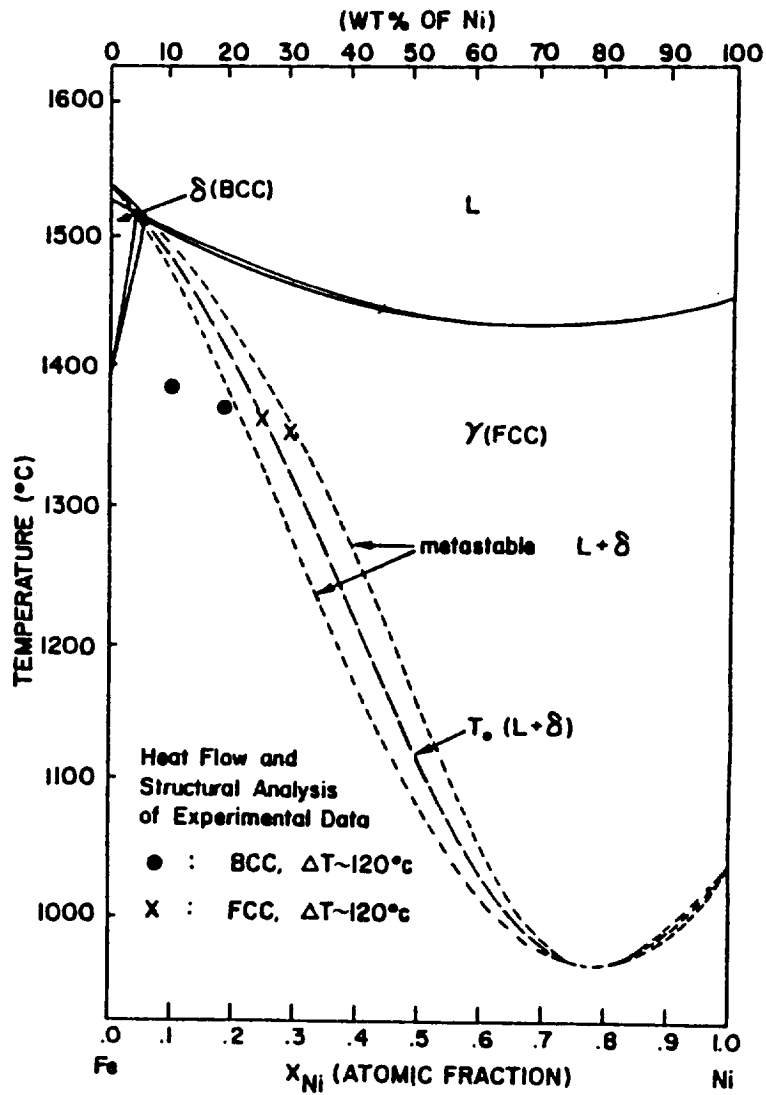
Fig. 11. Fe-Ni phase diagram showing metastable phase boundaries and estimated drop tube sample undercooling values.
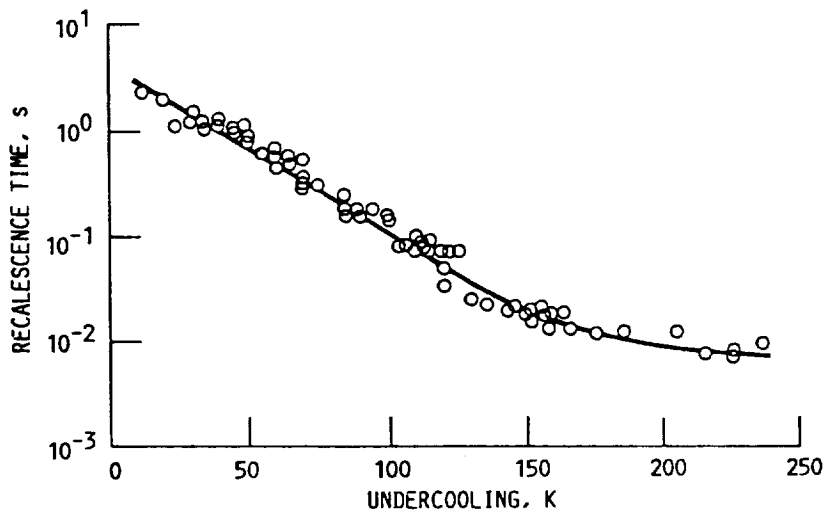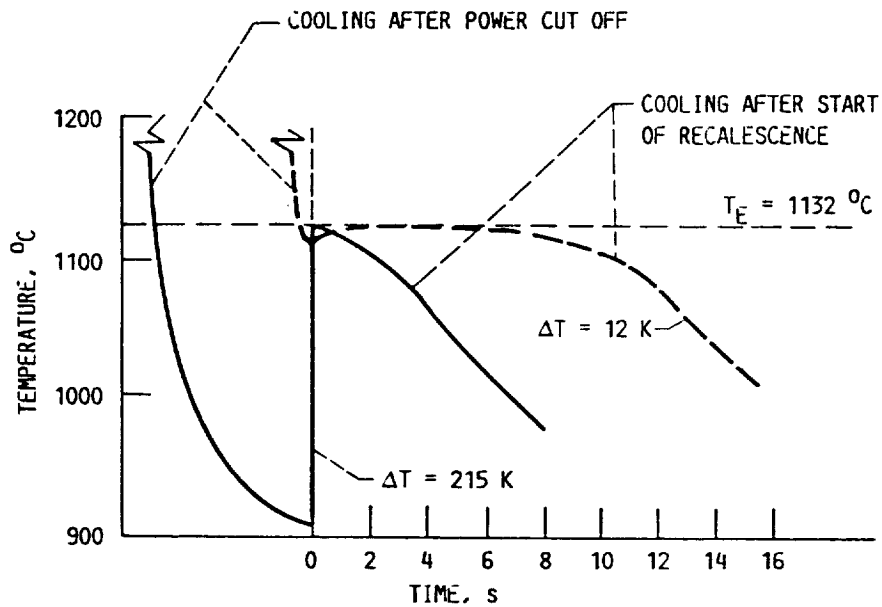
Fig. 12   a) Cooling curves for a eutectic Ni-Sn alloy at two levels
of undercooling. b) Recalescence time and initial
undercooling for a Ni-Sn eutectic sample. (From ref. 7).

Microstructure Prediction-Design

The overall development of a microstructure depends upon a number of processes occurring both serially and in parallel. For example, nucleation, growth, coarsening, convection, coalescence, and solid state reactions are some of the more significant processes. Ideally one would like to predict the outcome of these unit processes and develop methods for analyzing the resultant microstructure and properties. In a number of physical phenomena related to materials processing it is possible to identify material behavior in terms of a few characteristic parameters which can be expressed in terms of dimensionless groups. Over the range of values that the dimensionless groups are valid, the response of the material can be scaled so that the magnitude of the response at one value is related in some simple way to its response at some other value.

At present the most successful scaling laws are based on diffusional transport and morphological stability. Additional phenomena such as convection and nucleation are also included to complete the modeling of microstructure. For example the expected microstructures for growth conditions encountered in various domains of growth rate-thermal gradient are illustrated in Fig. 13 (8). It is important to note that the structural transitions occur at constant cooling rate which is the product of velocity and thermal gradient. The information provides a design tool for microstructure change. It also illustrates the importance of knowledge of temperature gradient as well as growth rate during solidification processing.

Another case where temperature gradient information is important is in the thermosolutal migration of bubbles and drops. When a system containing a second phase of vapor bubbles or liquid droplets is subjected to a thermal gradient an inbalance of intefacial tension around the drop or bubble will

SOLIDIFICATION MICROSTRUCTURE MAP
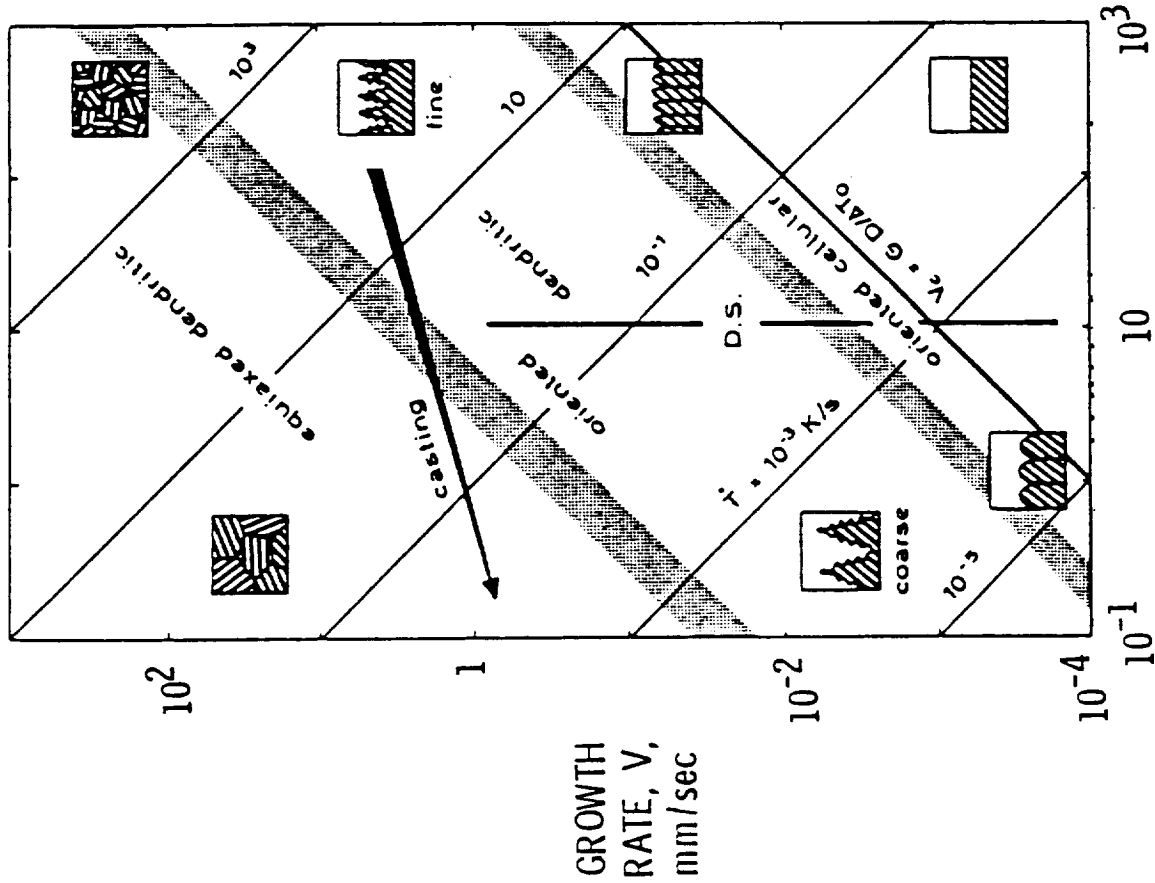
Fig. 13 Illustration of the expected microstructures from growth conditions encountered in various domains of growth rate and temperature gradient. (From ref. 8).

102

develop because the interfacial energy is a function of temperature. This force inbalance will drive convective flows called Marangoni Convection and is important to understand when a microgravity environment causes a suppression of density driven convection flows.

Summary - Non Contact Temperature Measurement Requirements

Based upon these few illustrations and a number of other important processing operations in the metals and alloys discipline area it is possible to formulate an initial set of recommendations for the types of noncontact temperature measurement capability that is important to support future materials research under microgravity conditions. These recommendations and requirements are summarized in Table 2. The three basic categories involve the ability to measure high temperature and to measure these temperatures with relatively rapid response rates and accommodate a range of heating rates as well as cooling rates encountered in containerless processing and other materials operations. A fine spatial resolution is required along with a rapid response in order to determine with accuracy the thermal gradients involved in processing as well as thermal profiles on relatively fine scale dimensions. With this thermal measurement capability one can not only monitor the growth rate on the average, but also develop thermal maps for the entire microstructural evolution which are needed in order to develop successful models to describe in analytical terms the evolution of microstructure in a microgravity environment.

Acknowledgement

Table 2

Metals and Alloys

Non-Contact Temperature Measurement

Requirement	Application
*High Temperature	- 500 to 4000 K, with ± 1K resolution (Containerless Processing) (Alloy Solidification) (Phys. Prop. Measurement)
*Fast Response	- Cooling Rates $(10^4 - 10^6$ K/s) - Recalescence Reheating $(10^5$ K/s) - Drop Tube Free Fall - Nucleation Undercooling $(T_M - T_N > 100$ K)
*Fine Spatial Resolution	- Temperature Gradients $(0.1$ K/cm - 10^5 K/cm) - Thermal Profiles in Phase Mixtures and Powders (<1 micron, dT $< 1°$ C $1 - 5$ cm^2) - Thermal Maps for Morphological Development and Thermosolutal Flows - Monitor Crystal Growth Rates $(10^{-2}$ cm/s to 100 cm/s)

References

1. "Metals and Alloys Goals Report: Science Priorities for Metals and Alloys Rsearch In Space", M. Glicksman, R. Naumann, J. Dantzig, H. Gray, D. Larson, F. Lankey, J. Perepezko and R. Pond, NASW 3991, 1985.

2. P. W. Voorhess and M. E. Gicksman, Acta Met. 32 2001, 2013 (1984).

3. S. R. Coriell and D. Turnbull, Acta Met. 30 2135 (1982).

4. D. S. Shong, J. A. Graves, Y. Ujiie and J. H. Perepezko, Mat. Res. Soc. Symp. Proc. 87 17 (1987).

5. J. A. Graves, NASA Contractor Report No. 175013, Washington, DC, 1985.

6. W. Hofmeister, M. B. Robinson and R. J. Bayuzick, Mat. Res. Soc. Symp. Proc. 87 149 (1987); L. L. Lacy, M. B. Robinson and T. J. Rathz, Jnl. Crystal Growth 51 47 (1981).

7. F. H. Harf, T. J. Piccone, Y. Wu, M. C. Flemings, Y. Shiohara, L. B. Gardner and E. A. Winsa, NASA TM 88909, Lewis Research Center, (1987).

8. W. Kurz and D. Fisher, "Fundamentals of Solidification", (Trans Tech, Switzerland) 91, (1984).

Table 1

Metals and Alloys

Science Priority Areas

A. Coarsening and Stability of Two-Phase Mixtures
    - Dendrite Coarsening
    - Ripening and Coalescence
    - Gravitational Settling
    - Liquid Phase Settling
    - Critical Wetting

B. Solidification of Supercooled Metals
    - Dendritic Growth/Diffusion Control
    - Interfacial Control (Kinetics)
    - Nucleation and Formation of Metastable Phases
    - Control of Supercooling
    - Containerless Processing

C. Interfacial Processes
    - Directional Solidification - Phase Spacing/Morph.
    - Particle Pushing
    - Bubble Formation - Porosity Control
    - Thermosolutal Migration of Droplets and Bubbles

D. Scaling Laws
    - Microstructural Prediction/Design
    - Anisotropic Surface Energy Effects and Kinetics
    - Polyphase Solidification

E. Measurements of Thermophysical Properties

F. Deposition and Dissolution of Metals
    - Deposition and Dissolution from Ionic Solutions
    - Vapor Deposition
    - Whisker Growth

106

NONCONTACT TEMPERATURE MEASUREMENT IN GLASS AND OTHER
TRANSPARENT MATERIALS

Robert H. Doremus
Materials Engineering Department
Troy, New York 12180-3590

Introduction

The temperature of a solid material can be measured with a radiation pyrometer, which is an optical device that measures the amount of electromagnetic radiation emitted from a solid in a narrow spectral region. An ideal blackbody radiator emits the maximum amount of radiation at any wavelength; the spectrum and intensity of emission of a blackbody depend only upon its temperature. To measure the temperature of a real material one must know how it compares with a blackbody. The ratio of emission from the solid to that of a blackbody can be calculated from the optical properties of the solid. If the solid is transparent at the measuring wave length, the temperature can be measured throughout the solid. The relationship between optical properties of glass and temperature measurements in it by radiation pyrometry are described in this note.

Emissivity

Consider a smooth slab of glass with a light beam of intensity I_o normally incident on its surface (see Fig. 1). Several different things happen to the light. A fraction R of it is reflected specularly at the glass surface. A fraction A of the light can be absorbed and converted to heat in the glass. Another fraction S can be scattered from the glass by imperfections in it; there is also a very small fraction scattering intrinsically by the glass structure. Finally a fraction T of the light is transmitted through the slab. The fraction R includes all light finally coming specularly from the
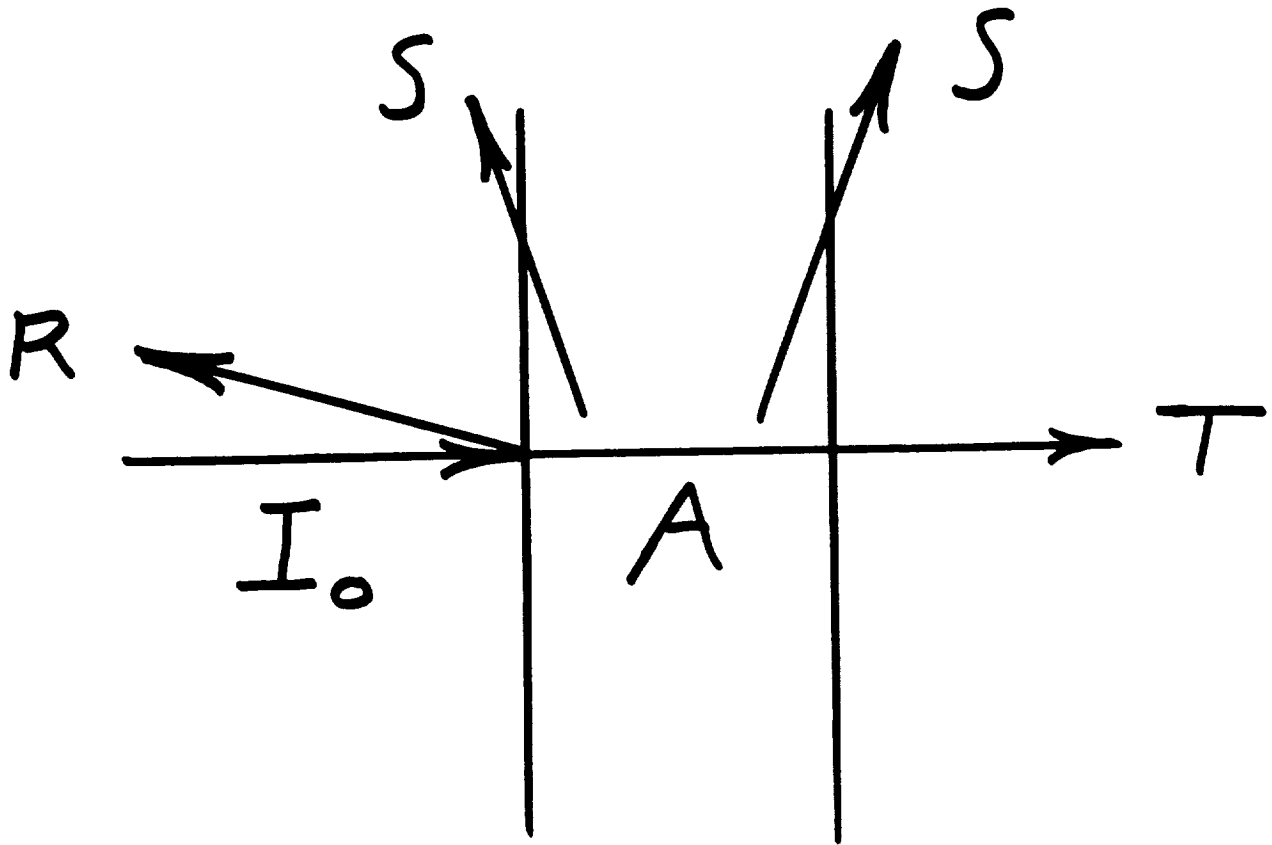
Figure 1 Schematic diagram of the fate of a beam of light of
intensity I_0 normally incident on a plane-parallel
slab of glass. R, specular reflectance; S, scattering;
A, absorbance; T, transmittance.

front surface, including that reflected from the back surface. From conservation of energy:

$$R + A + S + T = 1 \qquad (1)$$

If the solid body is at thermal equilibrium, it will have a uniform temperature and temperature constant with time. The emitted radiation E is then equal to that absorbed, as shown schematically in Fig. 2:

$$E = A \qquad (2)$$

The emissivity ε is defined as the ratio of radiation emitted from a solid to that E_B emitted from a blackbody of the same temperature, and over the same spectral range:

$$\varepsilon = E/E_B \qquad (3)$$

The emissivity can be specified for a narrow spectral range, or is sometimes described as "total" for the spectral range of "appreciable" emission in the visible and infrared parts of the spectrum. The spectral range for total emissivity shifts to lower wave lengths as the temperature increases, just as the range of blackbody radiation shifts.

Optical Properties of Glass

The transmittance T for a slab of commercial soda-lime silicate glass one cm in thickness is shown in Fig. 3 for the optical spectrum. In the ultraviolet region below about .3 μm light is absorbed by electronic transitions, first in impurities such as iron, and at shorter wave length from the main glass constituents. In the visible range (.4 to .65 μm) absorption of light is negligible, and the only losses are by reflection. For a transparent material the surface reflection in contact with a vacuum (or air) is:

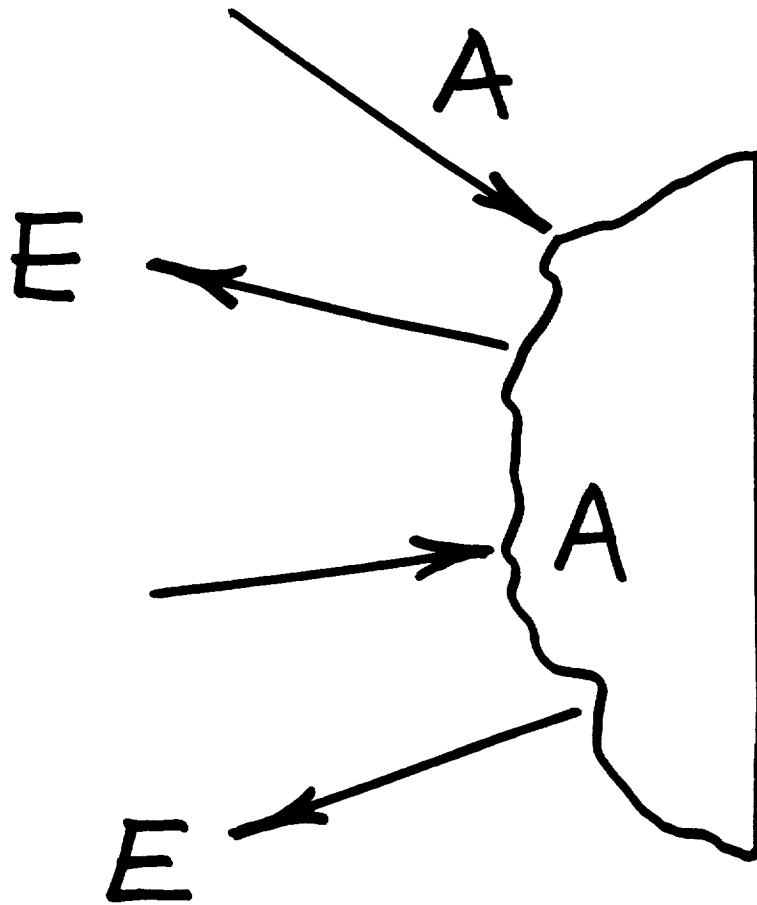$$R = \frac{(n-1)^2}{(n+1)^2} \qquad (4)$$

109

Figure 2   Schematic diagram of a solid body in thermal equilibrium.
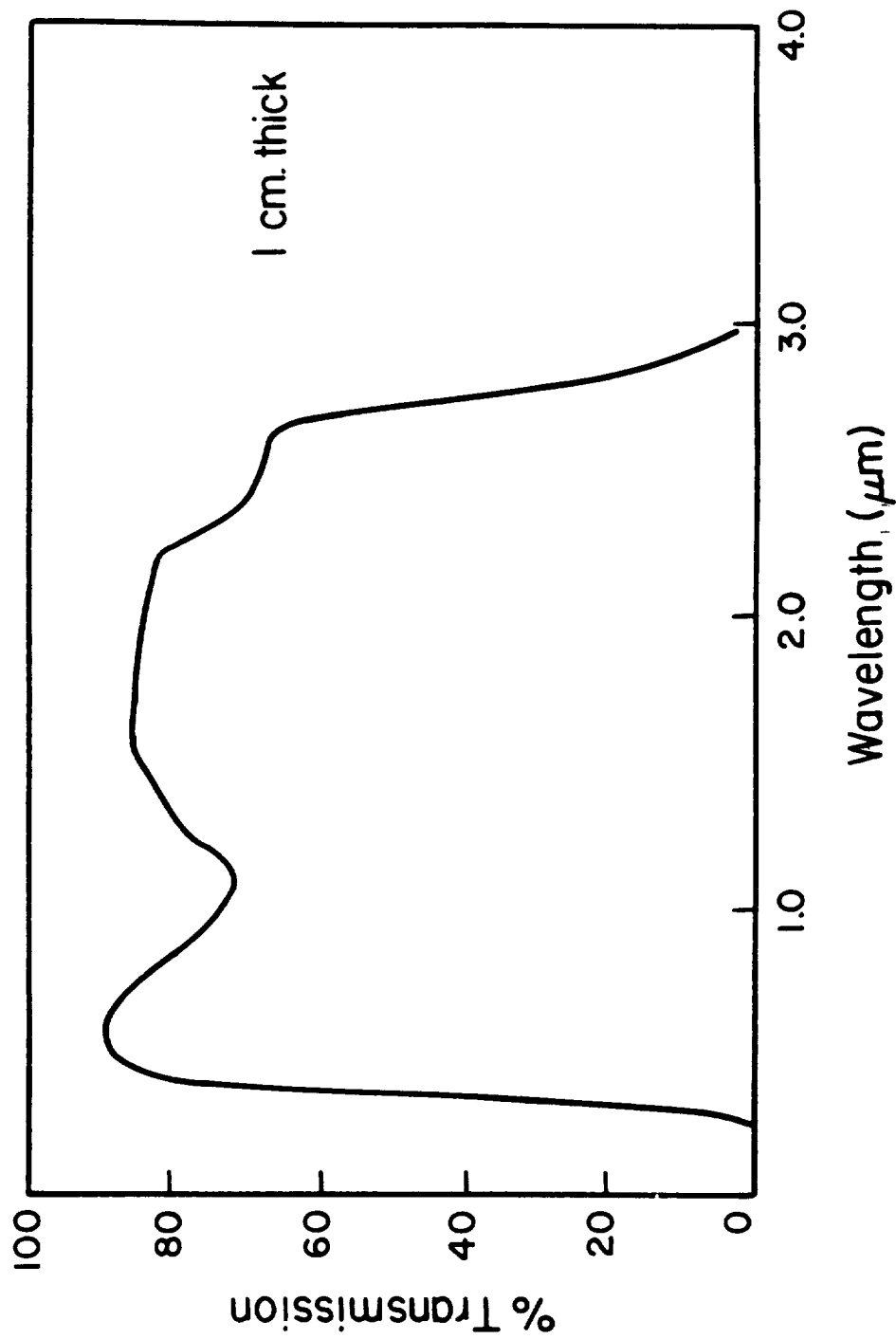E, radiation emitted; A, radiation, absorbed.

Figure 3   Optical transmission of a polished plane-parallel slab of glass one cm. thick as a function of wave length.

where n is the refractive index of the transparent solid. Since n is about 1.5 for most silicate glasses in the visible, the reflection loss is about .04 at each surface, or a total of about 8%, giving a transmittance of .92 if there is negligible scattering.

Absorption at wave lengths longer than the visible (infrared) result from impurities, especially iron and water, up to about 4.0 μm; at longer wave lengths there is a highly absorbing band resulting in vibrations of the silicon-oxygen bond. Data for refractive index of commercial and binary and ternary silicate glasses are given in N. P. Bansal and R. H. Doremus', Handbook of Glass Properties, Academic Press, Orlando, Florida, 1986.

The emissivity of glass can be calculated from known optical properties and Eqs. 1, 2 and 4, or measured directly by comparison with a blackbody. Some results of direct measurements are given in Table 1. As the temperature increases the total emissivity decreases because of the shift of the maximum in emitted light to lower wave lengths.

Temperature Measurement of Glass with a Radiation Pyrometer

For glass it is best to choose a pyrometer that is sensitive to radiation in a narrow wave length region because of changes in total emittance with temperature. Evan at a particular wave length there are changes of emittance with temperature, so it is best to use a comparative method in which a blackbody radiator, such as black cavity, has the same temperature as the glass. Then measurements of the radiation from the glass and the blackbody give the temperature and emittance of the glass directly. Often this is not possible, and the emittance of the glass must be measured in a separate experiment or estimated from known optical properties. If, the glass sample is quite transparent at the wave length of measurement, backing

TABLE I

EMISSIVITY OF COMMERCIAL SODA-LIME SILICATE GLASS

Temperature, °K	Total ε
0 - 800	.8 - .9
1100	.7 - .8

Temperature, °K	ε at .65 μm
300	0
1200	.05 - .1

Ref. Y. S. Touloukian and C. Y. Ho, eds., "Thermophysical Properties of Matter, TPRC Data Series", Vol. 9, Plenum Press, New York (1971).

113

or background effects can dominate. Thus it is preferable to choose a measuring wave length at which the sample is absorbing; for example, at 8 μm or greater.

If the glass sample is not at uniform temperature the measurement can "see" into the sample interior and will read an uncertain interior temperature, not the surface temperature. Of course sometimes it is valuable to measure temperature gradients in the sample.

More details are available from manufacturers of pyrometers, for example, "Technical Notes TN 101, Glass Temperature Measurement", Ircon, Inc., 7301 N. Caldwell Ave., Niles, Il., 60648.

Noncontact Temperature Measurements
in the
Microgravity Fluids and Transport Phenomena Discipline

Jack Salzman, NASA Lewis Research Center

Introduction

The objectives of the efforts conducted within the Microgravity Fluids and Transport Phenomena Discipline are to develop a further understanding of fundamental theories of fluid behavior, to provide improvements in basic thermophysical property measurements, and to provide scientific and engineering data related to a wide variety of fluids-related applications/systems.

The current understanding of fundamental fluid phenomena and the determination of many basic thermophysical fluids properties is severly limited by the masking effects and/or complexity factors induced by a gravitational force field. For example, in a gravity field, the buoyancy-driven flows which arise from density gradients preclude the study and subsequent understanding of other important transport processes. Similarly, it is these buoyancy-driven flows, and other gravity induced effects such as hydrostatic pressure which compress or collapse fluid specimens, that also preclude the accurate measurement of many thermophysical properties (e.g., diffusion coefficients, or properties such as viscosity and heat capacity near the critical point, etc.). Thus a significant reduction in gravity forces and their induced effects can enable measurements and observations of phenomena/processes which are impossible in a terrestrial environment. The pursuit of systematic studies of fluids under low-gravity conditions, and the resulting increased understanding will lead to refinements in existing theoretical models and potentially even new models to describe fluid physics and transport phenomena in both normal gravity and reduced gravity conditions.

The program of activities within the Fluids Discipline has been structured to enable the systematic pursuit of an increased understanding of low gravity fluid behavior/phenomena in a way which ensures that the results are appropriate to the widest range of applications. This paper will briefly discuss this structure and also provide an overview of some of the activities which are currently underway. Of significance is the fact that in the majority of the current and planned activities, the measurement and/or control of the fluid temperature is a key experiment requirement. In addition, in many of the experiments there is the requirement that the temperature measurement be nonintrusive. A description of these requirements together with the current techniques which are being employed or under study to make these measurements will also be discussed.

Program Structure and Status

The applications of the information and knowledge gained through microgravity or reduced gravity fluids experiments span over a wide range going from potential scientific advancement to the development of design data bases for future space-based systems. These applications can best be characterized by the following list of eight categories:

o   TESTING OF FUNDAMENTAL HYPOTHESES/THEORIES

o   MEASUREMENTS OF THERMOPHYSICAL PROPERTIES

o   PROCESSING OF METALS AND ALLOYS

o   FABRICATION OF GLASSES AND CERAMICS

o   GROWTH OF ELECTRONIC MATERIALS

o   BIOTECHNOLOGY

o   COMBUSTION SCIENCE AND SPACECRAFT FIRE SAFETY

o   SPACE-BASED FLUID/ENERGY MANAGEMENT

Experiments addressing the first two applications on the list emphasize the acquisition and application of highly specialized laboratory type data which can only be obtained under reduced gravity conditions. These data are intended to: 1) test theories which are of broad significance in fluid physics or dynamics, or in other fields of science; or 2) provide increased measurement accuracies of fundamental thermophysical properties such as the viscosity or heat capacity of a fluid near its critical point.

The remaining applications on the list generally can be classified as in-space applications since that is their focus. The resulting increased understanding of fluid behavior in these areas does however generally provide concomitant benefits for terrestrial operations. In the case of the materials processing applications (i.e., metal and alloys, glasses and ceramics, electronic materials, and biotechnology), it is important to note that virtually all of the materials are processed in their fluid state. Therefore, the understanding and control of reduced gravity fluid processes is of paramount importance to in-space materials processing research and development activities. By combustion science we specifically mean the conduct of in-space combustion experiments to further the understanding of combustion processes under terrestrial and reduced gravity conditions. Here, as in the case of spacecraft fire safety, the coupled fluid flow of the oxidizer and fuel stand out as key parameters in the ignition, flame spread, and extinction processes. Therefore, again the understanding and control of reduced gravity fluid processes become extremely important.

The last category on the list represents that one which is most directly focused on space applications in that the goal is to ultimately provide design data bases for use by space system developers. On-orbit storage, conditioning, and transport of fluids and energy through the use of fluids is pervasive in most current and future space-based systems and applications. The effectiveness and efficiency of space liquid propellant systems, thermal control devices, dynamic power systems, etc., all require a thorough understanding of fluid behavior and processes under reduced gravity conditions.

The Fluids Discipline faces a difficult, if not impossible, task in attempting to address all of the specific reduced gravity fluids issues of these applications. In general, there is a wide disparity in conditions encountered in these applications which make the number of application specific tests and the range of parameters they encompass completely unwieldy. Examine, for example, fluid temperature since it is always of importance. If it were necessary to conduct specific tests over the temperature range of the applications, the experiment test temperatures would have to vary from the extremely high temperatures of molten metals down to the near absolute zero degree temperatures of some cryogenic fluids. Fortunately, a closer examination of the large number of application specific issues reveals a much smaller set of fundamental issues involving basic fluid processes or phenomena. For example, surface tension driven convection is an important issue in both metals processing and liquid hydrogen propellant storage. It can be argued that while the temperature of the application varies dramatically, what is of prime importance is a basic understanding of the convection process under reduced gravity conditions. By extending this logic to the rest of the application issues one can arrive at a reasonably self-contained set of research topics or areas of fundamental understanding. These topics/areas include:

- o FIRST AND SECOND ORDER PHASE TRANSITIONS

- o MULTICOMPONENT/COUPLED TRANSPORT FLOWS

- o MAGNETO/ELECTROHYDRODYNAMICS

- o MULTIPHASE FLOW

- o CAPILLARY PHENOMENA

- o NUCLEATION AND CLUSTER PHENOMENA

- o ELECTRO-KINETICS AND ELECTRO-CHEMISTRY

- o DYNAMICS OF SOLID-FLUID INTERFACES

117

Obviously there will always be some unique issues in certain applications which do not conveniently fit into the above topics/areas. But, if necessary, they can be addressed on an individual basis. Therefore, it is felt that maximum value to all of the reduced gravity fluids applications can be achieved by maintaining a balanced basic and applied research program across all of the areas/topics.

The program of current and planned activities within the Fluids Discipline attempts to follow this balanced area/topic approach. While the current program is limited in scope and gaps exist, hopefully, as the program grows, the desired balance will be achieved. The current program is divided into ground-based efforts and space-based efforts where a set of space experiments either now exists or are under development. A representative sample of the ground-based activities includes the following topics:

- o TRANSPORT PROCESSES IN SOLUTION CRYSTAL GROWTH

- o SUPPRESSION OF MARANGONI CONVECTION

- o TRANSIENT HEAT TRANSFER STUDIES

- o NUCLEATE POOL BOILING

- o ELECTRODYNAMICALLY DRIVEN FLOWS IN MOLTEN SALTS

- o THERMODIFFUSOCAPILLARY TRANSPORT

- o CONVECTIVE FLOW BOILING

- o CRITICAL POINT VISCOSITY MEASUREMENTS

- o MASS TRANSPORT BETWEEN BUBBLES AND DISSOLVED GASES

- o THE CORRELATION LENGTH OF HELIUM II

- o ELECTROHYDRODYNAMICS

- o FREE SURFACE PHENOMENA

- o BENARD STABILITY

- o CRITICAL TRANSPORT PROPERTIES OF LIQUID HELIUM

The stable of flight hardware which is avilable or under development for actual space experiments is much more limited including only the following:

o   DROP DYNAMICS MODULE

o   FLUIDS EXPERIMENTS SYSTEM

o   CRITICAL FLUID LIGHT SCATTERING EXPERIMENT

o   SURFACE TENSION DRIVEN CONVECTION EXPERIMENT

o   LAMBDA POINT EXPERIMENT

There are also other sets of complementary experiment hardware which have been developed specifically for the other microgravity science disciplines (e.g., materials processing) which have some limited capability for fluids related experiments. However, even with the potential availability of this complementary hardware, the ensemble of space hardware for fluids experiments is severely limited and inadequate for the desired balanced program of low gravity fluids research. Fortunately, in several of the ground-based efforts, the conceptual designs of space experiments are nearing completion. It is anticipated that these concepts will be developed into actual space experiment hardware in a timely manner to provide a critically needed capability for acquiring low gravity data. There is also a renewed emphasis of more fully exploiting the limited capabilities of low gravity ground-based facilities (e.g., drop towers and aircraft) to also obtain the maximum reduced gravity data they can provide.

Temperature Measurement Requirements

As mentioned previously, the temperature of the fluid, which may be a liquid or a gas, is a dominant driving or controlling parameter in many of the processes/ phenomena of interest to the Fluids Discipline researchers. In experiments dealing with first order phase transitions such as boiling, condensation, or solidification, the importance of both the local and bulk fluid temperatures are obvious. Likewise, with studies of second order phase transitions such as critical point phenomena it is the precise control and measurement of the bulk fluid temperature that are primary experiment concerns.

In many of the other Fluids Discipline areas/topics the importance of fluid temperature is perhaps less understood than in the above examples. Unfortunately, it is impossible in this paper to elucidate the significance of temperature in all fluids processes/phenomena of interest. However, some discussion on the effects of temperature variations on surface tension forces

119

and their effects on low gravity fluid behavior does seem appropriate. As buoyancy induced flows are diminished as gravity forces are reduced, the relative importance of flows driven by gradients of surface tension become greatly amplified. The surface tension gradients can arise from a gradient of solute concentration but are more commonly the result of a thermal gradient across the surface between two fluids or two phases of the same fluid. Both cellular motion and general convective motion of the fluid can be generated. An increased understanding of the extent and magnitude of these "thermocapillary" flows, whether transient or steady-state, and their stability characteristics are of pre-emptive importance to low gravity fluids research and the applications which that research supports. Hence, in any reduced gravity experiment where thermocapillary flow is studied or may be encountered, the control and measurement of temperature is again a primary concern.

As was mentioned before, the actual fluid temperatures in reduced gravity experiments may range from $-271^\circ C$ (i.e., the Lambda point of Helium) to greater than $1000^\circ C$ (i.e., in liquid metals and eutectic salts.). The required control/measurement accuracies of these temperatures may be on the order of microdegrees. In some cases, spatially defined true surface (i.e., in the surface microlayer) temperature measurements are required across the extent of the surface and in other cases accurately defined point measurements within the bulk fluid are required. Obviously, this range of conditions presents formidable temperature measurement challenges.

Fortunately, just as the large number of applications specific fluids issues were reduced to a much more wieldy set of research areas/topics, the range of temperature measurement conditions and requirements can be reduced to a more tractable array for much of the low gravity fluids research within this discipline. The most common fluid temperatures encountered are from 0° to $100^\circ C$ with required accuracies in the $.001^\circ$ to the 1° range. Also, in many instances, standard contacting temperature measurement devices such as thermocouples or thermistors provide adequate results. However, a large number of experiments remain where nonintrusive temperature measurements are required. When the fluid processes/phenomena of interest are near the stability limits or when delicate flow pattern characterization is the core of the experiment, nonintrusive or, at a minimum, noncontact temperature measurement techniques are essential. Also, in some low gravity fluids experiments, a requirement for noncontact techniques is encountered which is not typical in terrestrial laboratories. This requirement involves containerless experiments. The major attribute of these experiments is the capability to float the fluid sample free of any of the contaminating or perturbing effects of a confining and contacting container. Obvious the use of contacting temperature measurement devices would defeat the purpose of a containerless experiment.

Noncontact Techniques

For many years, a number of noncontact temperature measurement techniques have been successfully exploited in ground-based fluids experiments. More recently efforts have been made to apply these techniques to low gravity experiments. An example of one such successful effort is the holographic interferometry subsystem of the Fluids Experiment System which was flown on Spacelab 3.

In discussing noncontact temperature measurement techniques, it is helpful to separate them into two categories: 1)those appropriate for surface temperature measurements and 2) those appropriate for measurements at sites within the bulk fluid.

The most common techniques for surface fluid temperature measurements involve the application of passive radiometry and/or pyrometry. Other techniques involve active light scattering and/or reflectivity. Most of these techniques are discussed in detail in the other papers at the Workshop and therefore these will not be discussed here. The only comment which must be made about these techniques as they apply specifically to fluids experiments involves the range of fluids of interest and their optical characteristics. Since, in many cases, the temperature of the actual surface is the parameter of importance, special consideration must be given to the transmission and emissivity properties of the fluid. This can make the choice of the spectral wavelength and bandwidth of the measurement system a difficult problem.

For the category of interior site measurements, the list of potential techniques which are available is already quite long but continues to grow as research advances are made. Perhaps the propensity for research directd at improving these techniques for this is due to the fact that in general the existing capabilities of such techniques are still considered too limited or inadequate for many fluids experiments. A particular problem in acquiring accurate data from the interior of the fluid is caused by the fact that the measurement must be made through a pathlength of fluid which is generally of an unknown or varying character. A general classification of the most promising techniques can be made in terms of: 1) index of refraction methods and 2) spectroscopic methods. Only a limited discussion of these techniques will be attempted.

Index of Refraction Method – These techniques rely on an interpretation of variations in the measured index of refraction and its known constituative relationships to temperature. Such constituative relationships are the Lorentz-Lorenz law for liquids and the Gladstone-Dale relation for gases. Techniques based on interferometry, either classical Mach-Zehnder interferometry or holographic interferometry, directly measure the index of refraction. Techniques based on deflectometry, such as those using schlieren or moire' fringe data, provide measurements of the gradient of the index of refraction which must be integrated to infer temperature. In those cases where the directionality of the gradient field is not known a priori, using deflectometry generally requires multiple measurements or complementary techniques to resolve the various components.

When applying any of the index of refraction methods the additional functional dependence of the index of refraction on concentration/density must be taken into consideration. In the simplest cases, the concentration field may be assumed to be sufficiently constant to allow accurate temperature interpretations. In other cases, additional measurement information must be obtained. One technique to supply this needed information when using interferometry is to collect the data at two or more optical wavelengths.

Spectroscopic Methods - These techniques generally rely on a determination of Boltzmann distribution of the molecular state populations of the fluid at the measurement site. The data necessary for the determination may be acquired through a variety of light scattering, fluoresence, or absorption technqiues. Because of the large number of technqiques that have been developed or are under development (e.g., spontaneous and stimulated Raman scattering incuding coherent anti-stokes Raman, Rayleight scattering, laser induced fluorescence, etc.), any attempts at discussing them in this paper would be totally inadequate. There are volumes of technical reports and books which discuss each of these separate techniques in detail. A common factor in most of the techniques is that lasers are used as a light source to supply needed energy fluxes and spatial resolution.

Concluding Remarks

In the above discussions of measurement requirements and techniques, an elaboration of the peculiar requirements of reduced gravity experiments has generally been omitted. This was done because, in reality, the measurement requirements for such experiments and the techniques like to be employed in them are equally applicable to the much larger field of terrestrial fluids research. There are many efforts currently devoted to the refinement of current techniques and the development of new techniques with significant advances rapidly emerging. The challenge presented to the reduced gravity fluids researchers and experiment developers is to expoit and adopt those techniques which can best satisfy their measurement requirements within the unique environment of a microgravity laboratory. Whether that laboratory is ground-based, such as in drop towers or aircraft, or space-based, such as in the Shuttle or the Space Station, the constraints of limited power, weight, and volume, the imposition of high shock loads, and the necessity for reliability and operational simplicity must be accommodated. Until this challenge is met, the future contributions of reduced gravity fluids research will be impaired.

MICROGRAVITY COMBUSTION DISCIPLINE WORKING GROUP
SUMMARY OF REQUIREMENTS FOR
NONCONTACT TEMPERATURE MEASUREMENTS

KURT SACKSTEDER
NASA LEWIS RESEARCH CENTER
CLEVELAND, OHIO

INTRODUCTION

Combustion systems consist of the complex interaction of competing, time-dependent mechanisms including: fluid motion (often- multi-phase), various modes of heat and mass transfer, phase changes, and chemical reactions. Low gravity experiments are conducted in combustion research in support of practical combustion systems in earth-based normal-gravity environments as well as the low-gravity environment of space.

The motivations for conducting combustion experiments in a low-gravity environment are of four basic types. The direct influence on combustion systems of gravitational acceleration, the influence of other mechanisms that are obscurred or masked by gravitational influences in a normal-gravity environment, the unique initial or boundary conditions that can be created in low gravity, and a determination of the mechanisms that limit low-gravity combustion are the underlying justifications for each low-gravtity combustion project.

Gravitational potential, acting on the large density gradients caused by the heat release typical of combustion systems, induces buoyant convection that asserts an influence on the flow field which in turn affects the mechanisms that control the rate of heat release. Thus, density gradients are a result of the net action of the participating mechanisms and are also the means by which gravity acts upon the system. Through buoyancy, gravitational influence is coupled directly or indirectly to most of the fundamental mechanisms of combustion systems.

In combustion systems containing dispersed solid or liquid particulates in a host fluid, a gravitational field acts on the interfacial density differences and results in the settling, or sedimentation of the denser particulates through the surrounding fluid. In addition to creating uncertainties in the distribution of the particulates, gravitational settling induces secondary flows in the wake of the settling particles. Low-gravity experiments remove the complexity introduced by the settling action.

Non-buoyant driving potentials for fluid motion are usually present in normal-gravity combustion systems, but are often overwhelmed by buoyant flow. Normal-gravity studies of forced-flow influences are common in combustion research, but become difficult to interpret when the forced-flow and buoyant-flow velocities are of comparable size. In systems involving a free liquid surface that is unevenly heated, gradients in the liquid surface tension provide a driving potential for motion in the liquid phase and,

through interfacial viscous interactions, motion in the vapor phase. Vaporization of a condensed phase fuel, because of the large density change associated with the phase transition, provides yet another source of fluid motion. Low-gravity studies permit the investigation of sub-buoyant velocities of each of these types.

Molecular diffusion of fuel, oxidizer, inert diluent and product species directly affect the statistical proximity of the reactant molecules in a combustion system. In systems where the fuel and oxidizer are not mixed before encountering the combustion zone, diffusion processes modified by buoyancy and perhaps other flow-field influences largely determined the flame characteristics. In low-gravity experiments the role of diffusional processes can be assessed under conditions of better flow-field control. Low-gravity experiments have also provided insight into premixed-gas systems where unequal rates of molecular diffusion of the reactants influence the limits of flammability.

Favorable boundary conditions, symmetries and initial conditions are possible in some low-gravity combustion experiments. Small masses of fuel can be mechanically isolated from the surroundings creating a spherical symmetry that is undisturbed by buoyant flows or motion of the fuel mass through the air. Dispersed fuel systems can be preconditioned for uniform distribution without contending with sedimentation or the various turbulent air disturbances that are required to distribute such fuels in normal-gravity environments.

Current efforts in low-gravity combustion research exploit each of these opportunities to obtain data of a fundamental nature for the enhancement of the modeling of normal-gravity combustion systems. As a distinct goal, a fundamental understanding of the limiting mechanisms of various combustion systems proceding in low-gravity environment is sought to enable the development of advanced concepts in spacecraft fire safety. To the extent that low-gravity experiment time becomes available, a data base for the combustion related properties of various potential spacecraft materials can be evolved.

Current Microgravity Combustion Efforts

Current work in the Microgravity Combustion Program includes efforts in solid, liquid and gaseous fuels. Work in solid fuels is concerned firstly with understanding the detailed physical mechanisms of the spreading of established flames and secondly with understanding the relationship between fuel properties and environmental conditions that together determine the flammability of a material. Work in quiescent and forced-flow systems of nonmetallic fuels is in progress and metals combustion efforts are contemplated. In related work, smoldering combustion is being studied to understand the controlling mechanisms of the propagation of the smoldering wave and the conditions under which the smoldering process transitions to either flaming combustion or extinction.

In liquid fuels two classes of problems are being addressed. Droplet vaporization and combustion studies are concerned with the rates at which these processes occur, the occurance of related processes such as soot formation and droplet microexplosions, and an understanding of the scaling of these processes between droplets large enough to observe and the microscopic droplets that are characteristic of engines, furnaces, etc. Pool fire studies are concerned with the effects of the extended-surface properties particularly surface tension, and how these properties affect both the ignition of such fires and their propagation.

Flames in gaseous fuels are of particular fundamental interest and provide insight into more complex multiphase systems. Premixed and unpremixed systems are being studied to understand the role of diffusional processes in propagation rates and flammability characterizations.

Temperature Measurement Requirements

Knowledge of the temperature field in a combustion system provides information about several of the key participating mechanisms. The maintenance or propagtion of a flame depends upon the magnitude and modes of heat transfer from the reaction zome to the unburnt fuel. The reinvestment of the chemical energy released in the flame is applied to the generation of fresh fuel through a phase change in a multiphase system such as solid surface flame spreading or droplet combustion; and is also applied to the continued ignition of fresh fuel and exidizer mixture. Multiphase heat conduction, convection and radiation are each characterized in part by a determination of temperatures and their first and second derivatives at well chosen locations in the system.

The chemistry of combustion systems and the rate at which the reactions occur are strong functions of local temperature. Models of system chemistry range in complexity from a lumped model of a single-step reaction to a detailed array of perhaps scores of elementary reactions. In each case the rate of such reactions are exponential functions of local temperature, and any approach to accurate modeling requires temperature information of fairly high quality.

Many of the combustion systems that are studied in the low-gravity environment are near-limit systems, that is, systems that are acting near the limit of flammability in terms of oxygen concentration or fuel concentration. Systems of this type are normally weak in the sense that there is a delicate balance between the heat released in the flame and the heat required to sustain the flame. Any externally induced losses of heat from the system can drive the system unnaturally to extinction. Intrusive or perturbative temperature measurement probes such as thermocouples can be inaccurate in these situations and in the limiting case extinguish the flame. Noncontact or nonperturbative techniques then become the only way to obtain the required measurements.

In the general sense, a temperature measurement system for use in combustion research must be capable of probing the temperature field in each thermodynamic phase of the system. In the gas phase local measurements must be made in the presence of highly luminous flames and soot particles. While measurements of temperature in the depth of condensed phases(s), viz. solids and/or liquids are helpful, quite often the determination of the surface temperature will yield the more important information of surface properties such as local surface tension in liquids, phase transition rates (sublimation or boiling,) and surface emissivity. Often these measurements must be attempted where the surface location changes with time because of such things as surface-tension induced distortions and phase-change induced surface regression.

While it would always be desireable to have complete knowledge of the temperature field throughout the vicinity of a combustion system, a choice must often be made between local or point measurements and two-dimensional measurements in a plane passing through the system. Even in systems that are temporally stationary, the durations of most combustion experiments are limited. Thus many repeated experiments can be required to map the temperature field using point measurement techniques. The limited number of experiments that can be performed in the various low gravity facilities thus result generally in unacceptable spatial resolutions for the temperature measurements. Planar measurements while providing full-field information generally do so at the cost of considerable reduction in the measurement accuracy and precision. Perhaps the best comprise for many combustion systems is to obtain planar measurements as a matter of course, augmented as required by carefully selected point measurements. Confronted with a choice of measurements of only one type, the planar measurement would most often be reluctantly selected.

The table below summarizes the noncontact temperature measurement requirements of the Microgravity Combustion Discipline, providing measurement ranges and resolutions in space and time for each of three thermodynamic phases.

MICROGRAVITY COMBUSTION DISCIPLINE
NONCONTACT TEMPERATURE MEASUREMENT REQUIREMENTS

	Temperature Range (^{O}K)	Resolution Spatial (mm)	Temporal (msec)	Measurement Accuracy (^{O}K)
Solid Phase (Surface)	270-800	1	20	5
Liquid Phase (Surface)	270-350	0.5	40	0.2
Vapor Phase	300-3000	1	20	5

Bibliograghy

1) Knight, B. and Williams, F.A., "Observations on the Burning of Droplets in the Absence of Buoyancy," Combustion and Flame, Vol. 38, pp.111-119, 1980.

2) Berlad, A.L., "Multiphase Combustion Experimentation in Microgravity," IAF-83-141, Presented at the 34th Congress of the International Astronautical Federation, October 1983, Budapest, Hungary.

3) Abramzon, B., Edwards, D.K., and Sirignano, W.A., "Transient Natural and Surface Tension Driven Convection in a Two Layer Gas and Liquid Enclosure with Nonuniform Radiative Transfer," Paper No. 86-0578, AIAA 24th Aerospace Science Meeting, 1986.

4) Dosanjh, S., Peterson, J., Fernandez-Pello, A.C., and Pagni, P.J., "Buoyancy Effects on Smoldering Combustion," Acta Astronautica IAF-85 Stockholm Special Issue: Microgravity Materials and Fluid Sciences, 1986.

5) Ronney, P.D. and Wachman, H.Y., "Effect of Gravity on Laminar Premixed Gas Combustion I: Flammability Limits and Burning Velocities," Combustion and Flame, Vol 62, pp. 107-119, 1985.

6) Ronney, P.D., "Effect of Gravity on Laminar Premixed Gas Combustion II: Ignition and Extinction Phenomena," Combustion and Flame, Vol 62, pp. 121-133, 1985.

7) Ronney, P.D., "Effect of Gravity on Halocarbon Flame Retardant Effectiveness," Acta Astronautica, Vol. 12, No. 11, pp. 915-921, 1985.

8) Wherley, B.L. and Strehlow, R.A., "The Behavior of Fuel Lean Premixed Flames in a Standard Flammability Tube Under Controlled Gravity Conditions," Tech, Rep. AAE 86-3, UILU-ENG 86-0503, University of Illinois, Urbana, Illinois.

9) Cochran, T.H., "Experimental Investigation of Laminar Gas Jet Diffusion Flames in Zero Gravity," NASA TN-D-6523, 1972.

10) Cochran, T.H. and Masica, W.J., "Effects of Gravity on Laminar Gas Jet Diffusion Flames," NASA TN-D-5872, 1970.

11) Edelman, R.B., Fortune, O., and Weilerstein, G., "Analytical Study of Gravity Effects on Laminar Diffusion Flames," NASA CR-120921, 1973.

12) Edelman, R.B., Fortune, O.F., Weilerstein, G., Cochran, T.H., and Haggard, J.R., "An Analytical and Experimental Investigation of Gravity Effects upon Laminar Gas Jet Diffusion Flames. 14th Symposium (International) on Combustion, pp.399-412, The Combustion Institute, Pittsburgh, PA.

13) Vedha-Nayagam, M. and Altenkirch, R.A., "Backwards Boundary Layers in Downward Flame Spread," 20th Symposium (International) on Combustion, pp.1583-1590, The Combustion Institute, Pittsburgh, PA.

14) Vedha-Nayagam, M. and Altenkirch, R.A., "Gravitational Effects on Flames Spreading Over Thick Solid Surfaces," Acta Astronautica, Vol 12, No.7/8, pp.565-572, Pergammon Press, 1985.

15) Olson, S.L., and Sotos, R.G., "Combustion of Velcro in Low-Gravity," NASA TN-88970, 1987.

Requirements for Temperature and Species Concentration Measurements in Microgravity Combustion Experiments

Paul D. Ronney
Department of Mechanical and Aerospace Engineering
Princeton University, Princeton NJ 08544

While microgravity combustion studies have proved to be very informative, ground-based facilities do not always provide a sufficient duration of microgravity for some experiments. Thus, it would be advantageous to perform certain experiments aboard the U. S. Space Station. Furthermore, ground-based experiments in drop towers are often limited by the available diagnostics. In particular, most microgravity combustion experiments could benefit from nonintrusive temperature and species concentration measurements but these diagnostics are impractical in ground-based experiments. In order to limit costs for Space Station experiments which employ these diagnostics, a facility must be developed which can be shared by many investigators performing a variety of combustion and non-combustion experiments.

The requirements for a nonintrusive optical diagnostic facility for Space Station are assessed by examining the needs of current and future combustion experiments to be flown aboard the Space Station. Requirements for test section geometry and size, spatial and temporal resolution, species type and concentration range, and temperature range are reviewed. The feasibility of the development of this system will also be addressed. The suitability of this facility to non-combustion experiments in gases and liquids is also considered.

Requirements for Temperature and Species Concentration Measurements in Microgravity Combustion Experiments

Paul D. Ronney
Department of Mechanical and Aerospace Engineering
Princeton University, Princeton NJ 08544

Abstract

The requirements for nonintrusive optical diagnostics for Space Station combustion experiments are assessed by examining the needs of experiments which are planned to be flown aboard the Space Station. Requirements for temperature measurements, species concentration measurements, test section geometry and size, and spatial and temporal resolution are reviewed. The feasibility of the development of a diagnostic facility is addressed. The suitability of this facility to non-combustion experiments in gases and liquids is also considered.

1. Introduction

While studies of combustion at microgravity (μg) have proved to be very informative, ground-based facilities do not provide a sufficient duration of μg for some experiments. Thus, it would be advantageous to perform certain experiments aboard the U. S. Space Station where much longer duration experiments may be performed. Furthermore, ground-based μg experiments in drop towers are often handicapped by the primitive diagnostics which must be employed due to impact loads and space constraints. These constraints may be relaxed in Space Station experiments. The principle drawback of Space Station experiments is limited flight opportunities, hence advanced diagnostics are essential in order to gain as much information as possible from each experiment. Thus, μg combustion experiments performed aboard Space Station will enable the use of advanced diagnostics and furthermore will benefit greatly from their use. In order to limit costs for Space Station experiments which employ these diagnostics, it appears practical to develop a facility which can be shared by many investigators performing a variety of combustion and non-combustion experiments. In this paper the requirements for such a facility is discussed and a specific facility plan is proposed.

Practically all μg fluid physics and combustion experiments exhibit fluid flow phenomena which are easily disturbed by external influences. Thus, it is essential that non-intrusive techniques, usually some type of optical method, be employed. Furthermore, most fluids are not blackbodies nor even greybodies;

130

I

rather they absorb, emit, and scatter radiation weakly and only in narrow bands. Thus, pyrometric techniques are entirely inappropriate for these experiments (except perhaps to measure solid surface temperatures as discussed in section 6); instead, other techniques such as absorption, scattering or fluorescence must be employed. Absorption measurements cannot provide spatial resolution, hence absorption will not be considered further in this study.

2. Characteristics of microgravity combustion experiments

Perhaps the most important characteristic of all combustion and fluid physics experiments for which μg experiments may be expected to provide new information is a low Froude number (Fr $\equiv U^2/gd$, where U and d are a characteristic velocity and dimension, respectively, and g is the gravitational acceleration) at earth gravity. In other words, a system must be "big" and "slow" in a sense if buoyancy effects are to be important. Another important characteristic of these experiments is that for systems at earth gravity which are of reasonable size, the low Froude number stipulation leads one to conclude that the Mach number must necessarily be quite low. Thus, compressibility effects are insignificant and only hydrostatic forces will result in pressure gradients. In gases hydrostatic forces are of course negligible.

Flames are often divided into two categories: diffusion and premixed. In diffusion flames, two phases or components exist which must be mixed before reaction can occur and reaction is usually restricted to a narrow zone where the fuel and oxidant have mixed to near-stoichiometric proportions. In premixed flames the reactants are intimately mixed on the molecular scale prior to the combustion process.

These two types of flames are affected by gravity in very different ways. In diffusion flames, because of the dominant role of mixing, buoyancy effects are significant whenever the Froude number based on the forced convection velocity (not S_u) is small [1]. In the case of premixed flames, however, buoyancy effects are usually unimportant unless the burning velocity S_u is comparable to the buoyant convection velocity, which is usually near limits of flammability [2], ignition [3], or stability [4]. In diffusion flames the reaction zone structure is unlikely to be affected by buoyant forces because of its thinness [1] (and thus its high Froude number), however, in the premixed case buoyancy may affect the reaction zone structure for sufficiently slow flames as discussed in section 5.

3. Representative experiments

In order to determine the most important requirements for Space Station combustion experiment diagnostics, five

representative experiments were selected for study. These experiments were chosen for their practical value and because they are among most likely to be performed aboard the Space Station. The representative experiments, recent references, and the principal investigators (PIs) of these experiments are shown in Table 1. These investigators were surveyed to obtain their opinions as to which measurements are the most important for their experiments and what temporal and spatial resolutions are required. From this information, a consensus of the most important diagnostics for Space Station combustion experiments may be formulated.

Experiment	Principal Investigator
Particle Cloud Combustion [5]	A. L. Berlad, Univ. of Calif., San Diego
Solid Surface Combustion [6]	R. A. Altenkirch, Univ. of Kentucky
Single Liquid Fuel Droplets [7]	F. A. Williams, Princeton Univ.
Gas-Jet Diffusion Flames [8]	R. B. Edelman, Science Applications, Inc., Chattsworth, CA
Premixed Gas Flammability Limits [9]	P. D. Ronney, Princeton Univ.

Table 1. Representative experiments

4. Diagnostic requirements

Based on this survey, the following consensus was reached by most of the PIs. While one would like to know everything about the system, the most important measurements are one-dimensional or preferably two-dimensional time-dependent measurements of temperature and (slightly less important) major species concentrations (e.g. fuel, fuel pyrolysis products, oxygen, nitrogen, water vapor, and carbon dioxide). Many PIs also wanted to measure soot particle size and number density in their experiments. Furthermore, two-phase combustion experiments required measurement of condensed phase surface temperature. Gas velocity and minor species concentrations were considered to be less important in most cases. In addition, each experiment was found to have certain specialized measurement requirements.

5. Premixed gas combustion diagnostics

The requirements for diagnostics in premixed gases seemed to form a "common ground" of measurements that all PIs wanted, both in the type of measurements desired and the relevant scales. Because of this, the characteristics of the premixed gas flammability limit experiments are considered first.

The range of temperatures to be measured in μg combustion experiments is the usual range for combustion processes, typically 300K to 2500K. The number densities of major species vary up to 2.5×10^{19} at atmospheric pressure. Obviously it would be desirable to measure species present in much lower concentrations if possible.

In order to determine the characteristic time and length scales of these experiments, we must first estimate the maximum Froude number for which gravitational effects may be expected. This may be accomplished by equating the buoyant acceleration term in the steady 1-d momentum conservation equation with the convective acceleration term, ignoring viscous effects. This yields

$$UdU/dx = g \qquad (1)$$

substituting S_u, the burning velocity for U, and $\delta = \alpha/Su$ for x, where δ is the flame thickness [1] and α is the thermal diffusivity, we obtain

$$S_u^3/\alpha = g \qquad (2).$$

Then the Froude number in this case is

$$Fr = S_u^2/g\delta = S_u^3/g\alpha = 1$$

as one might have expected. Thus, the Froude number must be of order unity or less for buoyancy effects to be important. A typical values of α for flames at one atmosphere would be 1 cm^2/sec, hence $Su \approx 10$ cm/sec or less for conditions where buoyancy would be expected to have an effect. Then $\delta \approx 0.1$ cm and the characteristic time $\delta/S_u \approx 0.01$ sec.

It should be noted that for any flame of sufficient size (i.e. low Froude number), no matter how fast the flame or thin the reaction zone, buoyancy will be important in characterizing the fluid mechanics of the system (but not the structure of the chemical reaction zone.) Only very slowly burning premixed flames have reaction zones which are affected by buoyancy, as the above analysis shows, but even for a very fast flame, as the flame grows larger, a rising "fireball" appears which will eventually be affected by buoyancy. In this case the system is merely a propagating density discontinuity in a gaseous medium, the characteristics of which are well known.

That buoyancy may effect premixed flames with burning velocities below about 10 cm/sec has been shown experimentally [9]. However, much more interesting interactions are found for burning velocities of about 1 cm/sec [9], for which $\delta \approx 1$ cm and the characteristic time is about 1 sec. In order to resolve

133

these time and length scales, resolutions of one-tenth these scales or less are necessary. Thus, the following requirements for Space Station premixed gas combustion diagnostics may be formulated:

Spatial resolution: 0.1 cm
Temporal resolution: 0.1 sec
Time aperture (to "freeze" the system):   0.001 sec
Test section size for 100 x 100 points: 10 cm x 10 cm

These requirements closely match those recommended by the PIs of the other experiments.

6. Special requirements for other experiments

Each of the other experiments have special requirements in addition to the basic ones outlined in section 5. These special requirements are discussed in the following paragraphs. Clearly, some very unique requirements cannot be met by a single common diagnostic facility, and thus should remain specific to the experiment, but it may be possible to satisfy some of these specialized needs in a common facility.

In the gas jet diffusion flame experiment, velocity measurements are considered to be very important. Because this requirement is unique to this experiment, and because velocity measurements require hardware which is very different from the other measurements which are contemplated, it seems that such hardware should be unique to this experiment and not be included in a common facility. Additionally, turbulence measurements may require very high temporal resolution, placing additional burdens on a common facility. Thus is appears that the special hardware needed by the gas jet diffusion flame experiment cannot be shared by other experiments.

In the liquid fuel droplet experiment, droplet surface temperature measurements are considered to be very important. It may be possible to incorporate this feature into a (primarily) gas diagnostic facility, as discussed in section 7. Furthermore, it is desirable to study very small droplets, as small as 0.01 cm. This mandates very fine spatial resolution, at least for the liquid phase measurements. Also, soot particle size and number density are valuable data. It should also be possible to incorporate these measurements into a common facility, as discussed in section 7.

The solid surface combustion experiment requires measurement of soot properties, as discussed above, and surface temperature. In this experiment it may be possible to measure surface temperature by pyrometric means as described in many other papers at this workshop.

|

The particle cloud combustion experiment is perhaps the most difficult of all to instrument with non-intrusive optical devices because of the very "dirty", particle-laden environment. This rules out the use of optical scattering methods except possibly for rather elaborate coherent scattering processes such as CARS [10]. Thus, gas phase optical diagnostics may prove impractical in this μg experiment. Additionally, particle surface temperature is desired. For these measurements, pyrometric methods may be sufficient if the flame is optically "thick."

7. Recommended facility

Based on the requirements furnished by the PIs, it appears that one facility could satisfy many of the non-intrusive diagnostic requirements of the candidate experiments. The most promising facility identified would employ light scattering techniques to measure gas temperatures and species concentrations, soot particle size and number density, and exciplex fluorescence [11] to measure liquid temperatures. A block diagram of the proposed facility in a gas-temperature or liquid-temperature measuring configuration is shown in Figure 1.

Obviously such a facility must conform to the size, weight, power consumption, and safety constraints imposed by the Space Station environment. While it is uncertain whether the proposed facility can meet such constraints, the proposed facility appears to be the type of system most likely to meet these constraints and still satisfy the diagnostic requirements of the representative experiments.

In this facility, two-dimensional gas temperature and species concentrations measurements could be made by employing Raman scattering techniques [12]. Raman scattering is a relatively simple technique to implement, is species selective, and is applicable to all molecules. The only major drawback to the method is the very low intensity of the scattered light. In the configuration shown in Figure 1, a Kr-F UV excimer laser is employed because of its high power output, relatively high efficiency, and short wavelength (Raman scattering cross-sections are inversely proportional to the fourth power of the wavelength of the incident light.) While others at NASA have proposed to employ excimer lasers in space experiments [13], for safety reasons it may be more practical to employ other light sources, for example a frequency-quadrupled Neodymium-YAG laser. The laser light is focussed onto a multipass optical cell which spreads the light into a thin uniform sheet. The advantage of the multipass cell method of creating the laser light sheet over conventional cylindrical lenses is greatly increased intensity. This method has been employed previously [14]. Interference filters are used to select the Raman scattered light of the species of interest. The laser pulses are synchronized to a rotating filter wheel so that different species may be imaged on
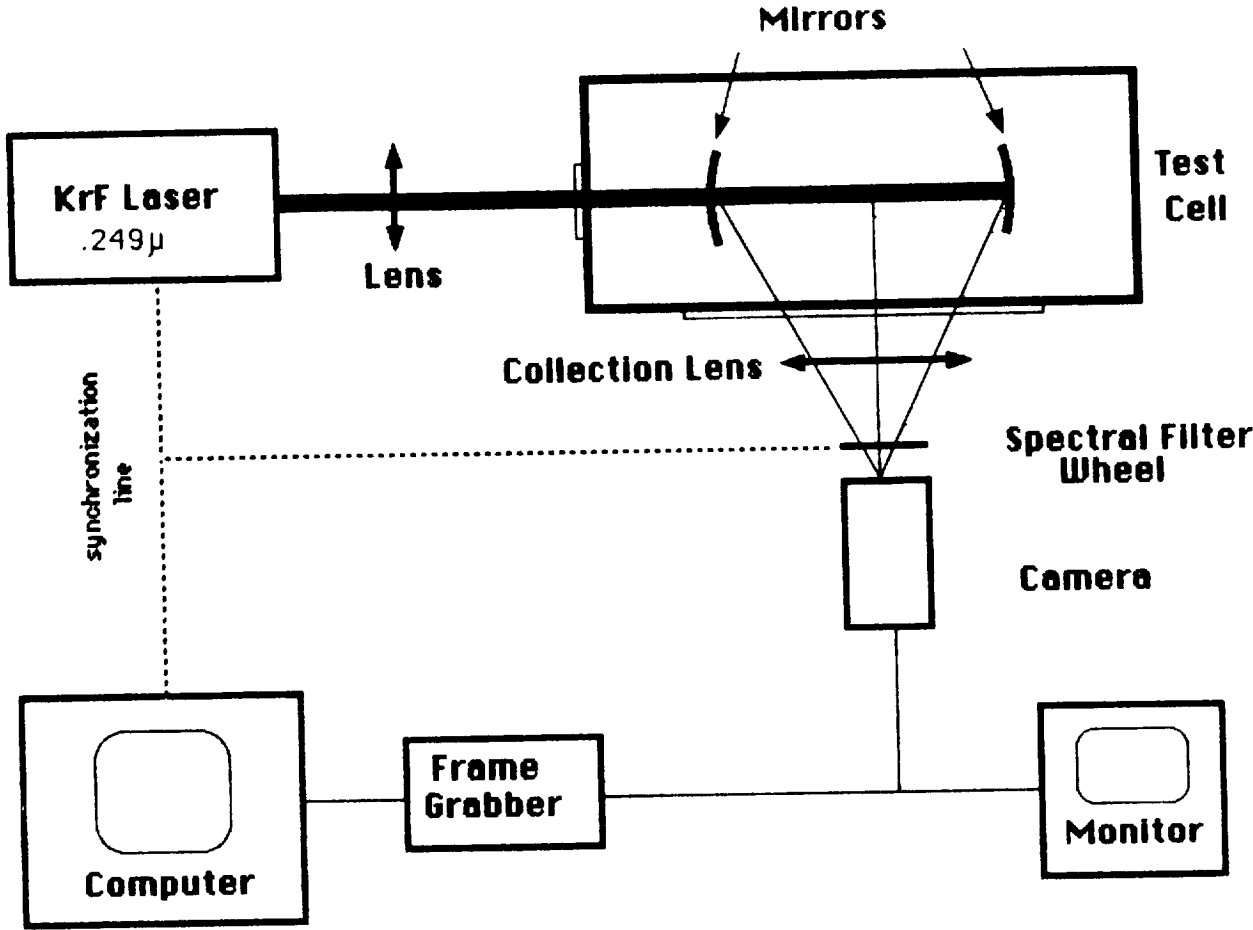
FIGURE 1: Proposed Facility

136

successive shots. A CID or CCD camera with single-photon sensitivity coupled to a microcomputer data acquisition system is used to image the scattered light. Because of the wide applicability of Raman scattering techniques, this facility may be applicable to many experiments with only a change of spectral filters and imaging software.

The same facility may be used for two-dimensional liquid temperature imaging by means of exciplex visualization [11]. In this method the liquid is seeded with a monomer which may form an excited state dimer, or excimer, with another molecule when the monomer is electronically excited through absorption of photons. The amount of excimer formed varies with temperature. The amount of excimer present may be determined from intensity of its fluorescence signal. Because the same hardware may be used for this technique as for the Raman scattering measurements, it is possible that liquid surface temperature measurements can be made concurrently with gas temperature and gas species concentration measurements on successive laser shots.

The same facility may be used for measurement of soot particle size and number density by Mie scattering techniques [15]. In this case, the multipass optical cell must be replaced by a cylindrical lens and a linear photodiode array for extinction measurements. Measurements could be made only in a one-dimensional system unless it can be assumed that the particle size or number density is constant along the length (parallel to the incident laser beam) of the test section, in which case two-dimensional measurements may be made.

8. Applicability to other experiments

The Raman scattering apparatus can certainly be used to measure gas temperatures and species concentrations in non-combustion experiments where large temperature and/or concentration gradients exist. For small gradients, schlieren or interferometric techniques are probably more appropriate.

This facility may also be used to measure liquid properties in non-combustion experiments. Generally the Raman scattering cross-section of a substance increases slightly upon transition from the gaseous to liquid phase [16]. Because the number densities of liquids are about 10^3 greater than that of gases, Raman scattering of trace species (in addition to major species) becomes practical. However, Raman bands in liquids tend to be broader, hence the Raman frequencies of the components of interest must be well separated. Because of the low thermal expansion coefficient of liquids, it is not practical to measure temperatures in liquids by Raman scattering unless the structure of the Raman spectrum is resolved, a difficult task for single-shot measurements. The exciplex methods discussed in section 7 may be more practical.

9. Conclusions

A wide variety of combustion experiments may benefit from microgravity experiments performed aboard the Space Station. These experiments will require the use of advanced diagnostic techniques. By analyzing several representative experiments, it appears that existing techniques may be able to satisfy many of these requirements. Furthermore, many of the requirements may be met by the use of a single flexible facility with minimal modifications for each experiment. Certain specialized requirements are necessarily experiment-specific.

10. References

1. Glassman, I. *Combustion*, 2nd. ed., Academic Press, Orlando, 1987.
2. Coward, H.F., Jones, G.W., *U.S. Bur. Mines Bull. 503*, 1952.
3. Lewis, B., von Elbe, G., *Combustion, Flames, and Explosions of Gases*, 2nd ed., Academic Press, New York, 1961.
4. Clavin, P., *Prog. Energy Comb. Sci.* 11:1 (1985).
5. Joshi, N., Berlad, A.L., *Comb. Sci. Tech.* 47:68 (1986).
6. Vedha-Nayagam, M., Altenkirch, R.A., *Acta Astronautica* 12:565 (1985).
7. Williams, F.A., *Acta Astronautica* 12:547 (1985).
8. Edelman, R. A., Fortune, O. F., Weilerstein, G., Cochran, T. H., Haggard, J.B., *Fourteenth Symposium (International) on Combustion*, Combustion Institute, Pittsburgh, 1973, p. 399.
9. Ronney, P. D., Wachman, H. Y., *Combust. Flame* 62, 107 (1985).
10. Eckbreth, A.C., Bonczyk, P. A., Verdieck, J.F., *Prog. Energy Combust. Sci.* 5:253 (1979).
11. Murray, A.M., Melton, L.A., *Appl. Opt.* 24:2783 (1984).
12. Long, D.A., *Raman Spectroscopy*, McGraw-Hill, New York, 1977.
13. MacKenzie, B., personal communication, NASA Ames Research Center, 1986.
14. Long, M.B., Fourguette, D.C., Escoda, M.C., *Optics Letters* 8:244 (1983).
15. Vandsburger, U., Kennedy, I.M., Glassman, I., *Twentieth Symposium (International) on Combustion*, Combustion Institute, Pittsburgh, 1984, p. 1105.
16. Weber, A., ed. *Raman Spectroscopy of Gases and Liquids*, Springer-Verlag, Berlin, 1979.

NON-CONTACT TEMPERATURE MEASUREMENTS FOR BIOTECHNOLOGY
DISCIPLINE WORKING GROUP

Robert S. Snyder

Space Science Laboratory

Marshall Space Flight Center

Abstract

There is no present need for non-contact temperature measurements in the space experiments being proposed in the biotechnology research areas, such as cell culturing, cell and protein purification or protein crystal growth. There is interest in measuring temperature changes over very small dimensions, such as the surface of a 10 micrometer diameter biological cell immersed in cell culture fluid. Non-interference measurements of other properties, such as chemical constituents and their concentration, are also needed. Contacting probes for pH have recently been developed to penetrate a cell but questions have been raised about their accuracy and net value.

In the extensive field of biotechnology, several processes have been shown to be modified in the microgravity environment. High quality single crystals of proteins and macromolecules are needed for the determination of the three-dimensional structure of the complex molecules and gravity influences the growth of crystals from solution. The separation and fractionation of biological cells and proteins by electrophoresis, isoelectric focusing and phase partitioning in aqueous electrolytes is hindered by buoyancy-induced convection and sedimentation. The culture of suspended cells requires lower shear forces in microgrvity and the totality of cell metabolism requirements appears to be different in space.

Each of these investigations occur under conditions that preclude non-contact temperature measurements. Each process takes place in an aqueous environment that is necessary to sustain the biological material in its active unmodified state. Biological cells require specific salts and nutrients to keep them viable and their fragility sets limits on these additives to the water. These properties of the environment are measured with probes for pH, conductivity, osmolarity and others. The temperature of the environment should also be kept within a temperature range around body temperature of $38^{0}C$ for maximum cell viability and function but it is unnecessary to make any of these measurements in a non-contacting manner.

Proteins are generally more resistant to changes in the environment and they are not as fragile during experiments. System measurements are also easier to make. Although proteins can be prepared so they retain their properties when dry (proteins are commonly freeze-dried for shipment and sale), all processes with proteins of present interest to NASA require the proteins to be dispersed in an aqueous environment subject to similar conditions as far cells.

Contacting probes have been developed to examine individual cells. Biological cells generally range in size from 5 to more than 50 micrometers in diameter and there is interest in studying particular cellular functions in vitro in addition to the various microscopic evaluations of cells outside of their normal environment. In the future, micron-size-probes will see more application in the study of specific cellular investiagtions.

The proteins to be separated or incorporated in cell culture facilities must be kept soluble and they cannot therefore be probed. Proteins that come out of solution as aggregates during separation processes are generally responding to improper environmental conditions and operations normally can be changed to restore the proteins to solubility. Protein crystal growth, however, can be considered as controlled aggregation. Experiment conditions are selected so proteins come out of solution and grow as crystals rather than precipitated aggregates. Measurements to date have concerned temperature measurements of the fluid environment in which the crystals of protein have grown. In fact, most protein crystal growth experiments have been conducted at "room temperature," either $20^{\circ}C$ of the laboratory or $4^{\circ}C$ of the cold room available in most biochemical laboratories.

Since cells are apparently healthy within a range of several degrees around normal temperature, processes involving cells have not controlled temperatures closer than a degree. There are no indications from experimental results that smaller temperature tolerances will modify conditions.

In summary, it is not anticipated that non-contact temperature measurements will be critical in biotechnology in the near term. Although temperature is important for biological experiments, the environmental temperature is usually sufficient for these isothermal or slowly changing systems. Since traditional temperature measurement systems are universally accepted, non-

contact temperature measurements will not see much use in the biotechnology space experiments now being planned.

MULTI-COLOR PYROMETRY

I

MULTI-COLOR PYROMETER FOR
MATERIALS PROCESSING IN SPACE

Michael B. Frish
Mark N. Spencer
Nancy E. Wolk
Jennifer S. Werner

Physical Sciences Inc.
Research Park, P.O. Box 3100
Andover, MA 01810

and

Henry A. Miranda Jr.
Miranda Laboratories
1 De Angelo Drive
Bedford, MA 01730

1. INTRODUCTION

This paper describes the design, construction, and calibration of a computer-linked multicolor pyrometer which can be used for accurately measuring the temperatures (between 300 and 2000 C, ±2.5 percent) of materials having emissivities known to only within ±25 percent. In addition, the device was constructed in a manner which demonstrates that it can be readily adapted to a spacecraft and used to control or regulate thermal processes for manufacturing materials in space.

The work is described in five sections. Section 2 presents background information including the theory underlying our pyrometer design. Section 3 describes the design in detail and justifies the selection of components. Section 4 discusses the procedure used to calibrate and test the resulting device, while a demonstration of its accuracy when measuring temperatures of surfaces having somewhat unknown emissivities is presented in Section 5. Section 6 shows how the device has been coupled to a computer and used as a non-contact temperature controller. A summary of the work comprises Section 7.

2. BACKGROUND

New techniques for processing of materials in space are presently being investigated by NASA and by others interested in expanding the frontiers of commercial materials manufacturing. As with any manufacturing process, it is essential that certain properties which vary during the processing, or which enable control of the process, be measured accurately. Commercial devices which are spaceworthy and capable of accurate, non-contact measurements with capablilties for incorporation into automated systems are quite inadequate. To help fill this void, we have developed an optical pyrometer, employing state-of-the-art optronics and computational techniques, capable of <u>accurately</u> measuring sample temperatures within the temperature range of 300 to 2000 C.

Pyrometry is a well-established technique for deducing the approximate temperature of a heated object by measuring the radiant energy which it emits. The radiant emission is determined by the Planck equation[1]

$$R(\lambda)d\lambda = C_1/(\pi\lambda^5) \left[\varepsilon(\lambda,T)/\{\exp(C_2/\lambda T)-1\}\right]d\lambda \tag{1}$$

where $R(\lambda)d\lambda$ is the radiant flux per steradian per unit area of emitter surface in the wavelength interval $[\lambda, \lambda + d\lambda]$, $C_1/\pi = 1.191 \times 10^{-12}$ W-cm^2/sr, $C_2 = 1.44$ cm-K, T is the temperature, and $\varepsilon(\lambda,T)$ is the spectral emissivity of the material at wavelength λ. In a typical pyrometer system, a portion of the heated target's surface is imaged by a lens or concave mirror onto a photodetector which converts the incident radiation into an measurable quantity. For measurement of temperatures over small, isothermal regions, a photodiode or photomultiplier is a commonly used transducer. The optical path generally contains several windows, mirrors, beam splitters or filters, each of which has a wavelength dependent transmittance or reflectance, $t_i(\lambda)$. They, together with the solid angle, Ω, subtended by the optical collection system, and the surface area, A_s, of the radiant target, determine the radiant power which reaches the detector,

$$P = \frac{A_s \Omega C_1}{\pi} \int_0^\infty \frac{\prod_{i=1}^n t_i(\lambda)\, \varepsilon(\lambda, T) d\lambda}{\lambda^5 \left(e^{C_2/\lambda T} - 1\right)} \qquad (2)$$

where n is the number of components in the optical train.

Rather than use Eq. (2), many commercial pyrometers determine the temperature of a surface by comparing the power emitted by it with that of a calibrated source having a known temperature. The temperatures deduced in this fashion are generally referred to as "brightness" temperatures, since they in essence compare, over a broad range of wavelengths, the brightness of the unknown target to the brightness of the calibrated source. Unfortunately, in addition to its dependence on temperature, the radiant emission depends on the emissivity of the hot object, an intrinsic property of the material. As indicated in Eq. (1), the emissivity may be a function of both wavelength and temperature. Due to differences in the emissivity functions of the calibration source and the target material over the range of wavelengths to which the photodetector is sensitive (typically ranging from the near-uv to the near-ir), this reported brightness temperature may differ substantially from the true temperature. In fact, since the wavelength dependence of the emissivity of the target is generally unknown, there is usually little effort made even to estimate the temperature uncertainty with this sort of device.

By using a narrow bandpass optical filter to select a particular wavelength (i.e., color) at which to compare the signal generated by the unknown target to that of the calibration source, a more accurate estimate of the true temperature, called the "color" temperature, can be obtained. This technique has the advantage that the emissivity of the target, and the transmittance or reflectance of other optical components, are essentially constant over the transmitted wavelengths. These variables can therefore be removed from the integral in Eq. (2) and, if the transmission curve of the filter is known, the integral may be evaluated, as

$$P = \varepsilon_\lambda C_\lambda \int_{\lambda_1}^{\lambda_2} \frac{t_f(\lambda)d\lambda}{\lambda^5 \left(e^{C_2/\lambda T} - 1\right)} \qquad (3)$$

148

|

where ε_λ is the emissivity at the central wavelength of the filter, C_λ is a constant (independent of temperature) determined by the optical system which may be evaluated by calibration, t_f is the (known) transmission function of the filter, and λ_1, λ_2 are the bandpass limits of the filter. When the photodetectors are operated such that they generate a voltage signal which is proportional to the power incident on their surfaces, Eq. (3) may be written as

$$V(T) = \varepsilon_\lambda B_\lambda F_\lambda(T) \tag{4}$$

where $F_\lambda(T)$ is a known thermal response function proportional to the integral in Eq. (3), and the constant $B_\lambda = GC_\lambda$ where G (Volts/Watt) is the responsivity of the photodetector and its associated amplification circuitry. Reported color temperatures are typically those which correspond to the the voltage signals generated by targets with unit emissivity, i.e., blackbodies. However, if the target's emissivity at the selected wavelength is known, then it is simple to use Eq. (4) to correct the color temperature to the true temperature.

Unfortunately, in most cases of interest the emissivity varies both with temperature and with wavelength, and therefore is difficult if not impossible to evaluate independently. In some instances, the emissivity even changes with time as chemical or structural changes occur in the heated material, as with ceramic materials proposed for manufacture in space which become glassy when heated beyond their melting point, or with many metals which oxidize rapidly when hot. Thus, it is often not feasible to correct the color temperature. A popular scheme for circumventing this problem is to employ a two-color pyrometer, a device which measures the radiant power at two, generally closely spaced, wavelengths. By making an assumption about the ratio of the emissivities at the two wavelengths, the Planck equation can be used to calculate the temperature, as well as the emissivity. Although this technique is useful when the emissivity ratio at the two wavelengths is well-known, its accuracy suffers tremendously by any small errors in that ratio.[2,3]

In contrast, with the appropriate selection of wavelength for a particular range of temperatures, color-temperature measurement with a single pyrometer can be a very accurate measure of the true temperature, being insensitive to a large uncertainty in the emissivity at that wavelength. For values of $\lambda T \ll 1$, the radiant power emitted by a heated surface increases faster than exponentially with temperature, but is only linearly dependent on emissivity. Thus, a large uncertainty in emissivity causes only a small error in temperature. Mathematically, this is seen by solving the Eq. (4) for temperature. The function $F_\lambda(T)$ may be easily evaluated by approximating the transmission function of the narrow bandpass filter by a rectangle of height t_λ and width $\Delta\lambda = \lambda_2 - \lambda_1$. Then we may define

$$F_\lambda(T) = \left(\exp(C_2/\lambda T) - 1\right)^{-1} \tag{5}$$

and

$$B_\lambda = (A_s \Omega t_\lambda G C_1/\pi)\left(\prod_{i=1}^{n} t_i\right)(\lambda^{-5}\Delta\lambda) \quad . \tag{6}$$

Solving Eqs. (4), (5), and (6) for temperature yields

$$T = (C_2/\lambda)\ \ln^{-1}\left((B_\lambda \varepsilon_\lambda/V) + 1\right) \quad . \tag{7}$$

Differentiating with respect to ε_λ gives the temperature error as

$$\Delta T/T = \left(1 - \exp(-C_2/\lambda T)\right)(\lambda T/C_2)(\Delta\varepsilon_\lambda/\varepsilon_\lambda) \tag{8}$$

which is plotted in Figure 1 for a selection of wavelengths using $\Delta\varepsilon_\lambda/\varepsilon_\lambda = \pm 25$ percent. Although the temperature uncertainty increases with temperature for all wavelengths, it is clear that, by selecting a sufficiently short wavelength for operation of the pyrometer, uncertainties below one percent can be achieved.

On the basis of Eqs. (7) and (8), it would appear that a single color pyrometer could be used to measure any temperature below a predetermined value to any degree of accuracy simply by selecting a sufficiently short wavelength.
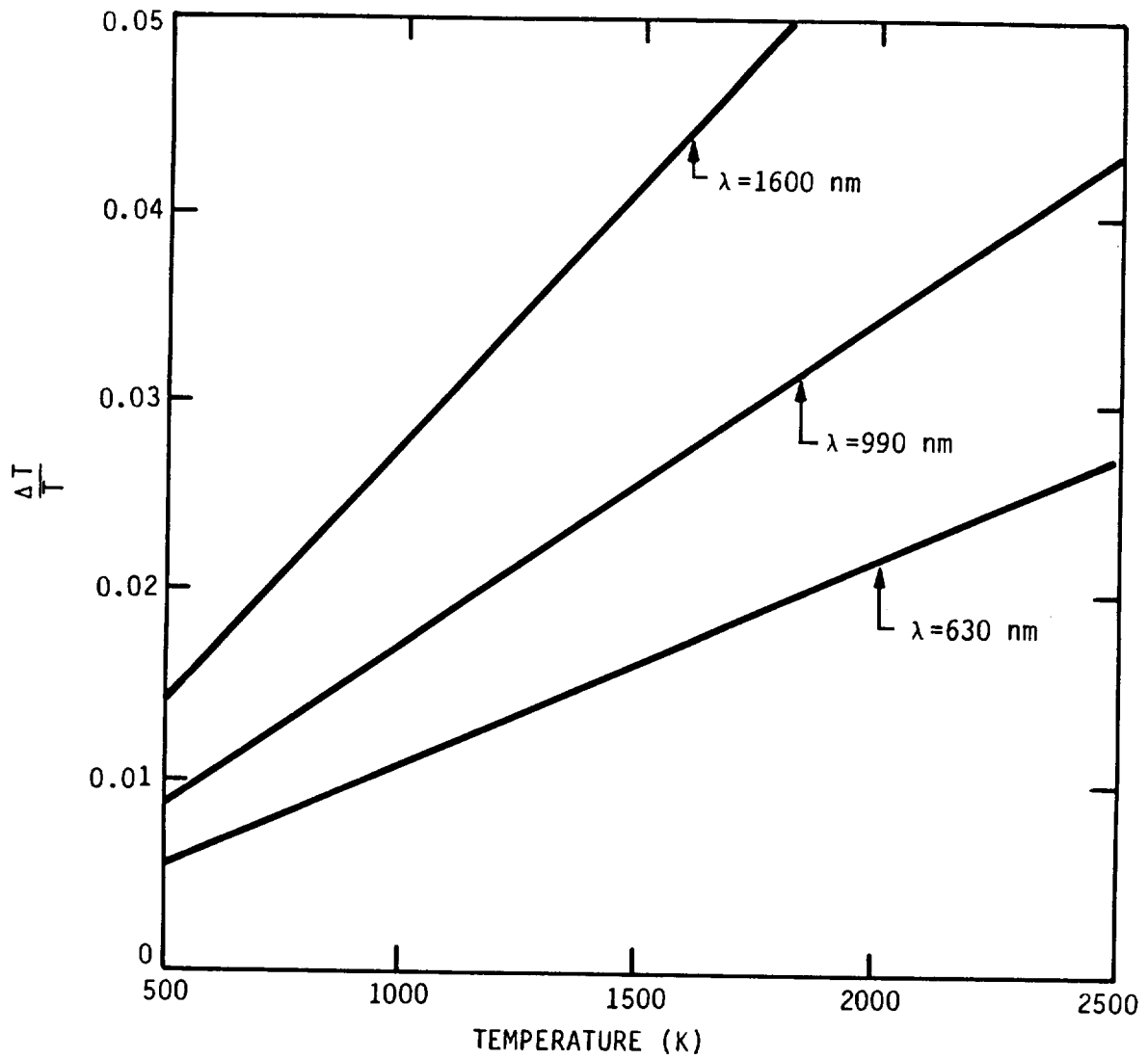
Figure 1. Temperature uncertainty resulting from an emissivity uncertainty of $\Delta\varepsilon/\varepsilon = \pm 0.25$ using a single color pyrometer

Although this is, in principle, true, there is a lower limit on the temperature sensitivity which, for the temperature range of interest, is determined by the noise inherent to the photodetector. In addition, there is a maximum temperature to which a particular optical pyrometer/ photodetector combination will be sensitive, fixed by the onset of detector saturation. A photodetector typically has a dynamic range of about five orders of magnitude. As shown in Figure 2, at a wavelength of 630 nm, where the emissivity related temperature error remains below 2.5 percent up to 2300 K, the radiant power spans well in excess of ten orders of magnitude as the temperature increases from 600 to 2300 K. It is clear that a single pyrometer operating at this wavelength is unsuitable for measurements over the entire temperature range of interest. In contrast, at a longer wavelength (1600 nm for example) the radiant power in this temperature range spans less than seven orders of magnitude. However, as shown in Figure 1, the emissivity related temperture uncertainty becomes excessively large at the higher temperatures. It is clear that, to have both the required range of temperature sensitivity and accuracy of better than ±2.5 percent, a pyrometer operating at multiple wavelengths is required. Examination of Figures 1 and 2 indicates that, using photodetectors which have a five order of magnitude dynamic range, and demanding temperature accuracy of ±2.5 percent, three colors are desirable. Thus, a device utilizing three wavelengths and three photodetectors was designed, as is discussed in the next section.
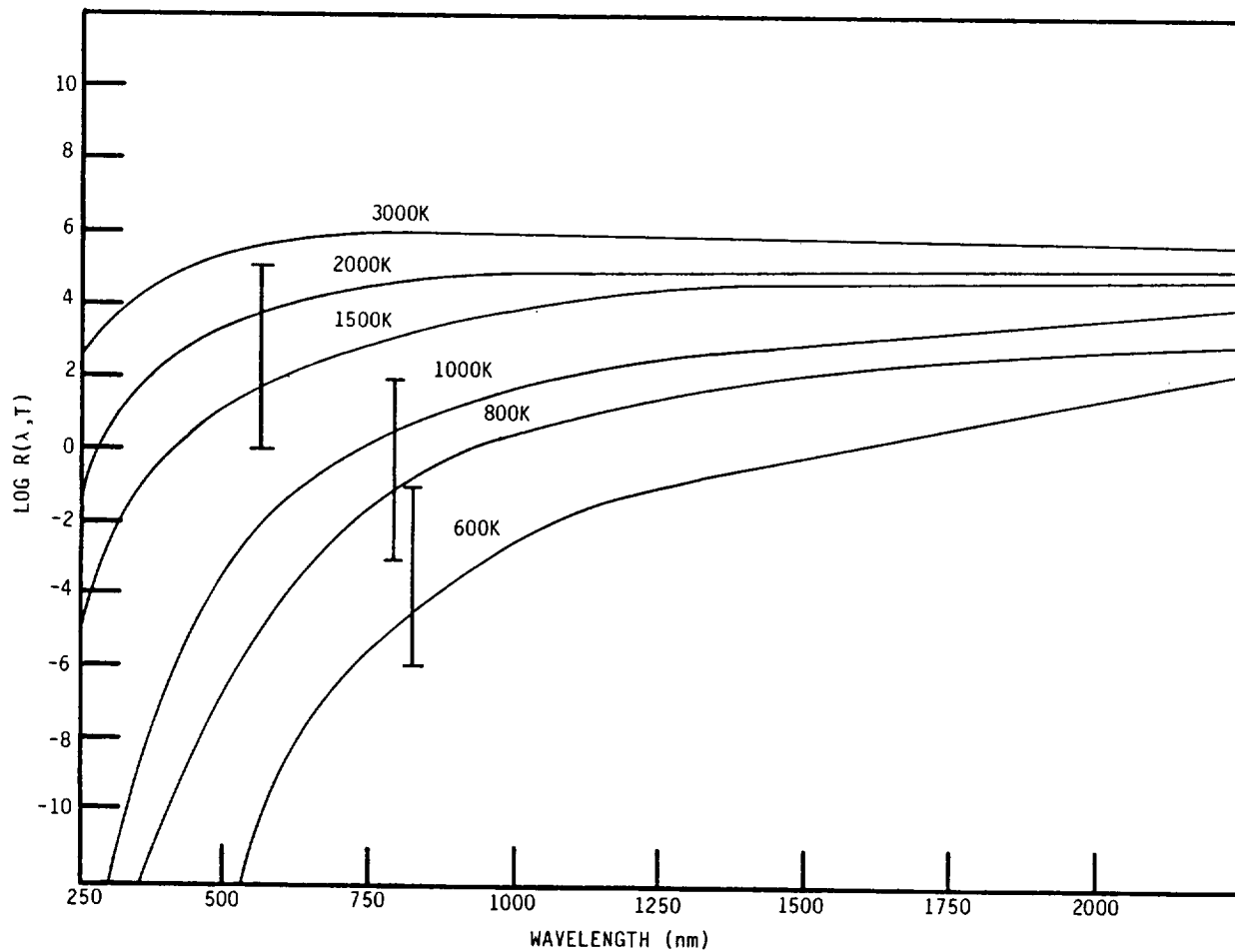
Figure 2. Radiant flux per steradian per unit area of emitter surface per
          unit wavelength interval emitted from a blackbody

153

3. PYROMETER DESIGN

3.1 Wavelength Selection

The three wavelengths to be used in the pyrometer were selected on the basis of the following criteria:

1. The device should be sensitive to temperatures ranging from 300 to 2000 C, or 573 to 2273 K.

2. The temperature measurements should be accurate to ±2.5 percent when the emissivity is known only to within ±25 percent of its true value.

3. For maximum precision, each of the three detectors should be sensitive to as small a dynamic range of radiant energies as possible.

The first two criteria specify the shortest of the three wavelengths. Inserting the values $T = 2300$ K, $\Delta T/T = 0.025$ and $\Delta\epsilon_\lambda/\epsilon_\lambda = 0.25$ into Eq. (8) yields a wavelength of $\lambda_3 = 626$ nm. The last criterion is satisfied by designing the pyrometer so that all three detectors cover the same dynamic range, which was found to be about 2.5 orders of magnitude. A surface having a constant emissivity at 626 nm will emit a radiance 2.5 orders of magnitude smaller than that at 2300 K when its temperature is reduced to 1460 K, which, for design purposes, was selected as the maximum temperature to which the mid-range detector is sensitive. Again invoking criterion 2, the optimum wavelength for this middle detector was found to be $\lambda_2 = 987$ nm. Iterating once again, it was found that the minimum temperature for this detector was 926 K. This specified the wavelength of the low-temperature detector as $\lambda_1 = 1556$ nm. At this wavelength, temperatures from 587 to 926 K span 2.5 orders of magnitude in radiance.

The three-color pyrometer was thus designed to use detectors operating at wavelengths around 1600 nm, 990 nm, and 630 nm, with each detector having a linear response over about 2.5 orders of magnitude. For the approximation

used in Eqs. (5) and (6) to be valid, namely that ε and t_i are constants over the bandwidth of each filter, it is essential that the bandwidths be only large enough to allow a detectable level of radiation to pass. For this reason we used three-cavity bandpass filters, supplied by Pomfret Research Optics, which have full-widths of one percent maximum transmission of approximately 20 nm. The precise bandpass filter characteristics are as follows:

Wavelength (nm)	t_λ	Bandwidth (nm)
1600	0.41	12
990	0.69	11
630	0.58	10

3.2 Optical Assembly

Examination of Eq. (2) reveals that, once the bandpass filters have been selected, the amount of radiant power which reaches the photodetector is determined by the solid angle subtended by the optical collection system and the area of the radiant source which is imaged onto the detector. To minimize ease of construction and operation, as well as cost, the electro-optic transducers chosen for construction of a demonstration pyrometer were simple photodiodes combined with operational amplifiers. A germanium photodiode, which is most sensitive to near-infrared radiation, was required for the low temperature detector, while silicon photodiodes were used at the shorter wavelengths. It was assumed that the radiant source would be greater than 1 cm in diameter, and could be positioned within about 10 cm of the pyrometer. Imaging optics were selected which would assure that sufficient radiation reached the detectors to generate a usable signal at the lowest temperatures sensed by each. An assembly structure was designed which allows the three detectors and all associated optics to be fixed in position once and for all time, is lightweight but rigid, and serves as a prototype of a spaceworthy device.

A schematic illustration of the pyrometer's optical layout is shown in Figure 3, and a photograph of the device is presented in Figure 4. A 50 mm

focal length glass condenser lens, comprised of two 100 mm focal length, 38 mm diameter, plano-convex lenses, images the radiant source onto a 1 cm diameter field stop. The radiation which passes through the stop reaches three 50 mm focal length, 25 mm diameter lenses, mounted on a plate in the configuration shown in Figure 5, which re-image the field stop, and thus the 1 cm diameter portion of the source, onto the three photodetectors with 1/3 magnification, resulting in a circular images 3.3 mm in diameter. The solid angle subtended by the optics is 0.012 sr, as limited by the three smaller lenses. The optical elements are all mounted in circular black anodized aluminum plates which are fixed in position with respect to each other by alignment rods passed through key holes in the plates.

The sensitive area of the germanium detector (Judson Infrared Model J16-5SP with a 741 operational amplifier) is a square 3 mm per side. When the image of the source is centered on this detector, an area of 0.080 cm^2 is irradiated. Because the source diameter is three times as large as its image,
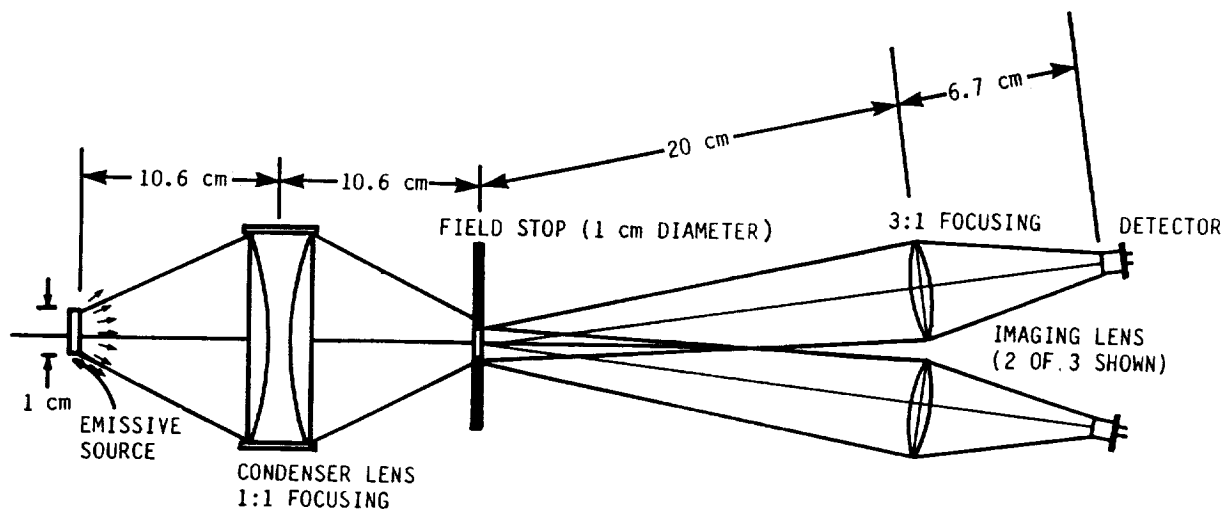
A-3559

Figure 3. Schematic illustration of multicolor pyrometer optical design
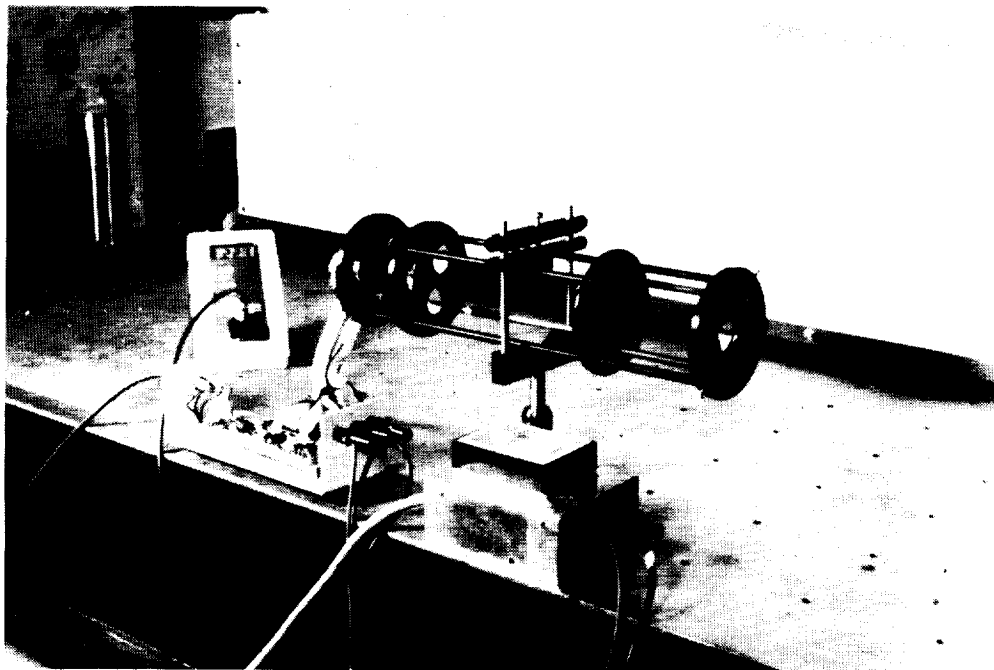
Figure 4. Photograph of pyrometer
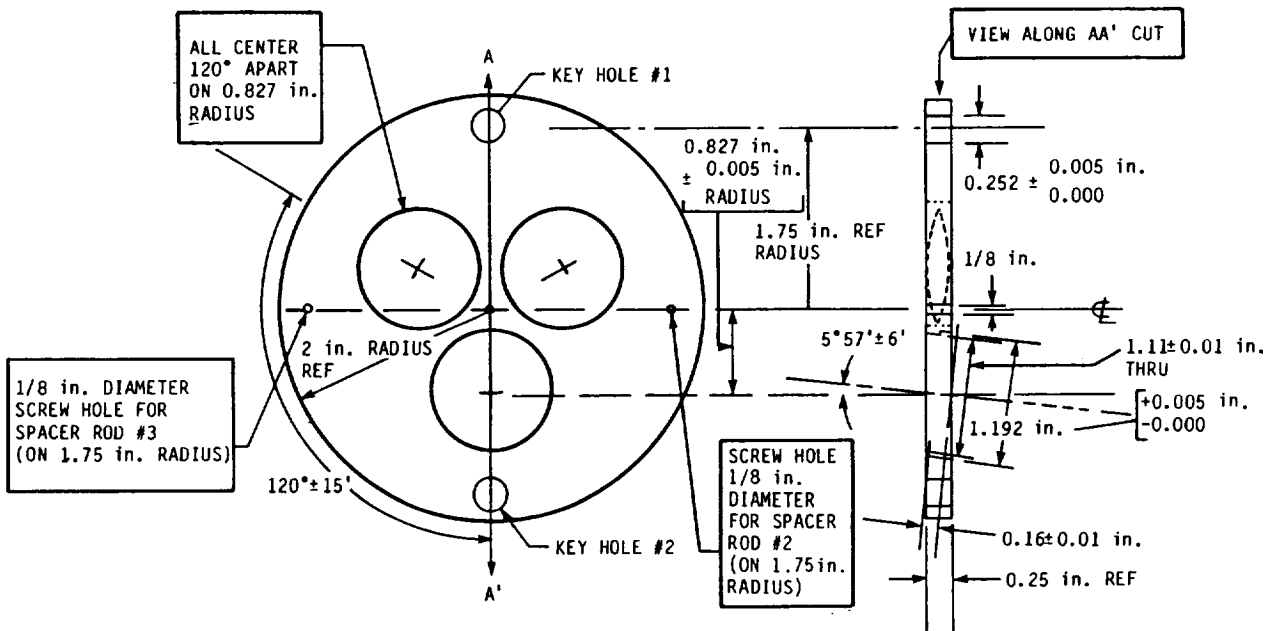
A-3584

Figure 5. Layout of three imaging lenses

157

the effective source area is 0.72 cm^2. The two silicon detectors (EG&G Model HAD-1100A photodiode/op-amp combination package) have sensitive areas which are circles 2.54 mm in diameter. When the source image is properly centered on these detectors the entire surface is irradiated. The effective source area is therefore $(9\pi/4)(0.254)^2 = 0.456$ cm^2.

These numbers can be inserted into Eq. (2) to demonstrate that measurable radiation will reach each detector. An example is presented for the low temperature portion of the pyrometer only. Assuming that: 1) the transmission function of the bandpass filter is a constant equal to t_λ over the wavelength region $[\lambda_1,\lambda_2]$ and zero elsewhere; and 2) the transmission through each of eight glass surfaces (three lenses and the photodetector cover glass) is $t_i = 0.96$, then, for a blackbody source, Eq. (2) can be written as

$$P = (A_s \Omega t_\lambda C_1/\pi)(0.96)^8 \lambda^{-5}\Delta\lambda \left(\exp(C_2/\lambda T) - 1\right)^{-1} \quad .$$

Inserting values for the 1600 nm filter and the germanium detector, and a temperature of 573 K yields a detectable power of 5.2×10^{-9}W. The noise equivalent power (NEP) of this detector with an amplifier bandwidth of 1 kHz is 6.3×10^{-11}W, and the response remains linear until the incident power reaches about 5×10^{-4}W. The incident power thus falls well within the linear regime for all temperatures at which this detector will be used, and the minimum power to which it must be sensitive is well above the noise level. The optical system is therefore well designed for the application. Similar calculations have been performed for the two silicon detectors, yielding similar results.

These numbers can also be used to estimate the calibration constants B_λ (defined in Eqs. (4) and (6)) for each detector. To convert values of incident power to voltages, the responsivity of the detectors (A/W) and the trans-impedence (V/A) of the op-amp associated with each detector must be known. The former can be found in the data sheets accompanying the detectors and the latter is simply equal to the resistance of the feedback resistor for each op-amp, which we have selected to be 10^6 for all three detectors. At 1600 nm,

the germanium detector has a responsivity of 0.85 A/W, so G for that detector is 0.85×10^6 V/W, giving an anticipated calibration constant of

$$B_{1600} = 2.9 \times 10^4 V \quad .$$

Similarly, $\qquad B_{990} = 1.7 \times 10^5 V$

and $\qquad B_{630} = 9.4 \times 10^5 V$

Evaluation of the actual calibration constants is discussed next.

4. CALIBRATION

The calibration constants just calculated are based on the design of the optical system assuming ideal thin lenses, and on idealized transmission functions of the bandpass filters and other optical components. Because the actual lenses have some spherical aberration which reduces the effective solid angle, and the bandpass filter function is not really rectangular, these calculations can only roughly approximate the true calibration constant for each detector. Calibrations were therefore performed using blackbody sources.

A low temperature blackbody, operable at temperatures between 300 and 1273 K, was used to calibrate the two longer wavelength detectors. The source was accurately aligned with the optical axis of the pyrometer by passing a He/Ne laser beam through centering holes in the pyrometer and thence through a 1 mm hole centered on the blackbody's exit aperture. The aperture was then positioned in the source plane of the pyrometer and imaged onto the field stop, thereby also being imaged onto the photodetectors. The aperture diameter was then increased to greater than 1 cm in diameter so that its image filled the field stop, as called for in the pyrometer's design. The temperature of the blackbody was set and allowed to reach a steady value, which was measured by a platinum/platinum-rhodium (13 percent) thermocouple and ice point reference. The voltages produced by the two detectors were measured by a computer-coupled data acquisition system (described in detail later in this report) with a precision of 0.030 mV. They are plotted as functions of temperature in Figure 6. Note that the long wavelength detector is sensitive to temperatures as low as 540 K and greater than 1000 K. The mid-wavelegth detector is sensitive from 750 K to beyond the limit of the blackbody source. Both of these temperature ranges satisfy and even exceed the design goals.

The detector voltages are plotted as functions of $F_\lambda(T)$ in Figure 7a. As expected the relationship between the two parameters is linear over the entire temperature range. The slope of the line is proportional to the calibration constant. After least-squares fitting of the straight lines, the calibration constants are found to be:
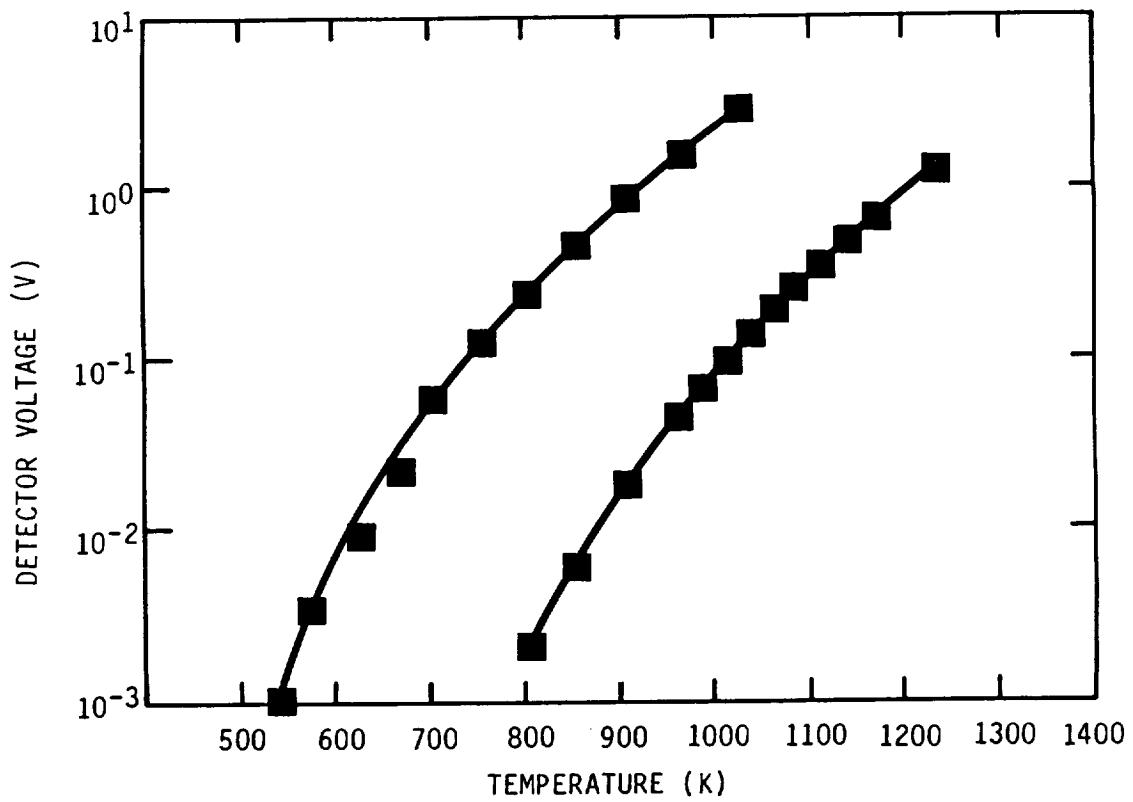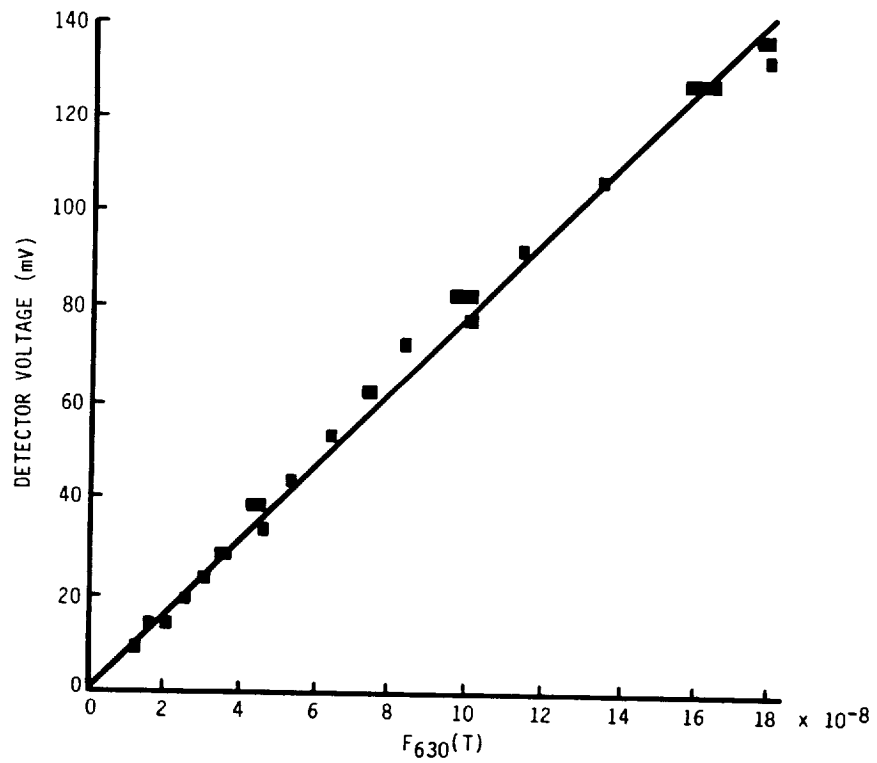
Figure 6. Output voltages versus temperature for the two low-temperature detectors

A-3553
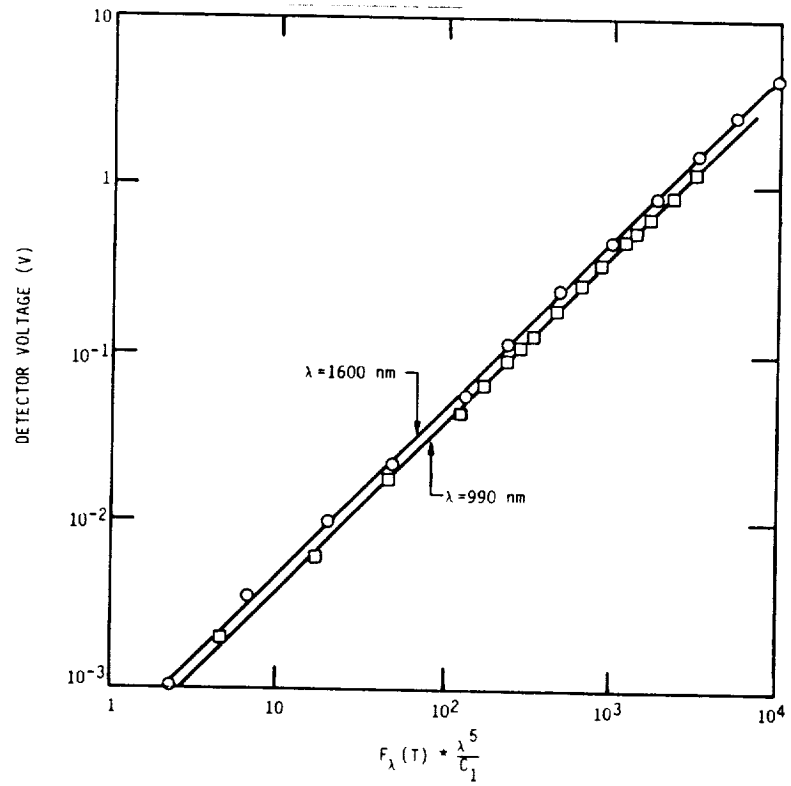
Figure 7. Output voltages versus radiance function for a) the two low-temperature and b) the high temperature detectors

$$B_{1600} = (1.69 \pm 0.01) \times 10^4 \text{ V}$$
$$B_{990} = (1.49 \pm 0.02) \times 10^5 \text{ V} \quad .$$

Because this blackbody source could only achieve a maximum temperature of 1000C, it could not be used to calibrate the short wavelength detector (630 nm). However, we did have available a second blackbody source capable of achieving temperatures in excess of 1800 K. Unfortunately, this source did not have a reliable independent means for ascertaining its temperature. To circumvent this problem we employed a bootstrap procedure. Although the short wavelength detector was designed to measure temperatures only above 1460 K, it was in fact found to be sensitive to temperatures as low as 1250 K. By using the mid-range detector to measure the temperature of this uncalibrated blackbody between 1250 K and 1460 K (above which the mid-range detector rapidly reached saturation) we were able to obtain sufficient data, plotted in Figure 7b, to calculate the high temperature calibration coefficient as

$$B_{630} = (7.81 \pm 0.03) \times 10^5 \text{ V} \quad .$$

All three actual calibration constants are within acceptable limits of their anticipated values. In fact, the calibration constants for both silicon detectors are about 85 percent of their pre-calculated values, while the germanium calibration constant is 55 percent of that anticipated. The larger discrepancy with germanium is probably due to the image of the source not being perfectly centered on the square sensitive area of the detector, resulting in a smaller than expected effective source area. However, since the alignment is mechanically fixed for all time, this calibration constant will remain accurate for any uniformly heated source which is imaged to fill the pyrometer's 1 cm diameter field stop.

5. ACCURACY DEMONSTRATION

To demonstrate the pyrometer's capability to make accurate temperature measurements on objects of unknown (or changing) emissivity, metal plates of copper, aluminum, and stainless steel were heated and observed by the pyrometer while simultaneously measuring their temperatures with an insulated chromel/alumel thermocouple coupled to an electronic ice point reference. The heating in all cases was performed by attaching the metal plates to a ceramic heater, and controlling the power input to the heater with a variable transformer. For the copper and aluminum measurements the thermocouple was inserted into a small hole drilled into the surface of the metal and placed within the pyrometer's field of view, thus assuring that it measured the temperature of the same region as the pyrometer. Good contact between the thermocouple and the metal surface was assured by pressing the metal surrounding the thermocouple junction into the drilled hole.

The 6.3 mm thick aluminum plate was heated to its melting point of 933 K. According to handbook data,[4] the initial emissivity of the aluminum at 1600 nm was less than 0.1, but as the plate heated and oxidized its emissivity increased to approximately 0.4. The copper plate was about 12 mm thick and was heated to approximately 900 K. Upon heating, it quickly oxidized to form a black surface having a fairly high emissivity of about 0.8. The stainless steel, only 1.5 mm thick, was also heated to about 900 K, and oxidized to present a surface having an emissivity intermediate between that of copper and aluminum (0.5 to 0.8). Sufficient time was given before the measurements to allow the oxide coat to cover the surface.

Figures 8a-c show the results of these experiments. In each figure, the temperature as determined by the pyrometer is plotted vs the temperature as measured by the thermocouple. The emissivity which has been assumed to calculate the temperature from the pyrometer data is indicated in each figure, and represents our best guess of the most probable value of the emissivity. Because the metal plates oxidize with time, and their emissivities vary with temperature, these assumed emissivities are certain to be somewhat different
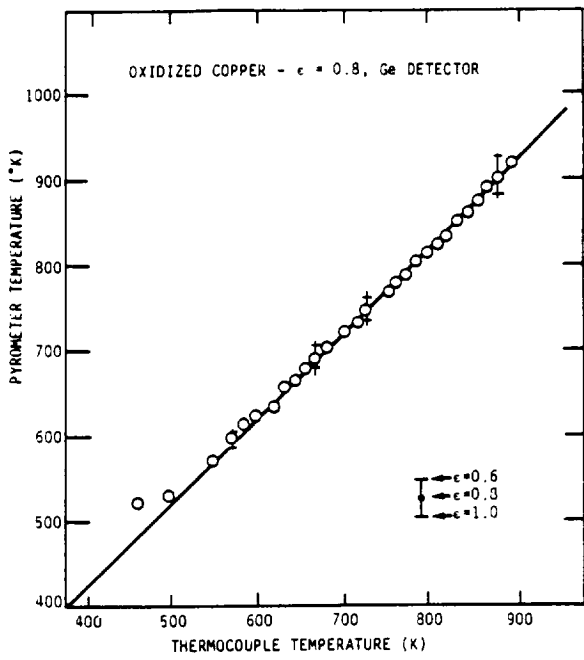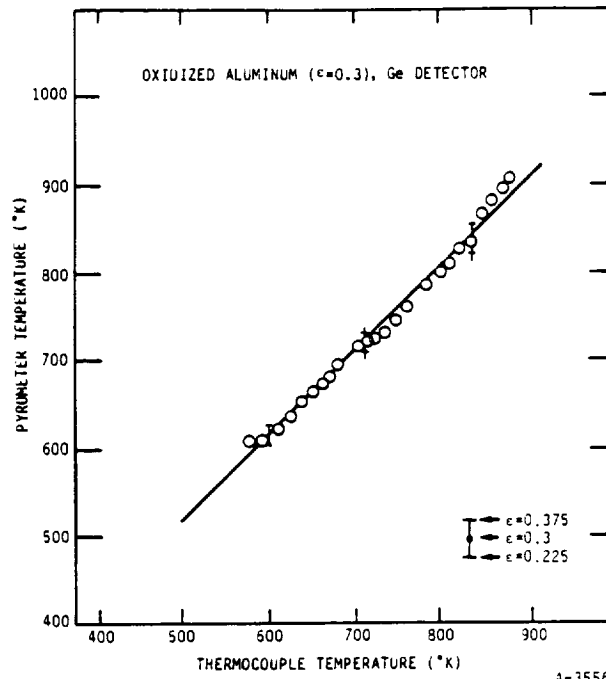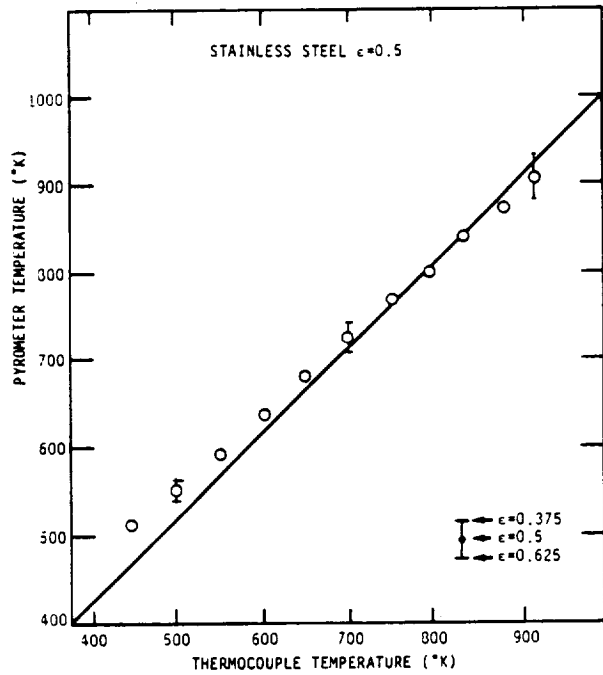
Figure 8.   Comparisons of temperatures measured by pyrometer versus
those measured by thermocouple for a variety of heated
metal plates

from the actual values. Nevertheless, excellent agreement between the pyrometer and thermocouple measurements is seen in all three experiments, as demonstrated by comparison with the "correct answer" line drawn in each plot as a guide for the eye. Examination of the data shows deviation from perfect agreement of less than one percent at temperatures above 500 K.

Included in these figures are "error bars" for selected temperature points whose endpoints show the temperature which would have been indicated by the pyrometer had an emissivity been assumed that is 25 percent higher and 25 percent lower than that which was actually used. In all cases the error bounded by these two limits is within the 2.5 percent figure predicted.

6. COMPUTERIZED TEMPERATURE CONTROL

For material processing applications, it is desirable to have a capability to not only measure but also control temperatures of heated materials using a non-contact device such as a pyrometer. We therefore chose to demonstrate that our multi-color pyrometer, when coupled with a laboratory computer equipped with a data acquisition and control card, could perform this function. We used a Compaq portable computer as the host for a Data Translation Model DT2801-A data acquisition card. This card simply plugs into one of the slots available for expansion of the computer, and is capable of simultaneously measuring voltages from up to 16 sources with 12 bit (1/4096) precision in the analog-to-digital conversion. It also has provisions for digital output, consisting of two bytes (16 bits) which can be programmed by the user. As described in the following, one of these 16 bits was used as a switch which controlled the power supplied to a heating element, and therefore was able to control the temperature of a heated body.

To use this system as a temperature controller, the three pyrometer voltages were measured by the computer, and a program was written which calculated the temperature corresponding to the voltage in each of the three channels. Obviously, for any given temperature, only one or perhaps two of the channels would give meaningful information. The other channel(s) would either be saturated at their maximum measurable voltage if the temperature was significantly above the maximum temperature for which that detector was designed, or indicate zero if the temperature was well below the design minimum. It was therefore easy to distinguish which channel was calculating the correct temperature, and this capability was built into the data analysis portion of the computer program. The measured temperature was then compared with a preset temperature, supplied by the user to the program, at which the user wanted to stabilize the temperature of a heated body. A subroutine was written which enabled the computer to act as a proportional temperature controller. When the difference between the measured temperature and the preset temperature exceeded a certain value, called the proportional bandwidth, the switch controlling the heating element was held either on or off, depending on whether

the temperature was below or above the preset value. If the switch was on, the body temperature would increase and, conversely, if the switch was off the temperature would decrease. When the temperature reached a point such that it was within the proportional bandwidth of the preset value, the switch was rapidly turned on and off with a duty cycle equal to $0.5\left(1 - (T_a-T_s)/T_b\right)$, where T_a is the measured temperature, T_s is the preset temperature, and T_b is the proportional bandwidth. Thus, as the temperature increased towards the preset value, the average power supplied to the heater gradually decreased, and vice versa causing the temperature to ultimately stabilize at a value close to T_s. In general, unless the heating source is grossly over- or under-powered, selection of an appropriate proportional bandwidth and switching speed causes this algorithm to stabilize the temperature of any heated object arbitrarily close to the preset temperature with minimal oscillation.

To test this program, the system was used to control the temperature of the copper block heated as described previously. Now, however, the ceramic heater was connected to an AC outlet through a solid-state relay operated by the output bit of the computer system; no variable transformer was used to control the heater power. From previous experience, it was known that, if the ceramic heater was left on continuously, the copper block would reach a temperature in excess of 900 K. Starting with the copper block at room temperature, a preset temperature of 723 K was entered into the computer and the temperature control program was run, with a proportional bandwidth of 5 K and a switching period of about 10s. A plot of the copper block temperature as a function of time is shown in Figure 9. The temperature rises rapidly, and, with no perceptible oscillation, stabilizes within 1 K of its preset value. Thus, the use of our pyrometer as a non-contact accurate temperature controller has been demonstrated.
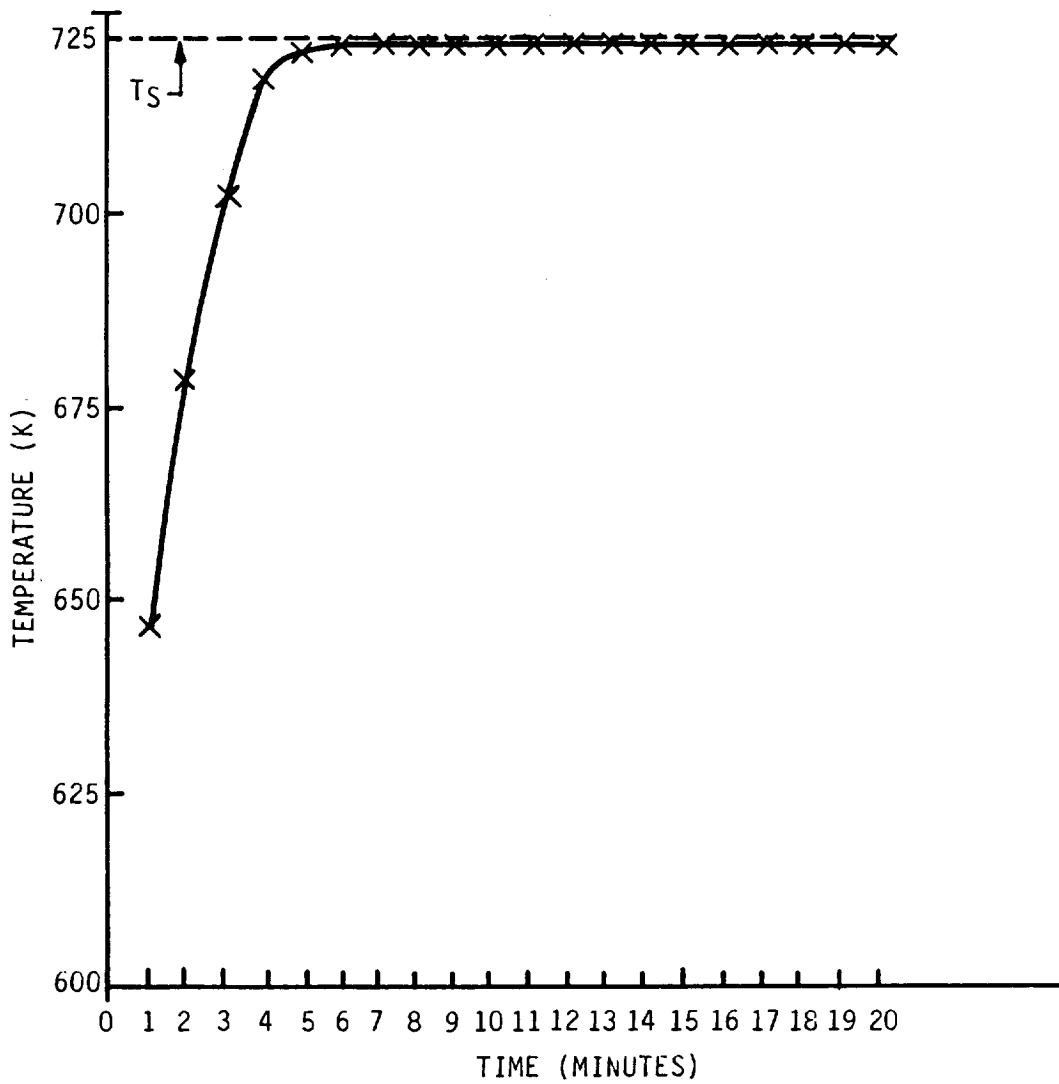
A-3558

Figure 9. Temperature history of a heated copper plate subjected to the temperature control apparatus

7. SUMMARY

The feasibility of using a multi-color pyrometer to measure and control the temperatures of heated objects, accurately and remotely, has been demonstrated. The pyrometer actually uses only one color at a time, and is relatively insensitive to uncertainties in the heated object's emissivity because the product of the color and the temperature has been selected to be within a regime where the radiant energy emitted from the body increases extremely rapidly with temperature. The device was designed for both simplicity and ruggedness, criteria which are important for an eventual flight instrument, and was constructed with fixed optics in a fashion which makes it easy to align. It was calibrated and shown to exceed its design criteria of temperature measurements between 300 and 2000 C, and its accuracy in the face of imprecise knowledge of the hot object's emissivity was demonstrated. Finally, it was shown that the pyrometer could be easily coupled to a computer and used as a temperature controller.

The demonstration device which has been constructed was designed for use with a hot source located 10 cm away and having a uniform temperature over an area at least 1 cm in diameter. Similar devices can be designed for different geometries. The possibilty exists for designing a pyrometer which incorporates variable focal length optics, although its operation would be more complicated than that described herein. However, by coupling the device to a dedicated computer, programmed with the required data analysis algorithm, the increased complexity could be made transparent to the user. Furthermore, the device can be made completely self-contained and portable by incorporating an appropriately configured and programmed microprocessor in place of the personal computer. We expect to address these possibilities in future work.

ACKNOWLEDGEMENT

REFERENCES

1. Siegel, R. and Howell, J.R., <u>Thermal Radiation Heat Transfer</u>, McGraw-Hill (1981).

2. Rosen, D., Lucht, R., Hastings, D. and Weyl, G., "Visible Laser Effects," Report No. TR-268, Physical Sciences Inc., Andover MA (1983).

3. Nordine, P.C., "The Accuracy of Multicolor Optical Pyrometry," High Temperature Science, <u>21</u>, (1986).

4. Multiple Authors, <u>Handbook of Chemistry and Physics</u>, CRC Press (1985).

DIRECT EMISSIVITY MEASUREMENTS ON LIQUIDS AND CORRECTIONS TO MULTI-COLOR PYROMETERS

Paul C. Nordine and Robert A. Schiffman
Midwest Research Institute
425 Volker Blvd.
Kansas City, MO 64110

ABSTRACT

Optical pyrometry provides a means for non-contact temperature measurements whose accuracy depends on the accuracy with which specimen emittance is known. Two methods for obtaining the required emittance data are discussed here in which the emittance is determined from measurements of the wavelength or polarization dependence of light emitted by the specimen.

The spectral technique, multi-color pyrometry, yields apparent values for the specimen emittance and temperature from emitted intensity measurements at two or more wavelengths. An assumption about the functional relationship between emittance and wavelength is required by this method.

Emittance corrections cannot be eliminated by increasing the number of spectral intensity measurements required by an n-color pyrometer. Even if this were possible, the accuracy of temperature measurement by n-color pyrometry decreases with n such such that pyrometers that require four intensity measurements would be impractical. Analyses of emittance versus wavelength data for solids show that two- and three-color pyrometry may have large emittance corrections as does the one-color pyrometer. In contrast, emittance values and corrections for one-color pyrometers can be accurately measured by the polarized light technique.

The polarized light technique involves measurement of the degree of polarization for light emitted at an angle of 45° to the specimen normal. At this angle, the reflectivities (r) for light polarized parallel (p) and normal (n) to the plane of emission are related by $r_p = r_n^2$. This leads, for opaque materials, to a simple relation between the intensity ratio, I_p/I_n, for light emitted in the two polarization states and the emittance, i.e., $e_n = 2 - I_p/I_n$. The true specimen temperature is also obtained if absolute intensities are measured.

Development of the polarized light technique in combination with one-color optical pyrometry is recommended to achieve accurate non-contact temperature measurements on liquids. Liquids provide the smooth and specularly reflecting surfaces that the method requires. In this way, precise and accurate temperature control and measurement may be achieved in the containerless liquid phase processing and property investigations that are possible in the low gravity environment of space.

INTRODUCTION

This paper reviews concepts and practical results concerning two methods by which optical pyrometry can be used to achieve non-contact temperature measurements on incandescent objects. The discussion is particularly motivated by opportunities to advance containerless processing technology via experiments carried out in the low-gravity environment of space. Many of these processing applications involve the liquid state of materials that melt at high temperatures to form very corrosive liquids. New methods for non-contact property measurements are needed for process control and to make material property measurements in this environment.

The intensity of radiation emitted by a blackbody depends on temperature and wavelength of the radiation as given by Planck's law. The temperature of a blackbody can thus be accurately measured by a carefully calibrated one-color optical pyrometer. The method is simple, accurate, and has been used in a large fraction of high temperature materials property studies on solids or with solid containers that are reported in the literature. In these studies, blackbody radiation was collected from a sufficiently deep hole drilled in the container or solid material of interest.

The emittance of a material equals the intensity ratio for light emitted by its surface and from a blackbody at the same temperature. Material emittances differ significantly from unity and depend on temperature and composition as well as the wavelength and angle of emission. The apparent temperature measured by an optical pyrometer also varies with these properties. It is not practical to achieve blackbody holes in liquid specimens and new methods for emittance measurement are therefore needed to correct the apparent temperature measurements in containerless experiments.

The first method to be discussed involves the measurement of emitted intensities at two or more wavelengths. The apparent emittance and temperature are then calculated with the help of an assumed functional relation between emittance and wavelength.

The second method relies on measurements of the intensities and the degree of polarization of light emitted at a single wavelength by the specimen of interest. Light is collected at an angle of 45° to the specimen normal. For opaque specular reflectors, the true specimen emittance and temperature can then be easily calculated.

The method of multi-color pyrometry is discussed with particular reference to papers by Coates[1] on the accuracy and precision of temperature measurement that may be achieved and by Nordine[2] on the corrections to multi-color pyrometers that actual emittance data require. Special use is made of three sets of emittance data[3-5] for solid tungsten. These are amoung the most accurate and precise material emittance values that have been

measured. Emittance values for a wide variety of materials have been compiled by Touloukian and DeWitt.[6]

The discussion of emittance measurements by polarization techniques is based on work by Tingwalt and Magdeberg[7]. They report measurements of the emittance of solid tungsten that are in precise agreement with accepted values[3-5]. The accuracy of this technique has thus been established but it has not yet been applied for measurements on liquid specimens in containerless experiments.

In the following sections we first present a thermodynamic analysis[8] of the need for containerless methods in the processing of materials at very high temperatures. Then the methods of multi-color pyrometry and of emittance measurements by polarization techniques are discussed.

CONTAINER INTERACTIONS AT HIGH TEMPERATURES

The concept of a regular solution allows lower limits on the extent of container-specimen interactions to be related to estimates of the maximum endothermicity of solution for solvent-solute pairs. A regular solution is one for which the Gibbs Free Energy of mixing, ΔG_{mix} is given by

$$\Delta G_{mix} = -RT[x_c \ln(x_c) + x_s \ln(x_s)] + x_c x_s \omega \tag{1}$$

where x_c and $x_s = 1 - x_c$ are the mole fractions of the container and specimen respectively. ω measures the departure from ideal solution behavior as the energy required to dissolve one mole of the container (solute) in the contained specimen (solvent). At equilibrium, $\Delta G_{mix} = 0$ and assuming $x_c \ll x_s$ we have

$$x_c = \exp(-\omega/RT) \tag{2}$$

We take 20% of the enthalpy of vaporization (H_v^o) of the container as a physically reasonable estimate for the maximum value of ω, since it would surely take much less energy to dissolve the container in a vacuum (i.e., evaporate it) that to dissolve it in another condensed phase. The most refractory container that is available is tungsten for which $\Delta H_v^o = 860$ kJ/mol so that a reasonable limit on ω/R is

$$\omega/R < 20,700 \text{ K} \tag{3}$$

Although the best container for a particular material of interest may not be tungsten, the chosen container will have an enthalpy of vaporization (per mol of atoms) less than that of tungsten and should satisfy Eq. (3). Values for the minimum solubility of containers in samples calculated from Eqs. (2) and (3) are given in Table 1.

Table 1

Estimate of Minimum Solubilities For
Containers in Specimens[8]

Process Temperature, K	Solubility, mol fraction
1,000	1.0×10^{-9}
1,500	1.0×10^{-6}
2,000	3.2×10^{-5}
2,500	2.5×10^{-4}
3,000	1.0×10^{-3}
4,000	5.7×10^{-3}

The table is a numerical representation of a well known fact illustrated by temperature versus composition phase diagrams, that the solubility of sparingly soluble phases in each other always increases with temperature. Most systems would exhibit solubilities much greater than those given in the table, which estimates limiting values for the least soluble materials that might be found.

MULTI-COLOR PYROMETRY

The intensity, W, of radiation emitted by an object at a particular wavelength, λ, and temperature, T, as given by Wein's law

$$W(\lambda, T) = C \exp(-C_2/\lambda T) \ e \qquad (4)$$

is within 0.2% of that given by Planck's law when $\lambda T < 0.2315$ cm·K, or at temperatures below 3562K at the common wavelength, 650 nm, of single-color optical pyrometers. We assume this relation holds in the following discussion. In Eq. (4) e is the spectral emittance of the specimen of interest and T is its true temperature. Apparent temperatures, T_a and emittances, e_a, appear in the equivalent expression that applies to an optical pyrometer:

$$W(\lambda, T_a) = C \exp(-C_2/\lambda T_a) \ e_a \qquad (5)$$

The true and apparent temperatures are thus related by

$$C_2[1/T - 1/T_a] = \lambda \ln(e/e_a) \qquad (6)$$

The temperature correction for a one-color pyrometer is easily derived by setting $e_a = 1$. For a two-color pyrometer, e_a is assumed independent of wavelength to obtain.

$$C_2[1/T - 1/T_a] = \lambda_1 \lambda_2/(\lambda_1 - \lambda_2)\ln(e_1/e_2) \qquad (7)$$

176

|

The temperature corrections for three-color pyrometers are similarily derived, usually with the assumption that e_a or $\ln(e_a)$ is a linear function of wavelength.

Coates' analysis of n-color pyrometry[1] is based on an assumed emittance function of the form

$$\ln(e_a) = \sum_{i=0}^{n-1} A_i \lambda^i \qquad (8)$$

Coates presents a general equation from which emittance corrections can be calculated for any value of n and n emittance measurements at different wavelengths. By numerical calculations with Eq. (8) as an approximation to model emittance data, Coates showed that the emittance correction becomes more sensitive to errors in the emittance function as such errors decrease with n. The net result is that the use of large values of n in Eq. (8) will not make a multi-color pyrometer accurate.

Nordine[2] explained the limits on the assumed emittance function in multi-color pyrometry in a slightly different way. He took Eq. (8) as a truncated Taylor series about a central wavelength, λ_0:

$$\ln(e_a) = \sum_{i=0}^{n-1} A_i [\lambda - \lambda_0]^i \qquad (9)$$

This would be exact if $n = \infty$. The temperature correction for an n-color pyrometer is then easily shown to be:

$$C_2(1/T - 1/T_a) = (-1)^{n-1}/(n-1)! \; \lambda_0^n [d^{n-1}\ln(e)/d\lambda^{n-1}]_0 \qquad (10)$$

Thus, the emittance correction remains, whatever the number of colors assumed. And as n increases, it becomes impossible to calculate the correction for an n color pyrometer because even the best emittance measurements are not sufficient for accurate calculation of $d^{n-1}\ln(e)/d\lambda^{n-1}$. For a similar reason, it becomes impossible to measure temperature accurately with an n-color pyrometer because the best intensity versus wavelength measurements will not give good precision in the derived high order derivitives of intensity with respect to wavelength.

Nordine also examined the precision that may be expected for two- and three-color pyrometry by analysis of emittance data for solid tungsten obtained by three different investigators[3-5]. These are probably the most accurate high temperature emittance data that exist. The values reported by the three investigators differ by less than ±1% at temperatures between 1600 - 3000K and wavelengths between 400 - 750 nm. The expected decrease in precision of apparent temperature measurement for two- and three-color pyrometers was illustrated. It was also shown that the emittance corrections for one-color pyrometers usually vary less with temperature than do corrections for two- and three-color pyrometers.

To be sure, the two- and three-color corrections for tungsten (and for molybdenum) are smaller than for the one-color

pyrometer. But for many other materials, the one-color pyrometer gives the smaller temperature corrections. Tungsten and molybdenum are convenient test materials but provide misleading demonstrations of these instruments' accuracy.

The advantages of one-color pyrometry are three-fold, as applied to opaque metallic materials for which sufficient data are available to support the analysis.

• One-color pyrometers often exhibit emittance corrections that are smaller than the corresponding values for two- and three-color pyrometers.

• One-color pyrometers nearly always exhibit temperature coefficients for emittance corrections that are less than the corresponding values for two- and three-color pyrometers.

• One-color pyrometers always measure apparent temperature with a greater accuracy than two- or three-color pyrometers.

The greater temperature dependence of emittance corrections for two- than for one-color pyrometers derives from a general phenomenon exhibited by metallic substances wherin emittance versus wavelength curves obtained at different temperatures cross at a wavelength denoted as the "x-point". The emittance is independent of temperature at this point. Consequently it varies much less with temperature near the "x-point" than do the slopes of the curves on which two-color corrections depend. Two-color emittance corrections usually have a greater dependence on temperature than do one-color corrections because "x-points" usually occur in the visable to near-infrared spectral region used by optical pyrometers. It turns out that the same is true for three-color pyrometers. Four- or greater-color pyrometers are of little interest because they are not accurate and are inherently imprecise.

For these reasons, it is superior to calibrate one-color pyrometers at the known melting point of a material of interest and assume emittance corrections are independent of temperature than to do the same with two- or three-color pyrometers. It is worse yet to assume the emittance correction is zero for a two- or three-color pyrometer. However, the major disadvantage of large emittance corrections remains with one-color pyrometry, and the assumption of temperature independent corrections may also be insufficient for thermophysical property studies.

Since blackbody holes can be used to achieve unit emittance in work with solids, development of methods for accurate emittance measurements on liquids remains as an outstanding problem in high temperature materials science. The following section shows how this problem may be solved.

178

POLARIZED LIGHT TECHNIQUE FOR EMITTANCES OF LIQUIDS

In 1962 Tingwaldt and Magdeburg[7] published measurements of the emittance of polished tungsten at temperatures between 1630 - 2190K and at wavelengths between 466.5 - 698 nm that agreed within ±1% with the accepted values[3-5]. The method was to measure the intensity ratio for light emitted at 45° to the specimen normal and polarized normal (n) and parallel (p) to the emission plane.

The equations that describe the polarized reflectivities, r_n and r_p are:

$$r_n = [\sin(\theta - \emptyset)/\sin(\theta + \emptyset)]^2 \qquad (11)$$

$$r_p = [\tan(\theta - \emptyset)/\tan(\theta + \emptyset)]^2 \qquad (12)$$

where θ is the angle between the specimen normal and the incident light beam, N is the complex index of refraction, and

$$N \sin(\emptyset) = \sin(\theta) \qquad (13)$$

It is easily demonstrated when $\theta = 45°$ that

$$r_p = (r_n)^2 \qquad (14)$$

For opaque materials, the sum of reflectivity and emissivity is unity:

$$r + e = 1 \qquad (15)$$

This leads to

$$e_n = 2 - e_p/e_n \qquad (16)$$

or

$$e_n = 2 - I_p/I_n \qquad (17)$$

where I_p/I_n is the intensity ratio for emitted light in the two polarization states.

Tingwaldt and Magdeburg measured I_p/I_n for a polished tungsten filament that was oriented at 45° to the observation direction. The value of e_n was then derived from Eq. (17). Intensity measurements were also made in a direction normal to the surface. Normal spectral emittances were thus obtained which agreed well with the accepted values[3-5] to demonstrate the accuracy of this method.

The polarized light technique should be easily adapted for non-contact temperature and emittance measurements on liquid phases in containerless experiments. Liquids have the smooth and specularly reflecting surfaces that are required and will assume a spheroidal shape that, at some point on the surface, emits

light at an angle of 45° to the specimen normal for any directioı
of observation. The emittance and temperature can then be
accurately measured by an instrument that identifies the 45°
point and measures the absolute intensities of the two components
of polarized light emitted at this point.

An instrument that would implement this method for liquid
temperature measurements is illustrated in Figure 1, whose
caption describes the labeled parts. The device relys on
reflection of a laser beam incident at an angle of 90° to the
observation direction to find the 45° point. Since the liquid
spheroid is a specular reflector, the instrument will collect
reflected laser light only from a small region centered at the
this point to which the instrument aperture may be adjusted.
Simultaneous measurements by the two photodetecters will insure
that the two intensities are measured at the same specimen
temperature. Very accurate determination of relative detection
sensitivities is possible by observing emission normal to the
specimen surface where $I_n = I_p$. Manual positioning of the
instrument would be possible if the suspended specimen has a
stable position and shape. Alternatively, automatic alignment
could be achieved via a quadrant detecter of the laser spot and
oppropriate feed back to a positioning mechanism. If the
specimen shape or position are not stable, electronic triggering
of the intensity measurements could be used at moments when the
reflected laser spot illuminates the instrument aperture.

CONCLUSIONS

Multi-color pyrometry cannot achieve accurate non-contact
temperature measurements without information about specimen
emittance. Emittance data for incandescent liquid specimens can
be obtained by measuring the polarization properties of emitted
light. Developement of a single instrument that combines this
technique with one-color pyrometry is recommended for application
to containerless materials processing in space experiments.
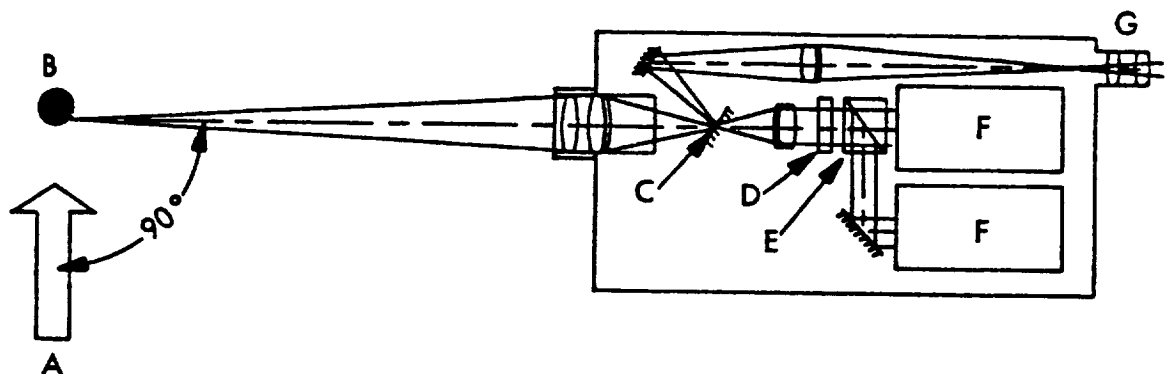
Figure 1. Instrument for Emittance and Temperature Measurement
on Liquid Drops. A - HeNe laser beam; B - Liquid specimen;
C - Instrument aperture; D - Color filter; E - Polarizing prism;
F - Photodetectors; G - Alignment telescope.

REFERENCES

1. P. B. Coates, Metrologia **17**, 103 (1981).

2. P. C. Nordine, High Temp. Sci. **21**, 97 (1986).

3. L. S. Ornstein, Physica **3**, 561 (1936).

4. J. C. DeVos, Physica **20**, 690 (1954).

5. R. D. Larrabee, J. Opt. Soc. Am. **49**, 619 (1959).

6. Y. S. Touloukian and D. P. DeWitt, eds., _Thermophysical Properties of Matter_, vols. 7 and 8, _Thermal Radiative Properties_, IFI Plenum, NY, 1970.

7. C. R. Tingwaldt and H. Magdeberg, in _Temperature, its Measurement and Control in Science and Industry_, vol. 3, part 2, Reinhold, NY 1962, pp. 483-486.

8. P. C. Nordine and R. A. Schiffman, "Containerless Laser Induced Fluorescence Study of Vaporization and Optical Properties for Sapphire and Alumina", J. Amer. Ceram. Soc. (accepted for publication).

COMMON BUT UNAPPRECIATED SOURCES OF ERROR IN ONE, TWO, AND MULTIPLE-COLOR PYROMETRY

Presented at the NASA Symposium for

Non-contact Temperature Measurement

R. Erik Spjut

Department of Materials Science and Engineering

Massachusetts Institute of Technology

Introduction

Optical pyrometry is commonly used to measure temperatures above 1000 K in environments where thermocouples would be unstable or cause interference with the system under study. When great care is used, optical pyrometers can have an accuracy of ±2 K or better. When used indiscriminately, errors in excess of ±100 K are easily obtained. Although most of the sources of error have been known for some time, they are still often neglected. For the purposes of this paper the errors can be classified in one of three areas:

i) Errors due to noise and non-linearity in the detection system or uncertainty about properties such as emissivity.

ii) Errors due to stray radiation.

iii) Errors due to the finite response speed of the detection system.

Background

All optical pyrometric systems are based on either Planck's law[1],

$$i_\lambda = \frac{2\epsilon_\lambda C_1}{\lambda^5(e^{C_2/\lambda T}-1)} ,$$ (1)

where i_λ is the intensity at wavelength λ, ϵ_λ is the emissivity of wavelength λ, T is the temperature, and C_1 and C_2 are the first and second radiation constants, or the approximation known as Wien's law[1],

$$i_\lambda = \frac{2\epsilon_\lambda C_1}{\lambda^5 e^{C_2/\lambda T}}$$ (2)

Most optical detectors generate a voltage proportional to the intensity. If one designates the voltage as V_λ, the temperature is calculated from V_λ as,

$$T = \frac{-C_2/\lambda}{\ln(V_\lambda) - \ln(G) - \ln(\epsilon_\lambda)} ,$$ (3)

where the term G accounts for the detector gain, the optical bandwidth and other similar quantities.

The equivalent expression for two-color pyrometry is,

$$T = \frac{-C_2(1/\lambda_1 - 1/\lambda_2)}{\ln\left(\frac{V_{\lambda_1}}{V_{\lambda_2}}\right) - \ln\left(\frac{G_1}{G_2}\right) - \ln\left(\frac{\epsilon_\lambda}{\epsilon_\lambda}\right)}$$ (4)

In multiple-color pyrometry, a functional form of ϵ_λ vs. λ is assumed such as a linear fit, and the temperature is calculated from a least-squares fit of Planck's law to V_λ vs. λ data.

Noise Errors

If an error analysis is performed on Equation 3, one obtains[2],

$$\delta T = \frac{T^2}{C_2/\lambda} \left[\sum \left(\frac{\delta n}{n}\right)^2 \right]^{1/2} ,$$ (5)

where δT is the error in T and the $\delta n/n$'s can represent the uncertainty in V_λ, ϵ_λ and any of the factors in G. The points to note are that for a constant uncertainty in the measurements, the error in the temperature increases as the square of the temperature and decreases linearly with λ. Figure 1 is a plot of the error in T as a function of T for a constant one-percent error in the measurement with λ as a parameter. The trends in T and λ stated above are clearly visible.
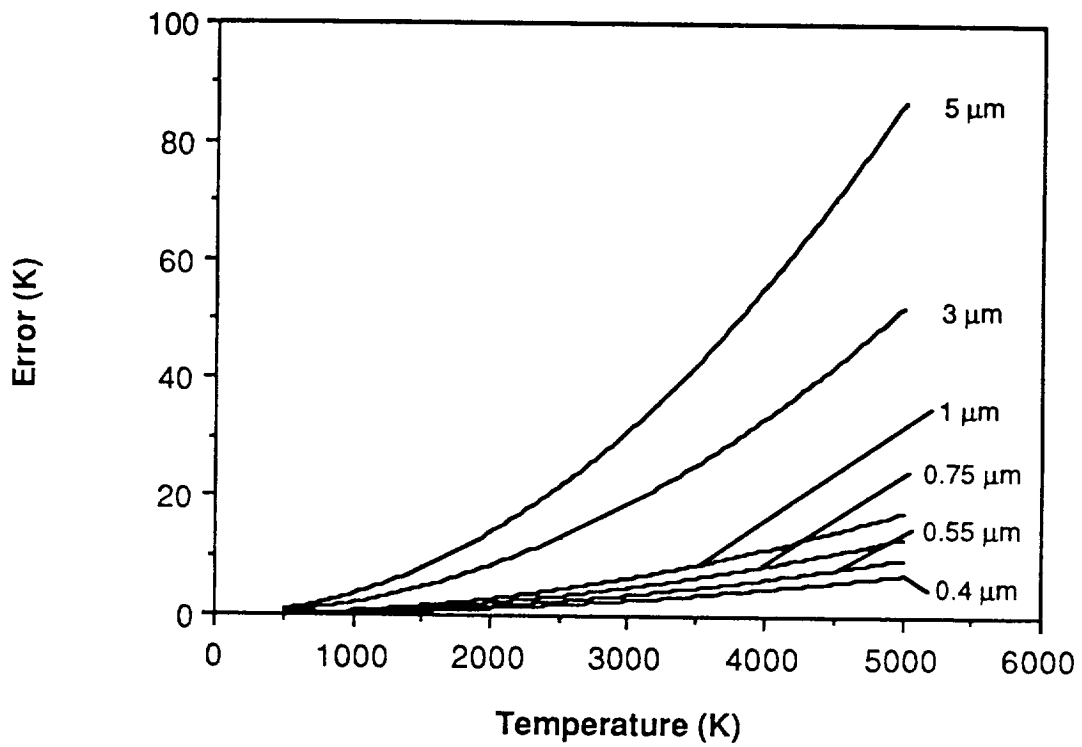
Figure 1 Calculated error in temperature for single color pyrometers for a 1% error in the signal

One effect that was neglected in Figure 1 is background noise or dark current. The background noise becomes a larger and larger fraction of the signal as the temperature drops. Figure 2 is equivalent to Figure 1 but includes this effect. Note the logarithmic scale on the Error axis. The 5μm, 3μm and 1 μm curves were calculated using typical D^* values for indium-antimonide detectors. The 750 nm, 550 nm, and 400 nm curves were calculated using typical D^* values for photomultiplier tubes. The steep initial decrease in the error is due totally to the dark current. The gradual rise is the same as on Figure 1. The exact placement of the minimum depends on the actual D^* and on the field of view of the detector.

For a two-color pyrometer the error equation is[2],

$$\delta T = \frac{T^2}{C_2(1/\lambda_1 - 1/\lambda_2)}\left[\sum\left(\frac{\delta n}{n}\right)^2\right]^{1/2} \tag{6}$$

where $\delta n/n$ is now the error in the ratio of ϵ_{λ_1} and ϵ_{λ_2}, G_1 to G_2, *etc.*, as well as the noise inherent in V_{λ_1} and V_{λ_2}. The point to note here is that for a constant uncertainty in the measurement, a two-color pyrometer always has a greater error than the one color temperature calculated from the shorter wavelength signal, and the closer together the wavelengths are, the worse the error. The only reasons to use two-color pyrometers are when the target area is unknown or changing with time, the intensity at the two wavelengths is being attenuated equally by an intervening medium, or there is strong reason to believe that $\epsilon_{\lambda_1}/\epsilon_{\lambda_2}$ is more than $\frac{1/\lambda_1}{1/\lambda_1 - 1/\lambda_2}$ times as accurate as ϵ_{λ_1}, where λ_1 is the shortest
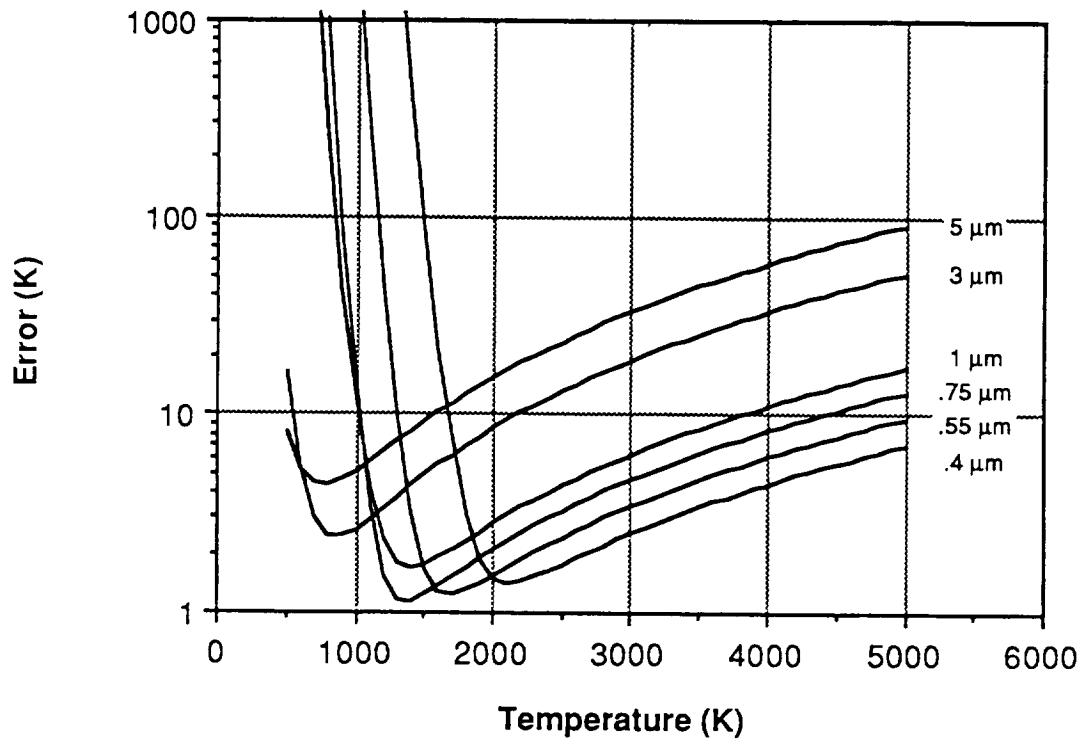
Figure 2   Calculated error in temperature for single color pyrometers
for a 1% error in the signal and accounting for dark current
or zero-signal noise

wavelength. Otherwise single color pyrometry is superior. Figure 3 is a plot of δT vs. T for some two-color pairs for a constant one-percent error. The 581 nm - 545 nm pair was used in reference [3] to measure the temperature of burning coal particles. The background noise in a two-color system will usually be dominated by the behavior of the shortest-wavelength detector.

The error analysis of multiple-color pyrometry is beyond the scope of this paper but some facts can be established. Even with good data the minimum in the least-squares error is very broad. The chosen functional form of ϵ_λ can have strong correlation effects with the Planck function. In computer simulations the uncertainty is typically one-to-five percent in the temperature[4] On actual data where the emissivity is not known the uncertainties are typically ten-to-twenty percent or greater[5].

Stray Radiation Errors

An object that is not perfectly emissive reflects or scatters a portion of the radiation incident on it. If this reflected or scattered radiation reaches the pyrometric detectors, they will indicate an incorrect temperature[6]. If the direct radiation from the target is i, and the stray background reaching the detector is i_b, the measured temperature for a one-color pyrometer is,

$$T_m = \frac{-C_o/\lambda}{\ln(1+i_b)-\ln(\epsilon_\lambda)} \tag{7}$$

In general the calculation of i_b requires a knowledge of the angular emissivity of the interfering background, the angular reflectivity of the target, and the viewfactors in the system. For
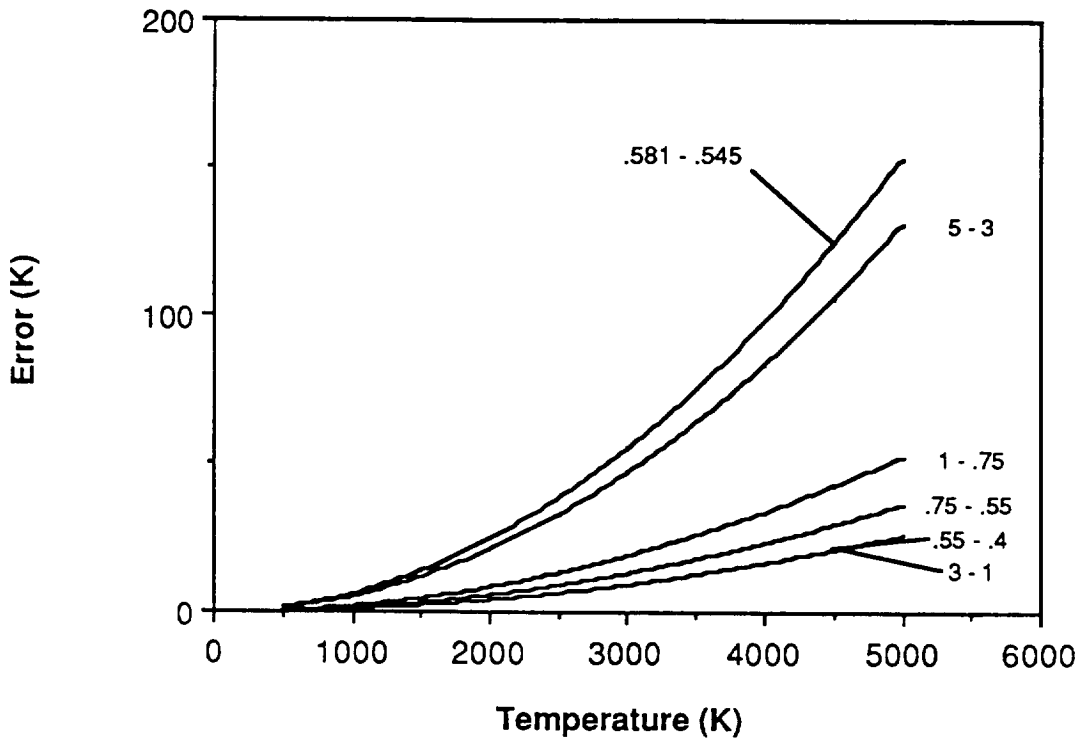
Figure 3   Calculated error in temperature for two color pyrometers for
a 1% error in the signal

the much simplified case where the background and the target are diffuse reflectors and emitters and the background surrounds the target, the measured temperature can be calculated as[6]

$$T_m = \frac{-C_2/\lambda}{\ln\left[e^{-C_2/\lambda T} + \frac{(1-\epsilon)\epsilon_b}{\epsilon} e^{-C_2/\lambda T}\right]} ,$$ (8)

where T and ϵ are the temperature and emissivity of the target and T_b and ϵ_b are the temperature and emissivity of the background.

Figures 4, 5 and 6 are plots of the measured temperature as a function of the background temperature as calculated by Equation 8 with the target temperature as a parameter. When the target is a good emitter and the background is a weak emitter, as in Figure 4, the background doesn't affect the measured temperature until the background temperature is substantially above that of the target. When the target and background emissivities are equal to 0.5, as in Figure 5, the background has some effect even at temperatures below that of the target. The effect of the background becomes more pronounced at higher temperatures as predicted by Equation 5. When the background is much more emissive than the target, as in Figure 6, the background must be much cooler than the target or the measured temperature will be grossly in error.

The equivalent general expression for two colors is,

$$T_m = \frac{-C_2(1/\lambda_1 - 1/\lambda_2)}{\ln\left(\frac{i_{\lambda_1} + i_{b\lambda_1}}{i_{\lambda_2} + i_{b\lambda_2}}\right) - \ln\left(\frac{\epsilon_{\lambda_1}}{\epsilon_{\lambda_2}}\right)} ,$$ (9)
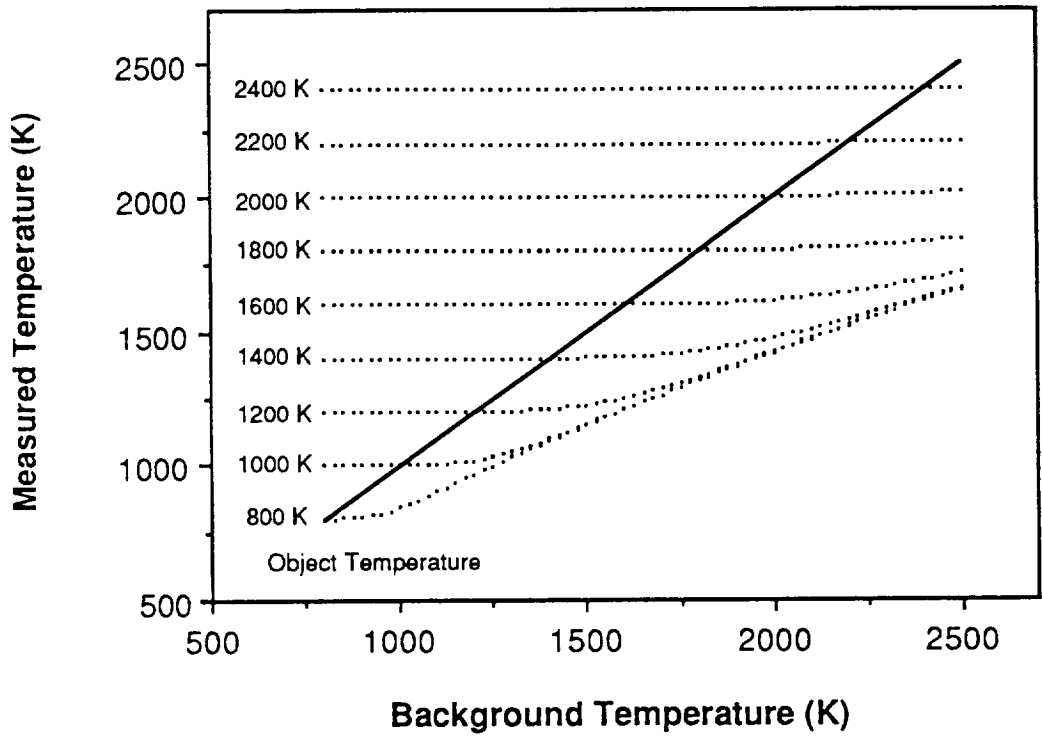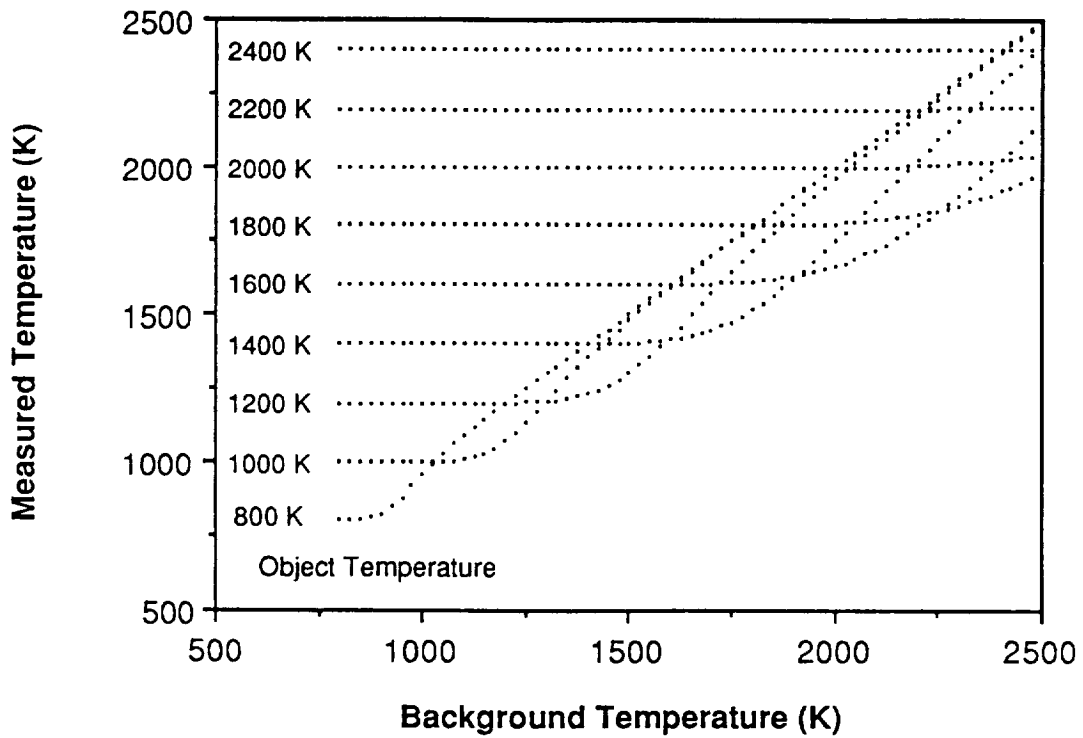
Figure 4   The temperature measured by a 650 nm single-color pyrometer for a given object temperature as a function of the background temperature, $\varepsilon = 0.9$, $e_b = 0.1$
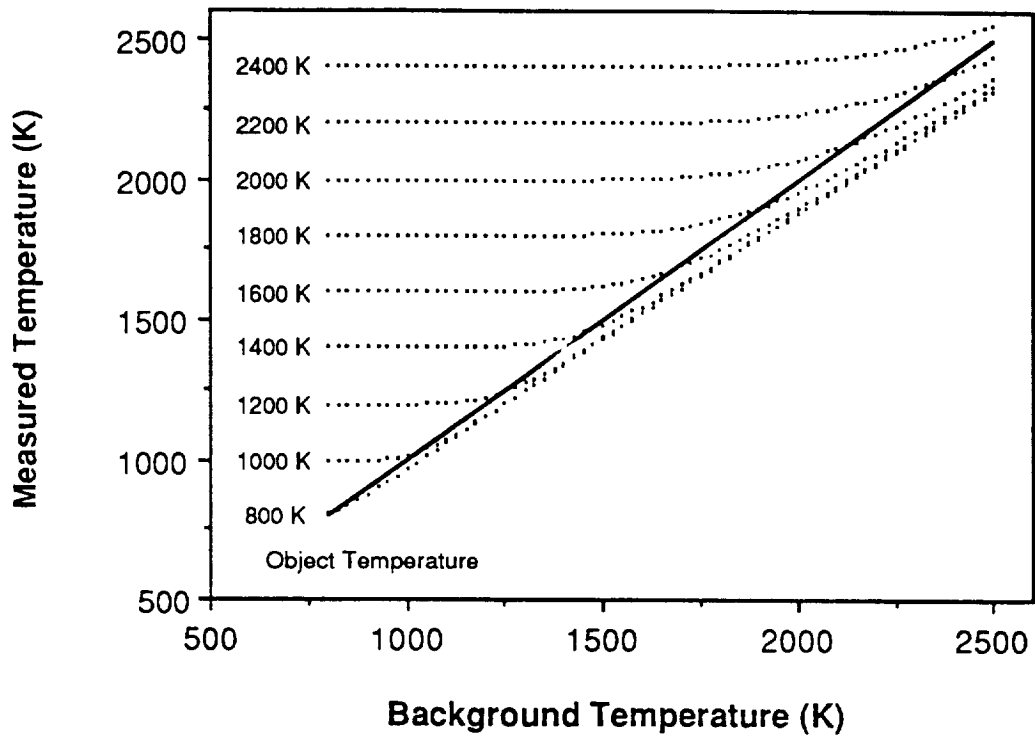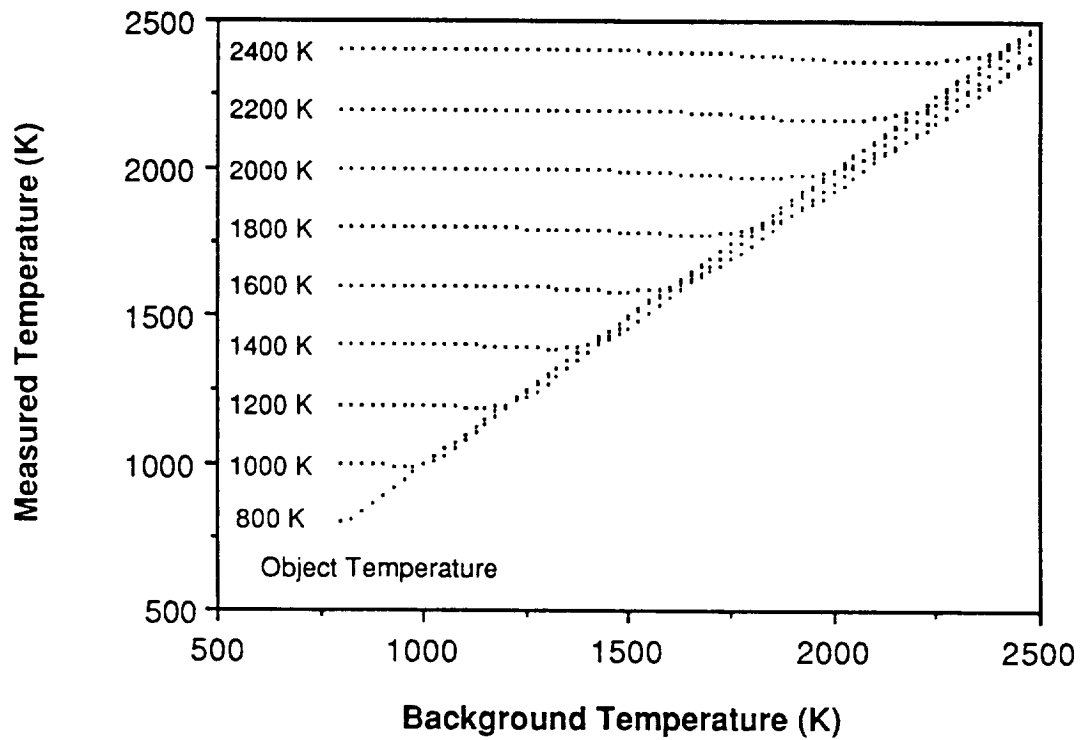
Figure 5   The temperature measured by a 650 nm single-color
pyrometer for a given object temperature as a function of the
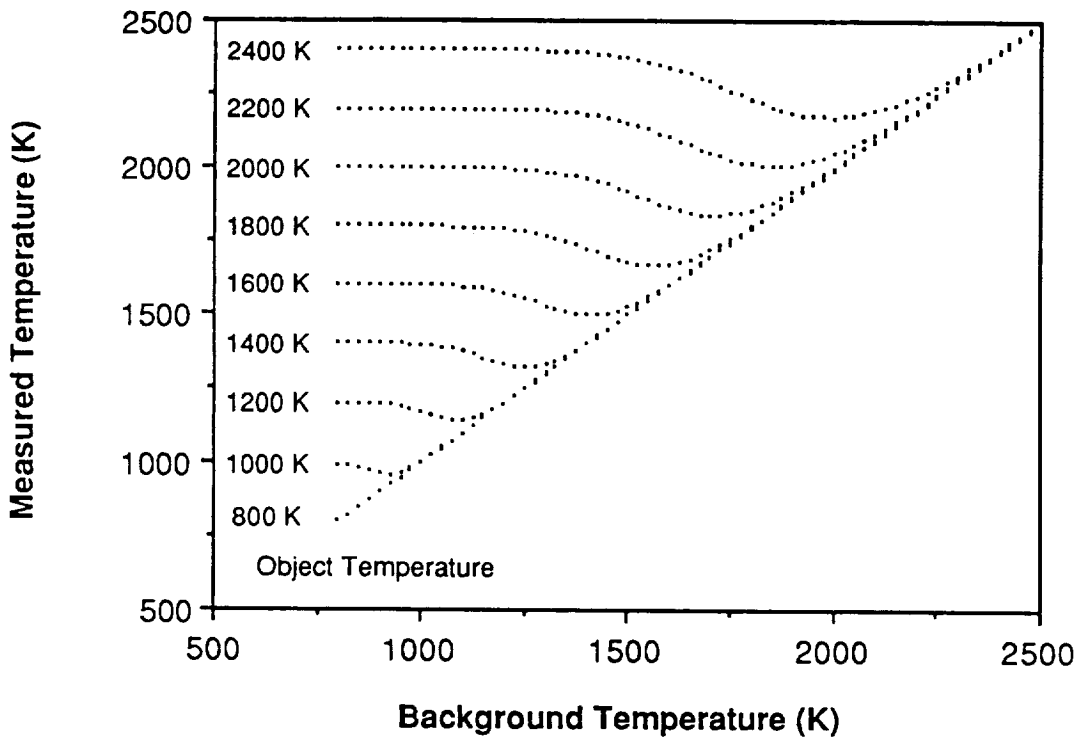background temperature, $\varepsilon = 0.5$, $e_b = 0.5$
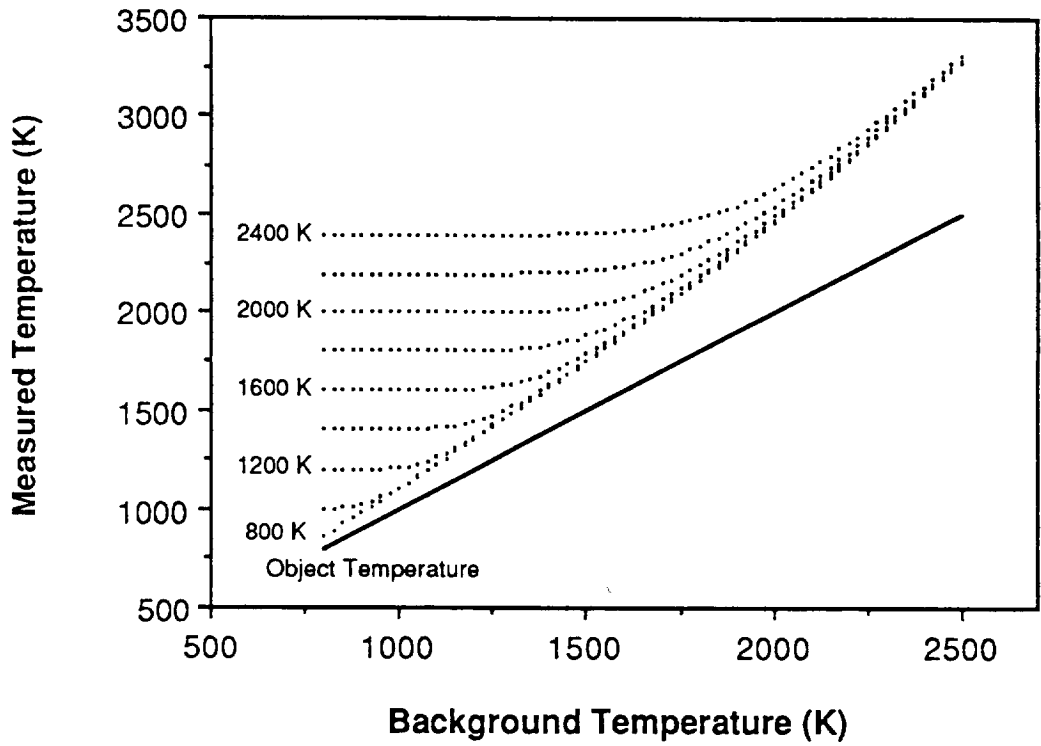
Figure 6 The temperature measured by a 650 nm single-color pyrometer for a given object temperature as a function of the background temperature, $\varepsilon = 0.1$, $e_b = 0.9$

and the general case involves a knowledge of the angular-spectral emissivities and reflectivities at λ_1 and λ_2, and all of the relevant viewfactors. For the much-simplified case of background and target being diffuse gray-bodies and the background surrounding the target the measured temperature can be calculated as,

$$T_m = \cfrac{-C_2(1/\lambda_1 - 1/\lambda_2)}{\ln\left[\cfrac{e^{-C_2/\lambda_1 T} + \frac{(1-\epsilon)\epsilon_b}{\epsilon} e^{-C_2/\lambda_1 T_b}}{e^{-C_2/\lambda_2 T} + \frac{(1-\epsilon)\epsilon_b}{\epsilon} e^{-C_2/\lambda_2 T_b}}\right]} \qquad (10)$$

where λ_1 and λ_2 are the two pyrometric wavelengths.

Figures 7, 8 and 9 are plots of the measured temperature as a function of the background temperature as calculated by Equation 10 with the target temperature as a parameter. Because of the gray-body assumption, the measured temperature always asymptotically approaches the background temperature at high T_b. In Figure 7 the target is much more emissive than the background. Consequently, the background doesn't really affect the measurements until the background temperature is substantially above the target temperature. In Figure 8 the emissivities are both equal to 0.5. The measured temperature is affected much sooner by the background and at higher target temperatures a slight dip is found in T_m. In Figure 9 the background is much more emissive than the target and the dip in T_m is much more pronounced. The effect is counterintuitive and is due to the nonlinear nature of the Planck function.

I

Figure 7 The temperature measured by a 650 nm - 550 nm two-color pyrometer for a given object temperature as a function of the background temperature, $\varepsilon = 0.9$, $e_b = 0.1$

Figure 8   The temperature measured by a 650 nm - 550 nm two-color
pyrometer for a given object temperature as a function of the
background temperature, $\varepsilon = 0.5$, $e_b = 0.5$

Figure 9   The temperature measured by a 650 nm - 550 nm two-color
pyrometer for a given object temperature as a function of the
background temperature, $\varepsilon = 0.1$, $e_b = 0.9$

The calculations for the general case are much more involved, especially if curved specular surfaces are present, but the trends are generally the same. One would prefer a hot emissive object in a very cold background.

The background radiation in a multi-wavelength system can masquerade as a wavelength-dependent emissivity and the magnitude and sign of the resultant error must be evaluated on a case-by-case basis and is not subject to heuristic interpretation.

Speed of Response Errors

In most pyrometric systems, the detector response time is considered fast with respect to the measured system's response time. The question of how fast is fast enough does not have a simple answer. An analysis performed in reference [7] of the transient response of a temperature measurement system shows that in some cases the transient response is enhanced in optical pyrometers and in some cases is retarded.

Most detector-system responses can be modeled as a first-order system, which is characterized by a unit step response of $1 - e^{-t/\tau}$, where t is the time and τ is the characteristic response time of a first-order system. For linear systems with higher order responses, the general trends shown below hold but the specific shape of the response is different. In a first-order system, the voltage response of a single detector for a step change in intensity from i_1 to i_2 (corresponding to temperatures T_1 and T_2) is given by

$$\frac{V(t)}{K} = i_2 + (i_1 - i_2) e^{-t/\tau} \tag{11}$$

where Wien's law is assumed and K is a constant that depends on the various gain factors. The temperature calculated from $V(t)$ has the transient response

$$T(t) = \frac{-C_2/\lambda}{\ln\left[e^{-C_2/\lambda T_2} + (e^{-C_2/\lambda T_1} - e^{-C_2/\lambda T_2})e^{-t/\tau}\right]} \tag{12}$$

For rises in temperature, the pyrometer temperature responds more quickly than expected, with the greatest enhancements for the largest ΔT's. For temperature drops, the response is retarded, with the effect being greatest for the largest ΔT's. These effects are due to the strong nonlinearity of i with respect to T.

The effect with two-color pyrometry shows the same general behavior but is even more dramatic. The equation for temperature analogous to Equation 12 is

$$T(t) = \frac{-C_2(1/\lambda_1 - 1/\lambda_2)}{\ln\left[\dfrac{e^{-C_2/\lambda_a T_2} + (e^{-C_2/\lambda_a T_1} - e^{-C_2/\lambda_a T_2})e^{-t/\tau}}{e^{-C_2/\lambda_b T_2} + (e^{-C_2/\lambda_b T_1} - e^{-C_2/\lambda_b T_2})e^{-t/\tau}}\right]} \tag{13}$$

An examination of the limiting cases can help to understand the much more pronounced effect with two colors than with one color If perfect noiseless detectors are assumed and the temperature is permitted to step from an initial temperature of $T_1 = 0$ K up to T_2, the single color temperature from Equation 12 would have the response

$$T(t) = \frac{-C_2/\lambda}{\ln\left[e^{-C_2/\lambda T_2}(1 - e^{-t/\tau})\right]} \tag{14}$$

whereas the two-color response from Equation 13 would be

$$T(t) = \frac{-C_2(1/\lambda_1 - 1/\lambda_2)}{\ln\left[\dfrac{e^{-C_2/\lambda_a T_2(1-e^{-t/\tau})}}{e^{-C_2/\lambda_b T_2(1-e^{-t/\tau})}}\right]} = T_2 \quad . \tag{15}$$

In other words, the ratio of the two signals responds instantly even though the signals themselves take much longer to respond. As T_1/T_2 approaches zero, the system response more closely approaches a perfect step change.

If, however, the temperature is permitted to drop from an initial temperature of T_1 to $T_2 = 0$ K, the single-color response is

$$T(t) = \frac{-C_2/\lambda}{\ln\left[e^{-C_2/\lambda T_1}e^{-t/\tau}\right]} \quad , \tag{16}$$

whereas the two-color response is

$$T(t) = \frac{-C_2(1/\lambda_1 - 1/\lambda_2)}{\ln\left[\dfrac{e^{-C_2/\lambda_a T_1}e^{-t/\tau}}{e^{-C_2/\lambda_b T_1}e^{-t/\tau}}\right]} = T_1 \tag{17}$$

The two-color system would indicate the initial temperature forever. The above situation corresponds to T_1/T_2 approaching infinity.

The calculated effect on a typical pyrometry system is seen in Figure 10. In this simulated example a two-color optical pyrometer with center wavelengths of 750 nm and 450 nm and a linear response time of 10 ms is used to measure the temperature of an object initially at 1000 K. The temperature of the object is instantaneously raised to 1500 K and maintained for 50 ms. The temperature is then instantaneously reduced to 1000 K and held there. On the figure the exp(-time/tau) curve corresponds to the temperature a thermocouple with a response time of 10 ms would
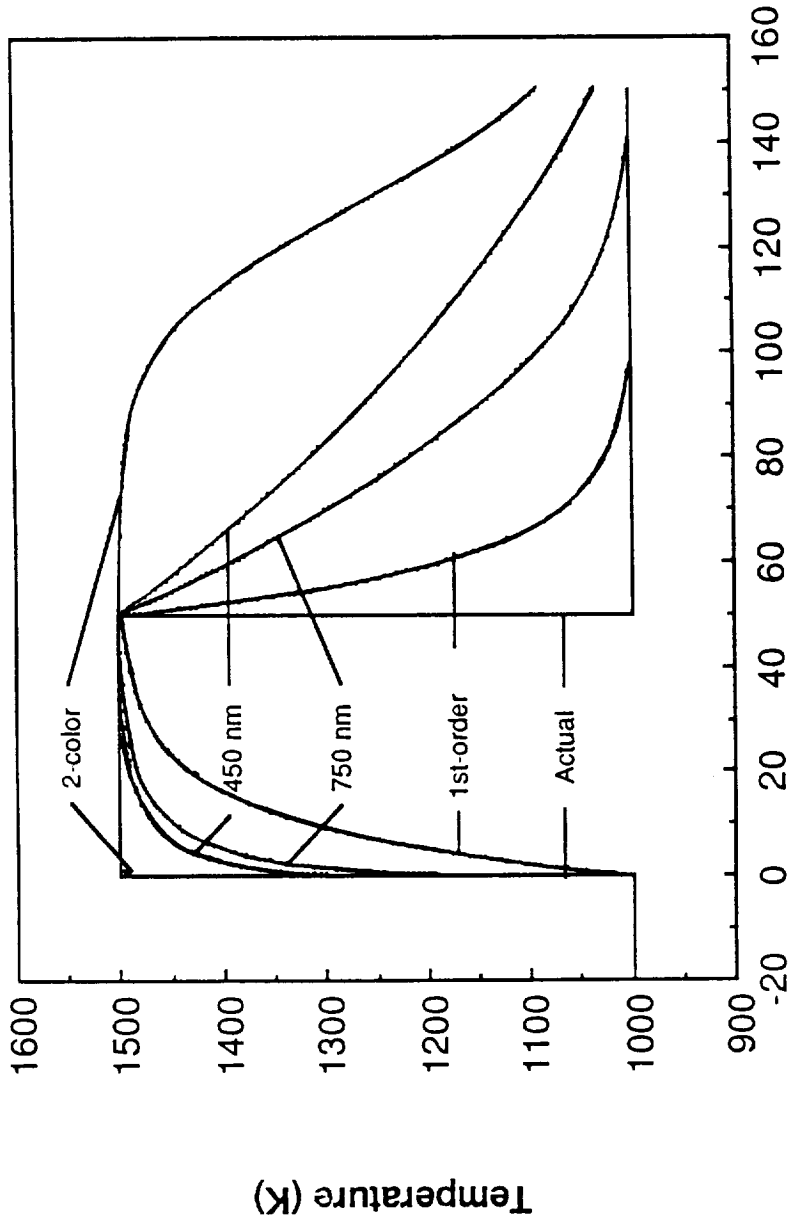
Calculated response of a linear thermo-couple, a 750 nm single-color pyrometer, a 450 nm single-color pyrometer, and a 750 nm – 450 nm two-color pyrometer, all with a first-order response time of 10 ms to a 50 ms temperature pulse.

Figure 10

201

indicate. The next two curves in ascending order are for the single-color temperatures at 750 nm and 450 nm. The top curve is the two-color temperature.

For the temperature rise the single-color temperatures respond more quickly than the linear thermocouple. The response is faster for the shorter wavelengths. The two-color temperature tracks the step so closely that it is difficult to distinguish from the true temperature. Clearly the two-color response is excellent.

The four curves maintain their relative orderings with respect to temperature for the temperature drop. The two-color temperature response, which was previously excellent, is now almost unacceptably slow. One must be careful when measuring temperature decreases with an optical pyrometer.

If signal-processing is applied to the signals, an option for improving the behavior is available. If one can take the logarithm of the signal before the filtering or averaging is performed, the response becomes symmetric with respect to the reciprocal of the temperature. In other words, if the first-order system processes $\log(i)$ instead of i, the transient response for both one- and two-color systems is

$$\frac{1}{T(t)} = \frac{1}{T_2} + \left(\frac{1}{T_1} - \frac{1}{T_2}\right)e^{-t/\tau} . \tag{18}$$

Actual results from the measurement of the transient temperature of a 60 μm platinum thermocouple heated by a laser are presented in Figures 11 and 12. In Figure 11 the thermocouple was initially at 1173 K. At time t = 0 the temperature was raised
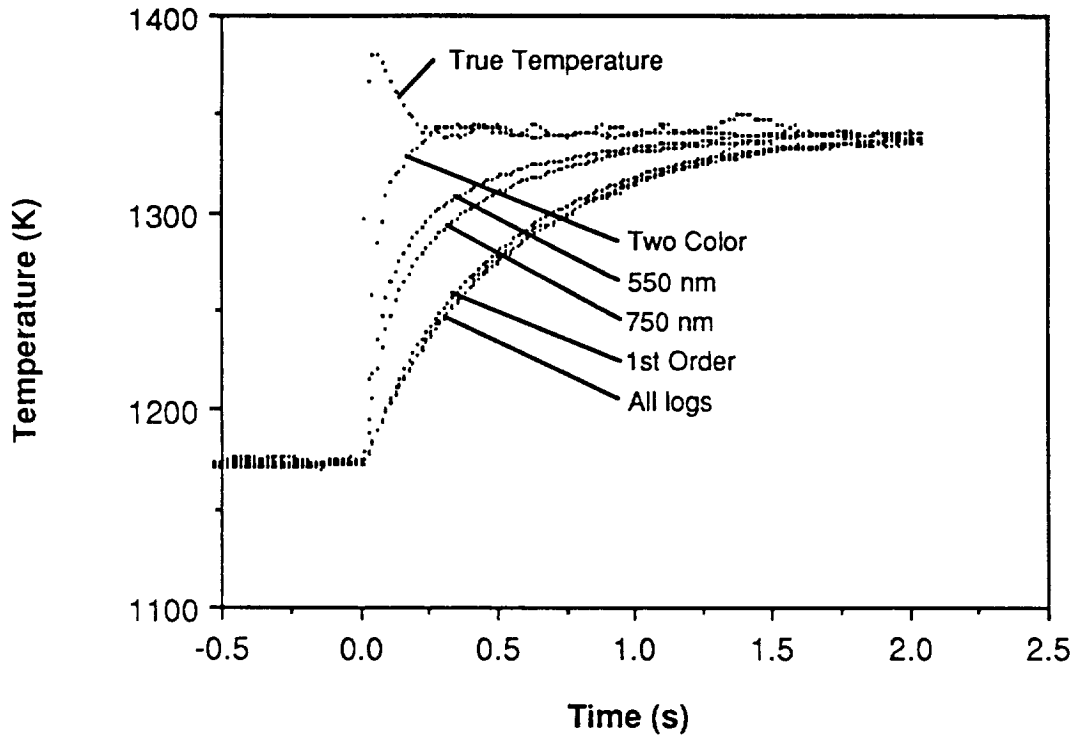
Figure 11 Experimental transient temperature behavior for a linear
temperature measurement system, a two-color pyrometer,
two one-color pyrometers, and all three pyrometers using the
log of the intensity, for a temperature jump
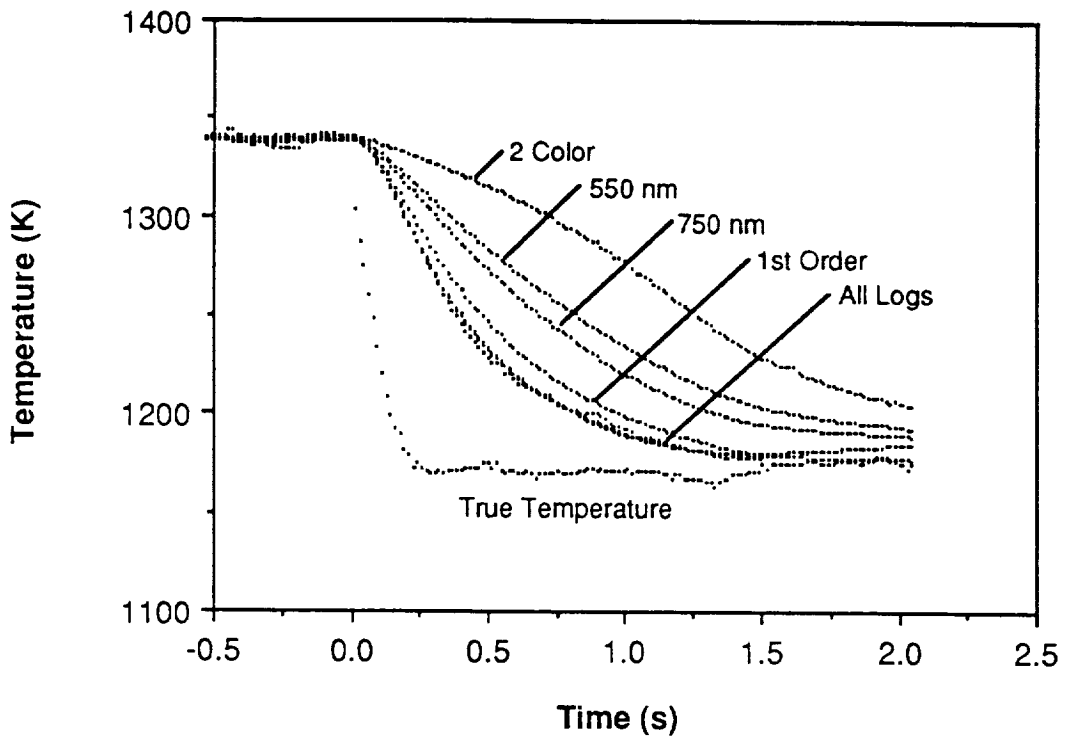
Figure 12 Experimental transient temperature behavior for a linear
temperature measurement system, a two-color pyrometer,
two one-color pyrometers, and all three pyrometers using the
log of the intensity, for a temperature drop

to 1341 K. The signal from the thermocouple and the signals from the photomultiplier tubes were recorded.

The actual temperature was calculated from the raw thermocouple data without any filtering. The data from the thermocouple and the two optical channels were filtered digitally with the exact equivalent of a first-order analog system to demonstrate the effect of a first-order response. The system time constant was set at $\tau = 0.509$ s. In Figure 11, as expected, both single-color temperatures responded more quickly than the filtered thermocouple response and are properly ordered with respect to wavelength. The two-color response was very close to the true response. It also shows more noise than the single-color temperatures, as one would expect from the error analysis mentioned above[2,8,9]. The logarithms of the signals were processed as well. All three temperatures calculated from the log-signals fell on the same curve and were very close to the linear first-order response.

A representative set of results for a temperature drop are plotted in Figure 12. In this experiment the thermocouple was initially at 1338 K and at time t = 0 the temperature was lowered to 1172 K. As expected, the log-intensity temperatures have the fastest response and the the filtered thermocouple is just slightly slower, the 750 nm temperature and the 550 nm are intermediate and the two-color response is the slowest. The theoretical responses predicted by Equations 12, 13 and 18 are not shown but agree very well with the experimental points.

Further insight can be gained from a frequency analysis of the two-color response. Because the system is nonlinear, the frequency response cannot be uniquely defined but is different for each combination of wavelengths and magnitude of temperature-oscillation. The results for a two-color pyrometer with wavelengths 350 nm and 550 nm at one frequency are given in Figure 13. Here a sinusoidally varying temperature is measured by a thermocouple and by a two-color pyrometer, each with response-time τ. The true temperature is given by $T = 1000\,K + 100\,K\,\sin(\omega t)$ where $\omega\tau = 1$. The two-color signal has an average temperature that is 50 K above the mean of the true temperature and has an amplitude roughly half that of the thermocouple temperature.

Figure 14(a) is a plot of the difference between the pyrometer average temperature and the true mean temperature as a function of frequency. Figure 14(b) is a Bode-type plot of the root-mean-square (rms) amplitude of the time-varying component of the pyrometer temperature about the average pyrometer temperature as a function of frequency. The rms response of a first-order linear system is shown for comparison.

The rms signal of the pyrometer decreases more rapidly with increasing frequency than for a first-order system, and it also displays an offset which the first-order system does not display. When measuring rapidly fluctuating temperatures, an optical pyrometer will not show the correct average temperature, and will under-indicate the magnitude of the fluctuations by a larger amount than a linear system with the same response time would do.
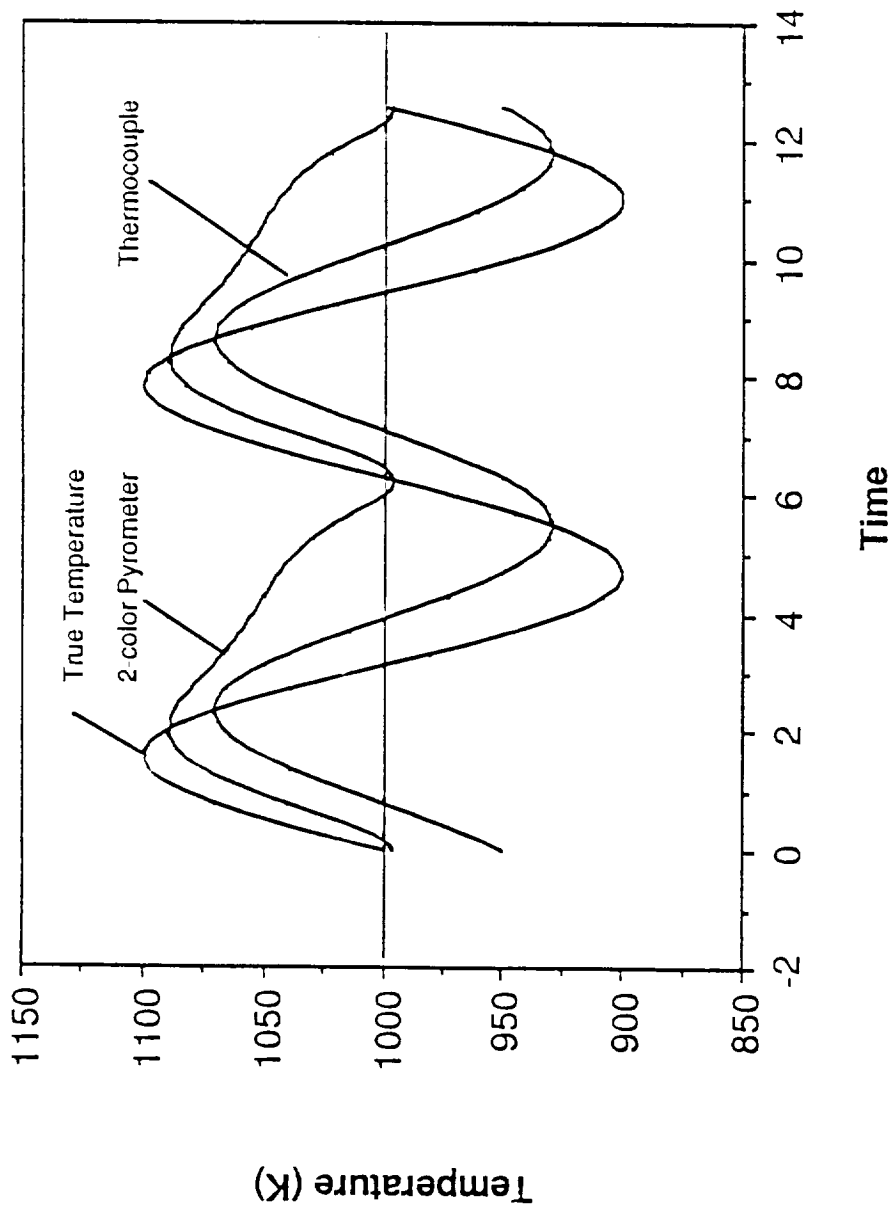
Figure 13 The actual temperature and the temperature reported by a linear device and a two-color pyrometer for an object with a sinusoidally varying temperature
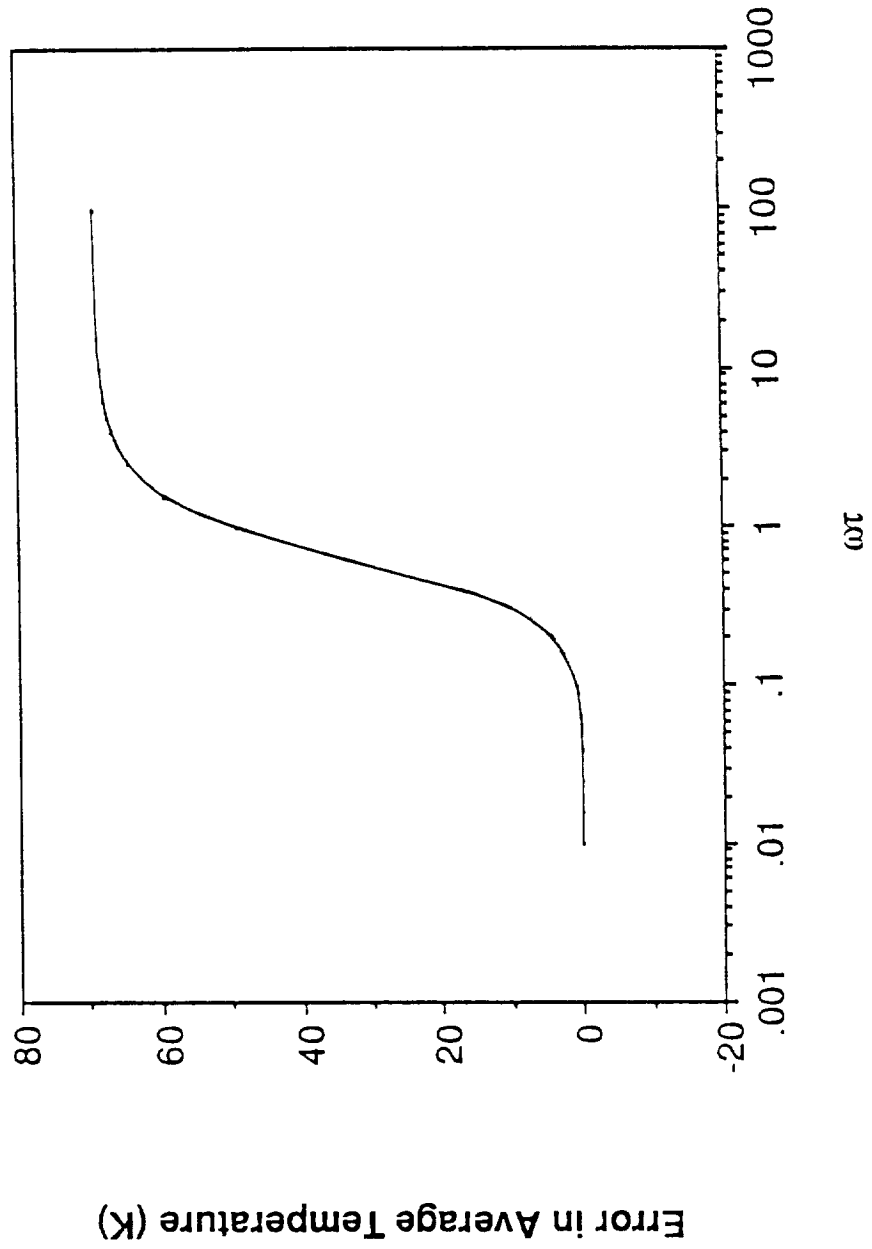
207

Figure 14(a) The error in the average temperature indicated by a two-color pyrometer for an object with a sinusoidally varying temperature as a function of the frequency of the sinusoid
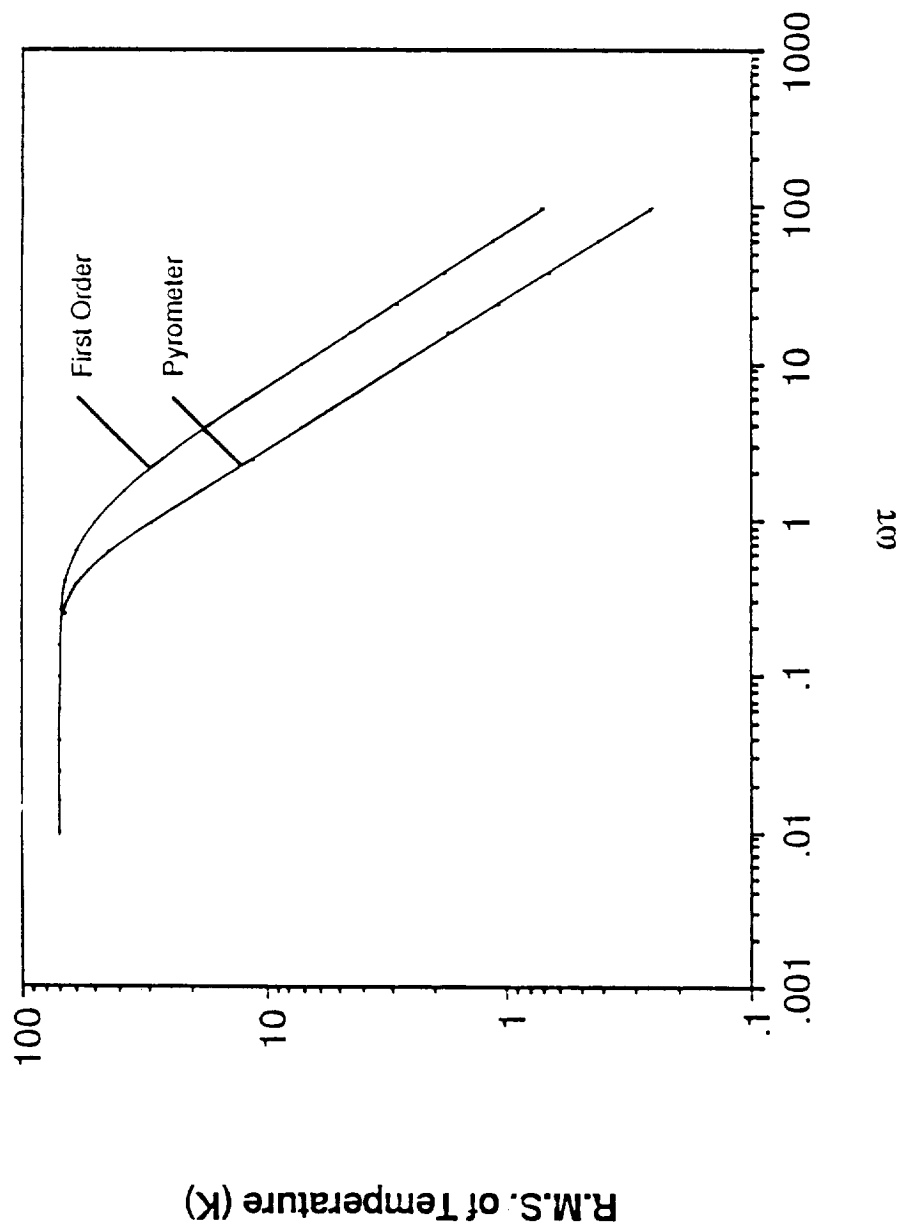
R.M.S. of Temperature (K)

First Order

Pyrometer

$\omega\tau$

Figure 14(b) A comparison of the root-mean-square amplitude of the measured temperature for a linear system and a two-color pyrometer for an object with a sinusoidally varying temperature as a function of the frequency of the sinusoid. The amplitude of the actual temperature does not change with frequency.

The effect of different τ's for the two detectors has also been investigated, and it was found that differences of up to three percent produce relatively minor perturbations and can be neglected.

The response time of a two-color system must be at least 100 times faster than the expected response time of the object being measured to ensure that reasonably accurate measurements are being made. Rapid temperature increases, which are often the features of interest, are measured quite readily by a slow two-color pyrometer. But measurement of temperature fluctuations will show gross errors if the system response is not fast enough. Because the trends are the result of nonlinearities between i and T and of the fact that the ratio of two signals responds much differently than do its constituent signals, these trends hold for systems with other than ideal first-order responses. They are also independent of whether the temperature calculation is performed by analog circuitry or digitally in a computer. For signal-processing applications, the log of the intensity and not the raw intensity data should be used.

Summary

The most common sources of error in optical pyrometry have been examined. They can be classified as either noise and uncertainty errors, stray radiation errors, or speed-of-response errors. Through judicious choice of detectors and optical wavelengths the effect of noise errors can be minimized, but one should strive to determine as many of the system properties as possible. Careful

consideration of the optical-collection system can minimize stray-radiation errors. Careful consideration must also be given to the slowest elements in a pyrometer when measuring rapid phenomena.

REFERENCES

1. R. Siegel and J.R. Howell, Thermal Radiation Heat Transfer, McGraw-Hill, New York, pp. 18-23 (1967).

2. R.E. Spjut, E. Bar-Ziv, A.F. Sarofim, and J.P. Longwell, "Electrodynamic Thermogravimetric Analyzer," Rev. Sci. Inst. **57** 1604-1610 (1986).

3. R.E. Mitchell and W.J. McLean, "On the Temperature and Reaction Rate of Burning Pulverized Fuels," in Nineteenth Symposium (International) on Combustion/The Combustion Institute, 1113-1122 (1982).

4. G.B. Hunter, C.D. Allemand, T.W. Eagar, "An improved method of multi-wavelength pyrometry", SPIE **520** Thermosense VII (1984)

5. R.E. Spjut, P.P. Bolsaitis, "Three Channel Optical Temperature Measurement of Laser-Heated Reacting Particles," in Proceedings of Symposium O, Materials Processing in the Reduced Gravity Environment of Space, **87**, Materials Research Society (1987).

6. D. Froelich, "Etude Experimentale et modelisation de la Combustion d'un Grain de Charbon," Doctoral thesis, Universite de Haute Aslace, Feb. 1985.

7. R.E.Spjut, "Transient response of one-and two-color optical pyrometry systems" Opt. Eng. **26** 467-472 (1987)

I

8. G.M. Foley, "Modification of Emissivity Response of Two-Color Pyrometers," High-Temperatures - High Pressures, 10, 391-398 (1978).

9. R.E. Bedford and M.C. Keung, "Effect of Uncertainties in Detector Responsivity on Thermodynamic Temperatures Measured with an Optical Pyrometer," High-Temperatures - High Pressures, 15, 119-130 (1983).

FAST OPTICAL PYROMETRY

Ared Cezairliyan
Thermophysics Division
National Bureau of Standards
Gaithersburg, Maryland 20899

Abstract

Design and operation of accurate millisecond and microsecond resolution optical pyrometers developed at the National Bureau of Standards during the last two decades are described. Results of tests are presented and estimates of uncertainties in temperature measurements are given. Calibration methods are discussed and examples of applications of fast pyrometry are given. Ongoing research in developing fast multiwavelength and spatial scanning pyrometers are summarized.

1. Introduction

Increasing interest in high-speed studies of high-temperature phenomena and the utilization of dynamic techniques for the measurement of properties of substances at high temperatures has necessitated the development of temperature measurement methods having high time resolution. The definite advantages of noncontact methods in high temperature measurements suggest the selection of optical methods in developing fast high temperature measuring systems.

Various optical methods developed in the past for fast pyrometry are reviewed in the literature [1,2]. Almost all the developments prior to 1970 have been of an exploratory nature. During the last two decades, advances in the field of electronics in general and in fast digital data acquisition systems in particular, coupled with interest in studies of high temperature phenomena, enabled the recent developments of accurate fast pyrometry.

In the present paper, pioneering developments of accurate fast pyrometry at the National Bureau of Standards (NBS) during the last two decades are presented. A summary of the areas of developments and ongoing research on fast pyrometry at NBS is given in Table 1.

Table 1. Fast Pyrometry at NBS

Target \ Wavelength (μm)	One (0.65)	Two (0.65,0.9)	Six (0.5,0.6,0.65, 0.7, 0.8, 0.9)
Single	Millisecond Resolution	Microsecond Resolution	Millisecond Resolution
Multiple (1024)	Millisecond Resolution		

2. Millisecond-Resolution Pyrometer

The first accurate millisecond-resolution pyrometer was developed by Foley [3] in connection with research on the measurement of high temperature properties of solids by dynamic techniques. The dynamic techniques consist essentially of rapid resistive self-heating of the specimen by the passage of an electric current pulse through it and, with millisecond resolution, measuring the pertinent experimental quantities, such as current through the specimen, potential across the specimen and the specimen temperature. Accurate data on selected thermophysical properties (heat capacity, electrical resistivity, hemispherical total emittance, melting temperature, thermal expansion, temperature and energy of solid-solid phase transformations) were obtained by these techniques up to the melting temperature of refractory solids, primarily metals. A summary of the results is given in the literature [4].

2.1. Salient Features

The salient features of the millisecond-resolution pyrometer [3] are:

1. The pyrometer operates near 0.65 μm. The detector (photomultiplier) is alternately exposed to radiation from the unknown source and to radiation from a reference source. This scheme eliminates errors caused by detector instability and/or drift.

2. The exposure to each source is of the same duration (0.2 ms) and the exposures are uniformly spaced in time.

3. The same detector and associated electronics are used to evaluate every exposure, whether to the unknown or to the reference.

4. Each unknown is evaluated with respect to a member of a "staircase" of three exposures to a reference. A rotating sectored attenuator produces the "staircase", in which successive attenuation ratios are roughly equal.

5. The output signals are recorded with a digital data acquisition system which has a full-scale resolution of about one part in 8000.

6. The pyrometer can measure the temperature of an unknwon source every 0.833 ms. (1200 measurements of temperature per second).

2.2. Optical System

A schematic diagram of the optical system of the millisecond-resolution pyrometer is shown in Fig. 1.

The unknown target X is focused by objective Ox onto a circular field stop Fx. The portion which passes the field stop is collimated by lens Mx1, and the aperture of the system is fixed by the circular stop Ax. A magnified image of the field stop is formed by Mx2, through right angle prism P, in the plane of the rotating shutter disk DS. When the shutter is open, the radiation passes on through interference filter IF to the photomultiplier PC. The pyrometer range may be extended upwards by inserting neutral density filters in the collimated beam between lenses Mx1 and Mx2.

Radiation from the steady reference source R is focused by objective Or on field stop Fr, is collimated by Mr1, and the aperture is limited by Ar. The collimated reference radiation then passes through the rotating attenuator disk DA, mounted on the opposite end of the motor shaft from the shutter disk DS. The image of Fr is focused in the plane of the shutter disk by Mr2. The reference radiation falls on the same circular area of the photocathode, when the shutter is open to the reference source, as does the radiation from the unknown source when the shutter is open to the latter.

The two pairs of stops (Fx-Fr and Ax-Ar) and the two pairs of lenses (Mx1-Mr1 and Mx2-Mr2) are all as nearly alike as possible. So that the two optical channels are substantially identical, except that the unknown channel contains prism P and the reference channel contains the attenuator disk DA. The differences in the optical channels are accounted for during calibration.

The metal attenuator disk DA has three pairs of sectors around its circumference. One pair of sectors is cut away so that light passes freely. Another pair of sectors is perforated in a pattern of small square holes, so as to transmit somewhat less than 50% of the radiation which falls on the sector. A third pair of sectors is similarly perforated with smaller holes, so as to transmit somewhat less than 25%. The number of holes is made very large, so that any fluctuation in transmission during the rotation of the disk because of the finite number of holes is negligible by comparison with the noise due to the finite number of photons in each sample. The effective transmittance of the attenuator is determined experimentally in a calibration procedure, accounting for any diffraction effects which occur. As the disk rotates, the reference illumination thus changes in three steps
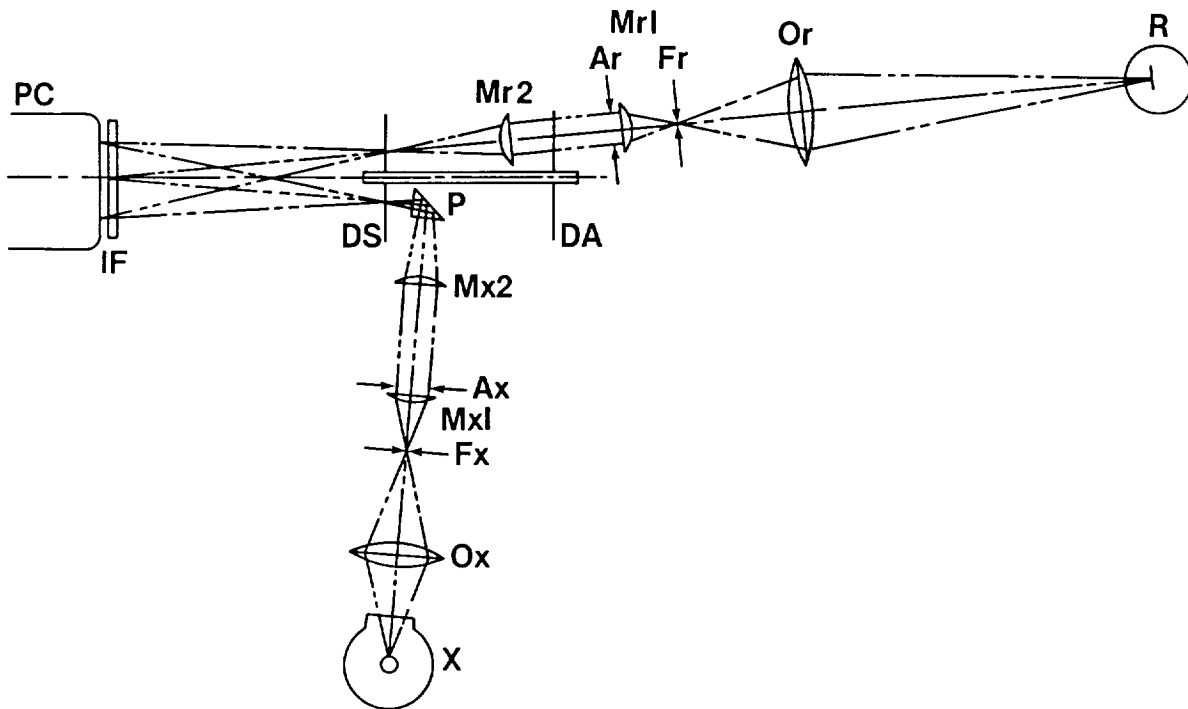
Figure 1. Schematic diagram of the optical system of the
millisecond-resolution pyrometer.

during each half-revolution. A film of transparent resin covers the
perforated areas to prevent dirt from changing the effective size of the
openings.

The shutter disk has six large apertures each subtending 15° at the
center of the disk. It and the attenuator disk are rotated at 200 rps by a
synchronous motor. The shutter disk opens the reference radiation path for
208 μs, then closes for 208 μs, then opens the unknown radiation path for
208 μs, closes for 208 μs, and then opens the reference path again. The
reference pulses form two "staircases" per revolution of the sampling motor;
the unknown pulses are interlaced with the reference pulses. The shutter
disk also has a circle of timing apertures, which is used to generate
photoelectrically the pulses to control the electronic system.

The optical system was designed to view a target circle 0.2 mm in
diameter on the unknown from a distance of 10 cm. The nominal wavelength
passed by the interference filter is 0.65 μm, and the nominal bandwidth of
the filter is 0.01 μm.

2.3. Electronic System

The radiation detector is an end-on type photomultiplier with S-20 cathode, mounted so as to reduce microphonism and to minimize the influence of magnetic fields. The photomultiplier anode is connected directly to the summing junction of an operational amplifier, which in turn feeds an integrator. The integrating capacitor is shunted by a silicon diode, connected so that it is reverse biased when photocurrent flows. 2×10^{-8} C from the photomultiplier anode will charge the integrator to its maximum value of 10 V.

A synchronization and control system accepts the timing signals from the pyrometer and separates them into two pulse streams, one containing the synchronizing pulses which occur per revolution of the sampling motor, and the other containing 12 start pulses per revolution. The start pulses trigger the digitization of the integrator voltage, and each generates a delayed pulse to reset the integrator after an appropriate time. The synchronization pulse, once per revolution, is used to store the data in orderly fashion for delayed processing by a computer.

The signals from the pyrometer electronics are recorded with a digital data acquisition system which has a full-scale resolution of about one part in 8000 (2^{13})

2.4. Calibration

A calibration is first made under steady-state conditions to determine parameters inherent to the pyrometer, by comparing the radiation of the standard lamp to that of an equivalent reference lamp. These parameters are then used in the determination to compare the reference lamp radiation with the specimen radiation under conditions of rapidly changing temperature. The Wien radiation equation, modified for use with this pyrometer, serves as the transfer mechanism. The steady-state calibrations utilizing the gas-filled tungsten-strip lamps are for temperatures up to about 2500 K, the limit of reliable operation for such lamps. For measurements at higher temperatures, calibrated optical attenuators are placed in the path of the radiation from the specimen.

2.5. Performance

The sources and magnitudes of uncertainties in temperature measurements with the millisecond-resolution pyrometer are discussed in detail in the literature [5] and are summarized in Table 2. It may be concluded that the uncertainty in temperature measurements is approximately 3 K at 2000 K and 6 K at 3000 K. It should be noted that factors such as departure from ideal blackbody conditions and temperature nonuniformity of the specimen are not included in the above figures. The resolution or sensitivity of the pyrometer defined as the standard deviation (of an individual point) from the mean of a large number of temperature measurements is 2 K at 1200 K, 0.6 K at 1500 K and about 0.3 K at 2000 K.

Table 2. Estimated Uncertainties in Temperature Measurements
with the Millisecond-Resolution Pyrometer [3,5].

Source of Error	Uncertainty, K	
	at 2000 K	at 3000 K
Standard Lamp Calibration	2	4
Instability of Standard Lamp	0.5	1
Radiation Source Alignment	1	2
Pyrometer Calibration Instability	1	2
Scattered Light Correction	0.5	1
Attenuator Calibration	1	2
Window Effects	1	2
Total Uncertainty in Temperature*	3	6

*Root sum square of above items rounded to the higher single significant figure.

2.6. Example of Operation

The millisecond-resolution pyrometer has been successfully used for the determination of selected thermophysical properties of solids at high temperatures utilizing a pulse heating technique [4]. As an example, measurement of the melting temperature of niobium [6] is shown in Fig. 2. The specimen was a tube of the following nominal dimensions: length, 102 mm; outside diameter, 6.3 mm; thickness, 0.5 mm. A small rectangular hole (0.5 x 1 mm) fabricated in the wall at the middle of the specimen approximated blackbody conditions for temperature measurements.
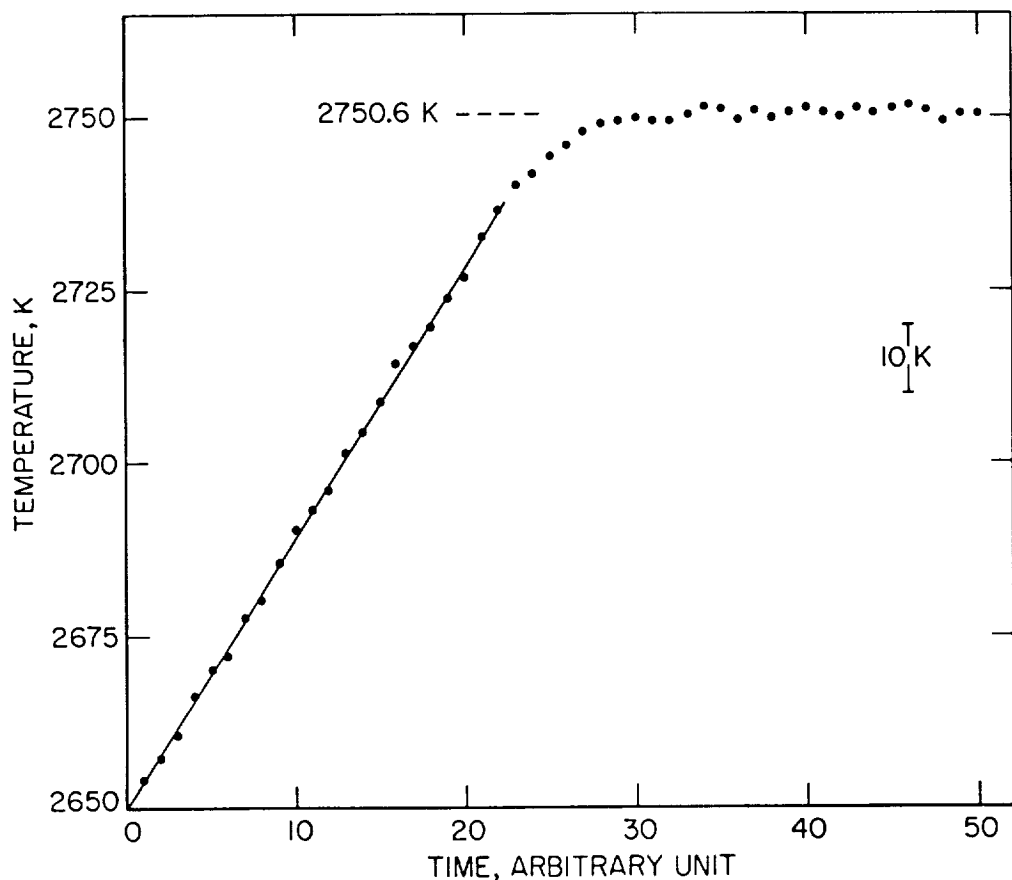
Figure 2. Temperature of a heating niobium specimen as a
function of time near and at the melting point
measured with the millisecond-resolution pyrometer.
The plateau in temperature indicates melting of niobium
(1 time unit = 0.833 ms).

3. Microsecond-Resolution Pyrometer

An accurate microsecond-resolution pyrometer was developed at the
National Bureau of Standards by Foley et al. [7] in connection with research
to extend the measurement of properties of substances far beyond their
melting temperatures and up to 6000 K. The unfavorable conditions
associated with very high temperatures, such as increases in heat loss,
chemical reactions, evaporation, etc., have brought forward an entirely new
set of experimental problems, which necessitated the development of
ultra-fast measurement techniques. The microsecond-resolution dynamic
technique, incorporates the pyrometer developed by Foley et al. [7], is
described in the literature [8]. Application of this technique to
measurements of heat of fusion and properties of liquid metals at high
temperatures is presented elsewhere [9].

3.1. Salient Features

The salient features of the microsecond-resolution pyrometer [7] are:

1. The pyrometer is sufficiently fast and precise to justify the recording of its signals by a digital data acquisition system at regular intervals as short as 1.5 μs with a resolution of 0.1 percent.

2. The pyrometer measures radiance temperatures in two narrow spectral regions, 0.65 μm and 0.9 μm.

3. In order to minimize the effect of electromagnetic interference, the electronics of the pyrometer are entirely outside the shielding of the room in which dynamic experiments are conducted. Radiation selected by the optics in each of the two spectral regions is transmitted by fiber optic cables through the shielding walls to the detectors and their associated electronic circuits.

4. The pyrometer uses high-speed automatic gain switching of linear amplifiers to achieve high stability, high resolution and wide temperature range.

3.2. Optical System

Figure 3 shows the optical arrangement of the pyrometer. An objective lens O forms two images of the target T at the field stops S1 and S2 by means of the beam splitter B. Filter F1 passes radiation near 0.65 μm to S2; each filter has a bandwidth of 0.03 μm. This design permits the two field stops to be focussed independently to minimize the effects of chromatic aberration. The field stops are 0.5 mm diameter and the magnification is unity, so the target is the same size. The radiation passing through each field stop falls on the end of one of two fiber optic cables, C1 or C2, for transmission to silicon diode photodetectors. The stops are so close to the ends of the cables that the stops, and not the cables, define the target areas. A mirror M can be swung into the path between objective lens and beam splitter to form the image of the target at a reticle R. The experimenter aims and focuses the instrument by viewing the reticle and target image through a microscope.

3.3. Electronic System

The silicon diode detectors used were specially chosen for good stability and linearity. The photocurrents are converted to voltages and amplified by a series of operational amplifiers. The analog output of each amplifier channel is applied to a 10-bit high-speed analog-to-digital converter (ADC). Other ADCs digitize voltages proportional to the heating current and to the voltage drop in the specimen. Another signal which gives the ranges of the pyrometer channels is also digitized. Various digitizing intervals from 1.5 to 512 μs may be chosen. 1024 10-bit words of digital data may be stored from each of five data channels in a semiconductor memory.
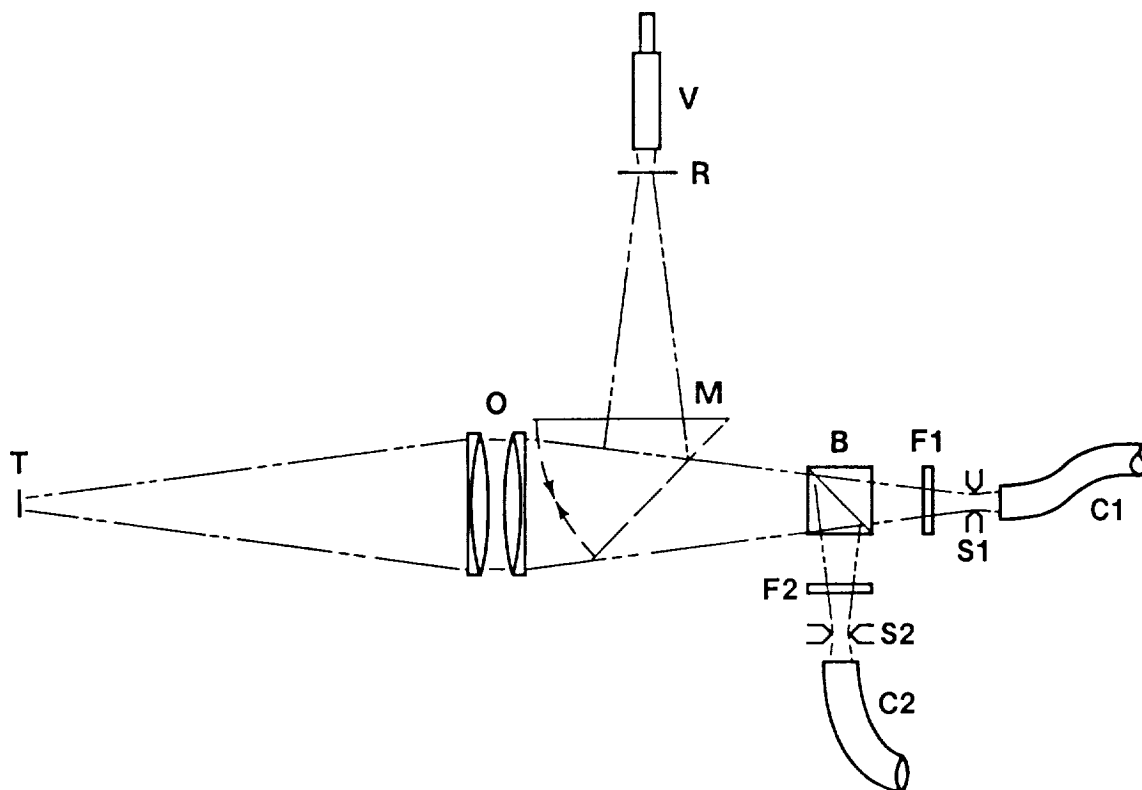
Figure 3. Schematic diagram of the optical system of the
two-color microsecond-resolution pyrometer.

The digital recording system limits the temperature resolution of the
pyrometer. If the photocurrents were amplified at fixed gain before
digitization, there would be adequate resolution, as compared with the
precision and accuracy, at the upper end of any selected temperature range,
but not enough at lower temperatures, even when the specimen emitted
sufficient energy for accurate pyrometry. Logarithmic amplifiers
theoretically would give wide range and acceptably uniform resolution. In
tests, however, several high-speed logarithmic amplifiers drifted so rapidly
that the results of steady state calibrations could not be used to interpret
the data from experiments which were performed only a few minutes before or
after the calibration.

The pyrometer uses linear amplifiers with high-speed automatic gain
switching. The output of each channel is switched through as many as three
overlapping ranges. This procedure uses fast, stable components, and
results in a response which approximates the logarithm of the input.
Changes in amplifier gain are completely negligible. The precision is
limited by short term zero drift which on the most sensitive (lowest
temperature) range is less then 0.05% over an hour. The useful range of the
amplifier extends over more than 3 decades of photo-current. Figure 4 is a
block diagram of the analog electronics of each channel.
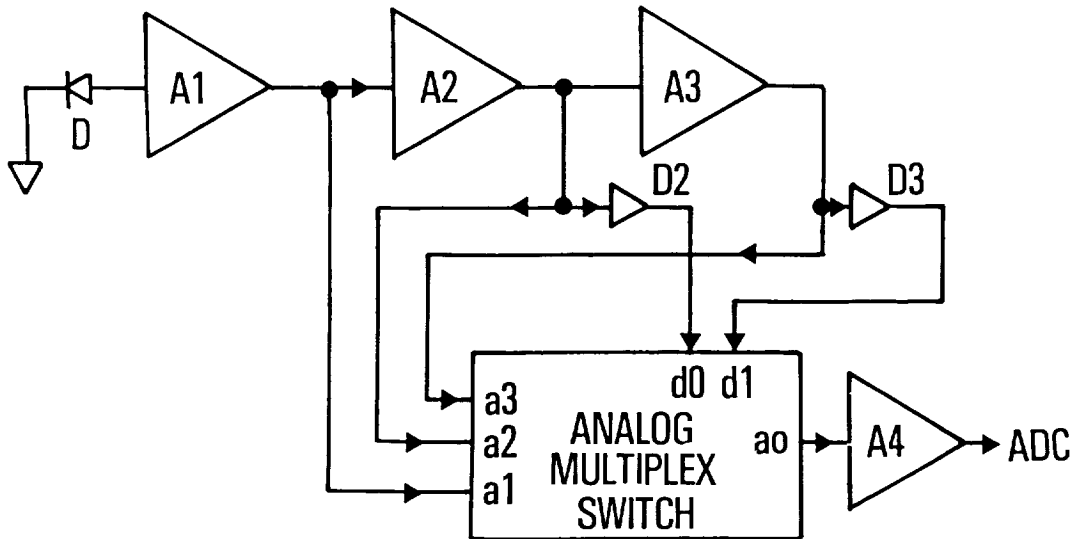
Figure 4. Block diagram of the analog electronics of each channel of the two-color microsecond-resolution pyrometer.

The output voltages of amplifiers A2 and A3 are compared with an 8 volt reference. If an amplifier output voltage exceeds the reference, that stage is switched out of the amplifier chain to reduce the gain; if it falls below the reference, the stage is switched in again, increasing the gain. The transresistance of amplifier A1 in each channel is 30,000 V/A and the gain of each amplifier A2 and A3 is 11. Switching from low to midrange occurs when the photocurrent rises above 2.2 μA, and from midrange to high range at a photocurrent of 24 μA. The maximum output on the high temperature range is reached at a photocurrent of 0.37 mA. The corresponding radiance temperature ranges are:

Range	0.65 μm Channel	0.9 μm Channel
Low	1960 - 2520 K	1545 - 2030 K
Mid	2500 - 3460 K	2015 - 2920 K
High	3430 - 5700 K	2885 - 5500 K

3.4. Calibration

A gas-filled tungsten-strip lamp was calibrated by the Radiometric Physics Division of the National Bureau of Standards. The calibrations covered the range 1873-2573 K at 0.65 μm and the range 1800-2425 K at 0.9 μm. The pyrometer was used to record the radiance from the calibrated lamp at eight values of filament current identical with those specified on

the certificate of calibration. Each measure of response, together with an appropriate measure of dark response was used to determine the calibration constant. These values were used in turn to calculate a weighted mean for each channel, using the measured response as the weighting factor. The weighted means for the calibration constant were than used to attribute spectral radiance temperatures to the lamp. The differences between the calibration values and the measurements lay between 0.1 to 2.0 K for the 0.65 μm channel and between 0.1 and 0.6 K for the 0.9 μm channel for each of eight spectral radiances.

3.5. Performance

The sources and magnitudes of uncertainties in temperature measurements with the microsecond-resolution pyrometer are discussed in detail in the literature [7] and are summarized in Table 3. The table gives the estimate of uncertainty in spectral radiance as a percentage of the radiance for the temperature and channel involved. The square root of the sum of the squares of the various individual uncertainties is taken to be the probable uncertainty of spectral radiance for the pyrometric system as a whole, and this number is converted to an uncertainty in temperature. To summarize the uncertainty in temperature measurements, data are given for the low and high end of each range in each channel. Since the temperature ranges of the two channels are different, twelve estimates are given for seven different temperatures, six of the estimates referring to each of the two channels.

3.6. Example of Operation

To demonstrate the measurement of temperature under dynamic conditions, a niobium rod, 25 mm long and 1.6 mm diameter, was heated rapidly with the use of the capacitor discharge system described elsewhere [8]. The results of the radiance temperature measurement by the pyrometer are shown in Fig. 5. The plateaus in the temperature plot show the melting of the niobium. It can be seen that the pyrometer followed the entire melting, and continued to show reasonable values of spectral radiance temperature for several hundred degrees into the liquid phase.

The entire time, from room temperature to near 3500 K, was only 100 μs. Melting of the niobium took place in about 15 μs. The average radiance temperatures measured at the melting point of niobium are 2431 K at 0.65 μm and 2250 K at 0.9 μm. The difference in the radiance temperatures at the two wavelengths is due to the difference in normal spectral emittance of the metal at the two wavelengths.

4. Multiwavelength Pyrometer

Recently, a fast multiwavelength (six-channel) pyrometer was designed and constructed at the National Bureau of Standards by Foley et al. [10]. The pyrometer is intended to be used for: (1) simultaneous determination of the radiance temperature of metals at their melting points at several wavelengths as possible temperature reference points and (2) exploration of the possibility of improving the determination of true temperature from measurement of the spectral radiance temperature of incandescent objects in a number of spectral bands.

Table 3. Estimated Radiance Uncertainties[*] of Two-Color Microsecond Pyrometer

0.65 μm Channel

	Low Range		Mid Range		High Range	
Temperature, K	2000	2500	2500	3450	3450	5500
Secondary Standard, %	0.7	1.0	1.0	1.0	1.0	1.0
Acceptance Angle, %	0.4	0.4	0.4	0.4	0.4	0.4
Effective Wavelength, %	0	0	0	0	0	0
Amplifier Drift, %	0.01	0.02	0.01	0.02	0.01	0.02
Nonlinearity, %	0	0	0	0.2	0.2	2.0
Total Noise, %	2.5	0.5	0.2	0	0	0
Quantization, %	1.0	0.2	1.0	0.2	1.0	0.2
Transfer, %	2.7	0.5	0.5	0.5	0.5	0.5
Root Mean Square, %[**]	3.9	1.3	1.6	1.2	1.6	2.3
Uncertainty, K[***]	7.1	3.7	4.4	6.2	9.9	32

0.9 μm Channel

	Low Range		Mid Range		High Range	
Temperature, K	1550	2025	2025	2900	2900	5500
Secondary Standard,%	1.0	1.1	1.1	1.1	1.1	1.1
Acceptance Angle, %	0.4	0.4	0.4	0.4	0.4	0.4
Effective Wavelength, %	0.1	0.1	0.1	0.1	0.1	0.1
Amplifier Drift, %	0.01	0.02	0.01	0.02	0.01	0.02
Nonlinearity, %	0	0	0	0.2	0.2	2.0
Total Noise, %	2.5	0.5	0.2	0	0	0
Quantization, %	1.0	0.2	1.0	0.2	1.0	0.2
Transfer, %	2.7	0.5	0.5	0.5	0.5	0.5
Root Mean Square, %[**]	4.0	1.4	1.6	1.3	1.6	2.4
Uncertainty K[***]	6.0	3.6	4.2	6.9	8.6	19

[*] Estimates of uncertainties are expressed as a percentage of radiance for a given temperature and channel.

[**] Root mean square of the listed individual uncertainties.

[***] Root mean square uncertainty expressed in temperature.
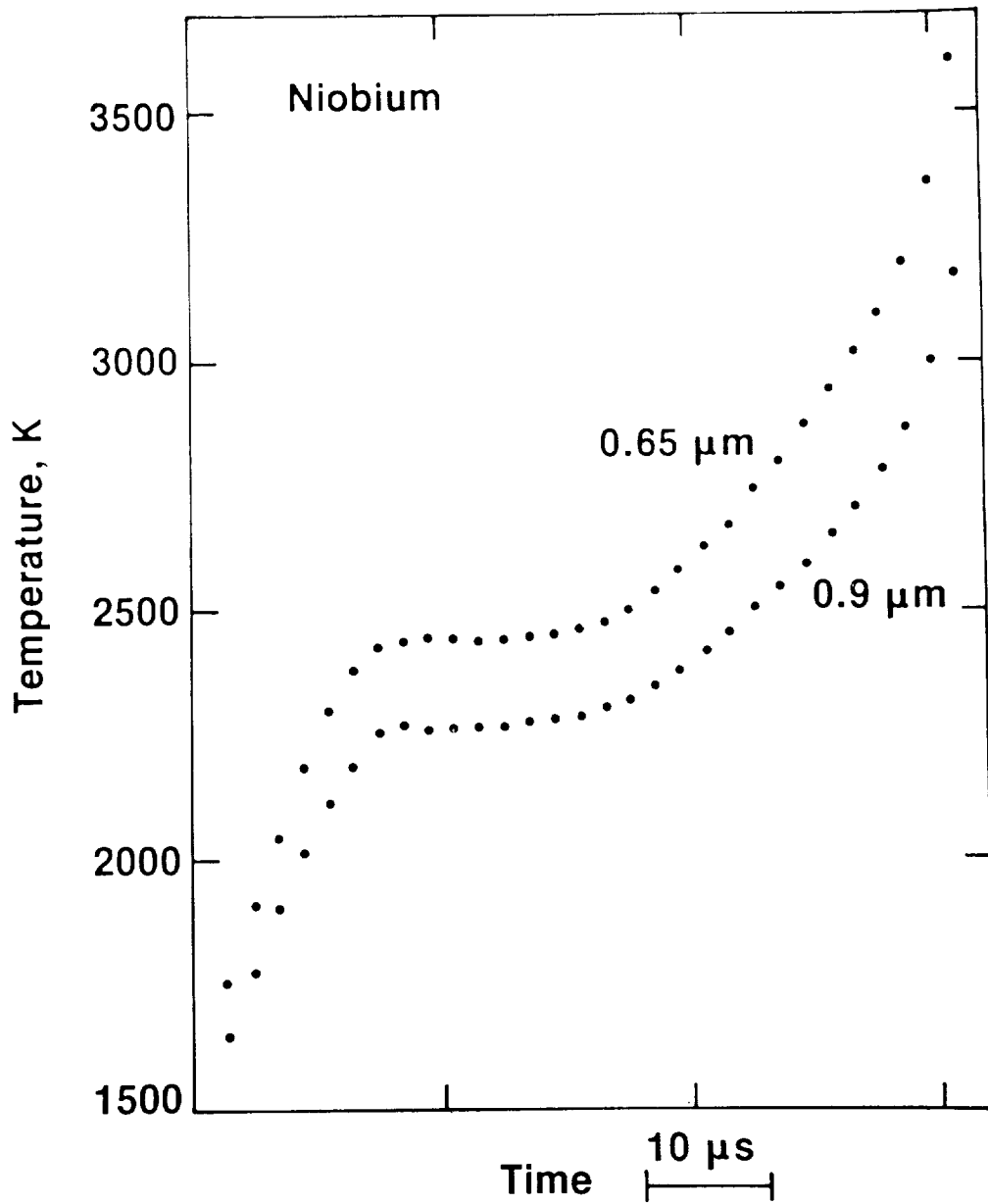
Figure 5. Radiance temperature of a rapidly heating
niobium specimen measured with the two-color
microsecond-resolution pyrometer. Plateaus in
temperature indicate melting of niobium. Data
on the right of the plateaus are for liquid
niobium.

4.1. Salient Features

The salient features of the multiwavelength pyrometer [10] are:

1. The pyrometer measures spectral radiance temperature above 1500 K.

2. The pyrometer has six channels. Five of the channels have a spectral bandwidth of about 0.1 μm, centered near 0.5, 0.6, 0.7, 0.8, and 0.9 μm. The sixth channel has a bandwidth of 0.03 μm centered at 0.65 μm.

3. The pyrometer can make a set of six measurements every 0.1 ms.

4. The pyrometer has two modes of operation. In the first mode, signals from all the channels are digitized and recorded simultaneously. In the second mode, the channels are multiplexed and thus signal from one channel is recorded at a given time.

4.2. Optical System

An objective lens of unity magnification, made up of a pair of identical achromats, focusses the radiation from the target on a single field stop, defining a circular target area of 0.5 mm in diameter. A mirror can be swung into the path between the objective lens and the field stop to form an image of the target on a reticle. The optical path length from objective to reticle is adjusted to equal that from objective to field stop. For aiming and focussing, a microscope is used to view a 0.5 mm circle drawn on the reticle.

The light passing the field stop illuminates a fiber optic bundle. The latter is divided, nominally at random, into six separate bundles which illuminate six interference filters and silicon diode detectors. The ends of the fiber bundles are placed as close as possible to the detectors in an effort to maximize efficiency, but the fibers cannot be allowed to come too close to the filters, nor the filters to the detector windows, lest optical interference effects distort the spectral response.

4.3. Electronic System

High-stability amplifiers convert the photocurrents from the diodes to proportionate voltages, which are switched sequentially through a semi-conductor multiplexor to feed a line-driver amplifier. Each conversion amplifier has three different manually selected feedback resistors to give "low", "medium" and "high" temperature ranges. The low temperature range feedback resistors were originally intended to give an output voltage of 0.4 V from each of the amplifiers when the spectral radiance temperature was 2000 K. This called for the resistors to differ from one another by as much as sixteen times because of the variation in spectral radiance of the source and in sensitivity of the detectors over the spectral range of the pyrometer channels. The medium temperature range resistors were intended to give 0.4 V at 2700 K and the high temperature range resistors to give 0.4 V at

4500 K. Experimental results with the completed pyrometer caused us to alter the values of some of the low range resistors. To maximize stability the largest resistors are 7 megohms.

4.4. Calibration

The channel centered near 0.65 μm with 0.03 μm bandwidth, was calibrated by averaging 100 successive values of output voltage when viewing the filament of a calibrated gas-filled tungsten strip lamp, and subtracting the mean of 100 successive values of output voltage when dark. The calibration was made at or near each of six or seven values of lamp current specified on the certificate of calibration. The calibration constant is the output voltage divided by the value of the integral, taken over the spectral band, of the pyrometer transmission times the window transmission times the Planck function at the radiance temperature given on the certificate. It should, of course, be the same for every temperature, but in fact noise and other errors give different values for each of the lamp currents. The calibration procedure is considered satisfactory if the variation among the values for the constant is small and is not systematic. For later determination of an unknown temperature we use the mean of the calibration constants, weighted by the pyrometer voltage. This gives greater weight to the higher temperature points where noise has less effect on the result.

The calibration of the 0.65 μm channel was transferred to the other channels in a dynamic experiment. The source was a graphite cylinder 6.4 mm diameter and 100 mm long, clamped to have an effective length of 45 mm., with a rectangular hole 1.6 mm high and 1 mm near the center of the length of the 1 mm thick wall. This tube was heated in argon by a pulse of direct current from large lead acid storage cells. The pyrometer viewed the radiation emitted from the hole at an angle of about 10 degrees from radial during the heating period. The blackbody quality of this specimen is calculated to be 0.994. The recording of the pyrometer output was begun before the heating current pulse was turned on, so that the dark response of all the channels was recorded and an average calculated for subtraction from the values recorded from the hot specimen. At intervals during the heating pulse, the measured output from the calibrated 0.65 μm channel was interpreted to find the radiance temperature at that wavelength. This was assumed to be the true temperature, and this "true" temperature was used with the data from all six channels to determine, by the same method of numerical integration as described above in connection with the calibration using the tungsten strip lamp, a calibration constant for each channel. A weighted average of these calibration constants was then calculated for each channel.

4.5. Performance

The multiwavelength pyrometer has just become operational, thus no significant amount of data have been obtained to assess its operation, the uncertainty of radiance temperature measurements, and its ability to yield true temperature from measured radiance temperatures. At present, work is in progress to test the pyrometer.

4.6. Example of operation

Preliminary measurements of the radiance temperature of niobium at its melting point were performed with the multiwavelength pyrometer. A total of ten experiments were conducted where niobium specimens were melted by utilizing a transient resistive self-heating technique in short times (less than 1 s). Measured radiance temperatures at a given wavelength were all within ±2 K of the average for that wavelength. The average radiance temperatures as a function of wavelength at the melting point of niobium are shown in Fig. 6.

5. Spatial Scanning Pyrometer

Recently, a fast spatial scanning pyrometer was designed at the National Bureau of Standards. Construction of this pyrometer has begun. The scanning pyrometer is a monochromatic optical pyrometer using a self-scanning linear array of silicon photodiodes as a detector. It will rapidly measure the spectral radiance temperature at 1024 points along a straight line in the target field. This will permit measurements of temperature gradients in a rapidly heating specimen providing data for both diagnostic purposes and determining thermal diffusivity which will be a novel approach suitable for measurements at very high temperatures.
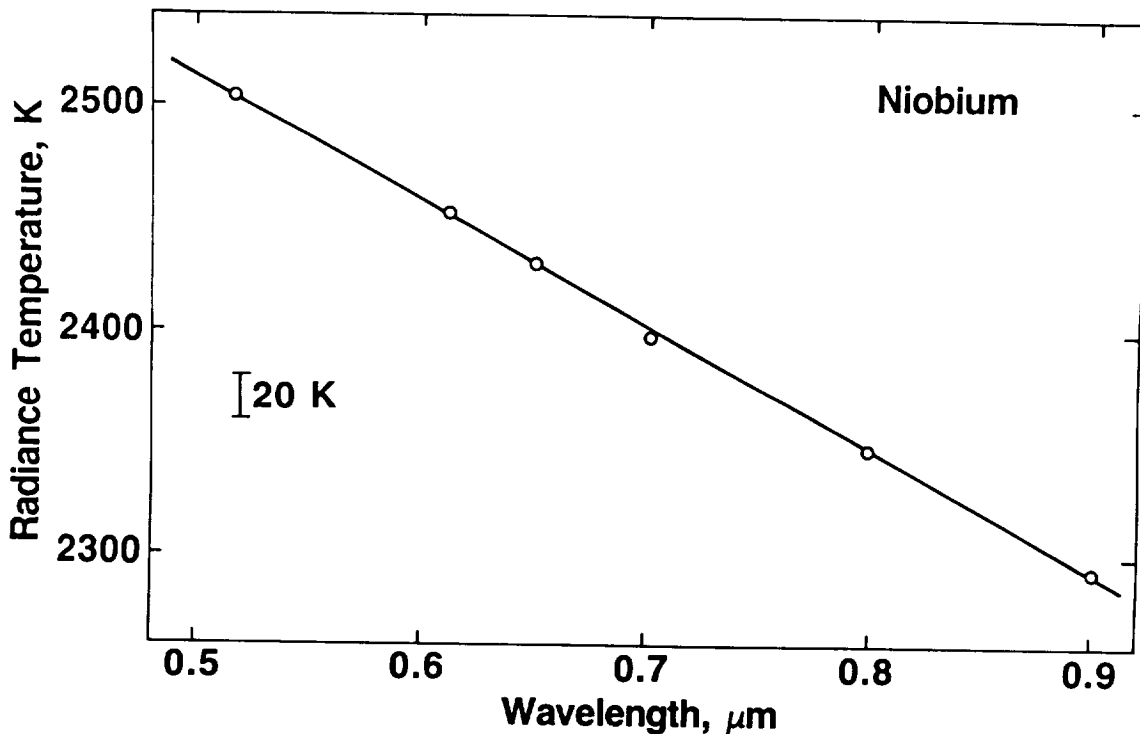
Figure 6. Radiance temperature of niobium at its melting point as a function of wavelength measured with the millisecond-resolution multiwavelength pyrometer.

229

5.1. Salient Features

The salient features of the spatial scanning pyrometer are:

1. The pyrometer will measure spectral radiance temperature at 1024 points along a straight line (25 mm long).

2. A complete cycle of measurements (1024 points) will be performed in about 1 ms.

3. The radiance temperature measurements will be performed at 0.65 μm (bandwidth: 0.03 μm).

5.2. Optical System

The basic optical design is a further modification of that used in the multiwavelength pyrometer. The design provides an unobstructed path slightly smaller than 50 mm in diameter from the back of the objective lens to the pyrometer faceplate. The objective lenses are made from a pair of standard achromats 52 mm in diameter, and 200 mm nominal focal length. The interference filter to establish the effective wavelength of the pyrometer is mounted as close as possible to the diode array. The peak of the interference filter is at around 0.65 μm, and the bandwidth is about 0.03 μm. A circular mirror is mounted on a platform hinged near the partition carrying the diode array so that it can swing down and intercept all of the light from the lens and direct it to a focus on a reticle carrying a scale 20 mm long graduated in tenths of a millimeter. A suitable eye-lens gives a reasonably magnified view of the whole scale.

5.3. Electronic System

The self-scanning array contains 1024 diodes with a center-to-center spacing of 25 μm and so is about 25 mm long. Each diode of the array is nominally 15 μm long and 26 μm wide. It is presently planned to use the array with a lens system having unity magnification so that the target region will be about 25 mm.

Each photodiode of the array has associated with it a shunt capacitance. One end of the diode-capacitor pair is connected to the positive end of the power supply and the other end is connected through an FET switch to a common video recharge line. The switch is closed briefly by a "start" pulse passing down a 1024 stage shift register being connected to each of the 1024 switches associated with the photodiodes. When the photodiode switch first closes another FET switch closes to connect the common video recharge line to the video buffer amplifier, which stores the voltage present on the recharge line. The video buffer FET is then opened and a recharge FET switch is closed to the negative power supply to recharge the photodiode capacitor. The "start" pulse then shifts to the next stage of the shift register, opening the photodiode switch on the preceding diode and closing the switch on the next. When the start pulse passes from the last stage of the shift register it goes to the external circuits as an End-Of-Line (EOL) signal.

The next "start" pulse is applied to the first stage of the shift register after a programmable delay of at least eight clock pulses, to connect the first photodiode and its associated capacitor to the video buffer. The voltage of the recharge line at this time is reduced below its value at the previous recharge time in proportion to the photocurrent flowing in the photodiode since the last start pulse. The voltage difference thus represents the integral of the illumination of the photodiode during the scanning period.

The signal from the buffer is summed with a signal from dummy diodes, to reduce switching noise and compensate for temperature effects, and passed to the motherboard. Here it is subjected to another sample-and-hold operation to clean up more of the switching noise and reestablish the dark level.

It seems that the linear range of the system is primarily fixed by the characteristics of the photodiode part of the array integrated circuit. Even if the photodiode capacitor is fully discharged after one scanning interval, the voltage to which the video recharge line stabilizes during sampling will be reduced by the ratio of the capacitance associated with each photodiode to the capacitance of the common video recharge line, the FET switch to the video buffer and the buffer itself. If this ratio is significantly affected by array temperature, both the sensitivity and saturation level will vary.

5.4. Status

At present, the spatial scanning pyrometer is being constructed. It is anticipated that by the end of 1987, it will be ready for testing.

6. Summary

Accurate fast pyrometers developed at the National Bureau of Standards have demonstrated the possibility of performing dynamic temperature measurements with an uncertainty of 3 K at 2000 K and 6 K at 3000 K with millisecond resolution, and 7 K at 2000 K and about 30 K at 6000 K with microsecond resolution. Recently, construction of a millisecond-resolution six-wavelength pyrometer was completed and its testing has begun. When fully operational, this pyrometer will yield important information on normal spectral emittance of surfaces and on reliablity of determining true temperature from spectral radiance temperature measurements. A new millisecond-resolution spatial scanning pyrometer is also designed which will be able to measure temperatures at 1024 points along a straight line in times of the order of 1 ms.

The fast pyrometers have already found applications in measurements of thermophysical properties at high temperatures utilizing millisecond and microsecond resolution dynamic techniques. In the future they will become important measuring and diagnostic instruments in research on time-dependent phenomena at high temperatures and related new fields in materials sciences.

7. References

1. A. Cezairliyan, "Measuring Transient High Temperatures by Optical Pyrometry", in Temperature, Vol. 4, Part 1, H.H. Plumb, ed. (Instrument Society of America, Pittsburgh, 1972) p. 657.

2. A Cezairliyan, J.F. Babelot, J. Magill, and R.W. Ohse, "Fast Radiation Thermometry", in Theory and Practice of Radiation Thermometry, D.P. DeWitt and G.D. Nutter, eds., in press.

3. G.M. Foley, Rev. Sci. Instrum., 41, 827 (1970).

4. A. Cezairliyan, Int. J. Thermophysics, 5, 177 (1984).

5. A. Cezairliyan, M.S. Morse, H.A. Berman, and C.W. Beckett, J. Res. Nat. Bur. Stand. (U.S.), 74A, 65 (1970).

6. A. Cezairliyan, High Temp.-High Press., 4, 453 (1972).

7. G.M. Foley, M.S. Morse, and A. Cezairliyan, "Two-Color Microsecond Pyrometer for 2000-6000 K" in Temperature, Vol. 5, J.F. Schooley, ed. (Am. Inst. Physics, New York, 1982) p. 447.

8. A. Cezairliyan, M.S. Morse, G.M. Foley, and N.E. Erickson, "Microsecond Resolution Pulse Heating Technique for Thermophysical Measurements at High Temperatures", in Proceedings of the Eighth Symposium on Thermophysical Properties, Vol. 2, J.V. Sengers, ed. (Am. Soc. Mech. Eng., New York, 1982) p. 45.

9. A. Cezairliyan and J.L. McClure, Int. J. Thermophysics, 8, No. 5 (1987), in press.

10. G.M. Foley and A. Cezairliyan, "Millisecond Resolution Multiwavelength Pyrometer", in preparation.

I

APRIL 30 AND MAY 1, 1987

THE ROLE OF FIBEROPTICS IN REMOTE TEMPERATURE MEASUREMENT

BY

RICCARDO VANZETTI

VANZETTI SYSTEMS, INC.
111 ISLAND STREET
STOUGHTON, MA

THE ROLE OF FIBEROPTICS IN REMOTE TEMPERATURE MEASUREMENT

Riccardo Vanzetti
Vanzetti Systems, Inc.
Stoughton, Massachusetts

INTRODUCTION

The use of optical fibers in conjunction with infrared detectors and signal processing electronics represents the latest advance in the field of noncontact temperature measurement and control. Infrared (IR) detectors have been around for many years, although R & D keeps adding to their numbers and performance characteristics.

Optical fibers are much younger and only recently have become the object of widespread interest, thanks to their ability to carry over long distances optical information signals.

Generally, IR detectors have been used in conjunction with conventional optical elements (lenses, mirrors, presumes). Fiber optics were excluded from consideration because they are made of either glass or plastics, both of which are opaque throughout most of the infrared spectral region. Thus, according to fundamental laws of physics, their marriage to infrared detectors could never work.

Defying all theoretical predictions, coupling fiber optics with infrared detectors resulted in several new families of instrumentation and control systems endowed with superior performance characteristics. How is this possible? Let us view the process step by step. For those not familiar with infrared, we shall start with the fundamentals.

INFRARED RADIATION

IR radiation, sometimes called thermal radiation, is the electromagnetic radiation occupying the spectral area between visible light and the radio microwaves (Figure 1). Infrared radiation is emitted by all physical matter, as a function of temperature and of emissivity, which is a numerical coefficient of proportionality related to the amount of electromagnetic power radiated by a blackbody at the same temperature.

Like visible light, IR radiation is made of photons carrying energy away from its source (the surface of a physical body) and traveling at the speed of light. The power emitted in this process is proportional to the fourth power of the absolute temperature of the emitting surface, as shown by Stefan-Boltzmann's equation (Figure 2):

$$W = E \sigma T^4$$

where W = radiant flux emitted per unit area (W/cm2)
      E = emissivity (unity for blackbody source)
      σ = Stefan Boltzmann constant (5.673 x 10-12 W/(cm2)(K4))
      T = absolute temperature of source (K4)

The power so emitted is of "incoherent" type, which means that the radiation takes place simultaneously at all wavelengths of the infrared spectrum. This is due to the fact that the emitting surface is made of an extremely large number of different "oscillators" (molecules, atoms and subatomic particles), which vibrate, rotate, oscillate and "jump" at their own resonant frequencies.

Intuitively, it is easy to understand why the higher temperature, the higher the infrared energy emitted by the source. Heat is directly related to the degree of molecular and submolecular motion: the more violently these physical particles move, the higher is the energy content of the photons emitted.

However, the power content of this radiation is not constant throughout the infrared spectrum, but its distribution varies as a function of wavelength and temperature. Figure 3 shows the blackbody radiation curves, that is, the distribution of infrared power emitted by an ideal surface having an emissivity factor E = 1. In the illustration, the slanted line indicates how the wavelength of the peak emission moves towards the visible region of the spectrum as the temperature of the emitting surface increases. This explains why physical matter becomes incandescent at high temperatures. Figure 4 shows the correlation between temperature and the wavelength of the peak emission.

BLACKBODY AND EMISSIVITY

It has been mentioned that the blackbody's emissivity is equal to unity. Blackbody is a term indicating an ideal surface having an infinite number of oscillators, one for each wavelength of the infrared spectrum. All the infrared radiation laws are formulated and are true for the blackbody. In practice, no such ideal body exists because every material emits infrared radiation according to its physical composition and characteristics. The degree to which this emission approximates the blackbody's emission is expressed as a fraction of unity and is called emissivity. Its symbol is E. From Stefan-Boltzmann's equation we see that once E is known, it is possible to establish a direct correlation between the power radiated by a physical surface and its temperature.

The concept of emissivity is not very easy to grasp; however, perhaps a comparison with the properties of visible light might help. Consider, for instance, an opaline electric bulb emitting white light. Set on "unity" the amount of light radiated. If the bulb is now painted in red, blue or any other color, the amount of light radiated shall be a fraction of the unity emitted when the bulb was white, could call it "emissivity," and it will always be less than unity.

In the infrared domain, the blackbody could be compared to the just-mentioned white bulb, while we could think of any other surface as emitting "infrared colors." And we should also include the color gray, with the only difference that the gray radiation covers the whole infrared spectrum (just as blackbody, only at a lower level) while the other "colors" are only covering a portion of the total infrared spectral area.

Unfortunately, often E is not known, either because it is a variable difficult to control, or simply because it is inconvenient to measure. In such instances, the ratio radiometer offers a practical solution. Its operation is based on the assumption that the incoherent radiation emitted by a nonblackbody curve in shape and wavelength with only the difference of being "dropped" to a lower level in the power scale (Figure 5).

For many surfaces, this assumption can be taken as true in first approximation. Consequently, every temperature of the target is precisely identified by a unique value of the ratio of conveniently chosen and independent from the level at which the corresponding graybody emission curve has been dropped.

Several versions of ratio radiometers have been developed, but until recently their operation was limited to the high-temperature region because of the difficulty of collecting enough radiant energy at the chosen wavelengths when using conventional optics, which necessarily have a small aperture number.

Conversely, the use of fiber optics, which have a remarkably larger aperture number, makes it possible to gather enough energy to allow measurement of much lower temperatures. At the time of this writing, approximately 200oC is the low-end temperature measurable with the most advanced fiber-optics ratio-radiometers. They are quite useful in a host of applications because they measure the temperature of a target independently from the emissivity value of its surface emissivity is not known, or when it varies during the measurement process due to changes in surface characteristics, such as oxidation and crystallization.

THE INFRARED RADIOMETER

Figure 6 is the basic block diagram of all single-channel infrared radiometric systems. The elements shown in solid lines are always present, while the ones shown in dotted lines are optional, their presence and features being dictated by the system's performance requirements. Ratio detectors and multichannel systems include additional blocks, generally of the same type.

In essence, these systems turn the infrared radiation emitted by the object located in their field of view, into an electrical signal that, after due processing and manipulation, can, in real time (1) be displayed as the temperature of the target, with the

desired degree of resolution (both thermal and spatial); (2) be recorded and/or stored in any of several existing ways; and (3) through a feedback loop, control the process to which the target is subjected, for instance heating or moving, etc. The following sections review in more detail the most important elements shown in basic block diagram.

THE OPTICS

Until recently, the optics used in infrared radiometry were of the conventional type, such as lenses and prisms. They are very similar to their corresponding elements with the visible radiation, the major difference being the optical materials of which they are made, which must have good transmissivity in the infrared spectral area.

Figure 7 shows the transmission spectral regions of a number of optical materials. These transmission regions are commonly called "windows," and their limits are indicated for a minimum of 10% external transmission and 2 mm of sample thickness.

In addition to refractive elements, such as lenses, reflective surfaces either flat or curved are frequently uses as optical elements handling IR radiation. The major advantage is their total freedom from chromatic aberration, which is a particularly serious difficulty in the infrared spectrum because the refractive index varies with wavelength, and the spectral area of interest is generally very broad.

Allowing for the infrared spectrum. This is due to the fact that the emitting surface is made of an extremely large number of different "oscillators" (molecules, atoms and subatomic particles), which vibrate, rotate, oscillate and "jump" at their own resonant frequencies.

Intuitively, it is easy to understand why the higher temperature, the higher the infrared energy emitted by the source. Heat is directly related to the degree of molecular and submolecular motion: the more violently these physical particles move, the higher is the energy content of the photons emitted.

However, the power content of this radiation is not constant throughout the infrared spectrum, but its distribution varies as a function of wavelength and temperature. Figure 3 shows the blackbody radiation curves, that is, the distribution of infrared power emitted by an ideal surface having an emissivity factor $E = 1$. In the illustration, the slanted line indicates how the wavelength of the peak emission moves towards the visible region of the spectrum as the temperature of the emitting surface increases. This explains why physical matter becomes incandescent at high temperatures. Figure 4 shows the correlation between temperature and the wavelength of the peak emission.

Optical Fibers

Optical fibers are transparent linear elements inside which radiation propagates by total internal reflection. Figure 8 show the physical principle on which the fiber operation is based. All the fibers used in infrared instrumentation are made of glasses especially chosen for their ability to transmit the radiation comprised in the chosen spectral region.

The illustration shows that after entering the front surface, all rays that acquire an inclination smaller than the critical angle are totally reflected inside the fiber core and keep traveling in this fashion until they reach the opposite end or are totally absorbed, whichever comes first. For a fiber having a critical angle of 67o, the illustration shows an acceptance angle of 70o, which means that all rays incident onto the fiber's front surface at a 35o angle or less with its axis are trapped inside the fiber by total internal reflection.

On the other hand, all incident rays entering the fiber with an inclination larger than the 35o angle will leave the fiber at the first contact with its internal surface. This behavior is commonly called "spilling."

The value of the critical angle is a function of the ratio between the refractive indexes n1 and n2 of the glass or which the core is made and of the medium surrounding it. Thus, by controlling the ratio n1/n2, we have a means of increasing or decreasing the acceptance angle of fiber optics, a feature that can be used to obtain special performance characteristics.

Cladding is the name of the technique used to establish a permanent n1/n2 ratio. It consists of coating the core with a layer of solid material (usually a different type of glass) having the desired index of refraction. Without this coating, two fibers touching each would "spill" light into each other since they have the same refractive index. The presence of the cladding prevents this happening.

Figure 8 shows a fiber core enveloped by a layer of cladding, whose outside surface, to the right of point P, is, in turn, coated with an absorbent layer of material. This will prevent stray rays, such as those surpassing the critical angle (for instance, where the fiber makes a curve) from spilling out: the outer coat will merely absorb them. Also, at a curve, radiation cannot get into the fiber from outside, and every chance of interference with the rays traveling along the fiber is eliminated.

How tight a curve can a fiber make without spilling? As long as the ratio of the bend radius to the fiber diameter is above 40, the losses are negligible. This means that a fiber with a 25-u core diameter can be wound around a 1-mm mandrel with no significant transmission loss.

Besides their ability to carry radiation around corners and through opaque obstacles, optical fibers provide quite large acceptance angles for incident radiation, thereby making them comparable to "fast" conventional optical systems; that is, systems having a large NA number. NA stands for numerical aperture number of an optical system and is a measure of its

ability to accept incident light rays. This, of course, is a function of the limit angle of acceptance. The larger this is, the larger the cone of radiation entering the optical fiber, transmitted along its length and out of its output end.

When compared with typical radiometers, which have optical f/no generally ranging between 4 and 8, optical fibers can capture remarkably higher radiating power. On the basis of correlation of equivalent f/no, such optical fibers theoretically are more effective by factors ranging from 20 to 88. Figure 9 graphically illustrates a comparison between the cone of radiating energy collected a conventional lens and an optical fiber.

As mentioned before, the optical fibers used with infrared instrumentation are made of special glass having good transmissivity in that portion of the infrared spectrum covered by the detector used in the system. In other words, fibers and detector must be matched to each other for best system performance. Figure 10 shows the transmission losses are indicated as a percentage of the radiation signal being transmitted. In other words, the signal magnitude is inversely correlated with the length of the fiber, which means that the signal magnitude will never drop to zero, although it will asymptotically approach the zero level. However, the noise traveling through the fiber also will follow the same laws; therefore, the S:N ratio will remain the same no matter how long the fiber is. Thus, the detector noise and the self-generated noise of the signal processing electronics become the limiting factors in signal readability.

Fiber Bundles

Thus far single fibers have been discussed. For practical purposes, however, fiber bundles are most commonly used. A fiber bundle is an assembly of a number of fibers, anywhere from just a few to many hundreds, lined inside a containing sleeve that can be either rigid or flexible. In Figure 11, fiber bundles of different length and composition are shown. As can be seen from the picture, the ends of these bundles are made rigid to hold firmly in place the terminations of all the fibers. Usually this is achieved with the use of a cementing compound, such as an epoxy resin that hardens to a degree adequate to permit optical finishing of the end surfaces.

Figure 12 shows the geometric representation of an end surface of a very small bundle of fibers. The majority of those used for infrared temperature measurement applications have several hundred fibers to pick up and transmit more signal to the detector. Typically, the outside diameter of a single fiber is 25u.

Fiber bundles are divided into two groups: coherent and incoherent. The coherent ones have the same identical geometrical distribution of the fibers at the two ends. In this fashion, the light distribution picked up at the front end is exactly duplicated at the output. In other words, an image is

239

transferred from one end to the other, with only the degradation resulting from (a) the transmission losses, and (b) the resolution allowed by the size of the individual fibers and the spacing in between.

Instead, the incoherent fiber bundles have a random distributic fibers at the two ends and no image is transferred from one end to the other. Only radiation is available at the output in quantity proportional to the total input, minus the transmission losses.

Most of the optical fiber bundles uses with infrared radiometers are of limited length, generally 1 or 2 meters long, occasionally up to 10 meters long. If they are not terminated with a lens, they have a field of 60o. This means that the diameter of the target area viewed by the detector through such optics is light larger than the distance between the front end of the fibers and the target surface. This can be easily verified by backlighting the target, which is achieved by injecting visible light at the opposite end of the surface. Figure 13 compares backlighting for two different types of fibers. The one in the right hand of the operator is terminated with a lens, and so has a focal point at a well-defined distance from it.

Fiber optics of the first type are used when the target is large, and the average temperature of the viewed area must be measured. Fibers of the second (focused) type are used for measuring the temperature of a small area when it is not possible to place the fiber's front end close enough to the target surface. The focal point for fibers of this type can be located at almost any distance from the fiber's front end, although for practical purposes this distance is usually set between 2 cm and 3 meters.

The backlighting capability assures perfect and easy target aiming, both as location and size of the viewed area, without parallax error. In some applications it might be desirable to check the fiber's aim at any time, during the operation. In this case, a bifurcated optical fiber can be used. One branch of it is connected to a high-intensity light that will go on by pressing a switch, thus allowing the operator to verify and, if needed, to achieve a perfect aiming of the fiber. The other branch will allow the infrared detector to "see" the target at exactly the same spot that was illuminated and to measure its temperature as soon as the aiming light has been turned off.

Advantages and Disadvantages of Fiber Optics

The first and major disadvantage of optical fibers is the poor transmissivity of any glass of plastic in the infrared spectral area. Radiation of intermediated and far infrared (wavelengths larger than 2.5u) is absorbed by the fibers after just a few millimeters of travel. This makes it extremely difficult to measure temperatures below 100oC, since most of the radiation emitted by a surface below 100oC is located around the 7u region. Of course, there is some radiation in the near-infrared area, but its energy content is so low that it lies buried under the noise level.

Another disadvantage of optical fibers is the impossibility if producing two bundles of identical characteristics because a bundle is made of many hundreds, and often several thousands of individual fibers, whose final number can differ by a few percentage points at the end of the manufacturing operation because of unavoidable losses due to breakage. And even if it were possible at the beginning to assemble two perfectly identical bundles, individual fiber breakage during usage would soon create a difference in their ability to transmit infrared energy. Consequently, the signal processing electronics must have the flexibility to adjust and compensate for this lack if fiber bundles consistency.

Finally, any glass has a softening thermal threshold that cannot be exceeded without damage to the fibers. This threshold for most glasses is around 600oC. Thus, fibers that are expected to operate in hotter environments must be cooled in any of several available ways (air purge, water circulation, etc.).

Concerning advantages, all fibers can be looked at as low-pass filters, with gradual cutoff of transmissivity above 2.5u in wavelength. If this is a disadvantage because it enhances thermal resolution. This is due to the fact that radiation power increments in the near-infrared area are larger than the corresponding power in the total radiation area for the same ^t of the target. The reason for it is the displacement of the peak radiation wavelength toward the visible region as the target temperature increases. Figure 14 illustrates this concept: it can be clearly seen that the area increments at the left of the vertical cutoff line are larger than the area increments of the total surface area subtended by the full radiation curves.

In second place, there is the advantage that optical fibers can be defined as "shielded radiation conduits" of constant transmissivity, no matter what environment they might have to cross. Smoke, water, vapors, dust, gases, etc. cannot affect the optical signal transmission through the fiber.

Among the other advantages are the following:

1. Inert, rugged construction. In addition to being unaffected by energy fields, optical fibers contain no moving parts and are specified and constructed for use in most heat, chemical or radiation environments. For example, they can be immersed in molten materials, such a polymer melts in extruders and injection molding machines, where direct, real-time response measurement has heretofore been impossible with thermocouples because of frictional heating and heat sinking of the heat sensing element.

2. Easy installation. Most fibers are flexible and of a size that permits bending around opaque obstacles for installation where ordinary instruments simply cannot fit. A direct line of sight is not required.

3. Simplified setup eliminates human error. All fibers can be aimed with pinpoint accuracy using a source of illumination from one end to carefully line the target area at the other end. This simple advantage overcomes most problems associated with proper alignment of conventional noncontact temperature detectors.

4. Optimum target viewing angle. With the addition of small lenses, the viewing angle of the fiber can be modified from the standard 60o cone, down to a spot 1 mm in diameter. Large or small areas are precisely monitored with optimum resolution and accuracy.

5. Wide range of temperature measurements. With the proper selection of quick-disconnect fibers, a single system may be used to cover the full range of temperatures and repeatability.

6. Very large NA. This characteristic allows one to capture from the target a very large cone of radiated energy, up to 100 times larger than it is practical with conventional optical systems.

THE CHOPPER

The majority of the IR radiometers incorporate a "chopper," that is, a mechanical device that periodically interrupts the flow of radiation from the target to the detector. In this way, the magnitude of the infrared signal can be easily measured by comparing it with the baseline of the no-signal level during the cutoff caused by the interposition of the chopper blade.

This alternating between radiation and no-radiation is reflected, at the detector output, as an alternating electrical signal, which by its own nature, is easier to produce than a dc signal. However, a minority of infrared radiometers does operate without a chopper. In this instance, the system's output is a dc signal that only varies as a foundation of the variations of the impinging radiation. The major difficulty of these systems is a signal drift.

In its most common configuration (Figure 15), a chopper is a slotted disc rotated by an electric motor. The detector's field of view is alternatively opened and closed by the slots and the blades of the disc rotating in front of it.

Lately, tuning forks have been used as choppers. Approximately designed vanes attached to the ends of the fork's tines to perform the chopping action. Chopping frequencies up to 25,000 Hz are attainable. When compared to motor-driven choppers, tuning forks have the advantage of small size, light weight, greater accuracy, long-term stability, low power drain and negligible heat dissipation.

Another class of IR radiometers operating without chopper are the scanners. In this configuration, the detector's field of view is mechanically deflected (usually by mirrors or prisms) along a preestablished repetitive pattern.

The infrared signal variations occurring along this path produce at the detector's output a modulated electrical signal that can be processed by conventional means to generate, for instance, a visual display representing the distribution of infrared radiation at each point of the field of view being scanned. the instruments of this class are commonly called "infrared cameras." A better designation would be "infrared-to-visible image converters."

INFRARED DETECTORS

The transducers capable of turning the infrared radiation into an electrical signal are called infrared detectors. They are divided into several groups according to their principle of operation, as follows:

Bolometers

The operation of bolometers is based on the measurement of an electrical characteristic variation induced by the heat absorbed by a temperature-dependent element. The metal bolometer is based on a positive conductance variation, the thermistor bolometer on a negative conductance variation, the ferroelectric bolometer and also the pyroelectric detector on a dielectric constant variation. Their response time is around 1/100 of a second, with 1/1000 of a second as a typical upper limit of response.

Photocells

When infrared radiation impinges on these semiconductor devices, electrons spinning in the outer orbits of the detector's atoms can "capture" those photons that have a compatible energy content. If the so added amount of energy is sufficient to allow escape from its orbit and will become a free charge carrier, which will immediately begin to move along the lines of the prevalent electromagnetic field towards the positive terminal of the detector. An electrical current flow is thus generated whose magnitude is directly related to the number of electrons "liberated" by the impinging photons.

However, should the energy added by the photons not be sufficient to "liberate" the electrons, the latter will merely spin faster in their orbit, thus increasing the kinetic energy content of the atoms and, consequently, their temperature. On the other hand, if the photons' energy content is excessive, they will escape capture by the electrons, so no electrical or thermal effect will be apparent at the detector terminals.

This is why the photocells, according to their composition, can only operate as photon detectors in limited areas of the infrared spectrum, that is, only in those areas in which the photons of the radiation possess the "right" amount of energy – just enough to liberate electrons that, according to the characteristics to the associated electrical circuitry, can:

1. become available as current carriers, thus decreasing the dc resistance of the semiconductor;
2. accumulate at the opposite sides of a self-generated potential barrier, thus developing a voltage difference across it; and
3. move in opposite directions because of external magnetic field, thus again generating a voltage across the semiconductor.

Case 1 deals with a conductivity effect, and the detectors of this class are called photoconductive. In case 2, there are the photovoltaic detectors. In case 3, there are the photoelectromagnetic detectors.

The time response of these photon detectors is on the order of microseconds or less, which is about three orders of magnitude faster than the thermal detectors and, of course, is independent from their physical mass, since no thermal effect is involved.

The infrared detectors used in fiber optics radiometric systems are mostly of the photon-detector type. their choice is dictated by the thermal range they must cover and by the response speed required. Lead-sulfide (PbS) cells operating in the photoconductive or photovoltaic mode. Since the transmissivity of optical fibers is limited to the near-infrared region of the spectrum, the detectors used in these systems do not need to be cooled. Figure 16 shows the response curves of several detectors that can operate at ambient temperature in conjunction with fiber optics. This chart plots D* (a figure of merit related to the detector sensitivity) versus wavelength. As mentioned before, the photon detectors cover just a limited spectral area, while the bolometers and the thermocouples have a flat response throughout the whole infrared spectrum.

THE REFERENCE BLACKBODY

All the infrared radiometric systems equipped with fiber optics are using the ambient temperature as their reference. For those based on ac operation, the chopper's blades are supplying a blackbody signal to the detector in the time interval during which they interrupt the flow of radiation transmitted by the optical fibers.

For systems based on dc operation, the detector must be "zeroed" from time to time to avoid drift problems. Zeroing can be achieved either manually or automatically by instantaneously closing a shutter in front of the detector to establish a ground floor level against which to measure the radiation signal from the target.

THE COOLING SYSTEM

As mentioned previously, no cooling is needed for the detectors matching the fiber optics spectral transmission area. However, since detector performance characteristics vary with its temperature constant or to compensate for the change of its electrical response whenever its temperature changes.

This is achieved by varying the gain of the detector output according to its temperature variation. One or more thermistors are used for this compensation.

SIGNAL PROCESSING

The electrical signal supplied by the detector is of analog nature. It is correlated with the infrared signal impinging from the target according to a nonlinear function. It is of very small magnitude, usually just below the millivolt level. According to how we want to use it, it must be amplified and recorded. Whenever a feedback function is required, dc voltages must be made available at the output terminals.

The basic block diagram depicting the signal flow was shown in Figure 16, in which the elements drawn with solid lines are essential and those with dotted lines are optional. Figure 17 is the picture of a basic industrial fiber optics radiometric system, Thermal Monitor. It consists of three separate subassemblies: the optical fiber bundle, the infrared detector head and the signal processing and display console.

The Optical Fiber Assembly

The optical fiber assembly shown in the photograph is 0.5 meters long and its front end termination is protected in a replaceable ceramic sleeve. This makes the front end totally inert to electromagnetic energy fields. Consequently, it can be inserted without any problem between the turns of an induction coil to allow the detector to "see" and measure the temperature of the object being thermally treated inside the coil.

The Detector Head

This contains a chopper, complete with its electrical driving network, an infrared detector whose bias voltage is supplied by the display console and a very low noise preamplifier, whose output is a low-impedance analog signal that can travel along a coaxial cable (up to 100 meters long) to the display console.

The Display Console

This contains a linearizing amplifier that turns the analog exponential detector output into a linear signal directly proportional to temperature. This signal is then converted into digital and displayed on a digital panel meter (DPM) for direct visual readout of the temperature either in *F or *C. A power supply is also contained in the console.

At the back of the console, several outputs are optionally available, such as the raw analog signal prior to linearization, the linearized signal or a dc voltage or current. These functions can then be used for recording and/or for control of a thermal process through the action of relays that will activate or deactivate the necessary functions.

More Complex Systems

These have evolved from the simple unit described above. Figure 18 shows a thermal monitor equipped with a Hi-Lo logic unit where the target must be kept during the manufacturing process. This is achieved through a feedback loop, with a high degree of precision. For instance, in semiconductor epitaxial deposition processes, where the critical temperature to be kept is 1030oC, the upper control limit can be set at 1031oC and the lower control limit at 1029oC.

Besides the Hi-Lo logic, there is an emissivity control, a gain multiplier knob, a jack for attaching a calibrator unit and, of course, a DPM for visual display of the target's temperature.

When the amount of power needed for target energization is large, a proportional controller is used instead of the Hi-Lo logic unit. In this way, the power correction is correlated to the magnitude of the deviation from the optimum level, instead of being an on-off correction.

Multichannel Thermal Monitor System

Figure 19 shows a multichannel thermal monitor system. Every channel with its own optical fiber and its own detector head is plugged into the control console, where according to the option, it can be processed separately all the way to its own output, or can be multiplexed through a time-shared common set of processing electronics. A knob controlling the time-sharing function is available for setting by the operator.

High Speed Thermal Monitor

A high-speed thermal monitor is shown in figure 20. Its three DPMs display the target temperature in three different ways and at different response times, the fastest of which can reach 1 usec. Systems of this family are ideal to control the power of lasers used for metal welding or surface heat treating, since they measure the target temperature exactly at the spot on which the laser beam is made to impinge.

Another version of these systems (Figure 37) is used to measure the temperature of the rotor blades in jet engines and other turbines. In this version, according to the setting of a control switch, a single DPM displays the average temperature of all the blades of the highest temperature of the hottest single blade. With these indications, fuel consumption can be controlled, engine temperature conditions can be observed and a catastrophic failure of the turbine from single-blade overheating can be avoided.

Emissivity-Independent Systems

Emissivity-independent thermal monitors have been mentioned at the end of the section entitled Infrared Radiation, p. 401. Figure 21 shows one such system, whose block diagram is sketched

in Figure 22. A key element is the bifurcated optical fiber, which can, according to the option, be made of different detectors are used. When the emissivity characteristics of the target are those of a graybody, these systems will indicate the target's true temperature no matter what its surface emissivity is. Thanks to the fibers' large numerical aperture, temperatures as low as 200oC can be measured with 1% accuracy.

APPLICATIONS

We have already listed, in the section entitled Advantages and Disadvantages of Fiber Optics, p. 412, the major advantages offered by optical fibers when compared with conventional optics in infrared radiometric systems. Consequently, in a host of applications in which temperature is a critical factor, it is now possible to make temperature measurements precisely where none was formerly possible, and to improve the accuracy of those measurements that until now were carried out with difficulty and lack of precision.

The main areas in which infrared fiber optics instrumentation is used to resolve difficult problems of temperature monitoring and control in industrial processes are the following:

Metal Production

Melting, continuous casting (Figure 23), annealing (Figure 24), galvanizing, roll-milling (Figure 25), etc. - in all these applications, the detector "watches" the target through smoke, fumes, vapors, water and even solid walls, thanks to the shielded path of constant transmissivity offered by the optical fibers.

Metal Induction Heating

Because of the strong RF inductive energy field needed to heat the metal parts to be treated, conventional temperature-measuring devices are useless because they will be heated directly by the induction field.

Figure 26 and 27 show two typical applications of fiber optic systems to monitor and control induction treatment of metal objects either stationary in, or moving through, induction furnaces.

Precise control of the temperature needed for perfect heat treatment of metal parts (bolts, cam shafts, axles, gears, etc.) is essential to produce the crystal structure that will ensure meeting or exceeding the mechanical characteristic specifications.

The use of fiber optics infrared control equipment:

o   allows the viewing end of the fiber optic to be placed in close proximity of the target;
o   saves energy by allowing only the precise amount of power to be used;

o   speeds up production by controlling process by temperature instead of time and by allowing faster heat injection rate;

o   prevents fiber optics from being affected by the induction energy field; and

o   allows electronics to be remoted to radiation-free area.

Metal Forging, Hot Stamping, Pipe Bending

Forging of metal parts includes both rough shape as well as precision forging, which requires less material removal and waste. Pipe bending and shaping is also included in this application. These operations are carried out by heating the parts to be worked on to the optimum temperature with any of the several means available (ovens, flame, induction field, etc.). If the part temperature is below the optimum, cracks and internal tensions will develop, while if it is above the optimum, drooping will take place. The precise temperature control afforded by the use of infrared fiberoptic controllers will:

o   avoid the formation of defective parts (from cracks or drooping), thus eliminating rejects and waste due to these defects;

o   save thermal energy by ensuring that no heat is wasted by heating the parts beyond the optimum level; and

o   speed up production by allowing a faster rate of heating the parts without danger of temperature overshoot.

Metal Casting

The die temperature is of critical importance in die casting of metals. Thermal cycling of aluminum products, with reference to die temperature has been successfully implemented with the help of optical fibers. Figure 28 shows schematically and in detail how the front end of the fiber is inserted through the mold frame and held in a corner of the runner plate, in contact with the aluminum flowing through it.

The major advantages offered by this solution are: (1) substantial savings of thermal energy by eliminating overheating and drastically reducing production rejects; (2) increased production due to the speedup the casting cycle, with the operation automatically controlled by the temperature of the casting material and not solely by time, resulting in faster operation; (3) improvement in the quality of the casting due to control of the process as a function of temperature, resulting in simpler operation and automatic compensation for a cold die startup or interrupted cycles; and (4) direct indication of the die and furnace pot temperature of the metal. Low metal level and blocked water lines are easily indicated several shots before the casting can display conditions visibly.

Saw Production

Teeth hardening, annealing, ends forming and joining (in the case of band saws) are operations in which the optimum crystal structure of the steel is obtained only if the correct

temperatures are reached, held and controlled within close tolerance limits. Infrared fiber optics systems used in these applications offer the following advantages:

1. Fast speed of response enables high production quantities to be processed.
2. Fiber optics are small and can get in close proximity of the areas under thermal treatment.
3. Very small spot size of the fiber optic enables focusing individually and sequentially on each and every tooth.

Control of Metal-Working Laser

Lasers, generally high-power CO_2 lasers, are used for welding, surface treating and finishing metals of various types. The conventional approach is periodically to sample the beam to keep its power at the desired level. This approach, however, cannot take automatically into account the emissivity variations of the target surface. These variations, in turn, affect the amount of laser power absorbed by the target and, consequently, the target's temperature, which is of paramount importance for the good performance of the operation.

This difficulty is overcome by the use of emissivity-independent infrared fiber optics system (EITM) aimed at the spot of laser beam impact (Figure 29). The infrared system is made blind to the laser wavelength and, in this way, it measures precisely the target temperature at the same spot. Further, via a feedback loop, it controls the laser power to ensure that the operation is carried out at optimum temperature.

Among the advantages offered by the fiber optics infrared approach are the following:

1. It allows noncontact temperature measurement in real time.
2. Fiber optics allow easy access to view the laser heating area because of their relatively small size.
3. EITM compensates for variations in emissivity as the part is being heated.
4. EITM response can be matched to the response speed of the laser.

Fusing Armature Windings in Electric Motors

This operation, better defined as thermocompression bonding, is carried out by near injection and mechanical compression on the point where the wire is looped around the commutator contact hook. Ac current flowing through the heating electrode brings it up to a temperature high enough to vaporize the wire's insulation, but not enough to melt the wire. According to its mechanical configuration, the joint rises to a level between 800oC and 2000oF in a very short time (typically between 50 and 100 usec).

249

Figure 30 shows an infrared fiber optics system mounted on top of an automatic high-speed machine that sequentially fuses every armature winding to its corresponding hook of the commutator lug. Figure 31 shows a typical electrical motor with the wire-to-hook ends prior to fusing. Note how some of the hooks are still standing up, while others already have been bent down. Figure 32 shows in detail the fusing area, with the electric motor at left and the optical focusing head of the fiber optics in the upper right corner.

Major advantages offered by the fiber optics controller are: (1) increased speed of operation due to the possibility of faster heat injection and faster indexing; (2) elimination of defects from unsoldered, poorly soldered or open joints because of melted wire; and (3) ease of precise aiming at the spot of heat injection.

Crystal Growing

In semiconductor manufacture, silicon and germanium crystals must be grown from their molten state. Similar growth procedure applies for the crystals used for lasers. In all these operations the perfect lattice structure of the crystal is of paramount importance. The temperature of the meniscus between the molten material and the emerging crystal is the element controlling the diameter of the "carrot." The heat necessary to keep the molten material at optimum temperature is supplied by an RF energy field. This prevents the use of conventional temperature-measuring devices and even the proximity of infrared detectors.

The use of fiber optics infrared control equipment (Figure 33) solves the problem and offers the following advantages:

1. Fiber optics can be inserted inside the system and focused on the meniscus while the detector can be placed outside the energy field;
2. If other than normal atmosphere is present, fiber optics can be sealed into the meniscus by the detector allows precise control of its temperature through a feedback loop acting directly on the induction energy field.

Semiconductor Epitaxial Deposition, Doping, Sputtering

Semiconductor wafer induction heating for doping, epitaxial deposition, sputtering, etc., is generally carried out in hermetically sealed quartz vessels, where vacuum or precisely controlled gas atmospheres are present. Precise temperature monitoring devices can possibly be used.

The use of fiber optics infrared monitoring and control equipment (Figure 34) solves the problem and offers the following advantages:

1. Fiber optics enable noncontact measurement of temperature.
2. Fiber optics can reach inside a hermetically sealed vessel and carry the radiation signal from the wafers to the remotely located detector head and electronics.
3. Thermal process can be automatically carried out within preset optimal temperature limits.

Furthermore, the optical fiber can be manually scanned along the length of the induction oven to determine its thermal profile and to eliminate temperature gradients by adjusting the spacing between the turns of the induction coil.

Semiconductor Eutectic Chip Bonding

Gold-silicon eutectic makes the most reliable chip-to-substrate bond in seamy-conductor manufacturing. However, temperature control of the process is quite critical. The eutectic flows at 385oC and the tolerance is -0o + 20oC. Outside said tolerances the chip might be just "tacked" or sitting above voids, or, at the high end, the gold would begin alloying into the silicon and spoil the doping.

A very thin optical fiber threaded through the collet allows the infrared detector to "see" the chip during the bonding operation. At the instant when the eutectic flows, a large increment of the infrared radiation emitted by the chip's upper surface signals that the optimum temperature has been reached and, through a feedback loop, the process is terminated.

Advantages offered by the fiber optics infrared approach are as follows:

1. Fiber optics can be threaded into the collet in a permanent, unobtrusive setup.
2. Real-time response enables precise control of the bonding process by signaling the precise time when scrubbing must start and when a good bond is made.
3. High speed of operation allows faster rate of heat transfer from substrate to chip.
4. It ensures reliable bonds of semiconductor chips to substrate.
5. It eliminates the high-skill operator requirements and allows fully automated mass production.

Figure 35 shows the detail of a typical fiber installation in the collet of a eutectic chip bonder.

Polymer Extrusion and Injection

Precise and control of melt temperature is essential to ensure optimum length of the polymer molecule and consequently, to maximize the physical properties of the product. Until now, thermocouples have been used to obtain an indication of the polymer temperature, but with the large errors due to the heat from the friction of the polymer against the thermocouple's protective capsule and the latter's thermal connection to the

heated barrel. To accurately measure the melt temperature, a fiber optic probe with a high-pressure window is inserted into the barrel flush with its inside wall, so that it will measure only the temperature of the polymer flowing in front of it. If the melt temperature is at least 10% higher than the barrel's temperature, a standard polymer probe can be used. If the melt temperature is equal to, or lower than, the barrel's temperature, an air-cooled polymer probe must be used.

Advantages of the fiber optics infrared approach, which is shown schematically Figure 36 are as follows:

1. Melt temperature measurements are accurate.
2. The response is 1000 times faster than thermocouples.
3. Since polymers are partially transparent in the infrared spectrum, the system measures average temperature to a depth between 5 and 20 mm into the melt, thereby avoiding errors caused by the barrel's temperature effect on the interface between the melt and the barrel.
4. A feedback loop ensures automatic temperature control within narrow tolerances.

Plastic Castings Ejection

Plastic material injected into molds must be ejected during its colddown process as soon as it has solidified to the desired hardness. This is achieved by special "ejector pins" equipped with optical fibers lined along their core. Through these an infrared detector can "see' the plastic material injected into the mold. Thanks to the partial infrared transparency of the plastic, the radiation reaching the detector carries thermal information not only from the area contacting the fibers, but also from a certain depth within the plastic material (approximately between 5 and 20 mm).

Advantages offered by fiber optics infrared controllers are as follows:

1. There is real-time temperature measurement in depth.
2. The high speed response enables material ejection at the precise moment of cooling.
3. Fiber optics are not affected by mold temperature.
4. They compensate for wrong temperature of the molds.

Mold Temperature Monitoring in Glass Production

The temperature of the mold into which the glass is blown is of critical importance because of the following:

1. If the mold is too hot and is opened by the time sequence, the glass just molded will not have developed hard skin and will sag.
2. If the mold is too cold, the glass will have stresses, causing it to shatter.
3. If the mold is too cold, the glass will tend to harden too quickly, thereby resulting in voids in the product.

By use of a fiber optic thermal monitor controller, the fiber optics can be focused on the inside surface of the mold that comes in contact with the molten glass during the time interval when the mold is open. The advantages of fiber optics are: (1) easy placement of the fiber optic to view the inside of the mold; and (2) long length of fiber to keep the infrared detector away from the heat of the molds.

Turbine Blade Temperature Monitoring (Figure 37)

During operation, the blades of the turbine rotors must be kept cooled constantly by circulating air through special channels located inside each blade. In the event that in one or more blades those channels should become blocked, overheating of said blades would develop, possibly reaching the softening temperature of the steel of which they are made. At this point, centrifugal force would produce deformations that could cause quick destruction of the turbine.

Optical fibers introduced through the outside "skin" of the turbine at a convenient location and with the necessary orientation will allow an infrared detector to "see" the rotor blades as they traverse, one by one, its field of view (Figure 38). In this way, thanks to its microsecond response time, the detector will be able to precisely measure the temperature of each and every balde.

In the event that even a single blade should exceed a preestablished temperature safety threshold, an alarm signal will appear at the system's output, and a feedback loop could automatically throttle down the turbine and avoid a catastrophic failure.

Spot Welding

Until now, spot welding operations were controlled by adjusting or setting pressure time, voltage and current. However, the key parameter, temperature, could not be measured because the metal where the "nuggett" was being formed could not be reached by any temperature-measuring device.

Not any longer. Optical fibers introduced inside one of the welding electrodes are now allowing an infrared detector to "look" at the center of the area where the "nuggett" is being formed. Feedback electronics make instant-by-instant current corrections to ensure that the temperature development of the nuggett matches an optimum thermal profile stored in the controller's memory. In this way, a perfect spot weld is produced every time. Figure 39 is a schematic diagram of such a control system, while Figure 40 shows the welding electrodes detail and the optical fiber insertion in the upper one.
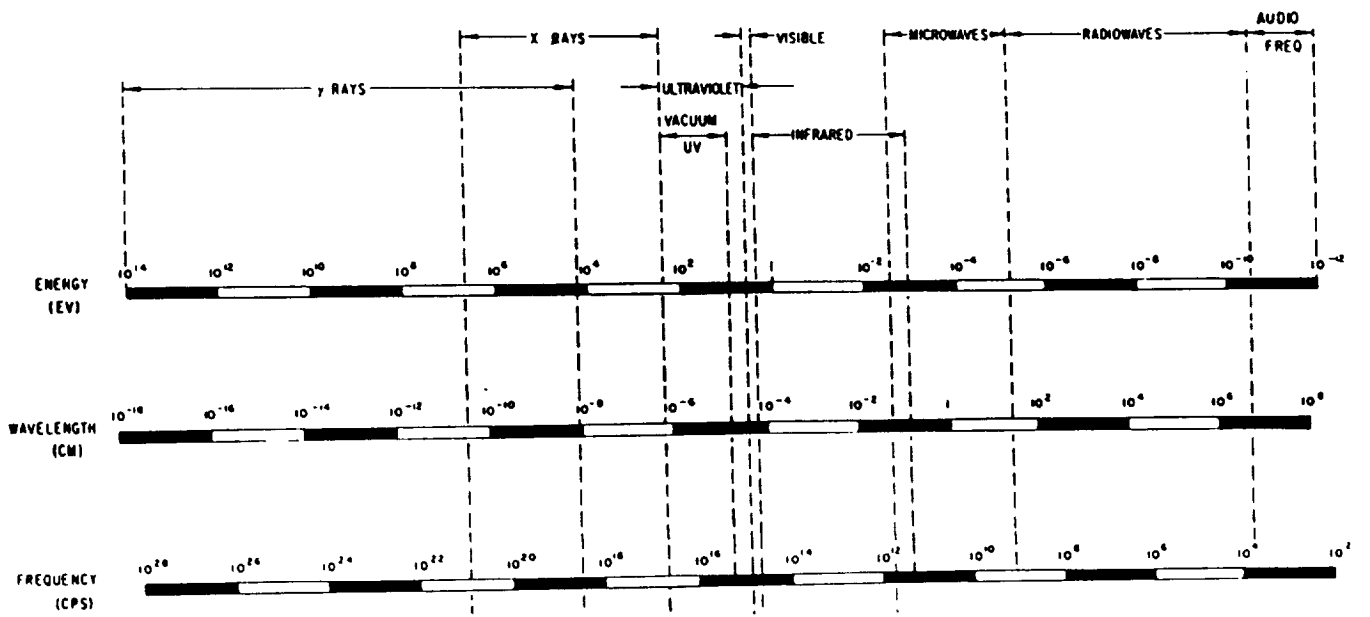
Figure 1. The electromagnetic spectrum.

Figure 3. Blackbody radiation curves.

E_λ, WATTS-M^{-2}-MICRON^{-1}

λ, MICRONS

Temperature, °K

Visible band

Figure 2. Stefan-Boltzmann law.

$B(T)$, radiance $[W/(cm^2)(sr)]$

T, temperature (°K)

$B(T)$

THE 0.1μ TO 1,000μ RADIATION BAND
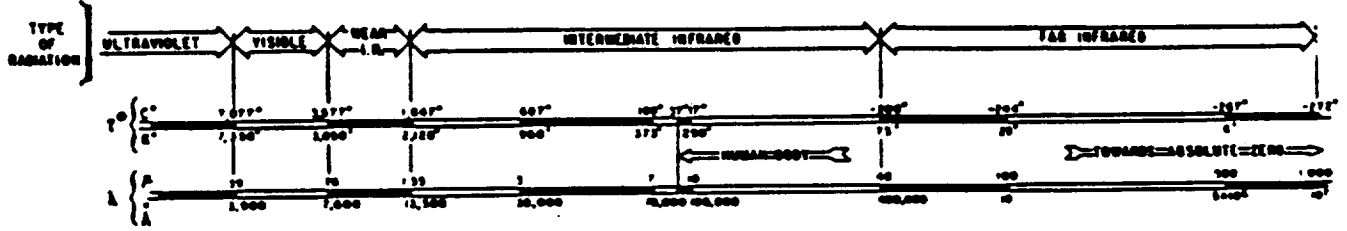
Figure 4.   T° and peak wavelength correlation.

$E\lambda$, WATTS $\cdot$ M^{-2} MICRONS
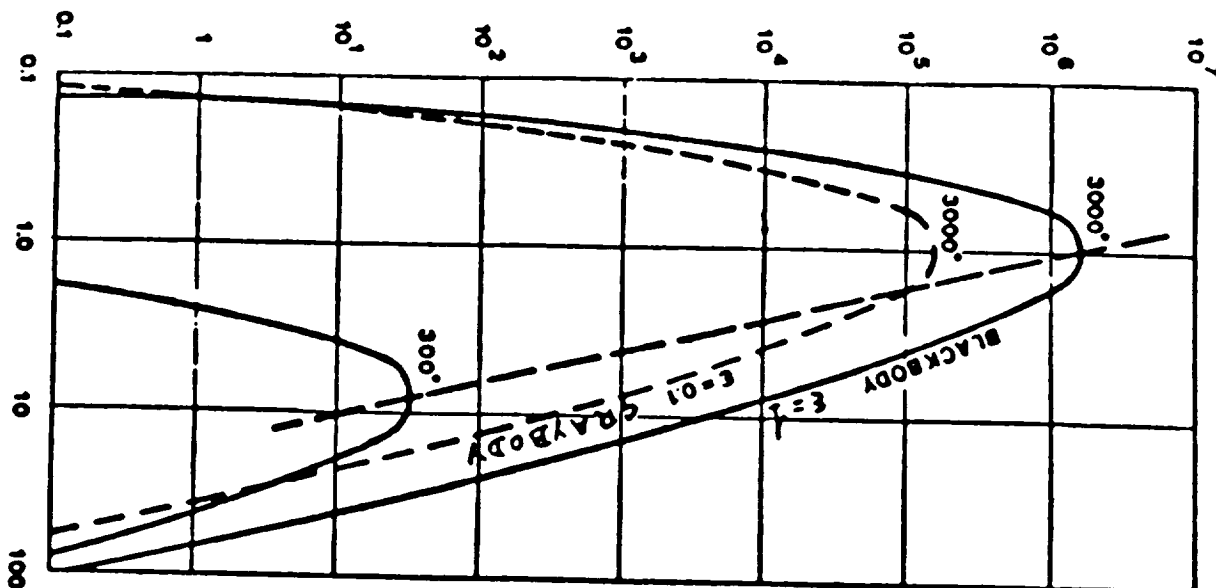
Figure 5. Blackbody and graybody curves.

Figure 6. Basic block diagram of a radiometer.
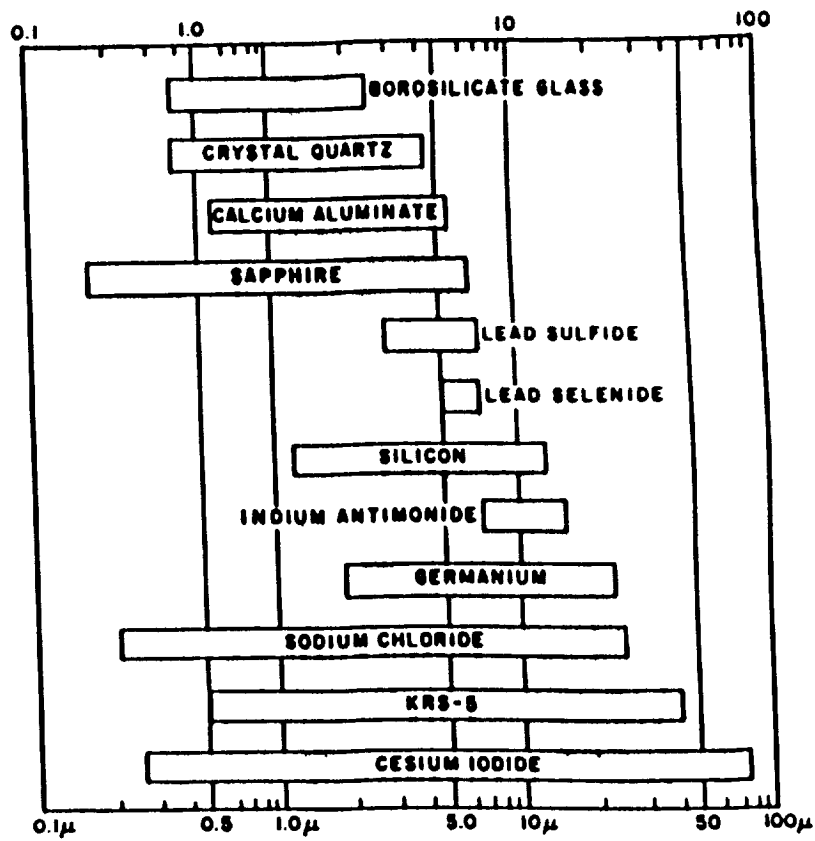
Figure 7. Transmission "windows" of selected optical materials.
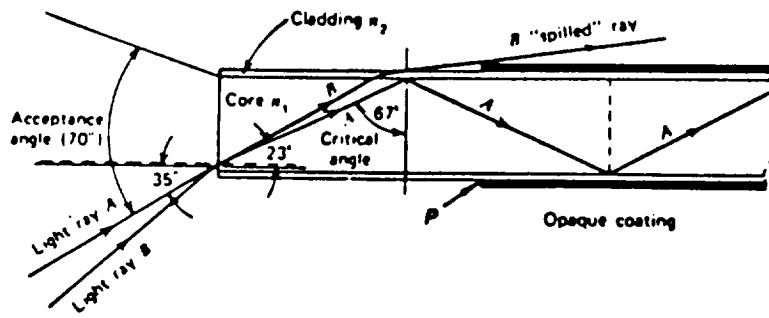
Figure 8. Ray propagation in optical fiber.
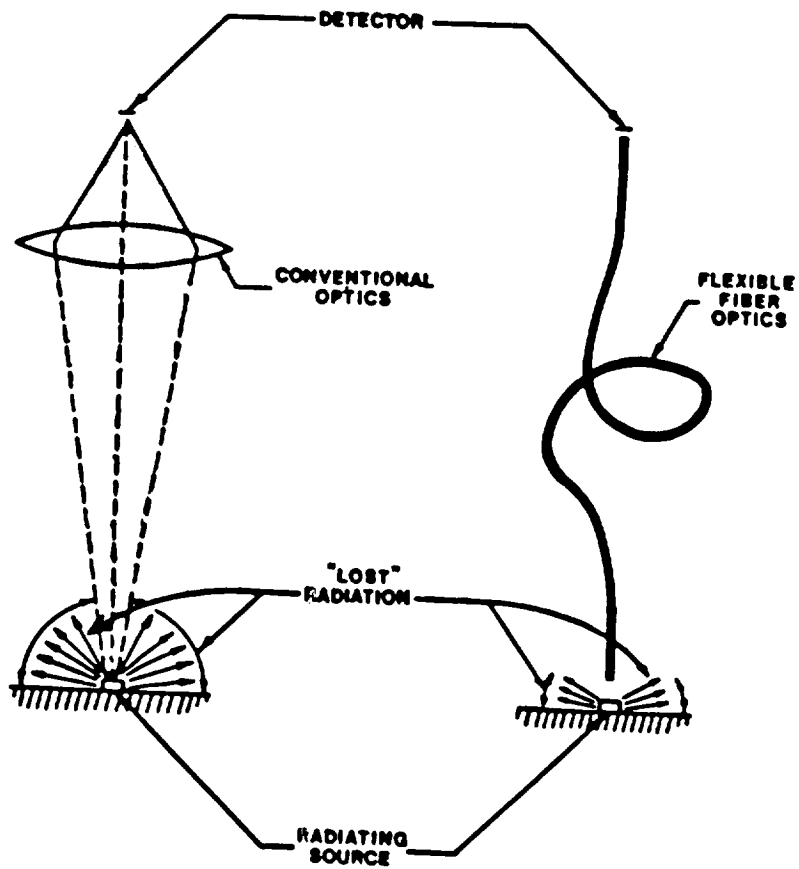
Figure 9. Capture of radiant energy.
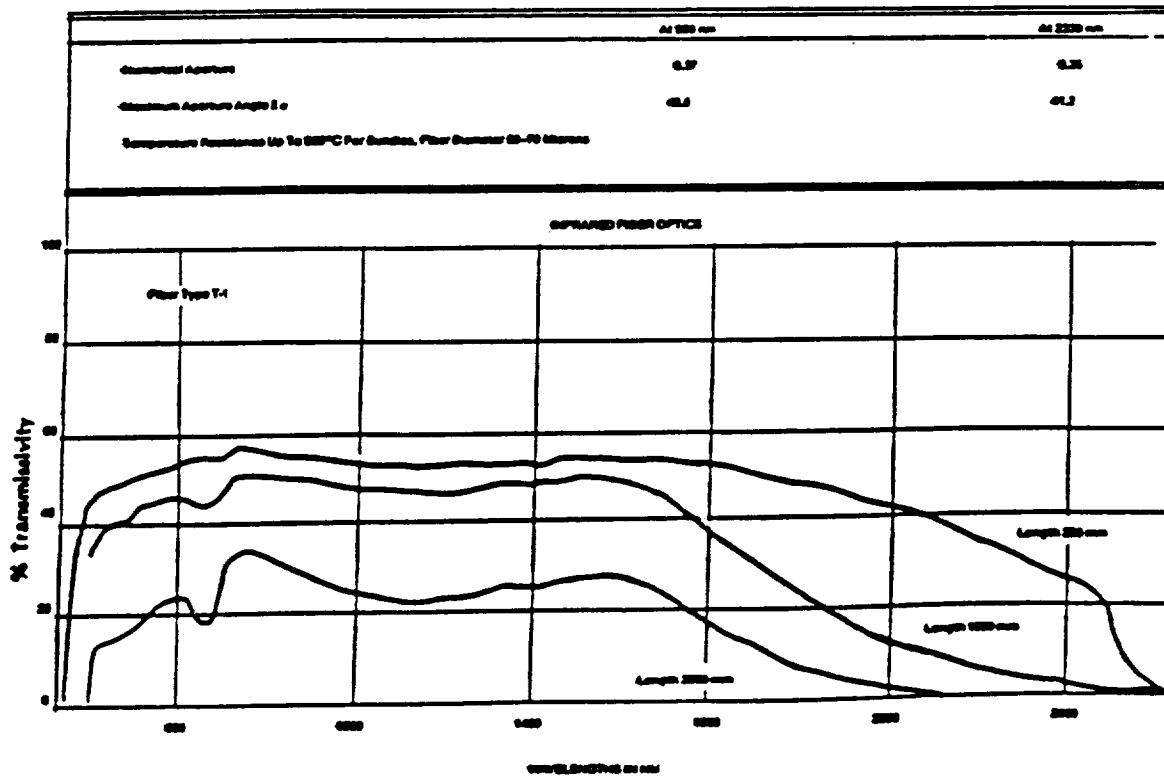
Figure 10. Spectral transmission of infrared fiber optics.

Figure 13. Viewing areas of open and focused fiber optics.
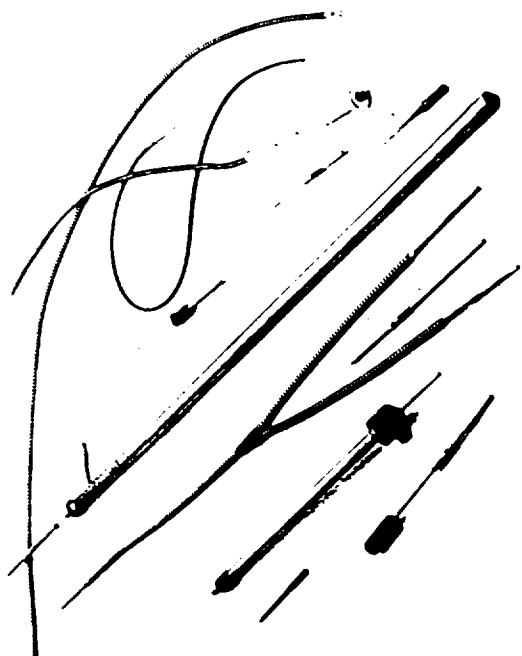
Figure 11. Various fiber optic bundles configurations.
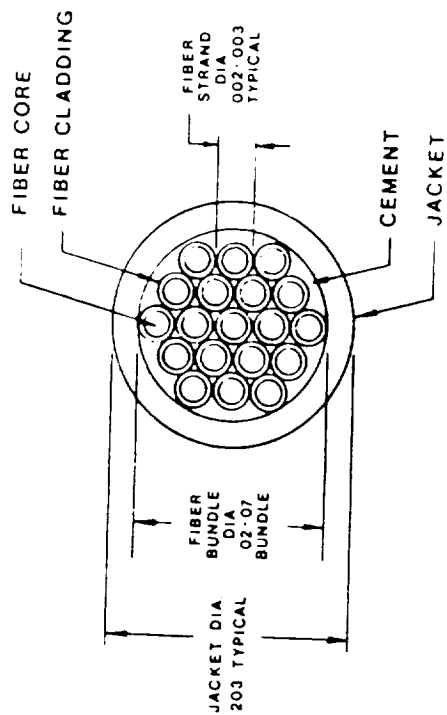
Figure 12. End view of very small fiber bundle.

261
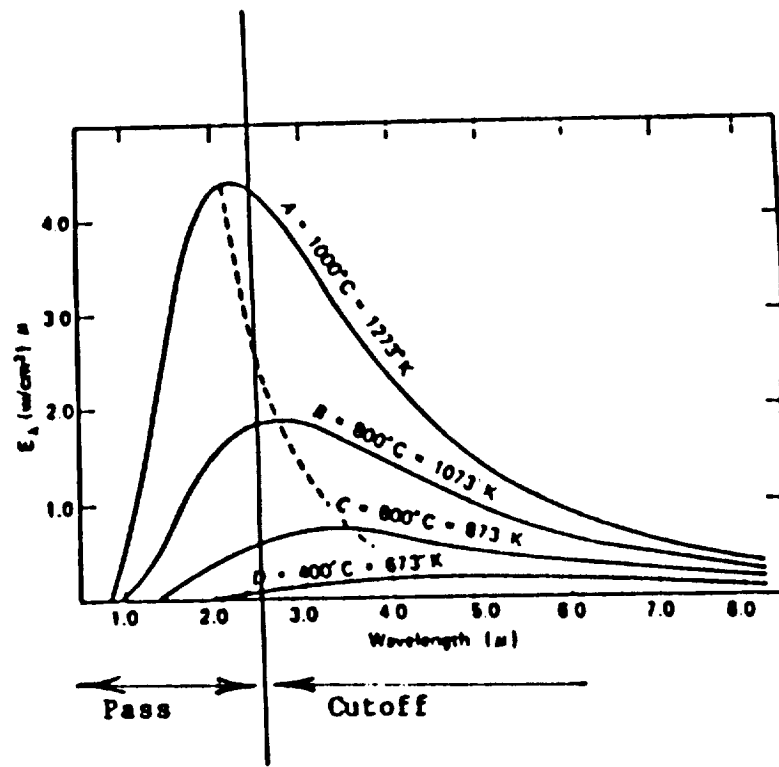
Figure 14. The filtering action of fiber optics.
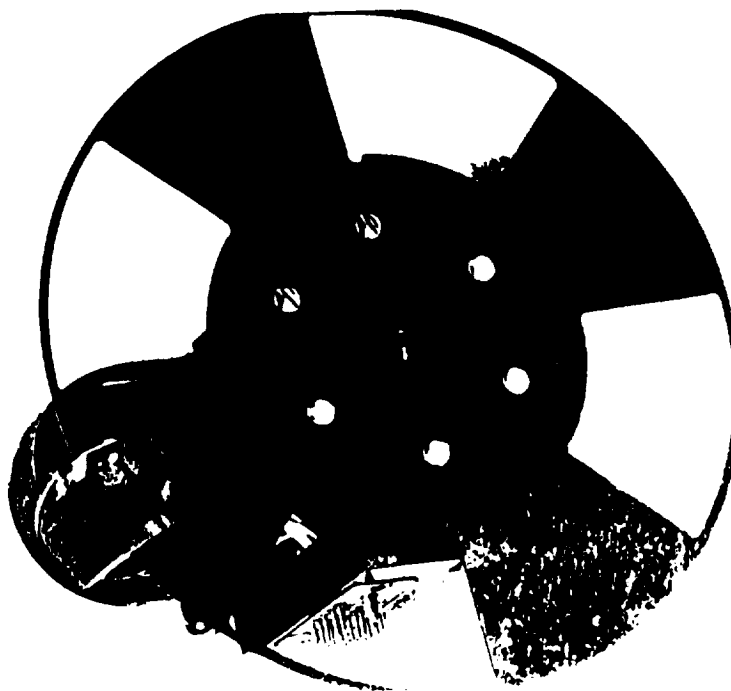
Figure 15. Basic configuration of chopper assembly.

262

Figure 17.   Basic industrial fiber optics radiometer.
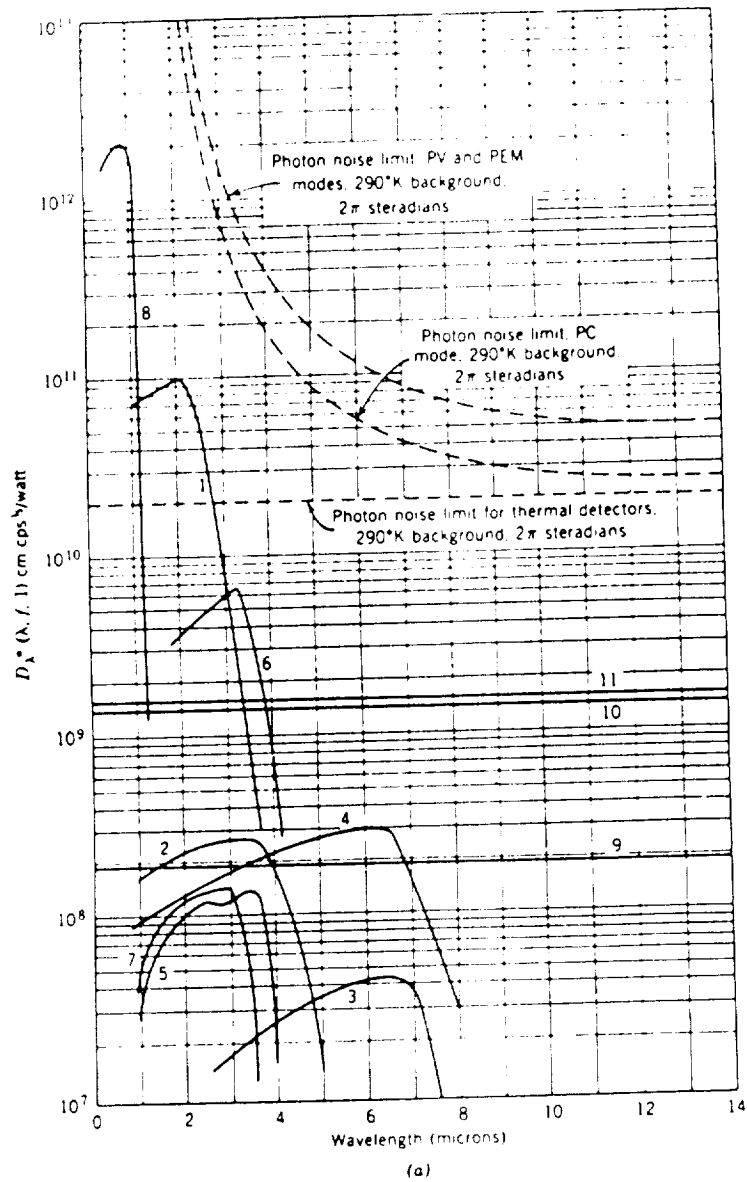
Figure 16. Spectral D_λ^* of room-temperature detectors. (1) PbS, PC (250 usec, 90 cps); (2) PbSe, PC (90 cps); (3) InSb, PC (800 cps); (4) InSb, PEM (400 cps); (5) InAs, PC (90 cps); (6) InAs, PV (frequency unknown, sapphire immersed); (7) InAs, PEM (90 cps); (8) Tl₂S, PC (90 cps); (9) thermistor bolometer (1500 usec, 10 cps); (10) radiation thermocouple (36 msec, 5 cps); (11) Golay cell (20 msec, 10 cps).

Figure 18. Hi-Lo thermal band controller.
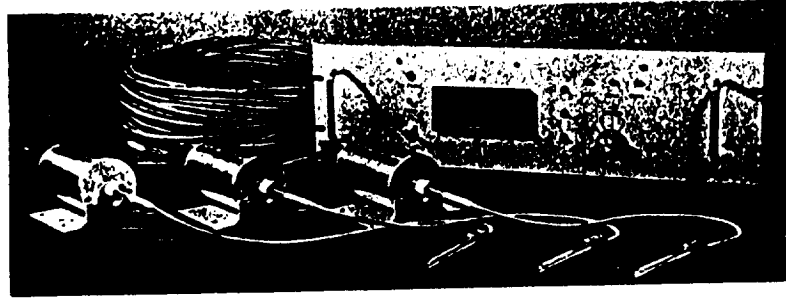
Figure 19. Multichannel multiplexing thermal monitor.
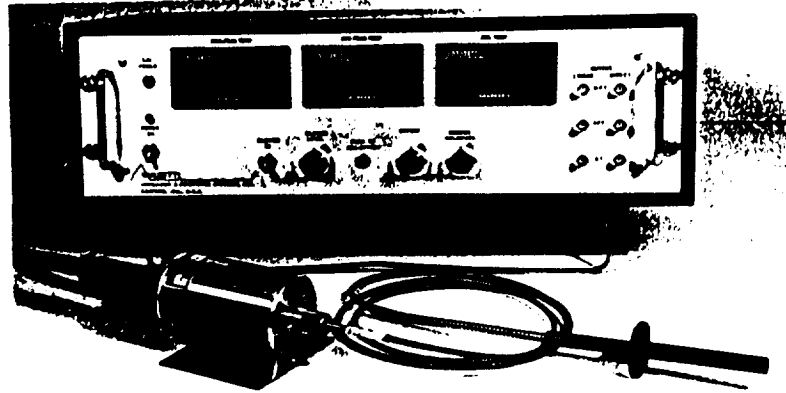
Figure 20. High-speed thermal monitor.
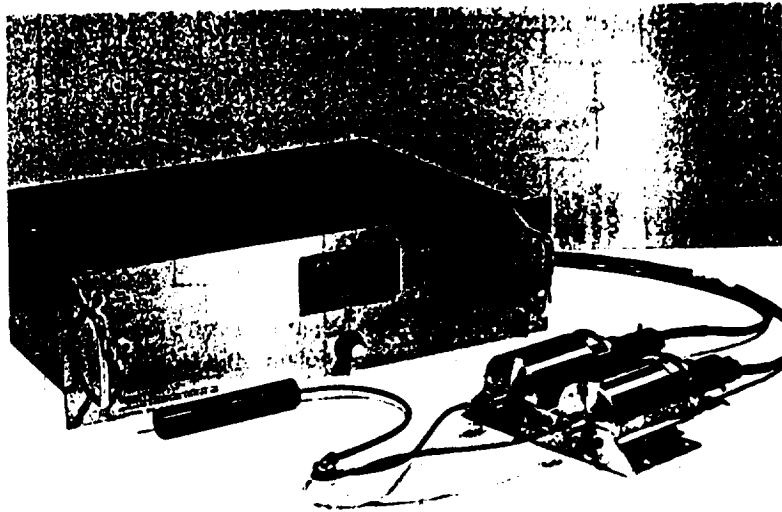
Figure 21. Emissivity-independent thermal monitor.

266

ORIGINAL PAGE IS
OF POOR QUALITY
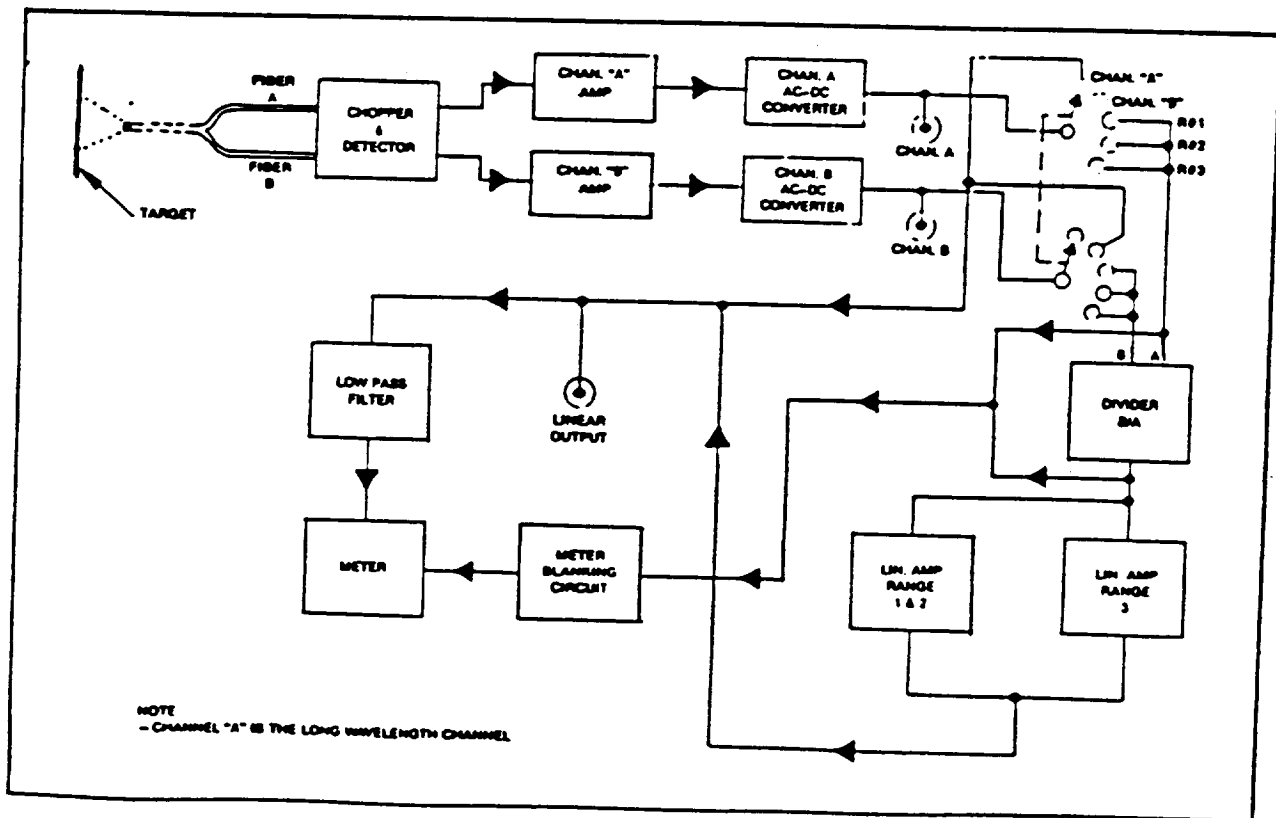
Figure 22. Block diagram of emissivity-independent thermal monitor.
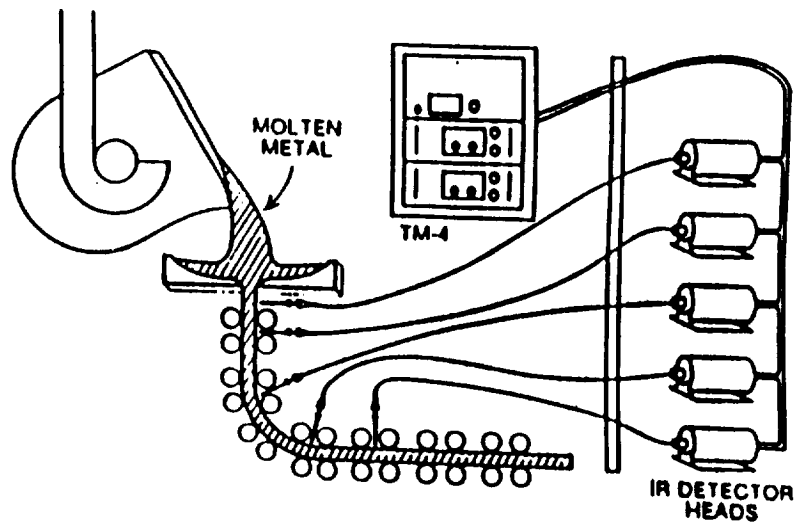
Figure 23. Continuous casting processes.
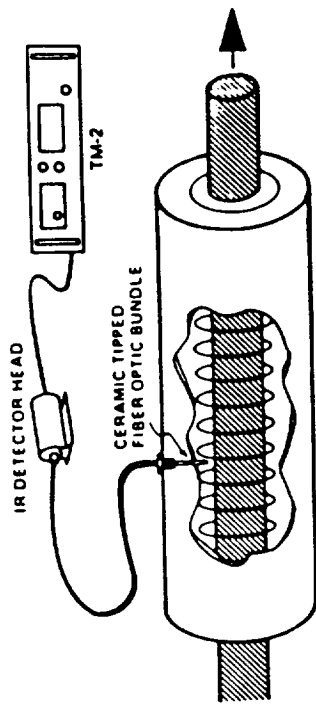
Figure 26. Monitoring steel rod continuous induction heating.

IR DETECTOR HEAD

TM-2

CERAMIC TIPPED FIBER OPTIC BUNDLE
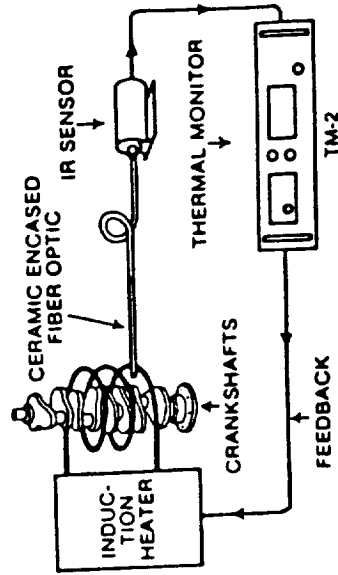
Figure 27. Controlling induction heating of automobile crankshaft.

CERAMIC ENCASED FIBER OPTIC

IR SENSOR

THERMAL MONITOR

TM-2

CRANKSHAFTS

FEEDBACK

INDUC-TION HEATER
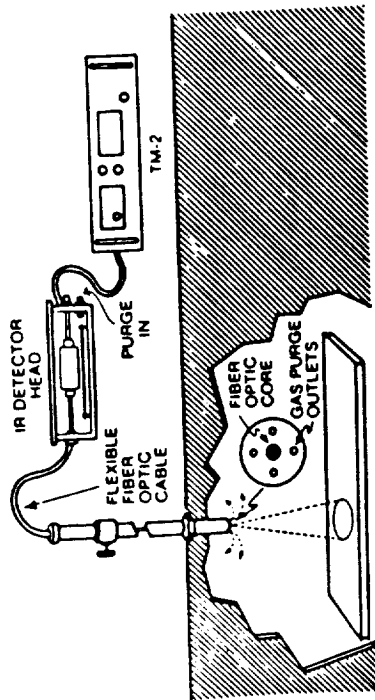
Figure 24. Annealing/heat treating processes.

IR DETECTOR HEAD

TM-2

PURGE IN

FIBER OPTIC CORE

GAS PURGE OUTLETS

FLEXIBLE FIBER OPTIC CABLE
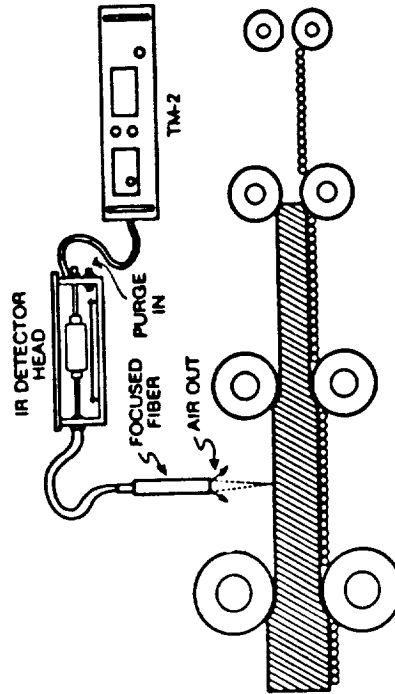
Figure 25. Roll-milling of metals.

IR DETECTOR HEAD

TM-2

FOCUSED FIBER

PURGE IN

AIR OUT
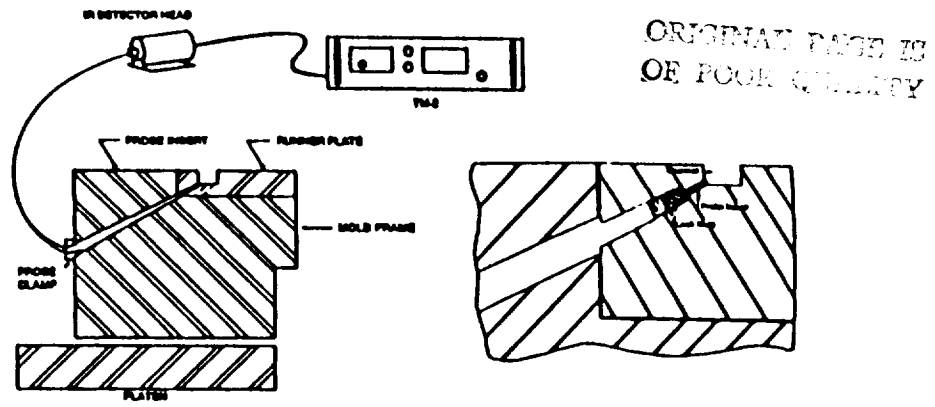
Figure 29. Metal die casting control.

Figure 29. Control of metal-working laser.

270

Figure 31. Electric motor prior to commutator fusing.

Figure 32. Detail of fusing area.

Figure 30. Electric motor commutator fusing machine.
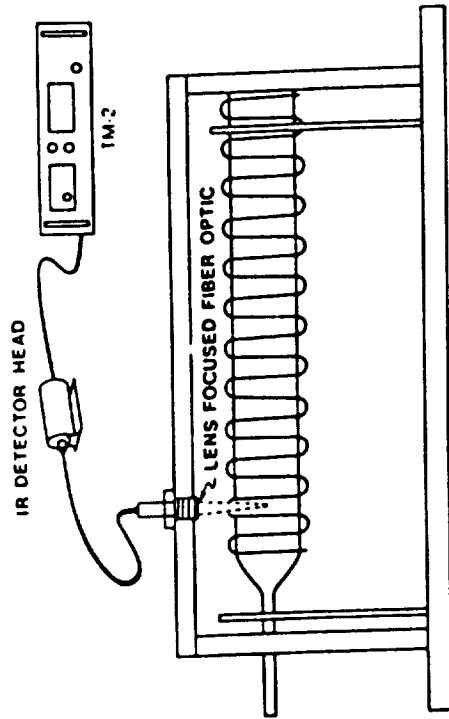
Figure 34. Semiconductor processing inside epitaxial induction oven.

IR DETECTOR HEAD

LENS FOCUSED FIBER OPTIC
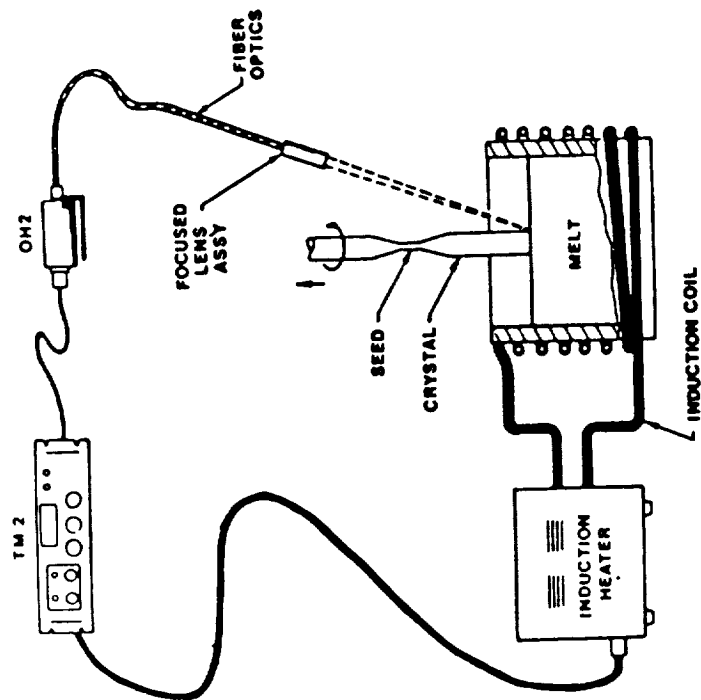
Figure 33. Crystal growth control.

FIBER OPTICS

FOCUSED LENS ASSY

SEED

CRYSTAL

MELT

INDUCTION COIL

INDUCTION HEATER

272
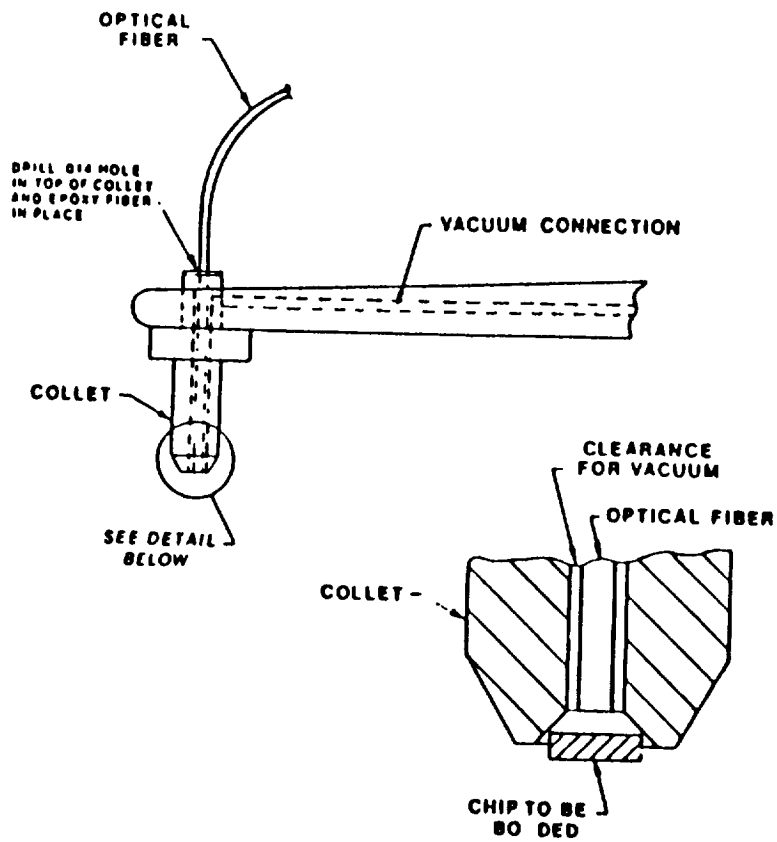
Figure 35. Eutectic bonding of semiconductor chips onto substrate.
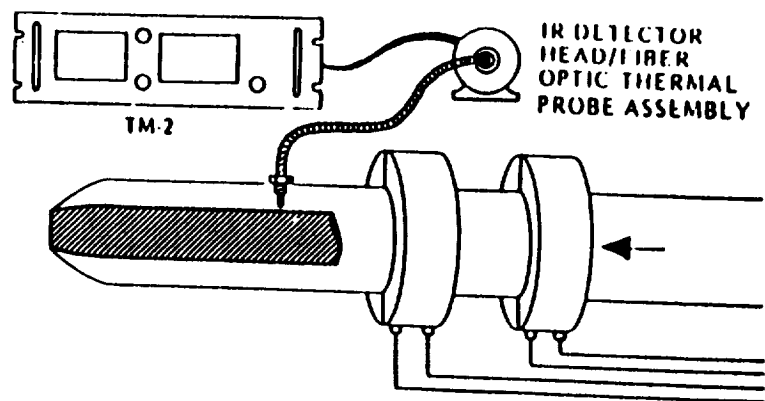
Figure 36. Polymer extrusion and injection.

273
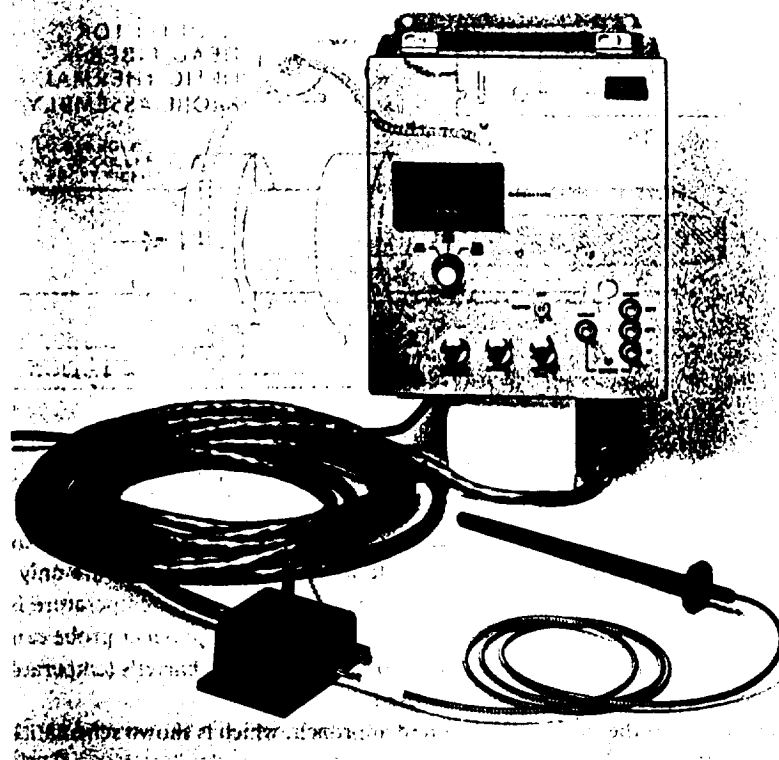
Figure 37.   Turbine blade thermal monitor.

Figure 39. Schematic of spot welder controller.
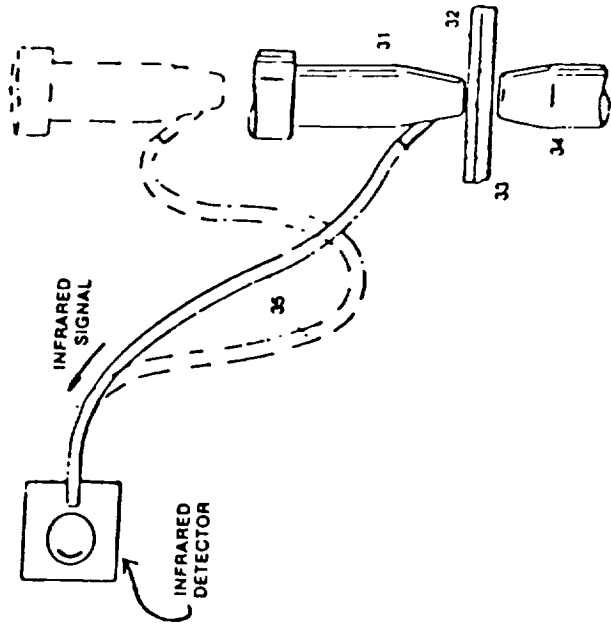
Figure 40. Detail of spot weld electrodes with fiber optics.

Figure 38. Schematic of fiber optics installation in turbine.

275

I

LASER PYROMETRY

LASER PYROMETRY

Alexander Stein

Quantum Logic Corporation
126 Andrew Avenue
Oakland, New Jersey 07436

(201) 337-3758

INTRODUCTION

This paper describes a new method of determining the emissivity of a hot target from a laser-based reflectance measurement which is conducted simultaneously with a measurement of the target radiance. Once the correct radiance and emissivity are determined, one calculates the true target temperature from these parameters via the Planck equations.

The earliest published work concerning the determination of emissivity from target reflectivity measurements dates back to 1905 when H. Rubin* employed an arc-lamp reflectometer to determine the emissivity of a (cold) gas lamp wick and then corrected the radiance reading for the hot wick with the emissivity value measured for the cold target. Liebmann** employed more advanced detection methods to determine the reflectivity (and hence the emissivity) of a hot target, i.e. at the temperature of the radiance measurement. The advent of the laser made this technique more attractive and in 1970 Traverse and Foex *** conducted reflectivity measurements with the help of a HeNe laser whose brightness on the target exceeded that of the thermal radiance. A disappearing filament pyrometer operating at the laser wavelength of 6328 Å was used to determine the target's spectral radiance at the laser wavelength with the laser on and off. The difference between the two radiance values is proportional to the target reflectivity. The proportionality constant was determined by replacing the target with a cold sample of known reflectivity.

Quantum Logic Corporation has continued this line of development and introduced a packaged, hand-held commercial instrument in 1985, and recently a fixed-mounted version with a computer interface (see Figs. 1 and 2). Patents for these devices have been awarded.

---

*Annalen der Physik   **Z.f. Physik   ***R.G.E. Tome 79,
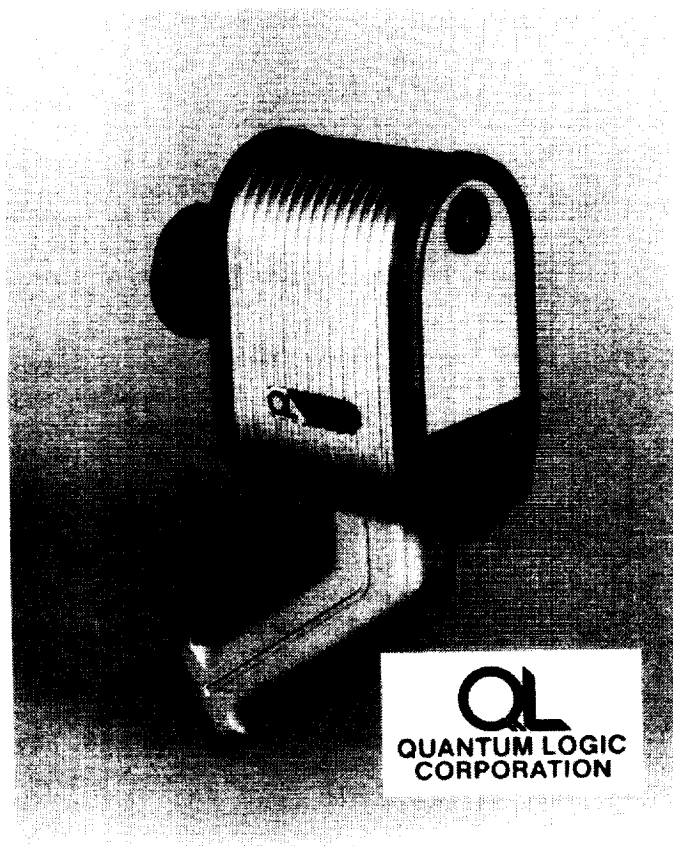   Vol 18, p 725 (1905)   Vol 63 p 404   No.10 pp 819-821

Figure 1.
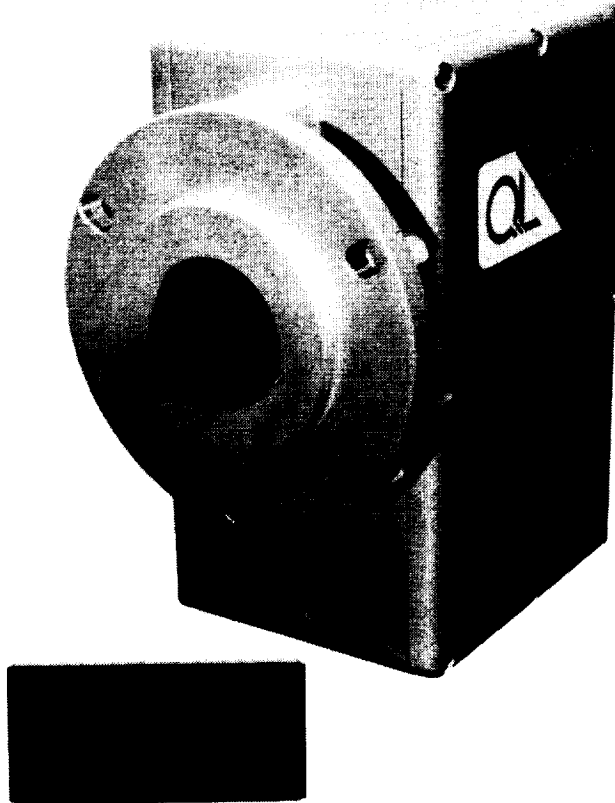
Hand-Held Laser/Microcomputer Pyrometer

Figure 2.

Fixed-Mounted Laser/Microcomputer Pyrometer

281

DESCRIPTION OF THE TECHNOLOGY

The method of determining emissivity from reflectivity relates to Kirchhoff's postulate that at thermal equilibrium all bodies in a closed environment must emit as much radiation as they absorb. This postulate leads to the conclusion that for opaque bodies

$$\varepsilon(\lambda,\phi,\theta) = 1 - \rho_H(\lambda,\phi,\theta) \tag{1}$$

where:

$\varepsilon(\lambda,\phi,\theta)$ is the spectral emissivity at wavelength λ and for emission in the direction (ϕ,θ). ϕ is the azimuth angle, and θ the elevation angle. (See Figure 3.)

$\rho_H(\lambda,\phi,\theta)$ is the directional hemispherical reflectivity for radiation incident in the direction (ϕ,θ).

Equation (1) also holds for freely radiating surfaces not in equilibrium in the thermodynamic sense.* Note that non-linear scattering processes are neglected here.

Bober and Karow** used an integrating sphere to determine the directional hemispherical reflectivity (and hence the directional spectral emissivity) of a laser-illuminated sample of UO_2 below and above the melting point.

The measurements of Traverse and Foex by contrast, were bi-directional reflectivity measurements. Implicit in their method was the assumption that the ratio of bi-directional to directional, hemispherical reflectivity was the same for the calibration target and the target of interest. In their case this was correct, since both targets were uniform diffuse scatterers, i.e. the apparent brightness of the laser spot on the target was independent of the viewing angle (ϕ,θ), see Fig. 4. Note that the radiation intensity in that case must vary as $\cos\theta$, where θ is the elevation angle of the emission direction. Each projected unit area corresponds to a physical area equal to $S/\cos\theta$ on the target surface. Thus, for the brightness of the laser spot to appear independent of angle θ, the radiated power per unit area on the target surface must vary as $\cos\theta$. Hence, the radiation emitted by the whole spot must follow the $\cos\theta$ polar distribution which is frequently called Lambertian. The closeness to the $\cos\theta$ polar distribution is indeed the measure by which one judges the closeness of a scatterer to the ideal diffuser.

---

* "Temperature" by T.J. Quinn. Academic Press, 1983, p.299
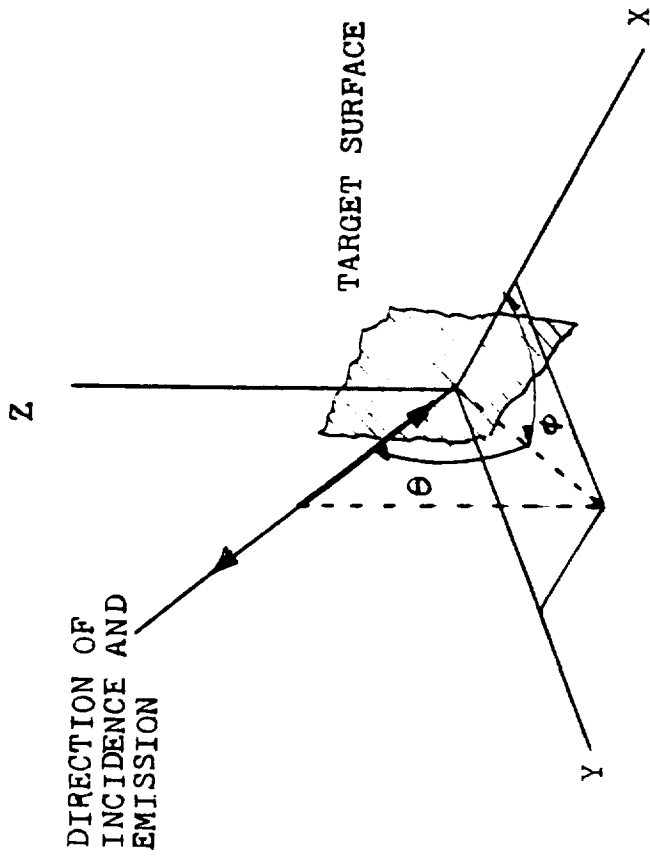** Proc. Symp. on Thermophys. Properties, 7th Series USBS; Published by ASME, NYC 1977, pp 344-350
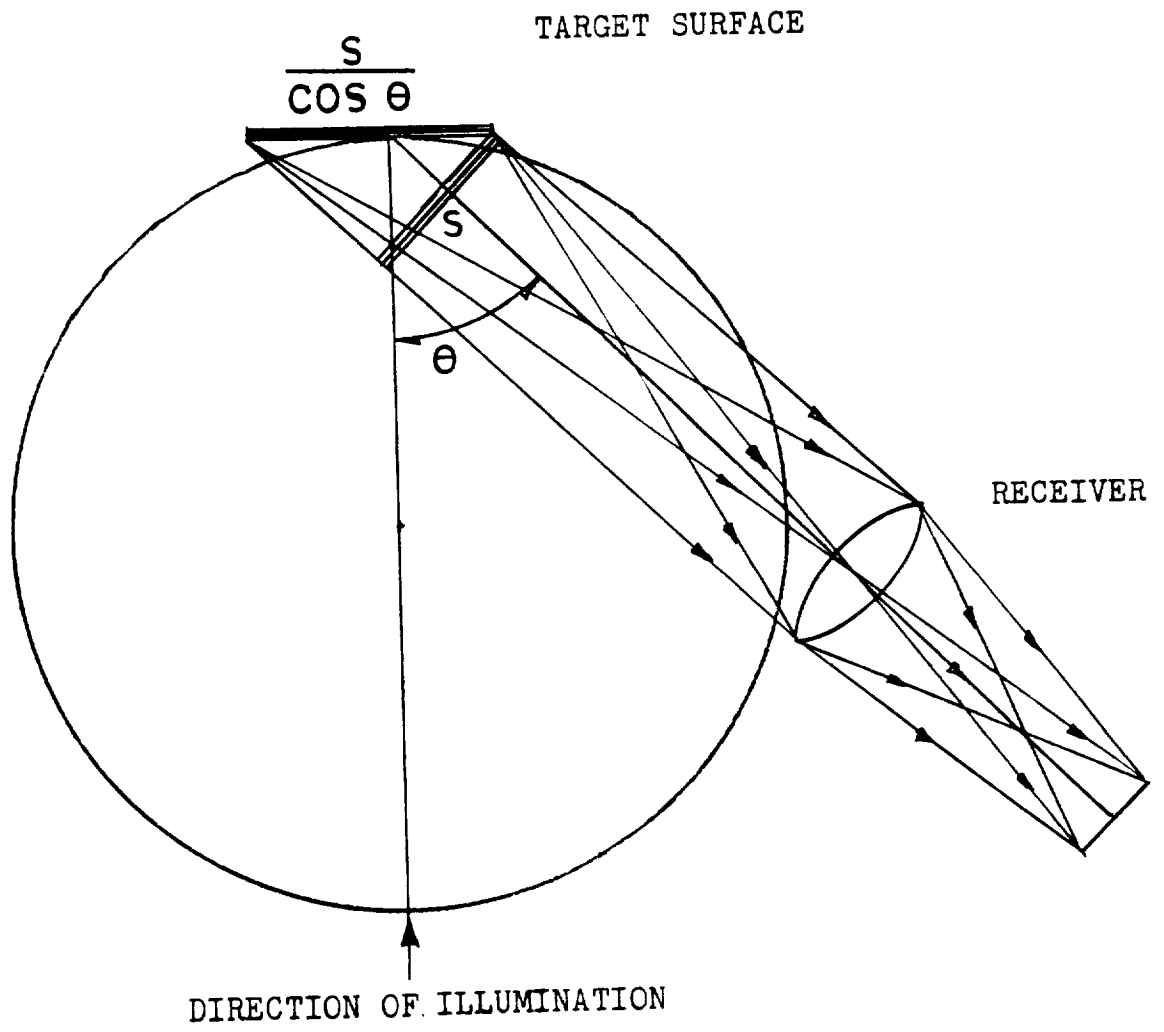
FIG 3 DIRECTIONAL REFLECTIVITY DIAGRAM

FIG. 4 LAMBERTIAN SCATTERING

Figure 5 shows the polar reflection patterns for metal furnace tubes, firebricks, and a $MgCO_3$ block used as a calibration target. Any variation from the $\cos \theta$ pattern leads to errors in the determination of th emissivity and hence errors and hence errors in the calculated temperature.

It may be shown that the calibration method of Traverse and Foex can be extended to cases where the target of interest and the calibration target are at different distances, as long as the distance ratio is known. One can thus calibrate an instrument in the laboratory at a certain target distance and then correct subsequent measurements for the actual target distance which must be determined separately.

In the hand-held Quantum Logic instrument, the target distance is determined with the help of split-image rangefinder optics. The lens is adjusted by rotation of a focusing ring which converts rotational into translational motion. The rotational motion is encoded. When the target of interest is in focus, an encoded lens position signal is fed to the instrument's micro-computer which calculates the target distance, D, via the Gaussian lens formula. Since the laser output varies with ambient temperature and other factors, it must be monitored. A monitor signal, V_2, is used to normalize the reflected laser signal. By normalizing the reflected laser signal, V_1, with the laser output signal V_2 and the square of the target distance, D, the emissivity is computed as:

$$\mathcal{E}_\lambda = 1 - C_{23} D^2 (V_1/V_2).$$

(2)

The target temperature is then obtained from the emissivity and the spectral radiance, L_λ :

$$T = \frac{hc}{\lambda k} \cdot \left\{ \ln \left(\frac{\mathcal{E}_\lambda}{C_{22}L_\lambda} + 1 \right) \right\}^{-1}$$

(3)

Here:

    h is the Planck constant

    c is the velocity of light

    k is the Boltzmann constant

    T is the target temperature in absolute units

    C_{22} and C_{23} are instrument constants.

Note that the radiance and reflectivity measurements are conducted at the same wavelength.
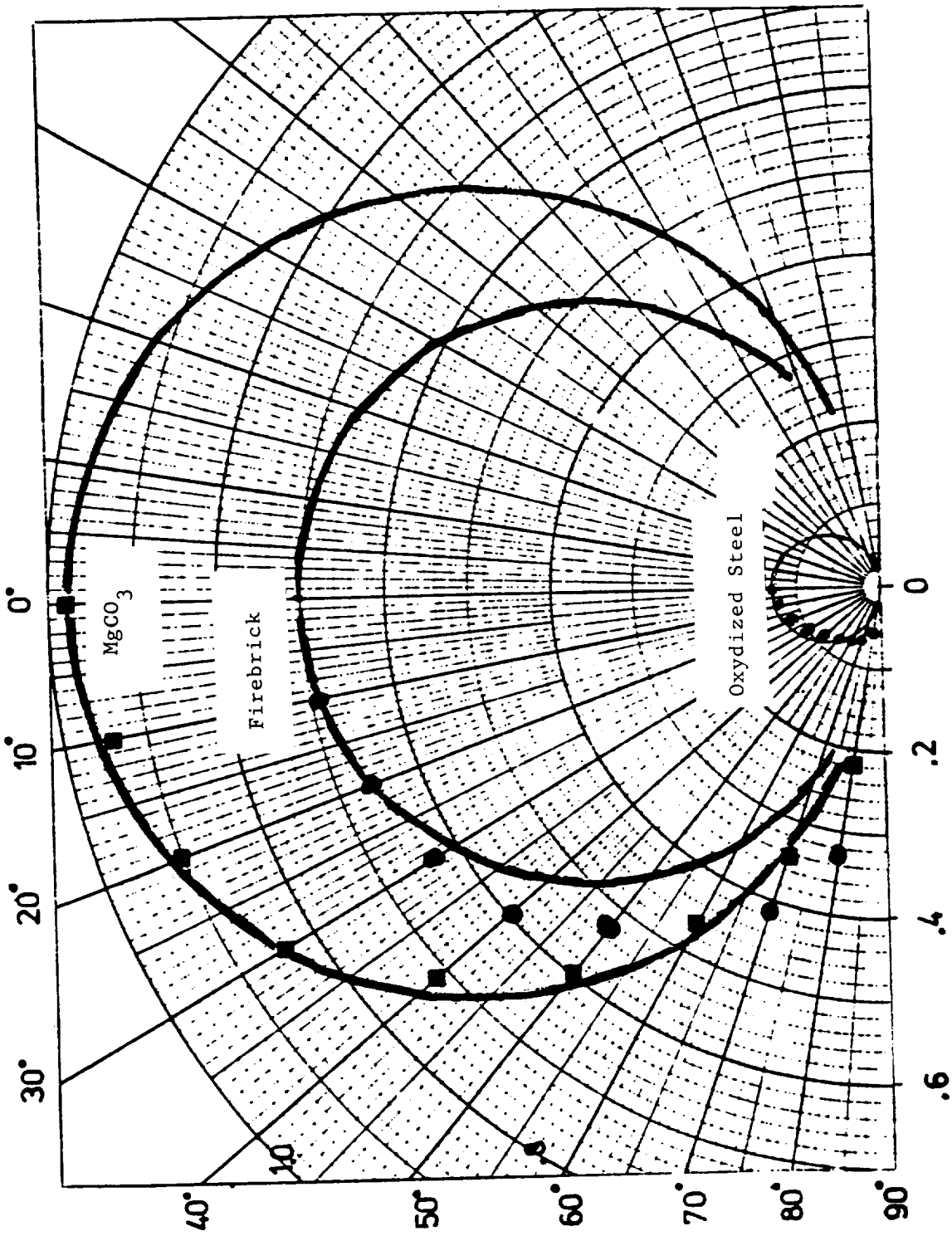
Fig. 5 Apparent Reflectivity vs. Aspect Angle

286

In summary, for uniformly diffusing targets, one can determine the emissivity from a bi-directional reflectivity measurement which must be normalized for target distance and laser power. When the target scattering deviates from the Lambertian uniformity, the emissivity determination and hence the calculated temperature values are in error.

ACCURACY ANALYSIS

To consider the effects of emissivity uncertainty or error on temperature accuracy, let us examine the dependence of temperature accuracy on the variances of the radiance and emissivity values.

By differentiating Equ.(3) one obtains the approximate expression:

$$\left|\frac{\Delta T}{T}\right| = \frac{\lambda kT}{hc} \sqrt{\left|\frac{\Delta L}{L}\right|^2 + \left|\frac{\Delta \varepsilon}{\varepsilon}\right|^2} \tag{4}$$

where $\dfrac{\Delta T}{T}$; $\dfrac{\Delta L}{L}$; $\dfrac{\Delta \varepsilon}{\varepsilon}$

represent the relative errors or uncertainties of temperature, radiance and emissivity, respectively.

It is worthwhile to study an example.

Let: $T = 1273^\circ K$ and $\lambda = 0.9$ microns.

In general, $\dfrac{\Delta L}{L} \ll \dfrac{\Delta \varepsilon}{\varepsilon}$, hence

$$\left|\frac{\Delta T}{T}\right| = \frac{\lambda kT}{hc} \cdot \left|\frac{\Delta \varepsilon}{\varepsilon}\right|$$

i.e., for our example:

$$\left|\frac{\Delta T}{T}\right| = \frac{1}{12} \cdot \left|\frac{\Delta \varepsilon}{\varepsilon}\right| \tag{5}$$

The 12-to-1 ratio between relative emissivity uncertainty
and associated temperature error expressed by Equ.(5) is
very helpful in reducing the requirements for emissivity
accuracy in pyrometer measurements. However, in many cases
of practical interest, the emissivity uncertainty is so
large that even with the above leverage, large temperature
errors are common if an actual emissivity determination is
not made. For example, take the case of iron, where the pure
material exhibits an emissivity as low as 35%, whereas the
oxidized surface can have an emissivity as high as 95% at
high temperatures. Or, the case of aluminum, where the
emissivity can vary from 10% to 40% depending upon the
degree of oxidation, surface treatment, etc. Other examples
of significant changes in emissivity caused by chemical
changes or depositions on the surface abound. It is
therefore not untypical to find relative emissivity un-
certainties of 50% and even 100%. In our example, the
associated uncorrected temperature errors would be between
$50^{\circ}C$ and $100^{\circ}C$. Laser pyrometry yields emissivity deter-
mination at least one order of magnitude better, namely: 5%
to 10%. The concomitant temperature accuracies would then be
-in our example- only $5^{\circ}C$ to $10^{\circ}C$.

Laser pyrometry is therefore particularly successful in
cases where large and unpredictable emissivity variations
are present. Here, improvements in the temperature accuracy
by one order of magnitude are not uncommon. Even more
dramatic improvements in temperature accuracy are achievable
in furnace applications as discussed in the next section.
Quantum Logic Corporation's laser pyrometers are in use in
industrial and laboratory applications where the substantial
improvements in temperature accuracy as described above are
now being realized.

The above discussion applies for materials whose polar
scattering patterns are uniformly diffuse. However, the
polar scattering patterns of many physical surfaces actually
fall between uniformly diffuse (Lambertian) and specular
(mirror-like). One can therefore not make a general calib-
ration of the above kind in such cases, since the relation-
ship between the bi-directional and the hemispherical
reflectivities is undetermined. For such cases, Quantum
Logic Corporation has designed a modification of the above
described technique. An instrument of this kind is being
developed. The technical details cannot be disclosed at
this time, since the patent application is still in review
by the U.S. Patent Office.

The general design concept adopted by Quantum Logic Corporation in each of its instruments is that of a co-axial arrangement between laser transmitter, infra-red receiver and optical viewer. This eliminates all parallax problems, but calls for a high degree of optical and electrical isolation between the transmitting and receiving systems. Of course there are many other difficulties and complications which must be overcome in producing a practical and accurate system, and this has required many years of effort.

AMBIENT RADIANCE EFFECT

Until now we have considered only free-radiating targets. In many cases of interest, however, such as inside a furnace, the target is placed in an environment where other sources of intense radiation are present. This radiation is reflected off the target of interest adding itself to the target's self-emission and leading to false temperature readings. One such case to which Quantum Logic Corporation has given particular attention is the measurement of surface temperatures for steel tubes inside pyrolysis furnaces where radiation from the furnace walls is reflected off the tubes. The range of emissivity values which we have measured for furnace tubes varies between 60% and 95% depending upon the tube alloy, the tube age and the type of fuel employed.

Let us consider one particular example where the tube temperature $T = 1273^{\circ}K$ and the hemispherically averaged ambient radiance is equal to that of a black body at $1473^{\circ}K$. At the measuring wavelength $\lambda = 0.9$ micron, the measured apparent temperature is $20^{\circ}C$ higher than the true temperature where the tube emissivity is 95%. However, where it is 60%, the apparent measured temperature is $110^{\circ}C$ higher than the true temperature. Therefore, without a knowledge of the actual tube emissivity and a correction for the reflected ambient radiance, a large uncertainty in the temperature measurement results.

The Quantum Logic Corporation Model QL1300 series of instruments are specifically designed for the measurement of tube metal temperatures in furnaces. These instruments have provision for the measurement of the ambient radiance as well as the target emissivity and radiance. By exploiting the above relationship between reflectivity and emissivity, the instrument's computer compensates each target measurement first for the ambient component and then for the (measured) target emissivity to yield the true target temperature. With the QL1300 system customers have achieved accuracies of $\pm 3^{\circ}C$ for tube metal temperatures in the $800^{\circ}C$ to $1100^{\circ}C$ range, where conventional, uncorrected instruments gave errors of between $50^{\circ}C$ to $100^{\circ}C$.

CONCLUSION

For uniformly diffuse scattering (Lambertian) targets, such as are typically encountered in furnaces, the Quantum Logic Corporation laser pyrometer technology currently in production is capable of reducing by more than one order of magnitude the non-contacting temperature measurement errors which frequently result from emissivity uncertainties and reflected ambient radiation when using conventional (passive) technology.

For non-contacting temperature measurement of general surface types, including specular (mirror-like), Lambertian, and surfaces in between, Quantum Logic Corporation is presently developing extensions of its laser technology which are expected to provide performances equivalent to, or superior to, that which has been achieved with its current technology.

NONCONTACT TRUE TEMPERATURE MEASUREMENT II

MARK C. LEE AND JAMES L. ALLEN

Jet Propulsion Laboratory, California Institute of Technology, Pasadena, CA 91109

ABSTRACT

A laser pyrometer has been developed for acquiring the true temperature of a levitated sample. The reflectivity is measured by first expanding the laser beam to cover the entire cross-sectional surface of the diffusive target. The reflectivity calibration of this system is determined from the surface emissivity of a target with a blackbody cavity. The emissivity of the real target can then be calculated. The overall system constant is obtained by passively measuring the radiance of the blackbody cavity (emissivity = 1.0) at a known, arbitrary temperature. Since the photo sensor used is highly linear over the entire operating temperature range, the true temperature of the target can then be computed. The latest results available from this on-going research indicate that true temperatures thus obtained are in very good quantitative agreement with thermocouple measured temperatures.

INTRODUCTION

Many nonintrusive thermophysical measurements require an accurate determination of the true temperature of the sample. For example, in space investigations of the undercooling behaviors of bulk metals, alloys, and refractories, it is mandatory that the measurements be made in a noncontact manner to prevent premature nucleation and crystallization. Unfortunately, conventional remote sensing techniques just detect the radiation of the sample and thus only the 'brightness temperature'; whenever the two sample surfaces show the same magnitude of radiance in the prescribed frequency band, the temperatures of the two samples are considered equal regardless of the emissivity characteristics of the

individual samples. In an improved version of this approach, an estimated single value of the emissivity for the entire temperature region of interest can be 'dialed in' in an effort to reduce the uncertainty introduced by the totally unknown emissivity. Still another approach employs a shorter-wavelength bandwidth for the photo detector to decrease the sensitivity of the calculated temperature to the emissivity [1]. However, without the in-situ real time emissivity information, it is not possible to accurately determine the true temperature of the sample.

This paper will report the latest data available from on-going research to develop a noncontact true temperature measurement technique. In addition to the conventional passive measurement of the radiation power, an active laser beam is incorporated for acquiring the reflectivity of the sample surface. The emissivity and thus the true temperature of the sample can be derived from the measured reflectivity and radiance signals.

Results previously reported showed excellent correlations between true temperatures acquired by this technique and those by thermocouple [2]. In these initial results, the pyrometer and thermocouple temperatures were normalized at one point using a different system constant for each target material. The data reported here represent a marked improvement over this initial data, with the need to normalize the data and use material dependent system constants having been eliminated. Although further refinement is needed to produce a viable technique, these latest results have reached the point of very good quantitative agreement between pyrometer and thermocouple measured temperatures.

THEORETICAL BACKGROUND

The uncertainty in a temperature measurement can be expressed as:

$$\Delta T/T = [(\Delta \varepsilon/\varepsilon)^2 + (\Delta I/I)^2]^{1/2} \lambda \kappa T/hc \tag{1}$$

where ΔT is the uncertainty in measuring the true absolute temperature T, ε is the spectral emissivity, I is the spectral radiation intensity at wavelength λ, c is the speed of light, and κ and h are the Boltzmann and Planck constants, respectively. For practical application in pyrometry, I can be closely approximated by Wien's equation:

I

$$I(\lambda,T) = c_1\, \varepsilon(\lambda,T)\lambda^{-5} exp(-c_2/\lambda T)$$

(2)

where c_1 and c_2 are constants with c_1 being 3.7403×10^{-4} watt·μm² and c_2 being 1.4384×10^4 μm°K. Therefore, $I(\lambda,T)$ is in watts/m²·μm.

Without knowing the detailed behavior of ε as a function of λ and T, shorter wavelengths are traditionally chosen so that I is more sensitive to the exponential term in equation (2). This manipulation at least reduces the relative contribution of $\Delta\varepsilon$ to the overall ΔT. In addition, by assuming ε is constant over the wavelength and temperature range of interest, the quotients of two or more I's can be taken to eliminate ε from consideration completely. The theoretical limitations of these so called 'multiple color pyrometry' approaches and their derivatives were reviewed in depth recently by Coates and Nordine [3,4]. Two conclusions indicated by these studies are that 1) the single color pyrometer provides the least experimental error in true temperature measurement, and 2) further improvements are needed to provide true temperature data in order to meet more stringent requirements in the next generation of thermophysical measurements.

In this paper a 'laser pyrometer' technique will be presented for simultaneous measurements of emissivity and radiation. In this technique, the surface emissivity, ε_s, of a calibration target with a blackbody cavity can be obtained by using the radiance channel of the pyrometer to alternately measure the radiance signal of the calibration target surface, V_{rs}, and the radiance signal of the blackbody cavity, V_{rb}. By the definition of emissivity:

$$\varepsilon_s = V_{rs}/V_{rb}$$

(3)

The reflectivity, Γ_s, of the calibration target surface is given by :

$$\Gamma_s = V_{\ell s}/V_{\ell c}$$

(4)

where $V_{\ell s}$ is the laser (reflectivity) channel signal of the calibration target surface and $V_{\ell c}$ is the laser channel calibration factor. By Kirkhoff's law, $\varepsilon_s = 1 - \Gamma_s$, and the calibration factor, $V_{\ell c}$, can then be found:

$$V_{\ell c} = V_{\ell s}/(1 - \varepsilon_s)$$

(5)

Once $V_{\ell c}$ is known, the spectral emissivity of a real target, ε_t, can then be calculated:

$$\varepsilon_t = 1 - V_{\ell t}/V_{\ell c} \tag{6}$$

where $V_{\ell t}$ is the measured laser (reflectivity) signal of the real target.

A conventional passive radiance measurement yields the radiance signal of the target, $V_{rt} = a_1 I(\lambda, T)$. From equation (2),

$$T(^oK) = 15916 / \{ln[\varepsilon(\lambda,T)/C_{sys} V_{rt}]\} \tag{7}$$

where C_{sys}, the system constant, can be obtained by calibrating the laser pyrometer against the blackbody cavity of the calibration target at a known, arbitrary temperature in the following manner.

The system constant can be calculated by solving equation (7) for C_{sys} and substituting the appropriate parameters as measured using the blackbody calibration target. This can be done in two ways:

$$C_{sys} = \varepsilon_s / V_{rs} \, exp \, (C/T), \tag{8}$$

or

$$C_{sys} = \varepsilon_b / V_{rb} \, exp \, (C/T). \tag{9}$$

ε_s is the emissivity of the calibration target surface, and $\varepsilon_b = 1$ is the assumed emissivity of the blackbody cavity. V_{rs} and V_{rb}, are the radiance signals of the calibration target surface and blackbody cavity, respectively. C is the constant 15916, and T is the true temperature as determined by thermocouple. A comparison of these two values of the system constant will provide a measure of the validity of this approach.

EXPERIMENTAL APPROACH

The prototype laser pyrometer developed consists of a passive radiance channel and an active laser channel, respectively. For all targets, chromel-alumel thermocouples were placed in intimate thermal contact at appropriate positions on the surfaces of the samples. This type of thermocouple places an upper limit on the calibration to not exceed approximately 1100°C at the present time. Each sample

I

was then heated by an electromagnetic coil powered by a Lepel 60kW RF generator. The RF coil is enclosed in a stainless steel belljar which can be evacuated to a diffusion pump vacuum.

Originally, shielded thermocouples were used to minimize possible RF effects while monitoring the target temperatures. Further tests indicated that exposing the thermocouple junction and placing it in direct contact with the sample surface produced more noise, but provided less of a heat sink, and gave a more accurate measurement of the target surface temperature than using shielded thermocouples.

The pyrometer views all targets through an optical window made of quartz which is transparent to .904 μm laser infrared. The laser is pulsed at 2000 pps with a time constant of 200ns. Depending on applications, the data acquisition rate can be as fast as 5×10^6 data per second. However, in this initial calibration phase, each datum point represents an integration of 50ms or 100 returned pulses. The radiance signal is also integrated for 10ms before digitization. The radiance and reflectivity signals are sampled sequentially, and each data pair is sent at one second intervals to a PDP 11/23 computer for further processing.

For a typical calibration run, the belljar is first purged with high purity argon gas and evacuated to mechanical pump vacuum. The procedure is repeated twice before the belljar is backfilled with 10 psia argon gas. The sample is then heated up by incrementally increasing the RF power. Once the target temperature as monitored by the thermocouple has stabilized at each increment, the pyrometer is then refocused to maximize the reflectivity signal. When the pyrometer is properly focused, fifty data points are taken by the computer and averaged. Each processed reflectivity datum point, therefore, represents an average of 5,000 returned raw laser pulses. The schematic for this laser pyrometer calibration system is shown in figure 1.

Originally the laser channel was calibrated by measuring the reflected laser signal from a gold-coated sphere (reflectivity = 0.99). In order to improve upon previous results, a method had to be established that 1) eliminated the need for a gold-coated target whose reflectivity must be independently verified, and 2) provided the laser channel calibration and system constant using the same experimental apparatus and optical paths as would be used with the real targets.

Therefore, to permit a calibration procedure as described in the previous section, two types of targets were made: 1) a blackbody calibration target to determine $V_{\ell s}$ and C_{sys}, and 2) spherical targets of different materials to allow the comparison of

pyrometer and thermocouple temperatures. A cylindrical calibration target was made from stainless steel with a blackbody cavity in the center. The diameter of the cavity opening is the same as the diameter of the spherical targets (0.95cm), and the outside diameter allows more than enough room for the pyrometer to view the surface without overlapping the outer edge or the cavity edge at the center. The pyrometer can be moved to alternate the point of focus between the surface and the cavity. All surfaces have been throughly sand-blasted to make all pyrometer viewing areas as diffuse as possible.
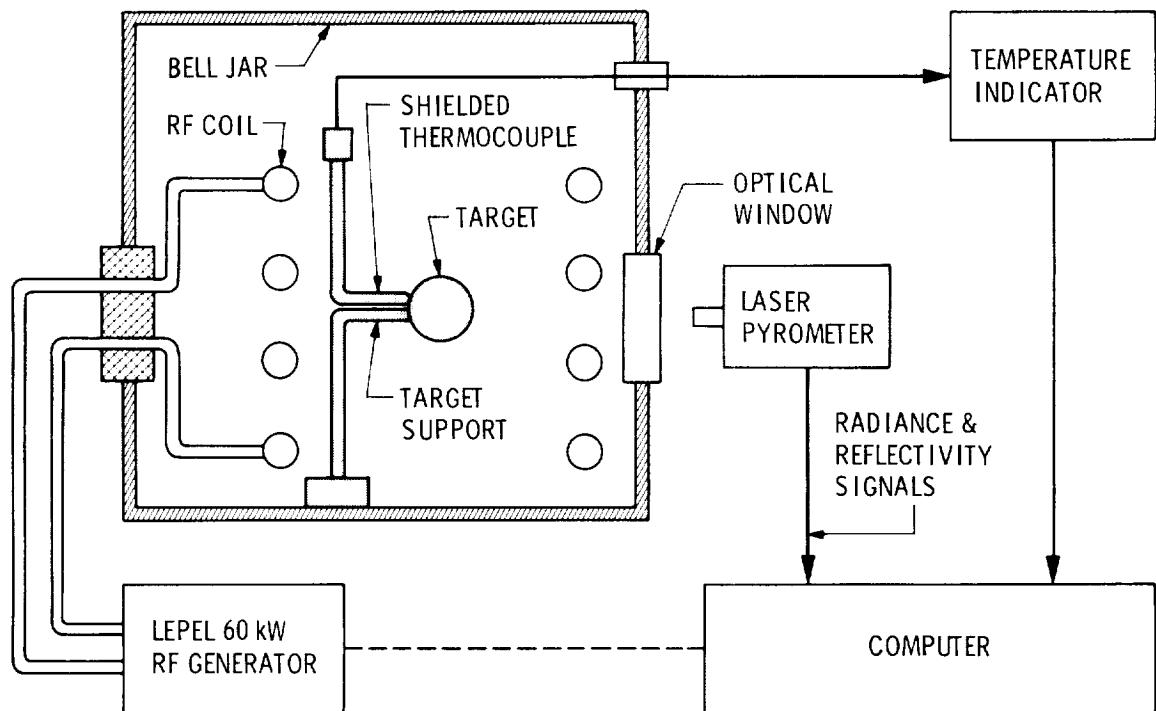
Figure 1. Laser pyrometer calibration system schematic.

The calibration target is placed in the coil at the same position relative to the quartz window and pyrometer using the same atmosphere and pressures as would be used for the spherical targets. The calibration target was initially oxidized in order to turn on the radiance channel of the pyrometer at about 750°C. Therefore, to follow the procedure as described in the previous section, the laser pyrometer

monitors three parameters of the blackbody calibration target: the radiance signal of the surface, V_{rs}, the laser (reflectivity) signal of the surface, $V_{\ell s}$, and the radiance signal of the blackbody cavity, V_{rb}. A schematic of the calibration target, the pyrometer and the pertinent calibration parameters is shown in figure 2.
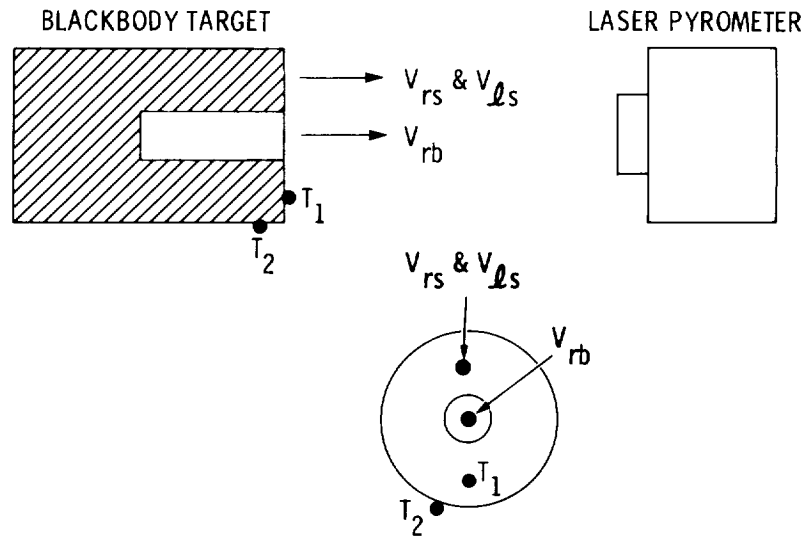

Figure 2. Calibration target schematic and parameters.

The calibration target has a high thermal mass to minimize errors due to temperature gradients on the surface. Two chromel-alumel thermocouples are placed at locations T_1 and T_2 to monitor the temperature of the calibration target as it is heated in the RF coil. T_1 is located at the same radius but opposite the focal point where the pyrometer monitors the calibration target surface. T_2 allows any gradients between the outer edge and the front surface to be monitored.

Once $V_{\ell c}$ and C_{sys} have been determined from the blackbody calibration, the true temperatures of the spherical targets can be measured. Three target materials were used: stainless steel, titanium, and carbon. Because the spectral emissivity can depend strongly on the viewing angle of the spherical surface, the two metal targets were thoroughly sand-blasted to make the surfaces as diffuse as possible. Also, the two metal targets were oxidized to activate the radiance channel at around 750°C.

RESULTS AND DISCUSSION

Figures 3 and 4 show the reflectivity calibration factor, $V_{\ell c}$, and the system constant, C_{sys}, respectively, as functions of temperature as obtained from the blackbody calibration target. The temperatures were obtained from the chromel-alumel thermocouple located at T_1. For the ideal pyrometer system, it is most desirable that both $V_{\ell c}$ and C_{sys} be independent of temperature and material. In both cases, $V_{\ell c}$ and C_{sys} are both clearly temperature dependent. Even though $V_{\ell c}$ and C_{sys} vary with temperature, the average values of each were used over the entire temperature range for each spherical target. By forcing $V_{\ell c}$ and C_{sys} to be constants, a comparison of the current data to the ideal can be made. Further investigation is needed to determine if this dependence can be decreased or eliminated.
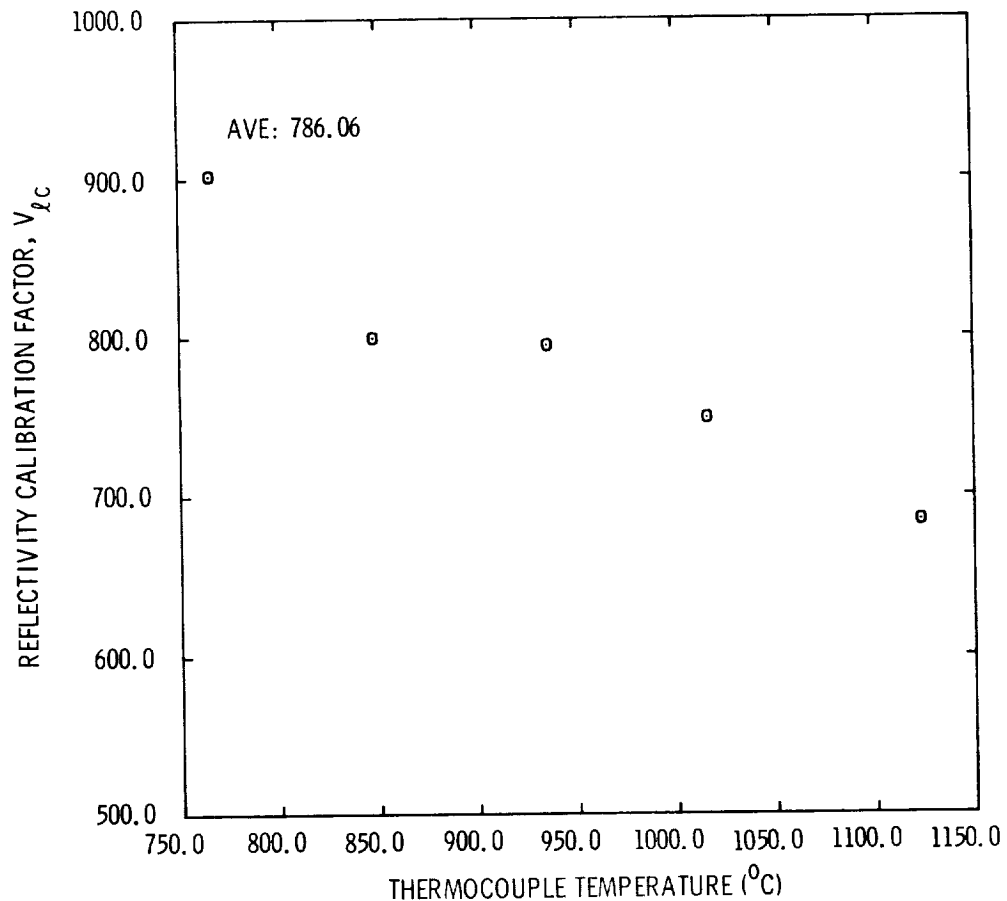

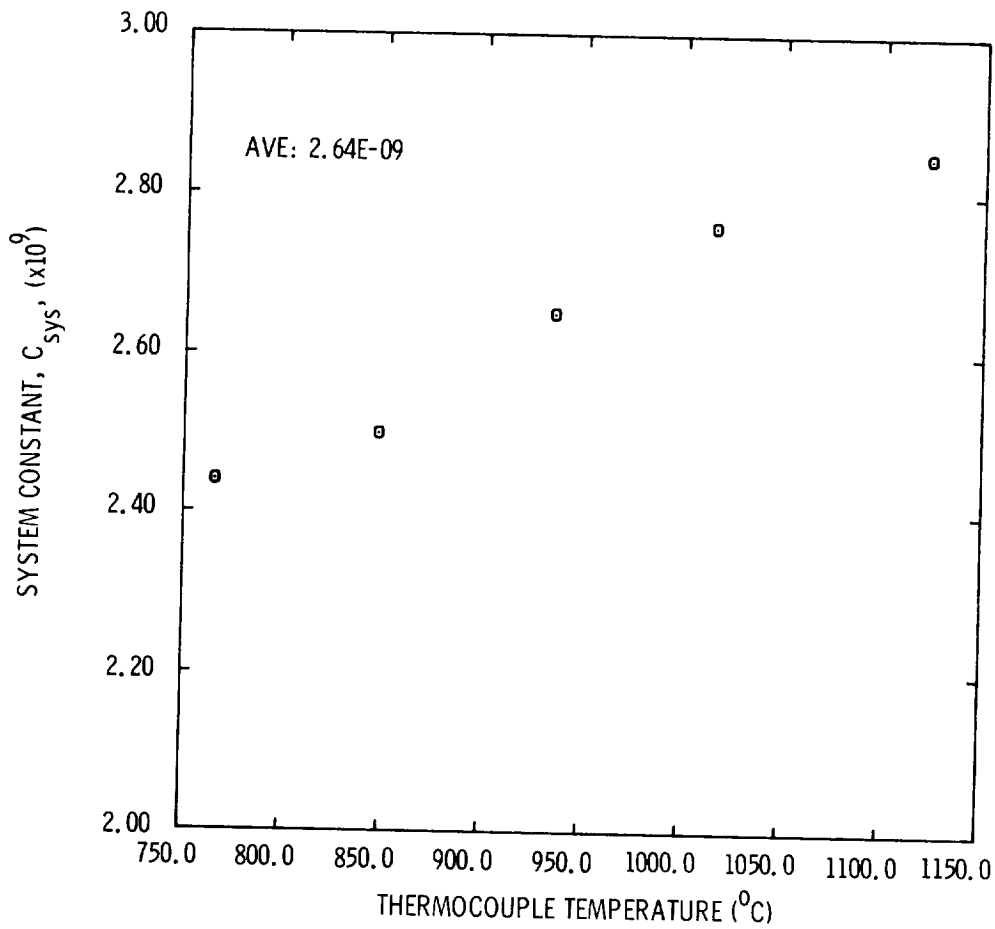Figure 3. Reflectivity calibration factor, $V_{\ell c}$, as a function of thermocouple temperature.

Figure 4. System constant, C_{sys}, versus thermocouple temperature.

$V\ell c$ varied between 684.0 and 902.2 yielding an average of 786.06. C_{sys} varied between 2.86×10^9 and 2.43×10^9 yielding an average of 2.64×10^9. C_{sys} was calculated using both equations (8) and (9) with the discrepancy between the individual data points being 1.2% in the worst case and averaging less than 0.4%. This kind of agreement indicates that the approach taken for calibration is quite valid.

The raw data from the passive radiance channel for all three targets are shown in figure 5. In general they closely follow a curve with increasing slope at higher temperatures.
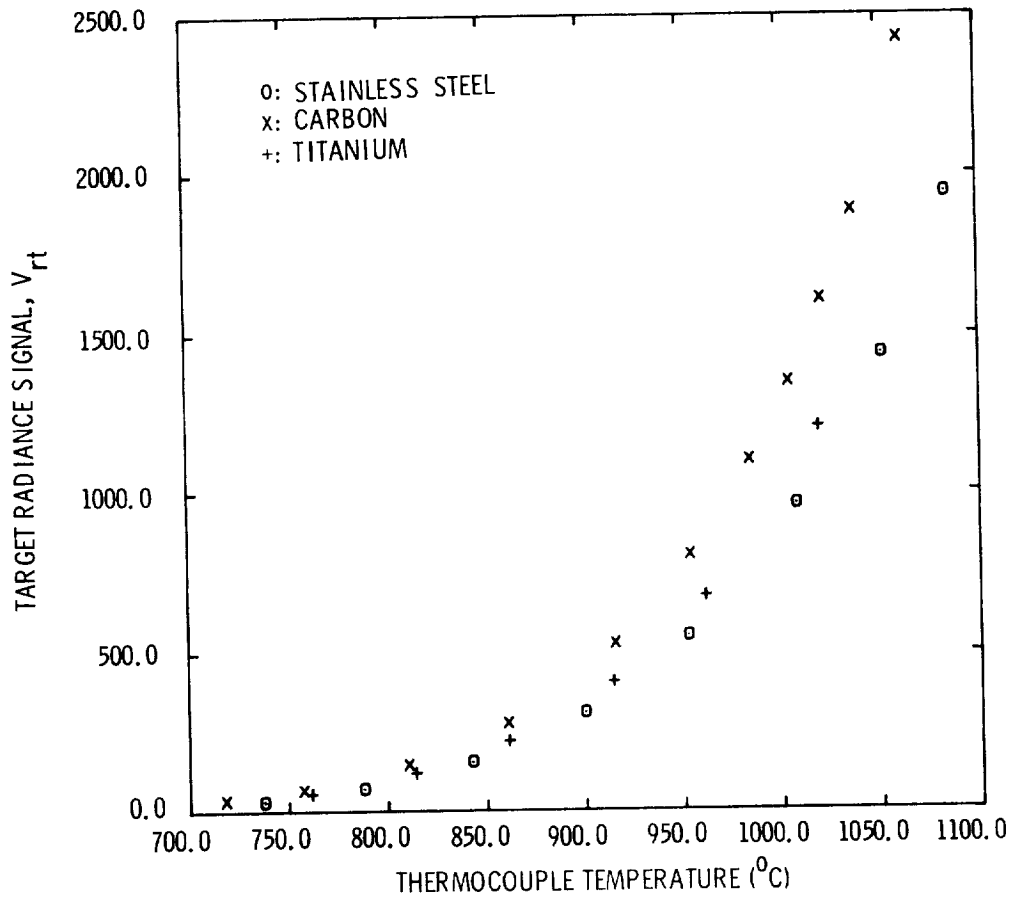

Figure 5. Raw radiance data versus thermocouple temperature.

Using the average reflectivity calibration factor , $V_{\ell c} = 786.06$, and the raw reflectivity data for each sample, the emissivity for each target can then be calculated using equation (6). The data for all three targets are plotted in figure 6. Note that the emissivity of the stainless steel target increased with temperature.

This process was completely reversible with the emissivity decreasing as the target cooled down. This is completely expected since the emissivity of iron oxide increases with temperature. The emissivity of carbon decreases with increasing temperature. which is just the opposite of what was observed. The carbon became more and more pitted as the temperature increased probably due to residual oxygen in the target or the atmosphere. The increase in the carbon emissivity was non-reversible and remained at the higher level after the target had cooled down. It is important to note, however, that any temperature variation of the emissivity is irrelevant in this technique since it is measured in-situ and in real time.
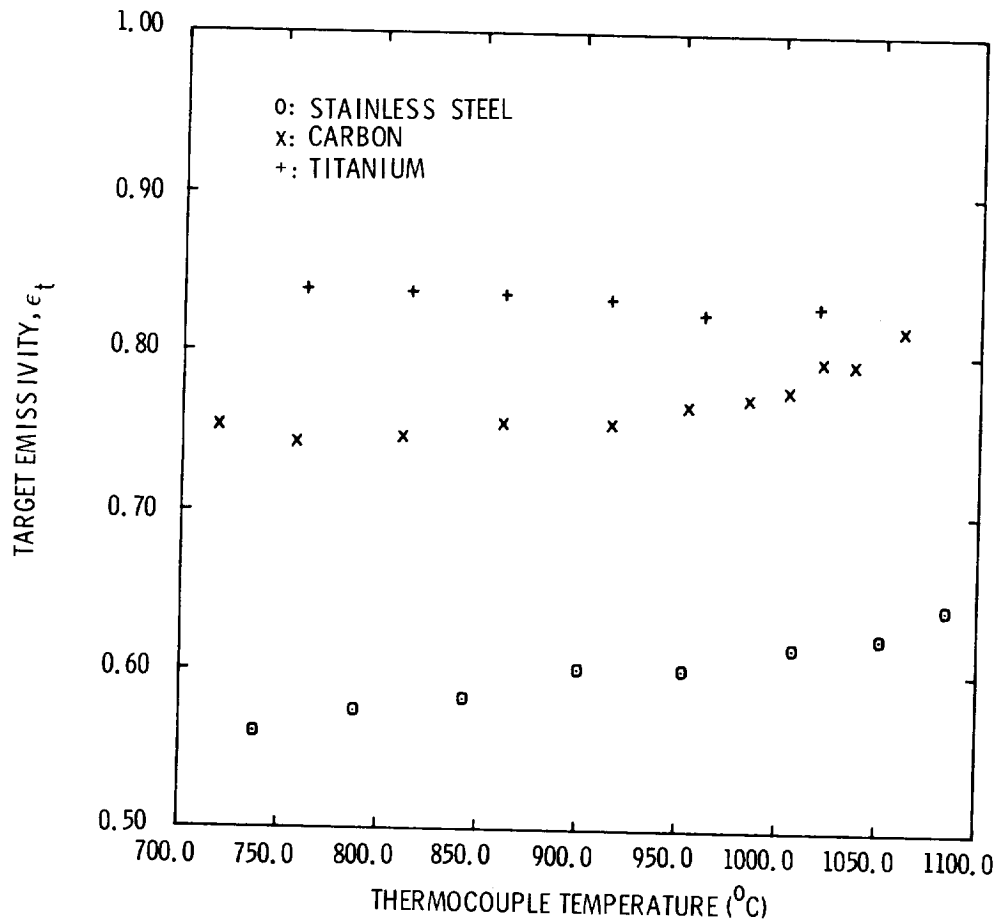

Figure 6. Target emissivity, ε_t, as a function of thermocouple temperature.

Using the average system constant, $C_{sys} = 2.64 \times 10^9$, for all targets, pyrometer temperatures can be plotted against thermocouple temperatures, as shown in figure 7. The 45° line represents the one-to-one correspondence between the temperatures. The pyrometer temperatures for the carbon are consistently too high while those for titanium are consistently too low. The stainless steel pyrometer temperatures fall almost on the line. The fact that the blackbody calibration target was also made of stainless steel suggests that the system constant has a slight material dependence.
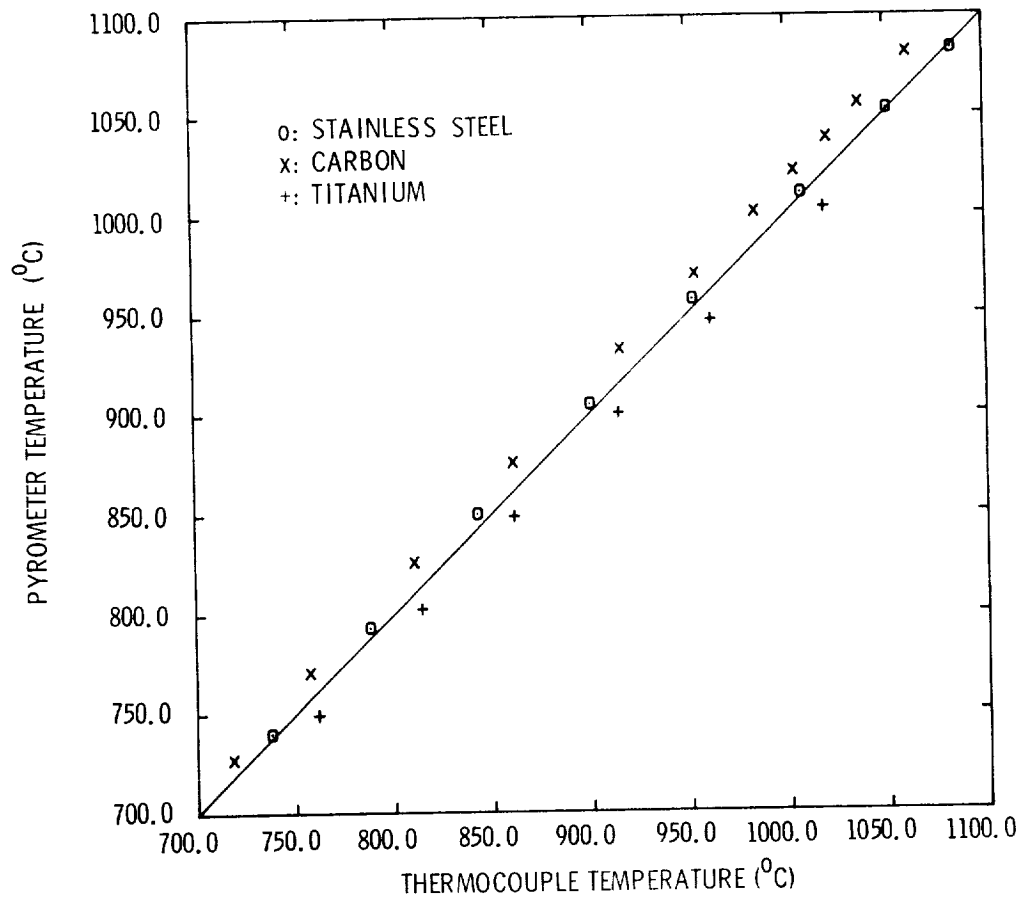

Figure 7. Pyrometer temperature versus thermocouple temperature.

However, these deviations are not very large. The carbon target produced the largest errors, with the worst ΔT being 19.5°C. The worst discrepancies for all three targets were 1.8% for carbon, -1.6% for titanium, and 0.87% for stainless steel. These values are approaching the accuracies with which the thermocouple measurements can be made. For example, the thermocouple lead wires provide a heat sink for the target and the thermocouple junction. This was evident for all targets from the fact that the lead wires remained black even when the junction and target were glowing very brightly. The thermocouple junctions were spot welded to the stainless steel and titanium targets, which was not possible with the carbon target. Thus, the thermocouple junction on the carbon target could very easily have been at a slightly lower temperature than the target itself. Additionally, the titanium target reacted quite strongly with the thermocouple junction and the argon atmosphere which could also affect the thermocouple readings.

Two assumptions were also made regarding the blackbody target calibration. First of all, it was assumed that no temperature gradient existed on the front surface of the calibration target between T_1 and the pyrometer view point. Secondly, the assumption was made that it was valid to extend the calibrations using the flat surface of the calibration target to the curved surfaces of the spherical targets. This assumption is only valid if all surfaces were perfectly diffusive.

Also, average values of the reflectivity calibration factor and the system constant were used for the entire temperature range even though both exhibited definite temperature dependences. The final results indicate that the pyrometer temperatures are insensitive to temperature variations in both $V_{\ell c}$ and C_{sys} which is exactly what is desired. Therefore, it is not obvious that any temperature or material dependences exist in either parameter. In light of the error contributing factors mentioned above, it is very promising that the discrepancies between the thermocouple and pyrometer temperatures are less than 2%.

CONCLUSIONS

A noncontact true temperature measurement technique has been presented, which employs the principle of simultaneous measurement of the radiance and reflectivity of the target sample. Current data represent a definite improvement over previously reported results and indicate that the material dependence of the

system constant has been greatly reduced with overall discrepancies in temperatures of less than 2%. The progress made thus far indicates that further refinement of this laser pyrometry technique will provide an improvement in accuracy of at least an order of magnitude as compared to passive techniques.

ACKNOWLEDGEMENTS

REFERENCES

1. M. C. Lee and J. L. Allen, Materials Research Society Symposia Proceedings, 87, 285 (1987).

2. M. B. Frish, M. N. Spencer, N. E. Wolk, J. S. Werner, and H. A. Miranda, Jr., Physical Sciences Inc. Final Report to Jet Propulsion Laboratory/NASA titlted, "Multi-Color Pyrometer for Materials Processing in Space", July 15, 1986.

3. P. B. Coates, Metrologia 17, 103 (1981).

4. P. C. Nordine, High Temp. Sci., 21, 97 (1986).

Laser Diagnostics for Combustion
Temperature and Species Measurements

Alan C. Eckbreth
United Technologies Research Center
Silver Lane
East Hartford, Connecticut   06108
(203) 727-7269

Introduction

Up to this point the workshop has focused primarily on surface or volume

thermometry using radiative emission techniques. In this presentation, we

will shift direction and focus on measurements that can be made in the gaseous

phase of temperature and/or species concentrations. Laser optical diagnostic

techniques will be emphasized [Refs. 1-4]. As shown in Panel 1, there are

many advantages of using lasers to diagnose combustion processes. Many of

these are, of course, self explanatory. Among the more important capabilities

is the absence of an upper temperature limit due to the fact that nothing of a

physical nature needs to be inserted in the combustion process under

examination. The techniques, that will be described, are all sufficiently

fast that measurements are possible under single pulse excitation, with a

single pulse typically lasting on the order of a microsecond or less. The

techniques are also concurrently spatially precise, that is these are

pointwise measurements. And the techniques are unambiguous in that they

provide in-situ measurements. For example, measurements do not have to be

corrected as in the case of a thermocouple for radiation or conduction

effects. Among the chief disadvantages is the fact that optical access is
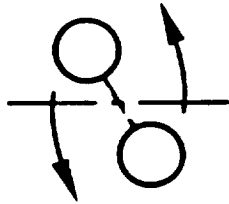
LASER DIAGNOSIS OF COMBUSTION

- Advantages
  - Remote
  - Non perturbing
  - High temperature capability
  - Fast
  - Spatially precise
  - Unambiguous

- Disadvantages
  - Optical access
  - Expensive
  - Signal strength
  - Interferences

PANEL 1

306

required. In practical devices this is often a major disadvantage in that such access may be difficult to provide. Another disadvantage, certainly compared with the radiation pyrometric techniques that have been discussed, is that these techniques are expensive. In addition to detection equipment somewhat similar to that used in radiation techniques, these methods also require one or more sophisticated laser sources. Another disadvantage resides in signal strength. The most ubiquitous technique, spontaneous Raman scattering, tends to be the most generic, but due to its weakness, it's typically constrained to look at only the major constituents. Stronger techniques, such as fluorescence, are suited only to examining a few species whose optical absorptions are spectrally accessible. In practical combustion environments, interferences may severely limit the applicability of certain of the techniques. In general, no single technique can provide temperature and species measurements of all of the constituents and a combination of complementary techniques needs to be applied. The techniques to be described derive information of temperature and concentration by interrogating individual rotational-vibrational states of the target molecules.
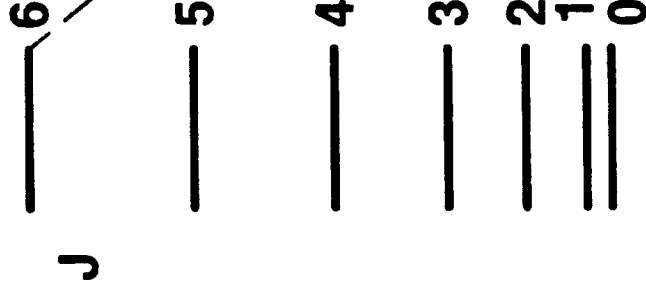
As a review, Panel 2 demonstrates that molecules are free to rotate with energies prescribed by the rotational quantum number J, molecules are free to vibrate with energies prescribed by the vibrational quantum number v, and molecules may have varying degrees of electronic excitation. However, at temperatures typical of most combustion processes, the degree of electronic excitation is relatively weak and most of the molecules reside in the ground electronic state as shown in the Panel 3. Also shown in the panel is the manner in which the vibrational and rotational state populations are
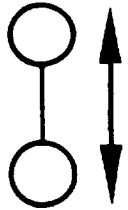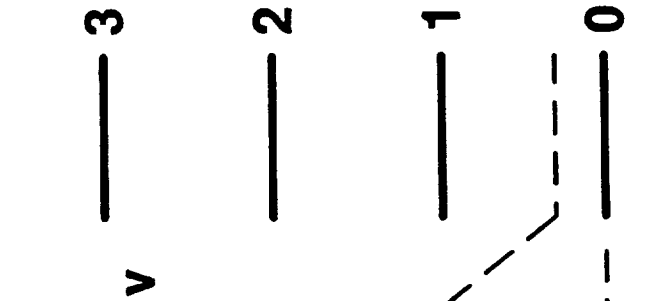
MOLECULAR ENERGY LEVELS

Rotation

Vibration

Electronic

$$E_r = hcB\ J(J + 1)$$

J

6

5

4

3

2

1

0

$$E_v = hc\,\omega_e\,(v + 1/2)$$

v

3

2

1

0

A

X

PANEL 2

308
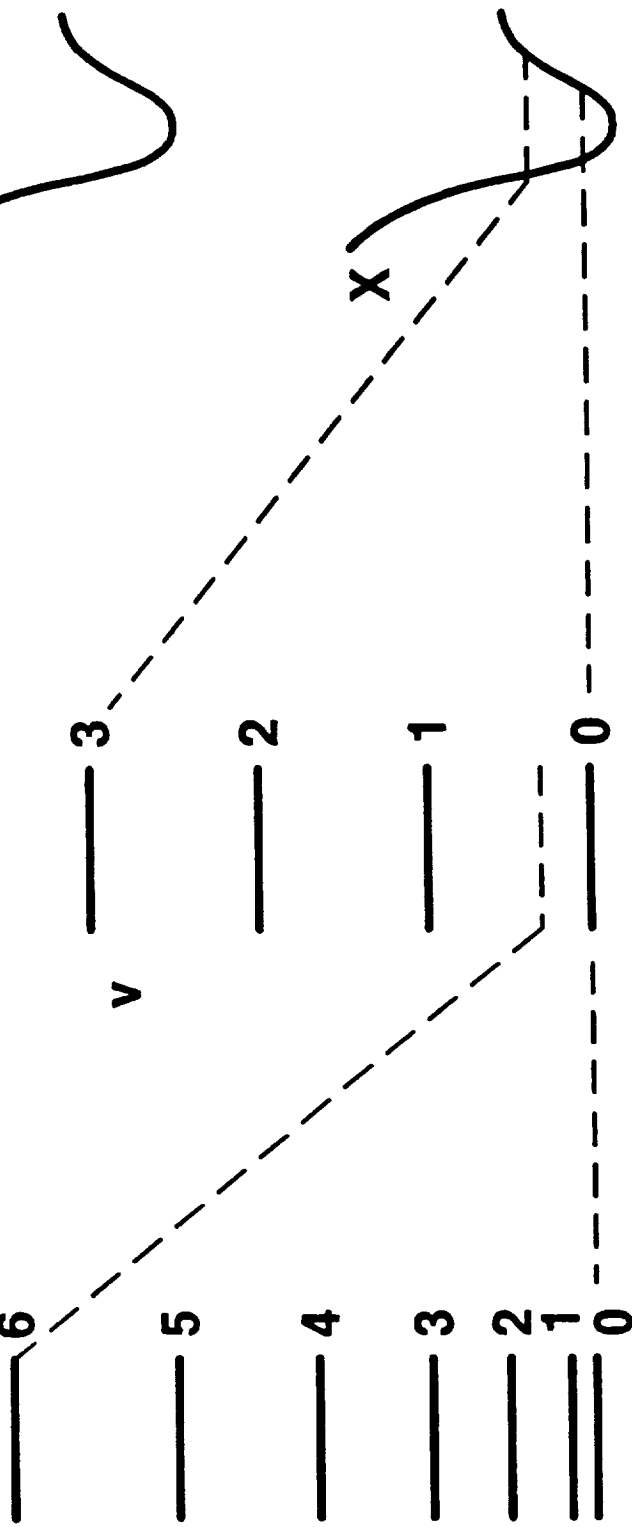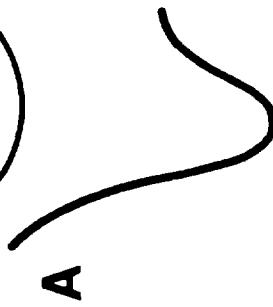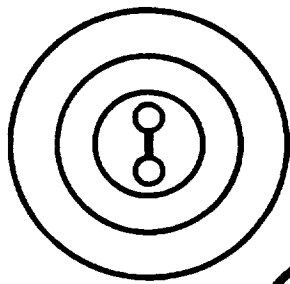
MOLECULAR POPULATION PARTITIONING

- **Electronic state population**

$$n_n = \frac{n}{Q_n} \, g_n \, e^{-\epsilon_n/kT} \qquad \text{generally } \epsilon_n/kT \gg 1$$

$$\therefore n_0 = n$$

- **Vibrational state population**

$$n_v = \frac{n}{Q_v} \, g_v \, e^{-\epsilon_v/kT}$$

- **Rotational state population**

$$n_J = \frac{n_v}{Q_J} \, g_J \, e^{-\epsilon_J/kT}$$

- **Individual vibration-rotation state population**

$$n_{vJ} = n \, \frac{g_v}{Q_v} \, \frac{g_J}{Q_J} \, e^{-(\epsilon_v + \epsilon_J)/kT}$$

PANEL 3

distributed in accordance with Boltzmann statistics. Putting these expressions together, one sees that the distribution over the individual vibrational-rotational states is highly temperature dependent. This then forms the basis for diagnostic utilization. By measuring the relative populations in several of the vibrational-rotational states, one can deduce the temperature. By making an absolute measurement of the population in any one given state, and knowing the temperature, one can then deduce the total species concentration.
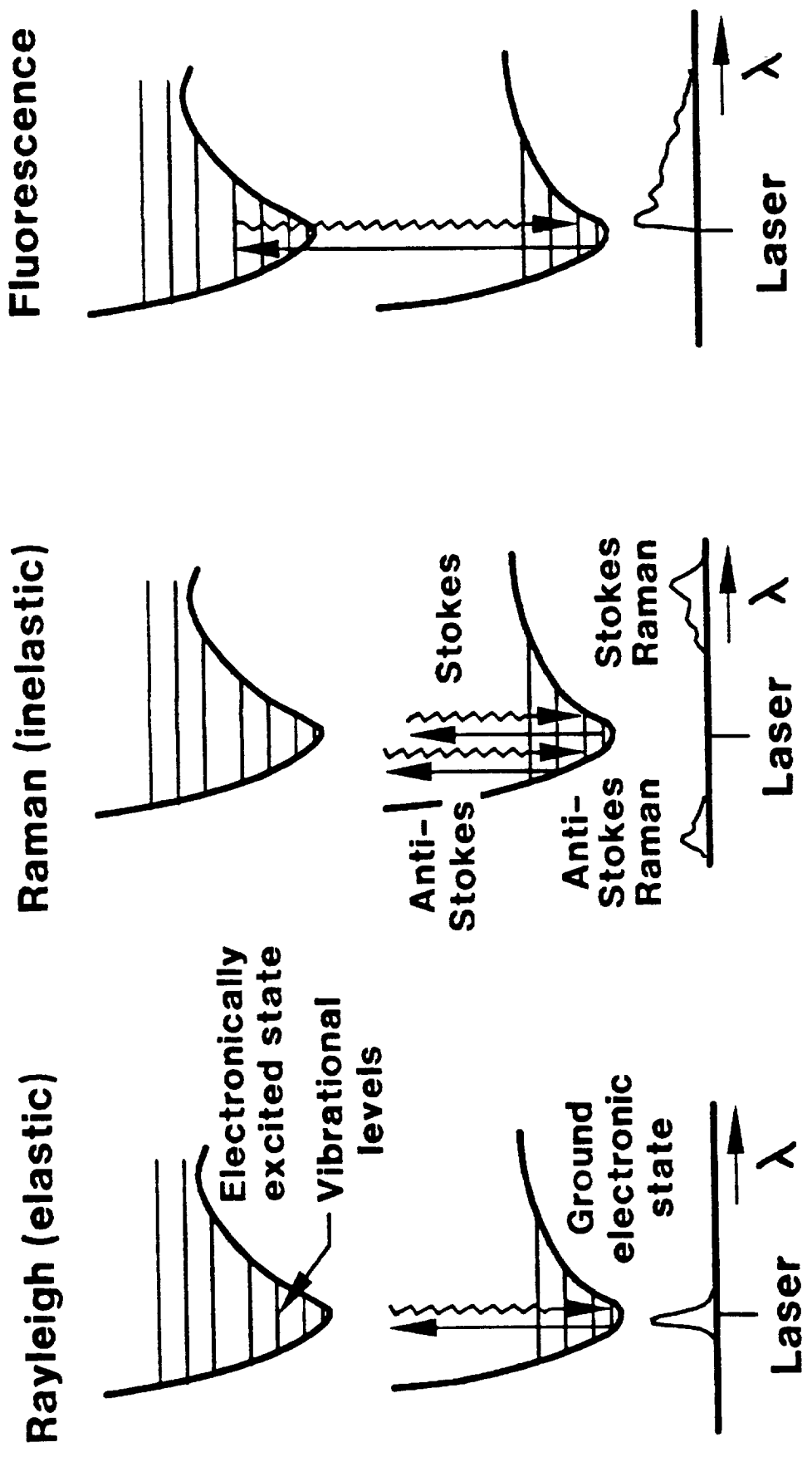
The techniques to be covered in this review fall into two major classes. There are the incoherent approaches and the coherent techniques as outlined in Panel 4. We will begin by considering three incoherent techniques: Rayleigh scattering, spontaneous Raman scattering and laser-induced fluorescence spectroscopy (LIFS). The one coherent technique to be examined is termed coherent anti-Stokes Raman spectroscopy which goes by the acronym CARS. The various incoherent scattering approaches are explained in Panel 5. In the panel, ground and upper electronic states are indicated by the parabolic-shaped potential energy diagrams. The curves represent the variation of potential energy with internuclear separation. The horizontal lines indicate various vibrational levels of excitation in each electronic state and, for simplicity, the rotational splitting within each vibrational level is not shown.

Rayleigh scattering is the elastic scattering of light by molecules. By elastic is meant that there is no energy exchange between the incoming photons and the molecules. Consequently, the scattering is unshifted from the incident wavelength and occurs at the same wavelength as the incoming light. This phenomenon is responsible for the blue color of the sky and was

SPATIALLY-PRECISE LASER DIAGNOSTICS FOR COMBUSTION TEMPERATURE AND SPECIES

- Incoherent approaches
  - Rayleigh scattering
  - Spontaneous Raman scattering
  - Laser induced fluorescence spectroscopy (LIFS)

- Coherent techniques
  - Coherent anti-Stokes Raman spectroscopy (CARS)

PANEL 4

311

SCATTERING PROCESSES

Rayleigh (elastic)

Electronically excited state

Vibrational levels

Ground electronic state

Laser

Raman (inelastic)

Stokes

Anti-Stokes

Stokes Raman

Anti-Stokes Raman

Laser

Fluorescence

Laser

PANEL 5

312

understood by Lord Rayleigh in his investigations over a century ago.

Spontaneous Raman scattering is the inelastic scattering of light and was

discovered by C. V. Raman in 1928 for which he received the Nobel Prize in

1931. In Raman scattering, energy exchange does occur between the incoming

photons of light and the molecules with which the light is interacting.

Recall that the frequency of a lightwave quantum is directly related to the

energy of that quantum. When the photon gives up energy to the molecule, the

photon is downshifted in frequency or scattered to a longer wavelength.

Because of the similarity of this long wavelength scattering to fluorescence,

this Raman process is often termed the Stokes branch. If the molecules are

excited prior to the interaction, they may give up energy to the photons

upshifting the photon frequency and scattering them to a lower wavelength.

This process, for historical reasons, is called an anti-Stokes process. Both

Raman and Rayleigh scattering are essentially instantaneous processes occurring

on the time scale of 10^{-12} seconds or less. Also note that, in spontaneous

Raman scattering and Rayleigh scattering, the incident wavelength can be

arbitrarily selected; there is no input wavelength requirement. Incident

laser frequencies in the visible and ultraviolet, however, are favored because

the scattering scales as the fourth power of the scattered frequency in accord

with dipole radiation laws. In laser-induced fluorescence, the laser is tuned

into an actual absorbing electronic transition of the molecule. Following

promotion to the electronically-excited state, the molecule, after some period

of time, may spontaneously radiate the energy which one monitors as the

fluorescence signal. In addition to radiating the excited energy away,

the molecule may lose its energy by any number of collisional channels, a

313

process termed collisional quenching. Quenching often complicates species concentration measurements but can generally be cancelled out in thermometric investigations.

The typical experimental arrangement for a laser light scattering system is shown in Panel 6. The beam from the laser is introduced through the medium under investigation. Scattering occurs nominally into 4π steradians in accord with dipole radiation laws. Spatial resolution is obtained by triangulation of the detection system, consisting of a field lens and an appropriate spectrometer, with the illuminating laser beam. Scattering is collected over some solid angle Ω at some angle θ to the incident laser beam. The spatial resolution 1 is determined by the field stop in the spectrometer or an iris in the optical detection chain. Although many experiments are performed with the scattering being collected at 90 deg., these techniques can be implemented in backscattering and, thus, are amenable to implementation as single-ported optical approaches. The laser beam is generally focussed into the measurement volume to enhance the spatial resolution. Typical focal diameters are on the order of 200 microns or less and the axial spatial resolution along the beam can vary from submillimeter to several millimeters.

Rayleigh Scattering

Beginning with Rayleigh scattering, Panel 7 displays both the advantages and disadvantages of this technique. This most important advantage is that it is very strong and, as we will see in the next panel, can provide high time resolution even with continuous wave lasers. It is a very simple technique,

I

LASER LIGHT SCATTERING

Laser

Detector

Burner

Spectrometer

Collection optic

θ

Ω
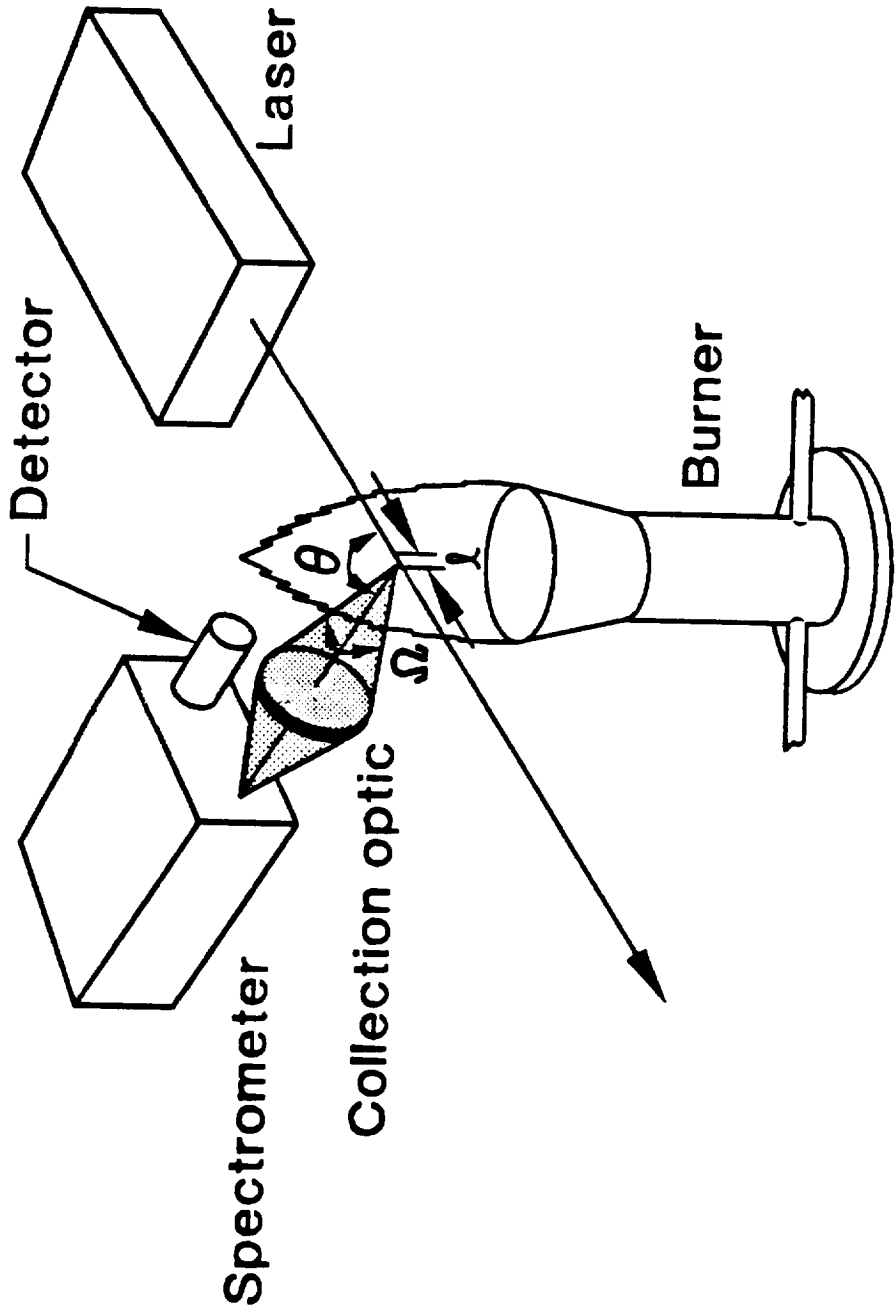
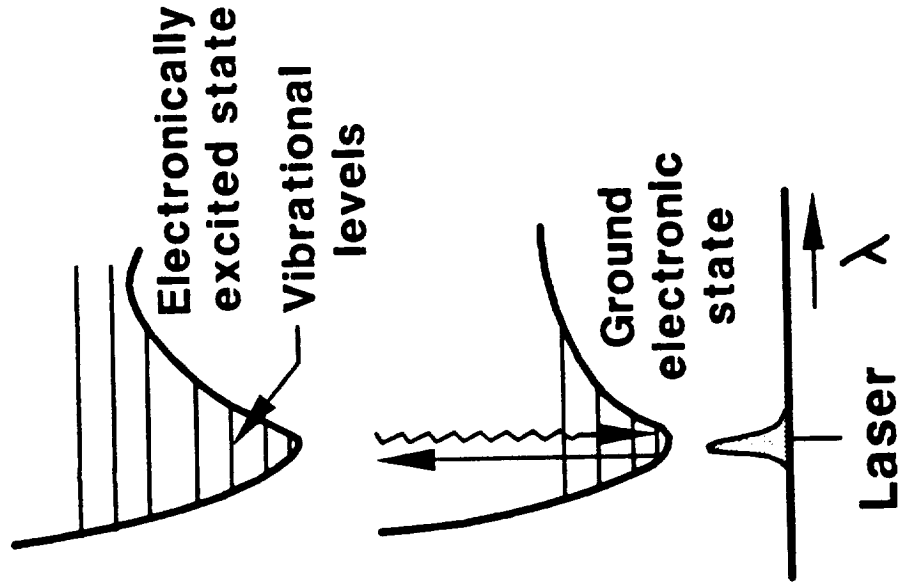# RAYLEIGH SCATTERING

Advantages

Strong

Simple

Quantitative

Spatially-precise

Disadvantages

Not species specific

Particle interferences

Composition dependent

Electronically excited state

Vibrational levels

Ground electronic state

λ

Laser

PANEL 7

316

is quantitative and, with the proper optics, is spatially precise. Its major disadvantage is the fact that it is not species specific. Since the scattering is not shifted in wavelength, there is no way to distinguish the scattering, for example, from a carbon dioxide molecule or from a water vapor molecule. So the technique looks primarily at the total gas density. Although the technique is composition dependent, by judicious tailoring of the reactant mixture of gases, one can arrange the Rayleigh cross section to be nearly invariant with reaction extent. Thus, as reaction proceeds from the reactants to the products, the total cross section can remain nearly constant solely tracking the density. Since the signal is not shifted in wavelength, it is subject to strong Mie scattering interferences from particles whose cross sections are typically much stronger than those for molecules. Thus, Rayleigh scattering is restricted to particle free environments. However, because of its signal strength, it is a very powerful technique as illustrated in Panel 8. There we present a feasibility calculation for a five Watt, continuous wave argon ion laser interrogating a one atmosphere pressure, 2000 K flame using an F3 optical collection system with a spatial resolution of one millimeter. Assuming an overall collection efficiency of 20 percent, one sees that the Rayleigh photon flux is nearly 10^8 photons per second. If one is sampling at a one kilohertz sampling rate, i.e. an aperture time of a millisecond, one gathers nearly 100,000 photons. If these are detected by a photomultiplier with a 20 percent quantum efficiency, the signal can be observed with a signal/noise greater than 100 resulting in an absolute accuracy to better than 1 percent. Since most combustion processes occur at very low Mach numbers, the pressure is essentially constant throughout. Application of the ideal gas

317

CW LASER RAYLEIGH FREQUENCY RESPONSE IN FLAMES

- **Rayleigh cross section**

$$\frac{\partial \sigma}{\partial \Omega} = \frac{2\pi^2(\mu-1)^2}{N_o^2\lambda^4}$$

- **Mixture Rayleigh cross section**

$$\left.\frac{\partial \sigma}{\partial \Omega}\right|_{mix} = \sum_i X_i \left(\frac{\partial \sigma}{\partial \Omega}\right)_i$$

$$\approx 8.6 \ (10^{-28}) cm^2/sr \ \text{postflame}$$

- **Rayleigh signal**

$$P_{Ray} = P_i \ n \ \left.\frac{\partial \sigma}{\partial \Omega}\right|_{mix} \Omega \ \ell \ \epsilon$$

$$\longrightarrow 2.4 \ (10^{-11}) \ \text{w for 5w @ } 5145\mathring{A}, 1atm, 2000^\circ K, f/3, 1mm, 20\%$$

- **Rayleigh photon flux** $\quad \dot{n}_{Ray} = P_{Ray}/\epsilon_P \longrightarrow 6.2 \ (10^7) \ \text{photons/sec}$

- **Rayleigh photons at 1 kHz** $\quad n_{Ray} = 6.2 \ (10^4) \ \text{photons}$

- **S/N at 20% Q.E.** $\qquad S/N = \sqrt{\eta \ n_{Ray}} \longrightarrow 112$

PANEL 8

318

law then allows one to make a temperature measurement by measuring the density.

An example of Rayleigh scattering used in the foregoing manner is llustrated in Panel 9. There one views probability density functions of temperature in a turbulent premixed methane/air flame. In this flame, hydrogen was added and the stoichiometry was adjusted in such a way that the total Rayleigh cross section remained invariant as the reaction proceeded. Low in the flame one sees very narrow pdf's typical of the cold core flow, very high in the flame one sees a broader, but hot, distribution typical of gases leaving the flame. In the intermediate zones, where the flame fluctuates, bimodal pdf's are seen typical of sampling alternately hot and cold pockets of gas. Rayleigh scattering can also be nicely integrated with laser Doppler velocimeters to add a temperature measuring capability. In these instances the particle seeding rate is kept low enough so that one can make the Rayleigh temperature measurements in between the various velocity realizations. Despite its limitations Rayleigh scattering is a very powerful technique when properly applied.

Spontaneous Raman Scattering

As seen in Panel 10, one advantage of spontaneous Raman scattering is that it is applicable to all molecules. All molecules have at least one vibrational-rotational mode which is Raman active. The technique is

RAYLEIGH TEMPERATURE PDF'S
IN A TURBULENT METHANE FLAME
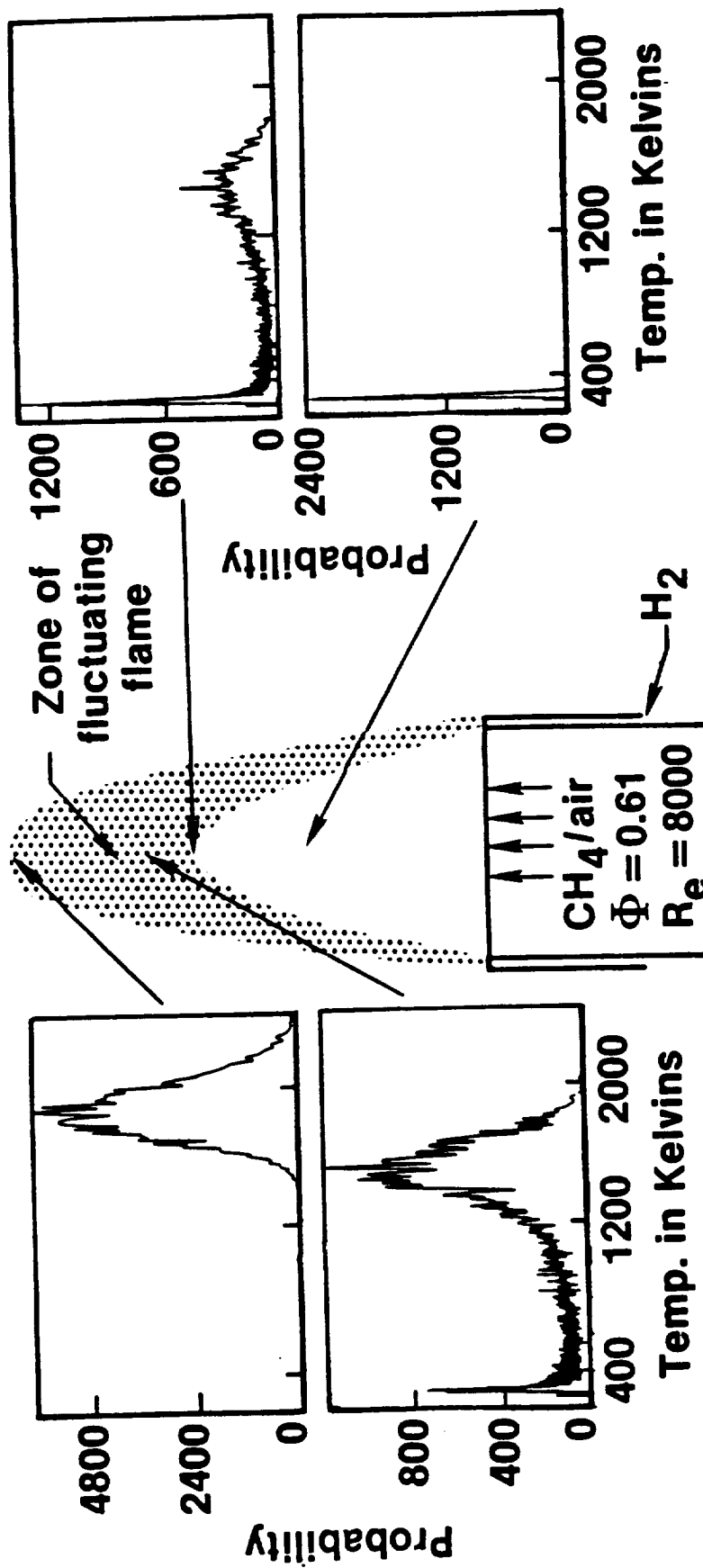
From: R.W. Dibble and R.E. Hollenbach: Laser Rayleigh Thermometry in Turbulent Flames. Proc. 18th Symp. on Combustion, pp. 1489-1499, 1981.

PANEL 9

320

SPONTANEOUS RAMAN SCATTERING
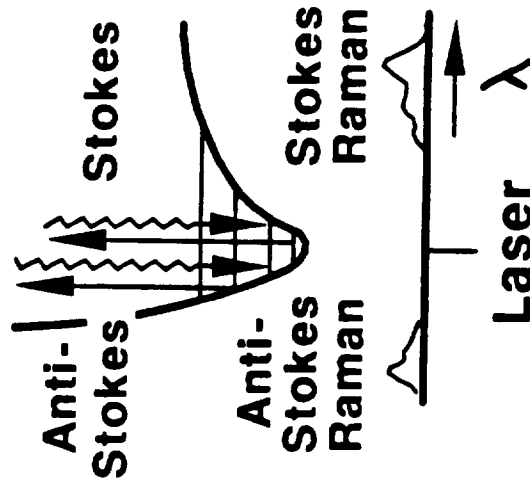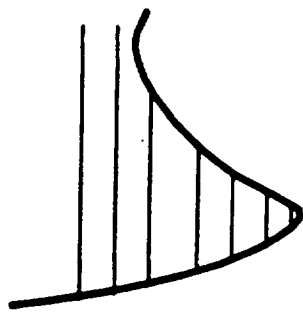
Advantages

Applicable to all molecules

Quantitative

Simple

Spatially-precise

Disadvantages

Very weak

Stokes

Anti-Stokes
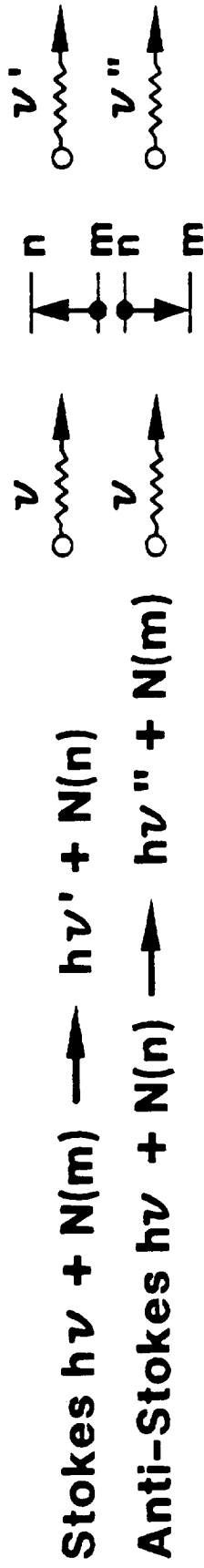
Stokes Raman

Anti-Stokes Raman

Laser

λ

PANEL 10

321

quantitative, simple and, as with all the incoherent scattering techniques, it can be made spatially precise. The major disadvantage of spontaneous Raman is that it is a very weak process. For example, in atmospheric pressure flame situations, the Raman signal is about 14 orders of magnitude less than the input energy.

The basis for thermometry using Raman scattering is illustrated in Panel 11 and stems from the interrogation of individual vibrational-rotational states as alluded to earlier. Here the focus is just on two individual vibrational-rotational states M and N. In the Stokes process, the molecules are taken from state M to N with energy being "absorbed" by the gas and the photon is down shifted in energy. In the anti-Stokes process, one has the converse process. Conservation of energy applies in these scattering processes and, since the energy levels of most combustion molecules are very well known, the scattered frequencies can be calculated precisely. The Raman scattering intensities vary linearly with the number density in the initial vibrational-rotational state from which scattering is observed. The frequency to the fourth scaling originates from the dipole radiation nature of the Raman scattering. For a gas in thermal equilibrium, the respective state populations are given by Boltzmann statistics. If one measures the anti-Stokes to Stokes intensities, by simple rearrangement of the equations it is observed that a temperature measurement can be made. In reality, one observes the spontaneous Raman scattering from an ensemble of vibrational-rotational modes. However this can be easily calculated with computer codes and, as seen in Panel 12, one can calculate the anti-Stokes to Stokes Raman scattering over temperature

I

RAMAN THERMOMETRY PRINCIPLE

Stokes $h\nu + N(m) \longrightarrow h\nu' + N(n)$

Anti-Stokes $h\nu + N(n) \longrightarrow h\nu'' + N(m)$

Conservation of energy

$h(\nu - \nu') = E(n) - E(m)$

$h(\nu'' - \nu) = E(n) - E(m)$

Scattering intensities

$I_S(\nu') \sim \nu'^4 N(m)$
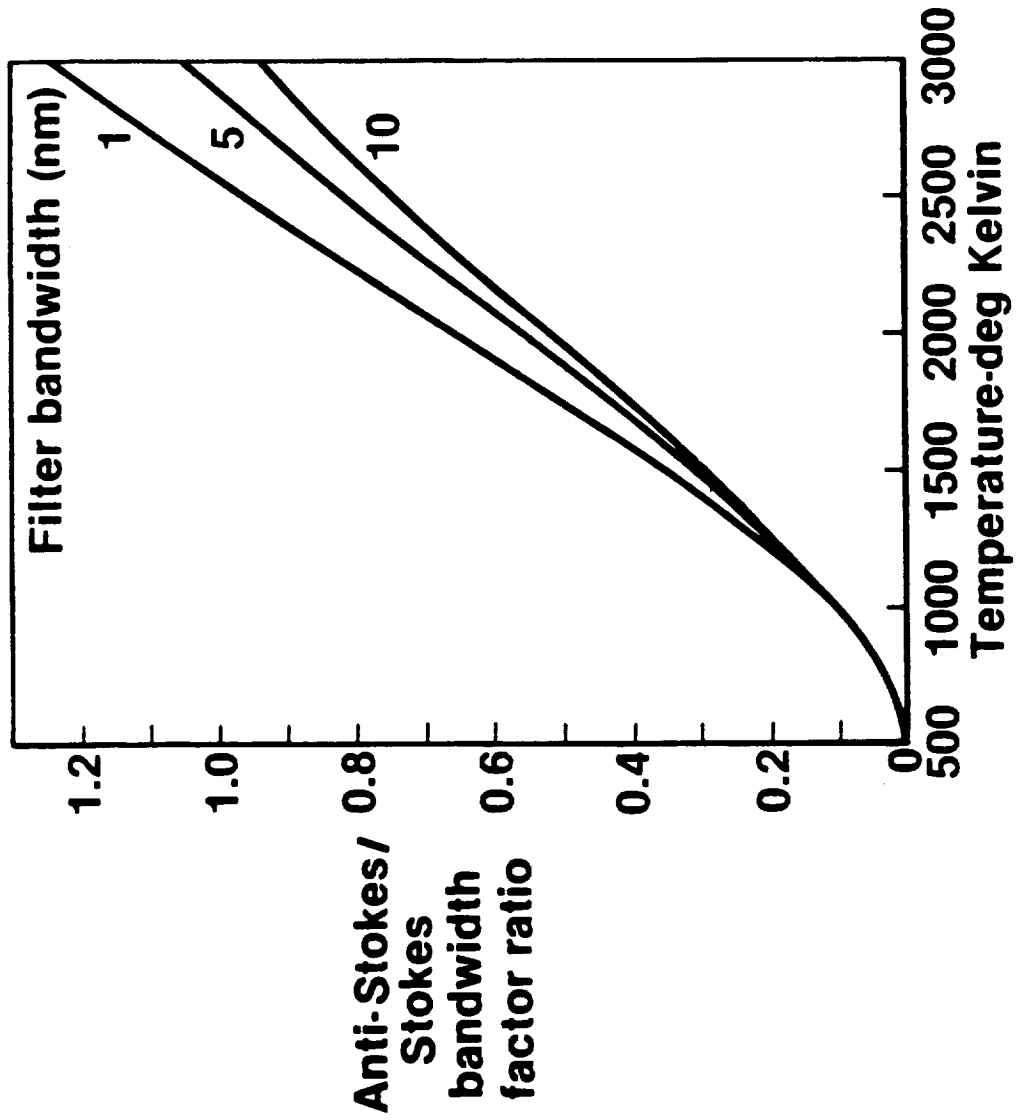
$I_A(\nu'') \sim \nu''^4 N(n)$

Thermal equilibrium $\dfrac{N(n)}{N(m)} = e^{-\left[E(n)-E(m)\right]/kT}$

Temperature measurement

$$T = \frac{E(n) - E(m)}{k \ln I_A(\nu'')/I_S(\nu') + 4k \ln \nu'/\nu''}$$

TEMPERATURE VARIATION OF AS/S RAMAN RATIO

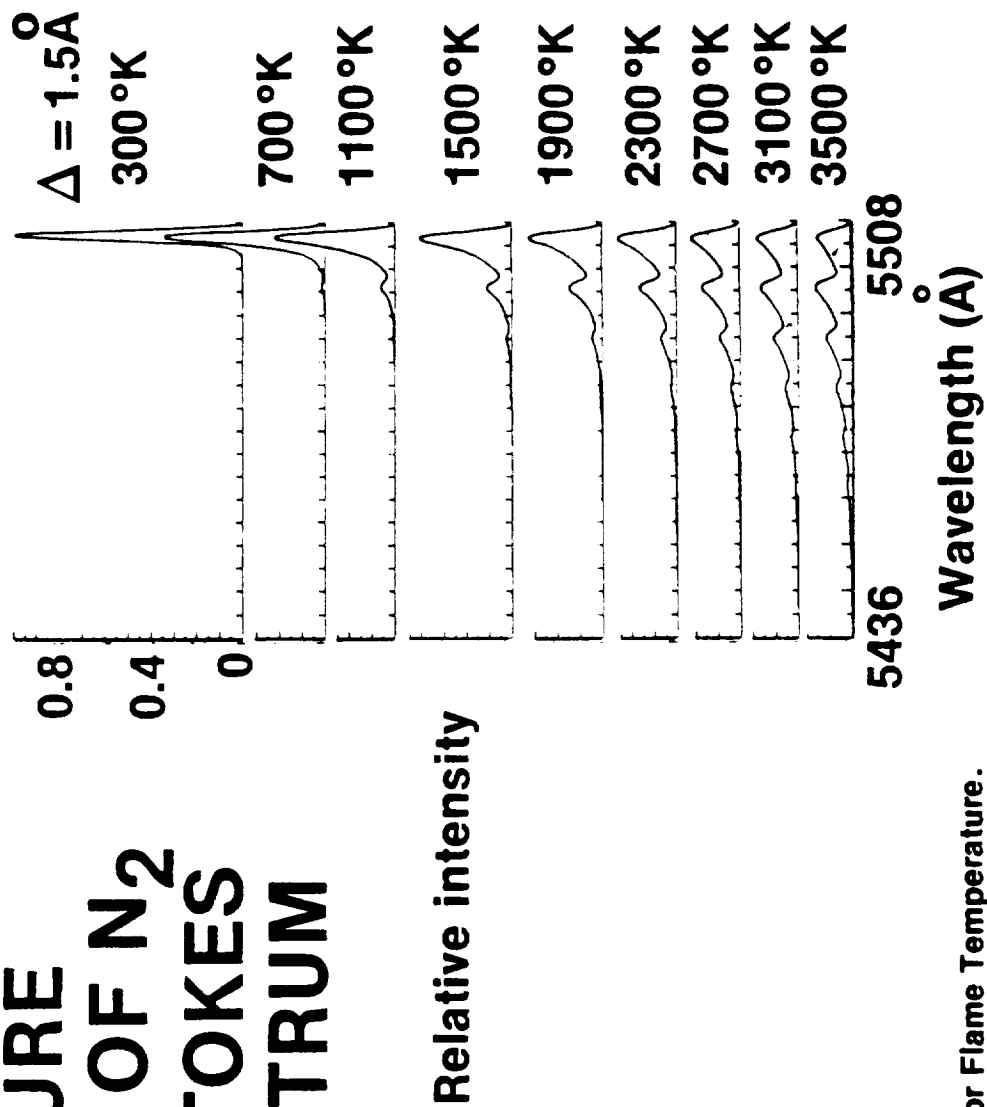## Visible excitation of nitrogen

PANEL 12

as a function of detection bandwidths. This anti-Stokes to Stokes method works quite nicely at temperatures above 600 or 700 K and results in a nearly linear behavior up to temperatures near 3000 K. At lower temperatures this particular approach does not work since there is very little vibrational excitation and, thus, not much of an anti-Stokes signal to detect.

Another approach to thermometry using Raman scattering is to spectrally resolve the Stokes Q-branch. The Q-branch is a spectrum in which the vibrational quantum number changes but the rotational quantum number does not. As can be seen in Panel 13, the vibrational Q-branch spectrum of nitrogen is quite temperature sensitive. At low temperatures, one sees a very narrow band made up of low lying rotational transitions. As the temperature increases and population shifts to higher rotational levels, the band broadens and smears. At still higher temperatures, one begins to see Stokes contributions from vibrationally-excited states. Since a typical Raman spectrum may only contain a few thousand photons at best, temperature measurements made by resolving these bands must be performed by time consuming scans and are not amenable to single pulse measurements under most low pressure applications.

An exception to this rule is illustrated by work that UTRC is currently performing for the NASA Marshall Space Flight Center in which Raman scattering is being applied to make measurements in the fuel preburner of the space shuttle main engine (SSME) [5]. The overall instrument concept is illustrated in Panel 14 and uses fiber optics to pipe a high power argon ion laser to an instrument package bolted to the preburner. Raman scattering is collected in a separate fiber and piped to a spectrograph and optical multichannel detector

325

TEMPERATURE DEPENDENCE OF N₂ Q-BRANCH STOKES RAMAN SPECTRUM

$\Delta = 1.5\overset{\circ}{A}$

300°K

700°K

1100°K

1500°K

1900°K

2300°K

2700°K

3100°K

3500°K

0.8

0.4

0

5436

5508

Wavelength ($\overset{\circ}{A}$)

Relative intensity

From: M. Lapp, et al.: Laser Raman Probe for Flame Temperature.
Project SQUID Technical Report GE-1-PU, April 1973.

PANEL 13

326

SSME FIBER FIBER OPTIC RAMAN
THERMOMETER DIAGNOSTICS

High power AR[+] laser

Spectrograph

OMD

OMD control

Computer

Thermal control

Fiber control

Stepping motor

Fuel preburner

SSME

PANEL 14

327
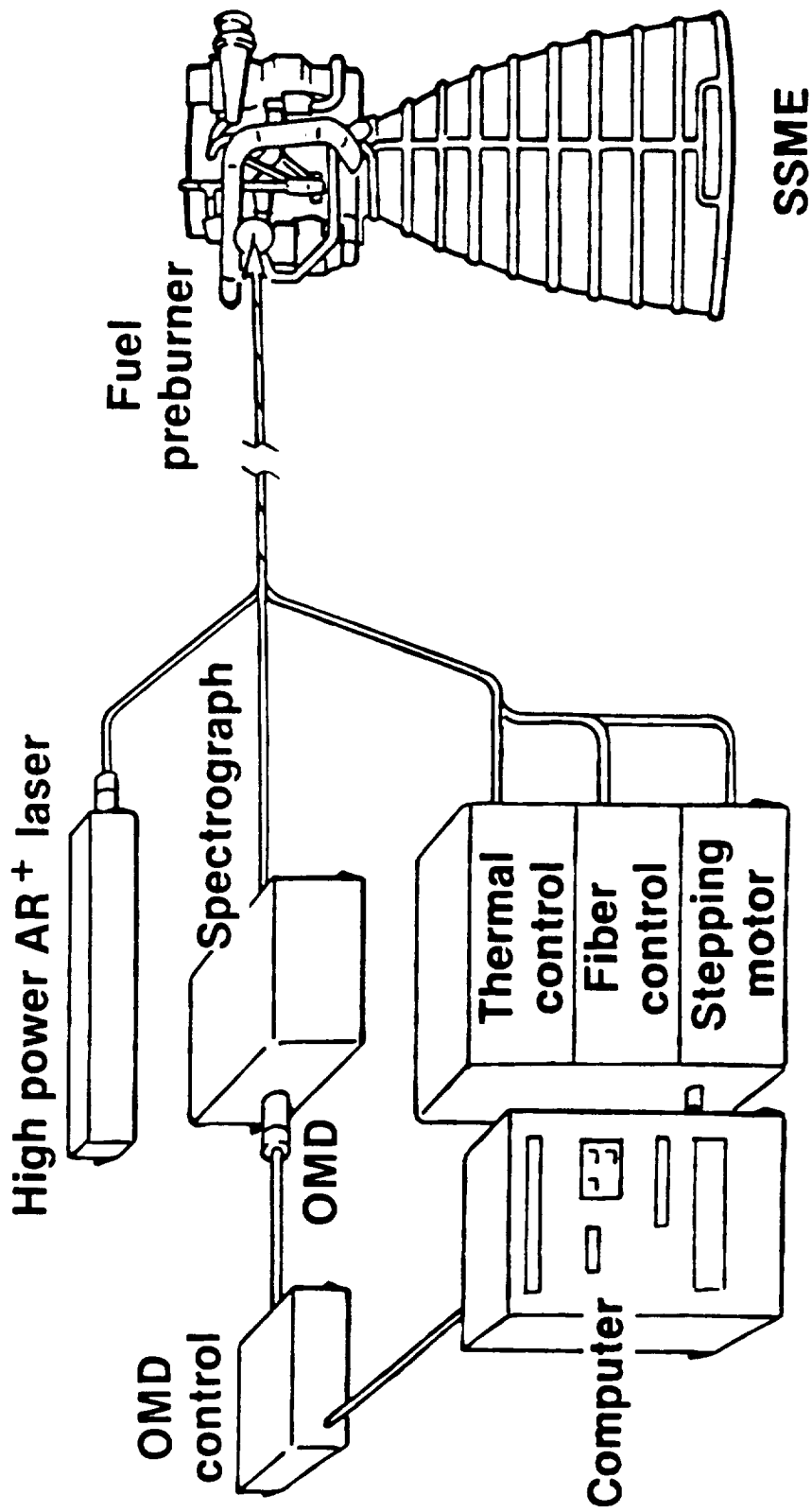
for recording and subsequent data analysis. The SSME preburner operates at pressures in excess of 300 atmospheres thus permitting use of a continuous wave laser with signal arrival rates high enough to permit measurements every 10^{-2} seconds. Details of the interior of the optical head, which bolts to the fuel preburner, are shown in Panel 15. The laser ray emanating from the transmitter fiber is recollimated and then directed by means of optics down the central axis of the instrument for focusing into the fuel preburner. The Raman scattered radiation is collected in backscattering and separately focused into a receiver fiber. The central portion of the receiving lens is purposely obscured to enhance the spatial resolution of the measurement in this coaxial backscattering arrangement [6]. Not surprising, as shown in Panel 16, the hydrogen spontaneous Raman spectrum is quite temperature sensitive and reflects the changing distribution of population over the various rotational states in the ground vibrational level. With hydrogen, due to its very large vibrational anharmonicity, the higher vibrational levels lead to Raman scattering far displaced from that produced by the ground vibrational state and they are usually not observed. Due to large rotational-vibrational interaction, the individual Q-branch transitions in the ground vibrational state are well separated permitting them to be easily resolved as the calculation suggests. Panel 17 displays as dots the spontaneous Raman spectrum obtained from a high pressure cell at 1000 K and over 300 atmospheres of pressure [3]. The solid line is the theoretical best fit to the data points read directly off of the optical multichannel detector. Plotting the integrated strength of each one of these rotational transitions against the

OPTICAL HEAD CONCEPTUAL DESIGN
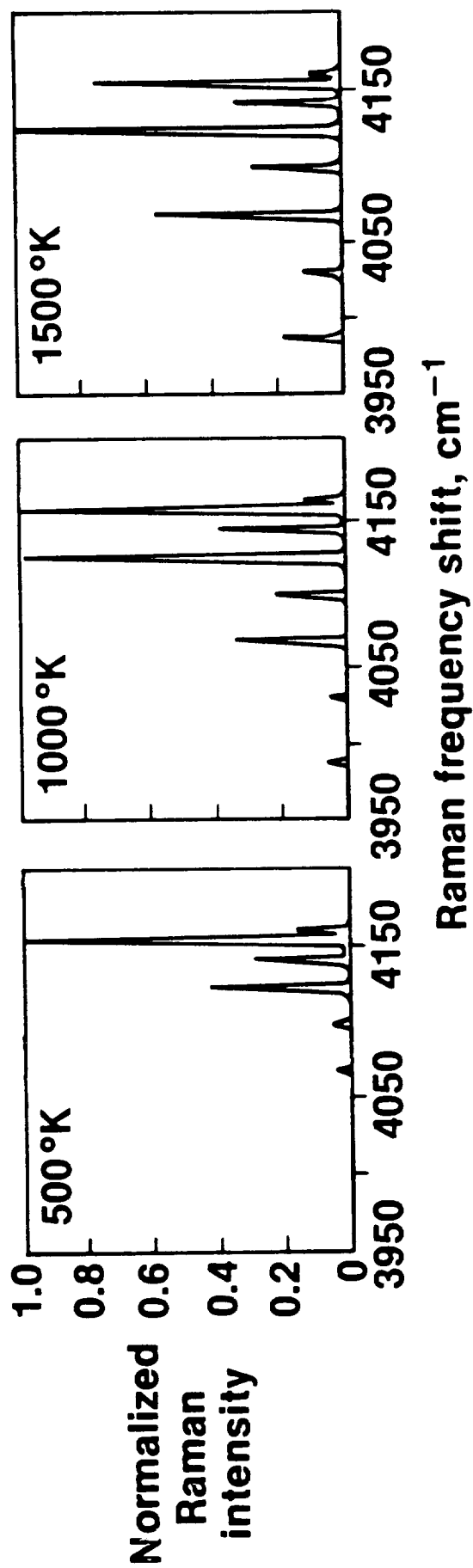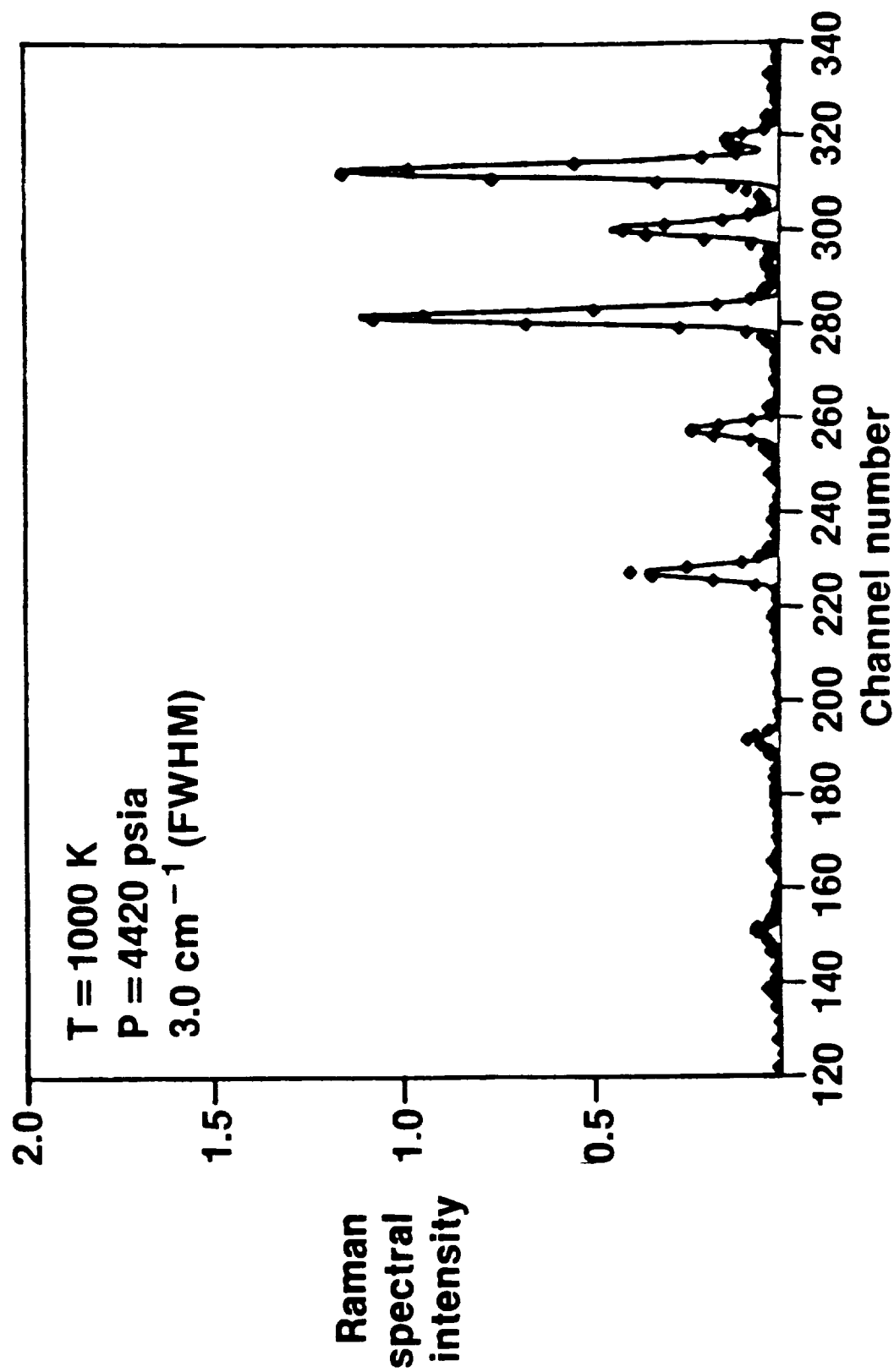

PANEL 15

329
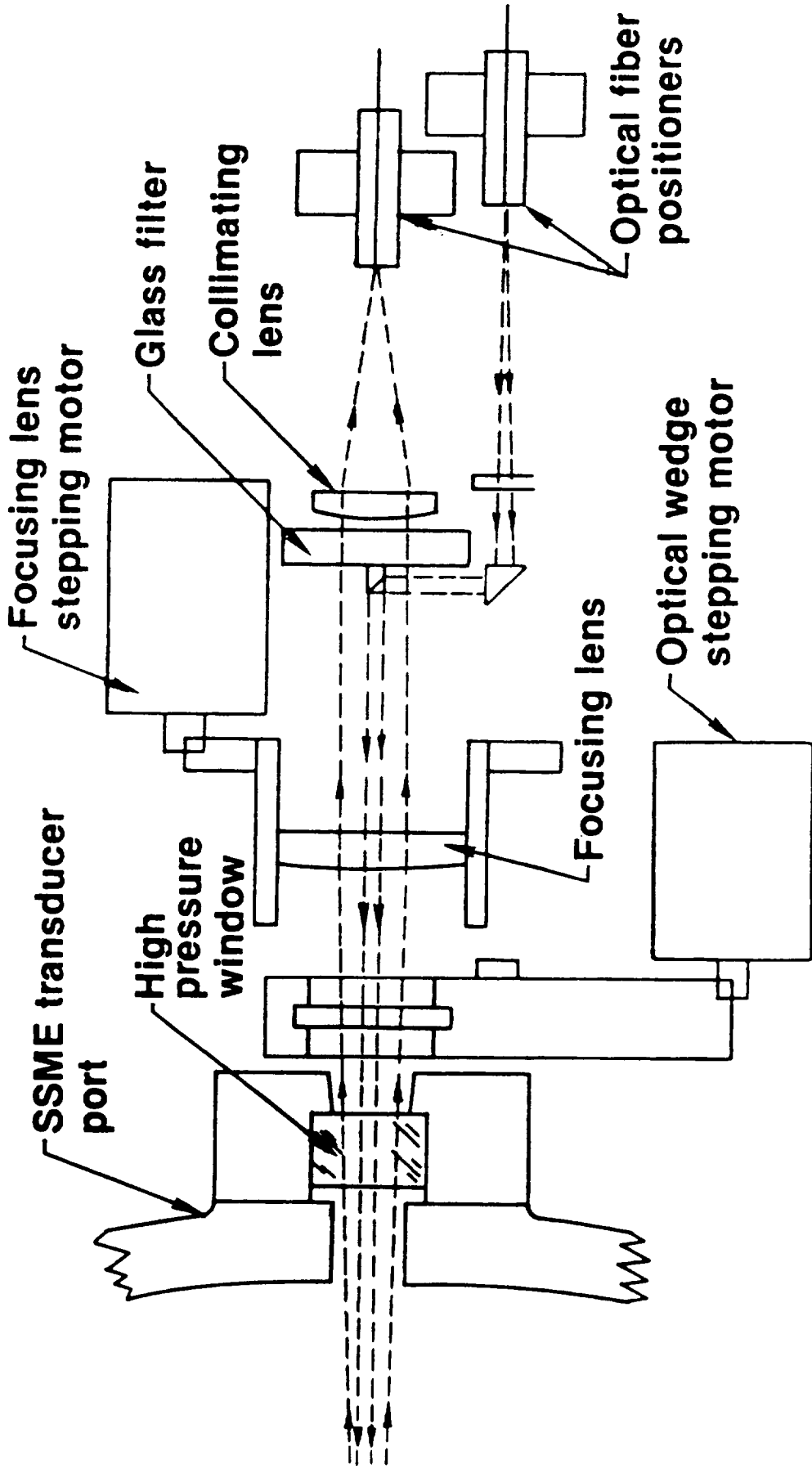
CALCULATED H₂ SPONTANEOUS RAMAN SPECTRA

p = 380 atm, slitwidth 2 cm⁻¹

HYDROGEN Q-BRANCH RAMAN SPECTRUM

T = 1000 K
P = 4420 psia
3.0 cm^{-1} (FWHM)

Raman spectral intensity

Channel number

PANEL 17

331

respective state energy, as shown in Panel 18, leads to a typical Boltzmann plot from whose slope the temperature derives. This instrument is typically capable of making such measurements every 10 milliseconds with accuracies on the order of ± 3 percent. This is a highly favorable situation since it involves very high pressures and hydrogen combustion is characterized by very low luminosity and lack of particulate formation typical of hydrocarbon-fueled flames.

Hydrocarbon flames pose quite a challenge and a limitation to spontaneous Raman scattering. Practical flames, typically nonpremixed, lead to large amounts of soot formation in fuel-rich regions leading to very high luminosity levels. The high luminosity typically precludes use of a continuous wave laser, rather a pulsed laser is used to induce Raman scattering in a time period short enough to minimize collection of a significant amount of the background radiation. However, as illustrated in Panel 19, the use of pulsed lasers with the spatial resolutions typically employed, leads to very high laser fluxes in the focal volume. This results in laser heating of the soot particles which occur in the combustion process. These soot particles are heated into the 3000-5000 K range. Because of the strong dependence of the Planck function on temperature, this results in greatly enhanced amounts of laser modulated soot incandescence. As shown in Panel 20, this laser modulated soot incandescence can approach or in many instances exceed the spontaneous Raman scattering signal leading to very poor signal to interference ratios. Shown in the panel are signal to interference ratios calculated over soot number density/soot particle diameter parameter space.

H₂ RAMAN TEMPERATURE ANALYSIS

T = 1000 K
P = 4420 psia

T = 1005 ± 32 K

Integrated count/w_J

Rotational energy, cm⁻¹

PANEL 18

333
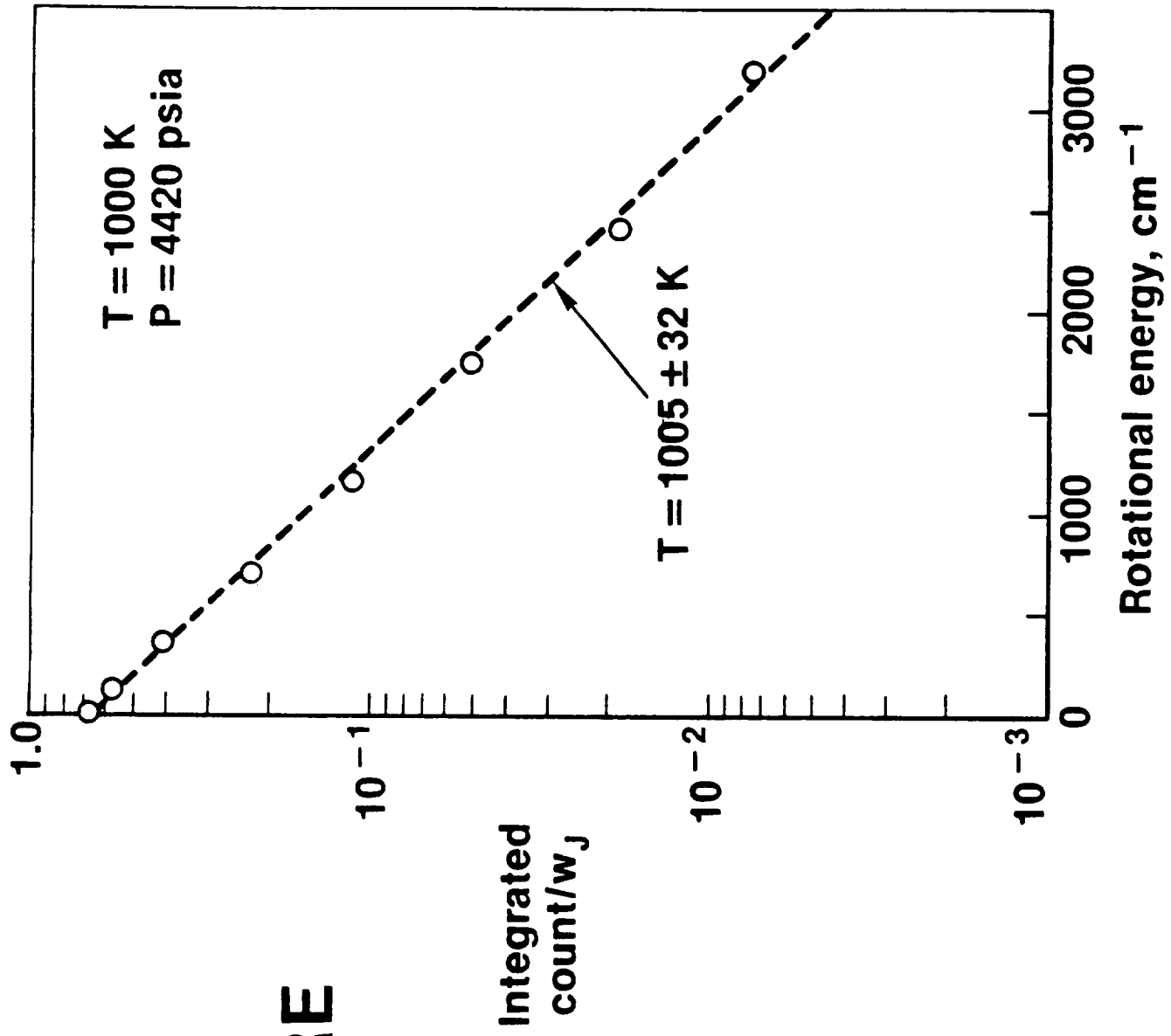
Laser Irradiated Particle Temperatures

PANEL 19

334

RAMAN S/I MAP

Soot number density — cm^{-3}
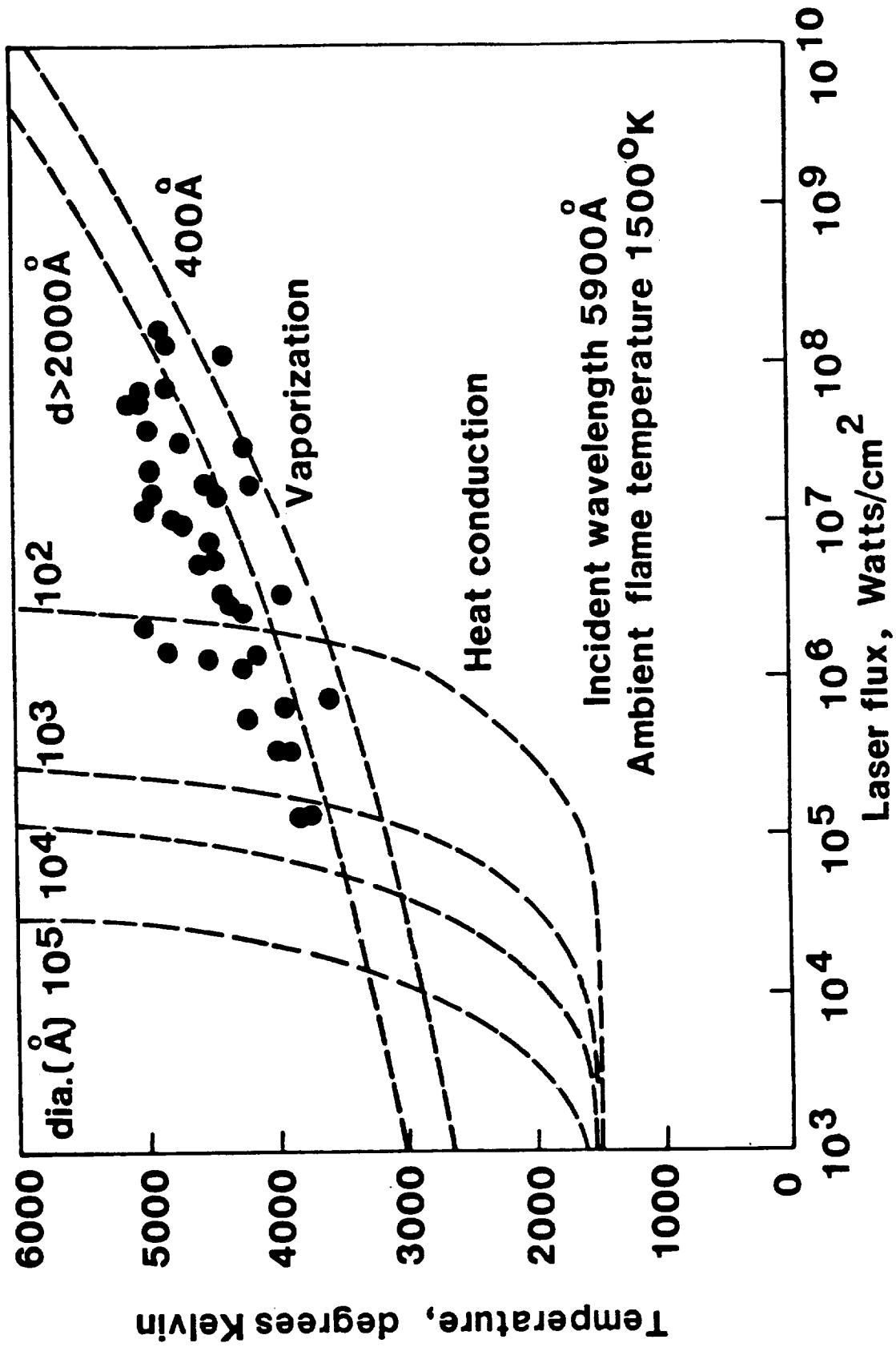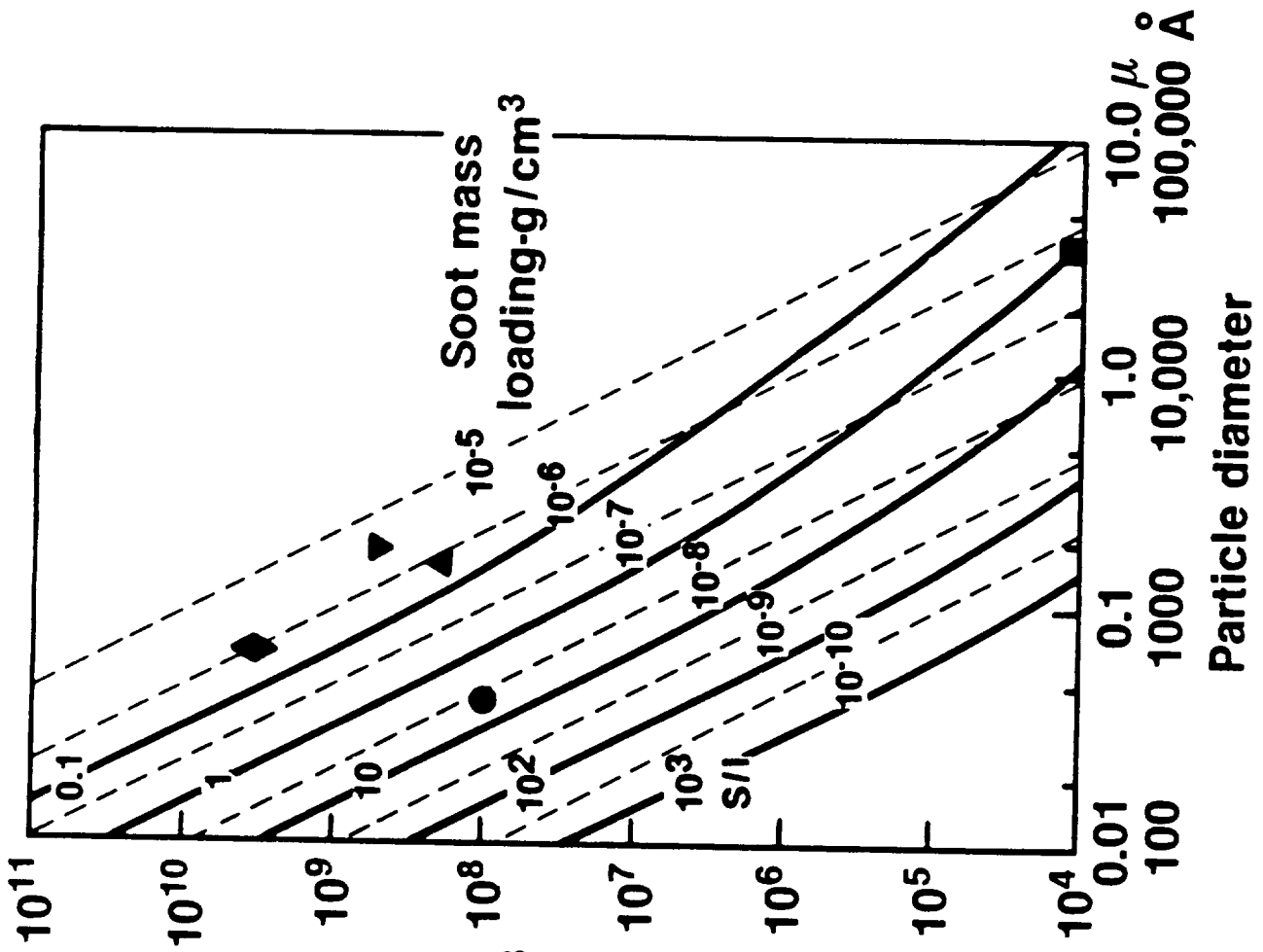
Laser: 0.5J, 532nm, 10^{-8} sec
Raman: N_2, 2000 K, 1atm

- ■ Combustor JP-4
- ◆ CH_4:O_2 premixed flame
- ▲ C_4H_{10} diffusion flame
- ● Combustor C_3H_8 (g)
- ▼ C_3H_8 diffusion flame

Soot mass loading-g/cm^3

Particle diameter

PANEL 20

335

The dashed lines are soot mass loadings and the solid points are soot conditions typically found in practical combustors.

Because of these severe interferences, spontaneous Raman scattering has seen very little practical utility in devices typical of the real world, i.e. gas turbines, furnaces, internal combustion engines. This conclusion is certainly valid for pulsed lasers which operate in the visible region of the spectrum and was the motivation for the development of the much stronger coherent techniques nearly a decade ago. However, in the past few years, highly energetic and reliable pulsed ultraviolet lasers have emerged. With these sources, a reexamination of spontaneous Raman scattering is merited even for practical utilization. For example, the Raman scattering from a pulsed krypton fluoride laser operating at 248 nanometers is nearly twenty times stronger than that from a laser operating at 532 nanometers, the wavelength of frequency-doubled neodymium:YAG lasers. Furthermore, as one operates deeper into the ultraviolet, the incandescence from the laser heated soot particles diminishes resulting in much larger signal to interference ratios for Raman excitation in the ultraviolet. Calculations that I've made recently indicate that pulsed uv Raman scattering appears to be potentially applicable to practical combustors having modest particulate loadings. However, there are other interference effects such as laser-induced fluorescences from fuel fragments and/or photodissociation of target molecules that also have to be considered before one can comment definitively on the practical utility of uv spontaneous Raman scattering. Further experimentation is clearly needed to examine the applicability of spontaneous Raman scattering in the ultraviolet.

However a decade ago when conclusions about the practical utility of Raman scattering were first being reached, such high power and reliable ultraviolet lasers did not exist.

Coherent Anti-Stokes Raman Spectroscopy (CARS)

Consequently, to be able to make measurements in flames of practical interest, one searched for much stronger techniques than spontaneous Raman scattering. The technique which emerged is depicted in Panel 21 and is a coherent form of Raman spectroscopy known as CARS. It is a very strong technique with signal levels being anywhere from 4 to 6 orders of magnitude stronger than spontaneous Raman scattering. It is a coherent technique which means that the signal emerges as a laserlike beam. This has two important implications. One is that all of the signal can be collected. This is in contrast to an incoherent scattering process where, even with fast optics, for example F3, only about one percent of the total signal can be collected. In addition, because the signal is coherent, one can collect it with extremely small solid angle collection optics greatly minimizing the collection of interfering radiations. With CARS, the interferences do not go away; it is simply that one can operate with much higher signal to interference ratios, perhaps 10 orders of magnitude greater, than those commonly available with spontaneous Raman scattering. The technique is spatially precise depending on the beam crossing geometries which are employed and, like all Raman techniques, it is applicable to all molecules. One of its major disadvantages
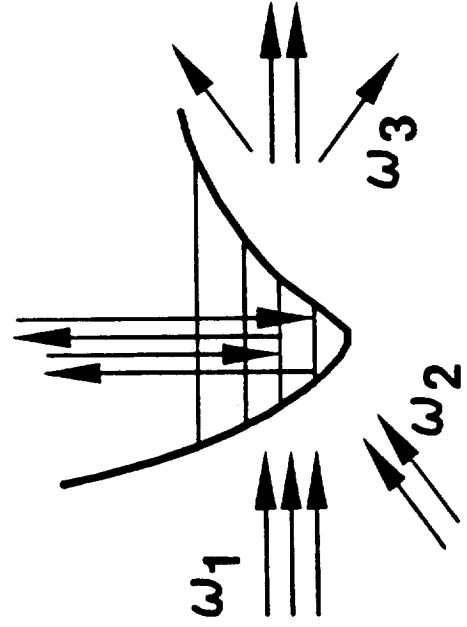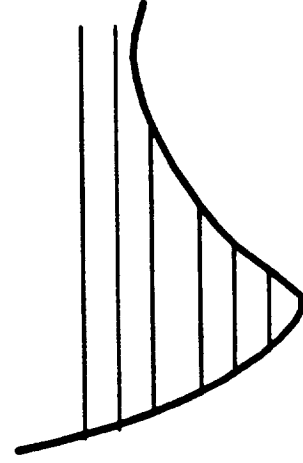
337

COHERENT ANTI-STOKES RAMAN SPECTROSCOPY (CARS)

Advantages

Strong

Coherent

Spatially-precise

Applicable to
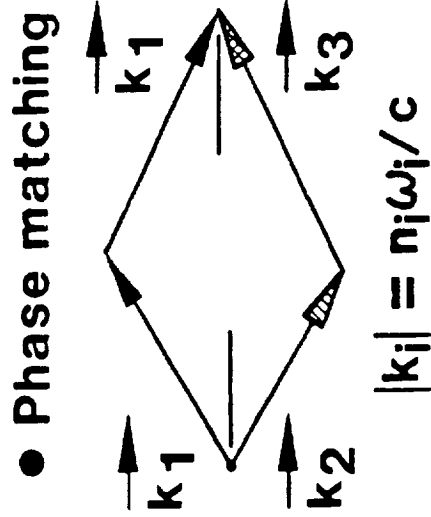molecules

Disadvantages

Double-ended

Complex

Refraction
sensitive

ω_1

ω_2

ω_3

PANEL 21

338
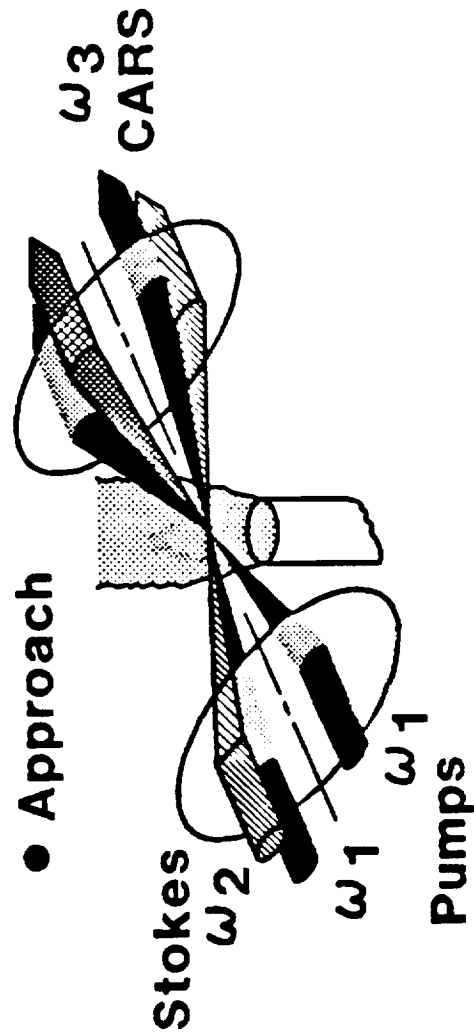
is that it is double ended. Although it is a spatially precise technique,

line of sight optical access is generally required. This makes it very

difficult to employ in some situations, e.g., to annularly-shaped gas turbine

combustors. It is a much more complex technique than spontaneous Raman

scattering and it can be sensitive to refractive index gradients in the

medium. However, even in these instances there are special beam geometries

which minimize these sensitivities.

As shown in Panel 22, CARS occurs when laser beams at frequencies ω_1,

the pump, and ω_2, the Stokes, are mixed in an appropriate fashion. Mixing

involves focusing and orientation of the laser beams in accordance with

so-called phase-matching considerations. Phase matching ensures that the

signal generated at one point will be in phase with the signal generated at

subsequent points so that the signal builds up in a constructive manner and

does not destructively interfere. There are many geometries to achieve phase

matching and, in practice, this is an easy requirement to fullfill. The CARS

signal always occurs at $2\omega_1 - \omega_2$. What is key in the process is the

frequency difference between ω_1 and ω_2. When it coincides with a Raman

active rotational-vibrational resonance in the gas, the CARS signal becomes

resonantly enhanced and uniquely characteristic of the constituent being

interrogated. Although the spectrum can be generated at very high resolution

by scanning the Stokes laser sequentially over the transitions of interest,

diagnostically this is generally unacceptable. Rather, for fast pulse

diagnostics, the Stokes laser is made broadband accessing simultaneously all

of the vibrational-rotational transitions in a given band region and leads to

COHERENT ANTI-STOKES RAMAN SPECTROSCOPY (CARS)

- Approach

Stokes

ω_2

ω_1

Pumps

ω_3
CARS

ω_1

- Energy level diagram

$\omega_1 \omega_3$

$\omega_1 \omega_2$

ω_v

- Phase matching

k_1

k_3

k_1

k_2

$|k_i| = n_i \omega_i / c$

- Spectrum

Scanned

ω_2 ω_1 ω_3

Broadband

PANEL 22

340
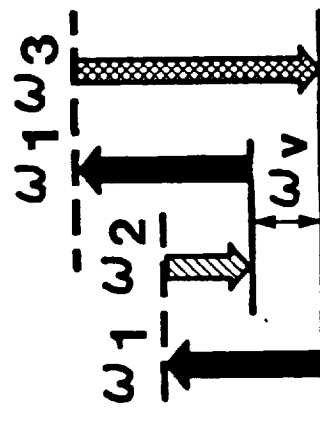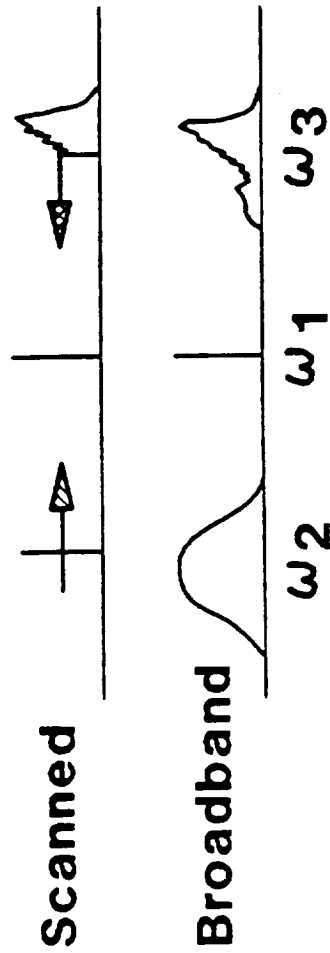
generation of the entire CARS spectrum with each pulse. Capture of the
spectrum then permits instantaneous temperature and density measurements to be
made. One of the disadvantages of CARS also becomes apparent in this diagram;
one nominally can only interrogate one constituent at a time, i.e., the
constituents whose Raman resonances coincide with the frequency difference
$\omega_1 - \omega_2$. This is in contrast to spontaneous Raman scattering where, with
one laser beam, all species Raman scatter and can be monitored. There are
advanced multicolor CARS techniques emerging [Ref. 8] which overcome this
limitation but they are even more complicated than the straightforward CARS
process outlined here.

Panel 23 summarizes the measurement capabilities of CARS for combustion
processes. With CARS, because of the higher photon yields, one can
simultaneously capture the entire spectral signature and obtain temperature
from it analogous to what we saw earlier with spontaneous Raman scattering.
At atmospheric pressure, the typical accuracies are about ± 1% time averaged
and about ± 3% for a single 10^{-8} sec pulse. Species concentrations are
gathered from the strength of the signal in general, although CARS is a unique
spectroscopy in that, in certain concentration ranges, its signatures are also
concentration sensitive. This is a very important advantage when one is
making measurements in practical media where attenuation by particulates and
fuel droplets may be significant or where windows are subject to fouling after
a period of time. Due to a number of reasons, CARS is typically restricted to
viewing only the major constituents, i.e. species concentrations on the order
of 1/2% or greater. For a variety of reasons, the accuracy is not as good on

CARS MEASUREMENT CAPABILITIES – COMBUSTION

- Temperature

  - From spectral signatures

  - Accuracy at flame temperatures   ± 3% single pulse
    ± 1% time averaged

- Species concentrations

  - From signal strength in general

  - From spectral signatures in certain ranges

  - Sensitivity restricted to major constituents, > 0.5%, for either broadband or narrowband background suppressed

  - Relative accuracy to with ± 5%

PANEL 23

342

concentration as it is with temperature. Species concentration measurements are typically accurate within about ± 5%.

Panel 24 displays the temperature variation of the nitrogen CARS spectrum. It is conceptually similar to those spectra seen earlier from spontaneous Raman scattering but differs in the actual spectroscopic details. Basically, one again is looking at rotational and vibrational state population distributions. Temperature measurements are performed by capturing such spectra and then using computer codes to deduce which of a library of spectra produces the best fit to that particular experimentally-captured spectrum.

CARS has been successfully applied to a wide range of practical combustion devices as summarized in Ref. 9. It is capable of making temperature measurements under extremely high soot loadings as evidenced by the measurements in Panel 25 performed in laminar ethylene air diffusion flames [Ref. 10]. In these small-scale laboratory flames, the measurement volume was roughly cylindrical with a diameter on the order of 100 microns and an axial extent of 700 microns. Contrast these measurements with the application of CARS to actual afterburning jet engine exhausts [Ref. 11]. In that particular application, a hardened CARS instrument was mounted about an afterburning Pratt & Whitney F-100 jet engine, which, at full thrust, creates an acoustic environment on the order of 150 decibels. Spatially-resolved temperature and species concentration measurements were made throughout the one meter diameter exhaust flow. The CARS signal is piped out of the hostile environment using fiber optics and sent to remotely located spectrographic and detection equipment. The CARS instrument was operated completely remotely due

TEMPERATURE SENSITIVITY OF N_2 CARS SPECTRUM
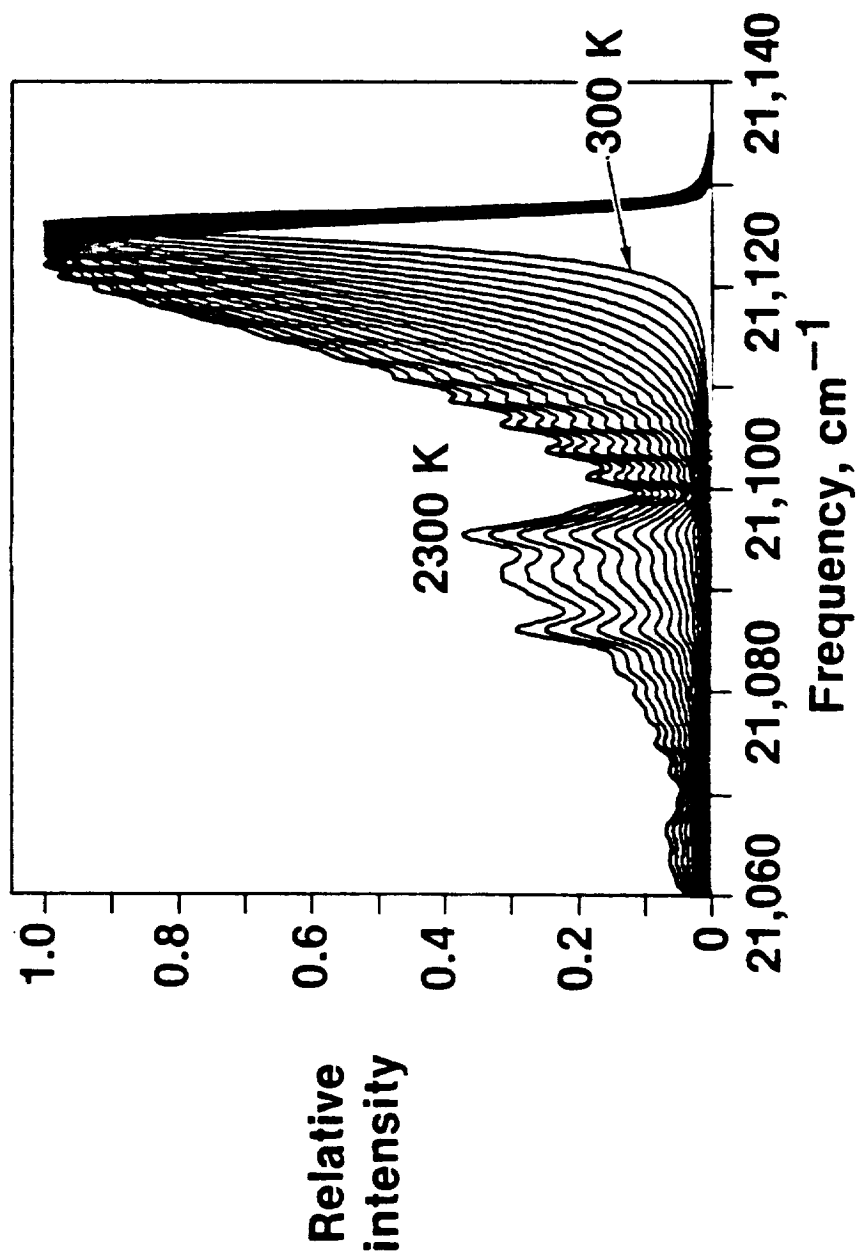
EFFECT OF DILUENT N₂ ON A LAMINAR ETHYLENE/AIR DIFFUSION FLAME

PANEL 25
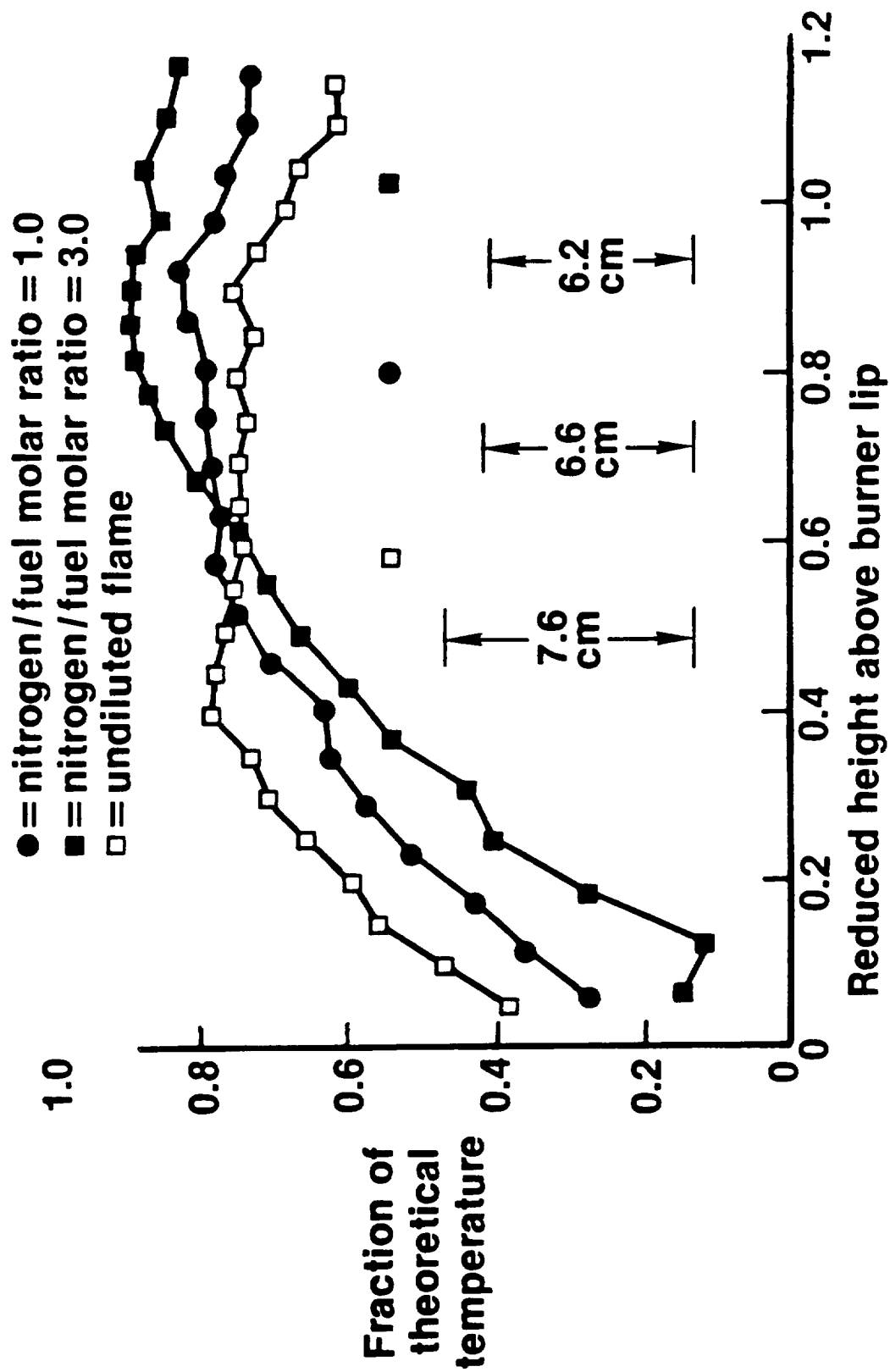
to the hostility of such jet engine environments. This illustrates that, despite the sophistication of these laser techniques, they can be engineered for hostile real world environments. The CARS instrument operates at 20 pulses per sec and therefore, in a 20 sec measurement period, gathers about 400 single shot temperature measurements as illustrated by the histogram displayed in Panel 26. From the histogram one can deduce the average temperature in the medium as well as deduce the magnitude of the turbulent temperature fluctuations. One can also display the time history of the measurements as they occurred.

Laser-Induced Fluorescence Spectroscopy (LIFS)

Laser-induced fluorescence spectroscopy has received much attention due to its very good sensitivity, i.e., it is capable of detecting constituents in trace levels at either the part per million or occasionally the part per billion type levels. Its primary utilization is in detecting trace quantities of constituents. However, because it interrogates individual vibrational-rotational states, it can be used for thermometry although it is hardly ever the method of first choice for thermometric utilization. It is a very sensitive technique because one probes an actual allowed electronic absorption in the constituent being observed as illustrated in Panel 27. Indeed fluorescence may be viewed as a very sensitive method of monitoring absorptions in a spatially precise manner. Following promotion to the upper

SINGLE PULSE CARS TEMPERATURES IN AUGMENTED JET EXHAUST

Center: 1398 K
Total count: 347

RMS deviation: 163 K
Spread test: 200 K

Time history

Histogram

PANEL 26

347
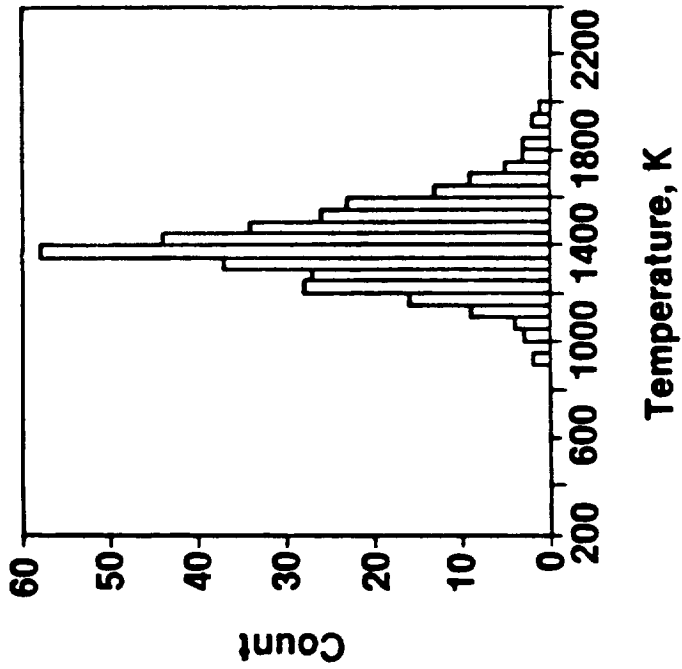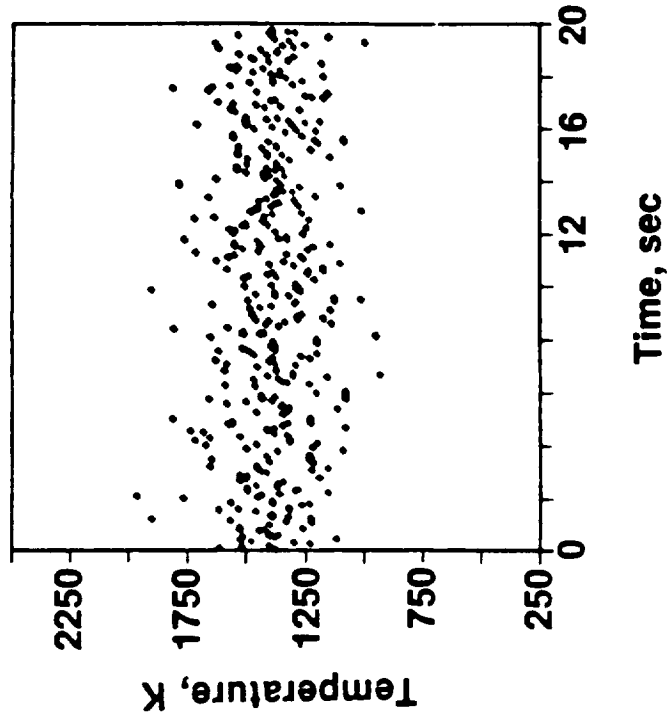
LASER-INDUCED FLUORESCENCE SPECTROSCOPY (LIFS)

Advantages

Simple

Spatially precise

Semi-quantitative

Ground state observed

Sensitive

Disadvantages

Limited species

Fluorescence efficiency

- Collisional quenching
- Photodissociation
- Chemical reaction

Laser

λ

PANEL 27

348
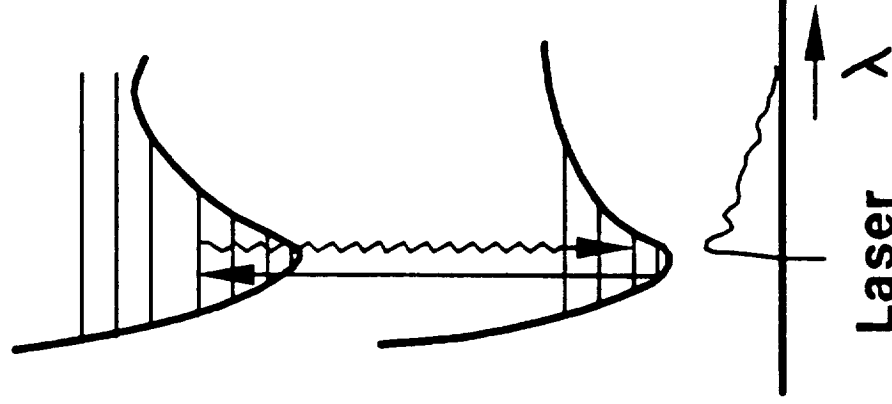
state by absorption, the fluorescence signal results from the spontaneously-emitted photons from the upper level. This is not an instantaneous process since the promoted electronic state has a finite lifetime. In addition to spontaneously radiating, there are a number of mechanisms by which this upper state can be deactivated, for example, by collisions with other molecules, the molecule may fly apart or photodissociate upon being excited, or it may disappear by a chemical reaction because the excited state may have an enhanced reactivity. These processes all diminish the efficiency of the fluorescence process and have to be taken into account in order for the measurements to be quantitatively precise. This is often difficult to do with great accuracy, so, in some respects, laser-induced fluorescence spectroscopy is often a semiquantitative technique.

The general approaches for using laser-induced fluorescence for thermometry are summarized in Panel 28. The first approach involves excitation scans. Here the laser is tuned over the various absorption transitions of the ground electronic state and the fluorescence from the entire upper manifold is typically monitored. This, in essence, allows the various rotational-vibrational states of the ground electronic state to be monitored from whence a temperature can be deduced. The difficulty with this approach is that one requires a tunable laser with a large tuning range and the technique is time consuming which precludes instantaneous measurements. A simplified extension of this approach is the two line technique. Here just two individual vibrational-rotational states in the ground electronic state are monitored. By exciting to the same upper state, the fluorescence

LASER INDUCED FLUORESCENCE THERMOMETRY APPROACHES

Excitation scans

Two line

Thermally-assisted
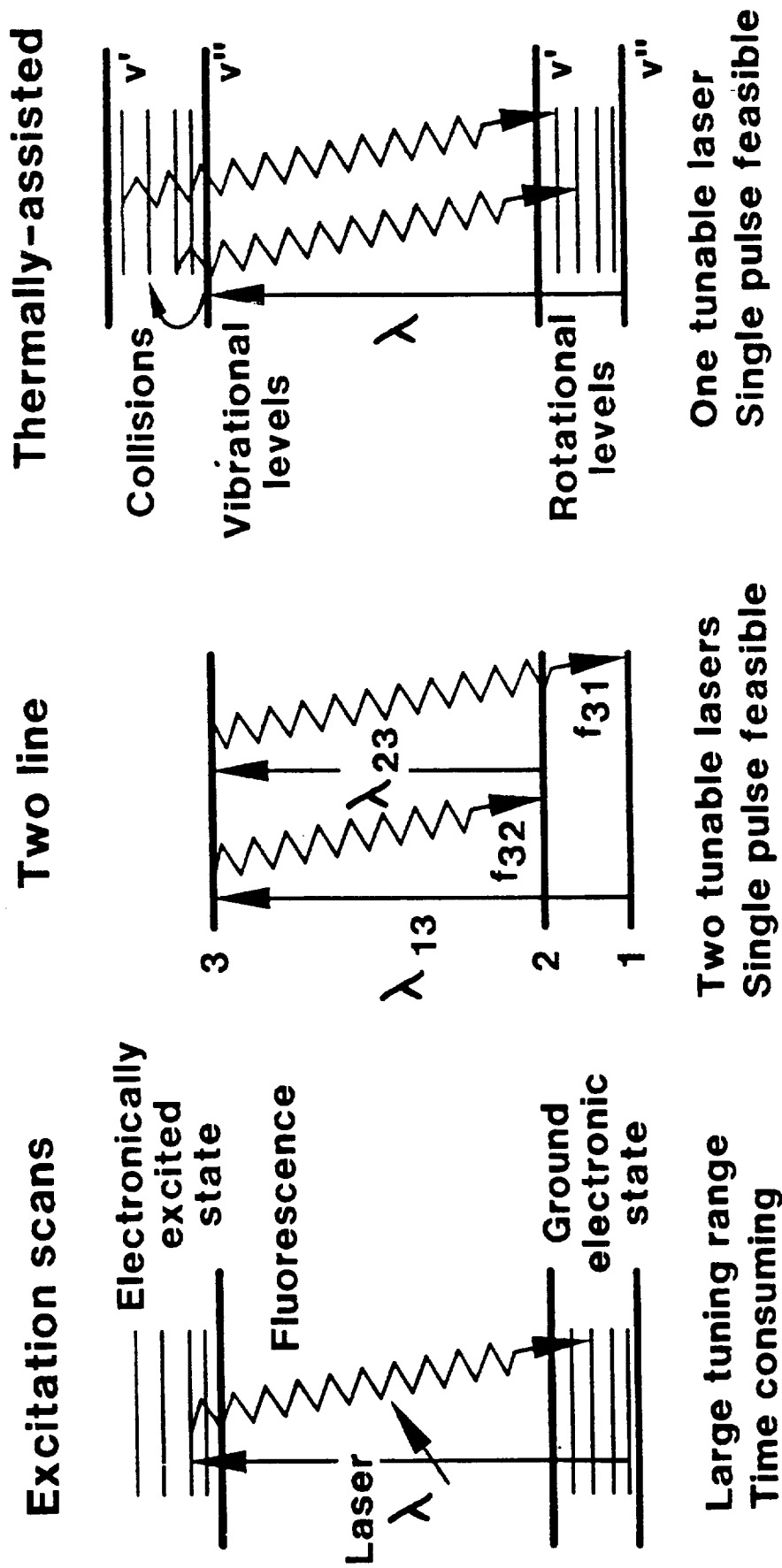
Large tuning range
Time consuming

Two tunable lasers
Single pulse feasible

One tunable laser
Single pulse feasible

PANEL 28

efficiency cancels out in the relative population determination making this a temperature measurement technique which is completely insensitive to quenching effects. Furthermore, if the two pulsed lasers are sequenced within a characteristic time for the medium to change, single pulse measurements become feasible. Such techniques have seen widespread utilization using atomic species such as thalium, indium, tin or lead seeded into the flames to perform highly accurate temperature determinations [Ref. 12]. One can also use this technique with naturally-occurring flame constituents and it has been employed, for example, with the hydroxyl radical to make temperature measurements in flames [Ref. 13]. However, the OH radical is present in sufficiently high concentrations only at high temperatures and so this approach is restricted to elevated temperature thermometry.

The third class of approaches is the so-called thermally assisted where one laser is used to promote excitation to a single vibrational-rotational level in the electronically excited state. Collisions with that state then redistribute population over the manifold of vibrational-rotational states and the resulting fluorescent distribution is a function of temperature. By monitoring the distribution of the fluorescence, the temperature can be deduced. This technique has also been demonstrated on seeded atomic species and on naturally occurring molecular species. In the latter instance, detailed computer modeling is required to predict the resulting fluorescence intensity distribution. With atomic seeds in flames, excellent results have been obtained with thermally-assisted laser-induced fluorescence thermometry. Panel 29 shows one such example of measurements from thalium in an acetylene/

oxygen/air flame. The temperature was independently measured to be 2465 K. Single-shot thermally-assisted fluorescence thermometry was demonstrated with a histogram mean at 2470 deg. Furthermore, the width of the resulting histogram was quite narrow as seen in Panel 29. However, as stated earlier, because of the need for a tunable laser, often in the ultraviolet, and the requirement to introduce seeds to achieve measurements at low temperatures, fluorescence thermometry is generally not the method of first choice.

Two-Dimensional Field Techniques

To this juncture we have concentrated on measurements made at a single point. However the incoherent techniques lend themselves readily to extensions of simultaneous measurements in one and or two dimensions. Two dimensional laser imaging [Ref. 14] is illustrated in Panel 30. Rather than illuminating the medium with a single ray or pencil of laser light, the laser is formed by various means into a sheet of light which intersects the medium under study. The scattering from various points along the sheet is then imaged onto a two-dimensional array detector which can spatially resolve the fluorescence emanating from each point along the illuminated sheet. The motivation for two dimensional imaging is summarized in Panel 31 and stems from the fact that it permits entire fields to be mapped at a single instant of time. This not only expedites data collection but, quite importantly, permits spatial correlations to be developed between various points. Such correlations enable one to gain phenomenological insight into the fundamental

SINGLE PULSE THERMALLY-ASSISTED LIFS THERMOMETRY IN FLAMES

Number of occurrences

$C_2H_2/O_2/air$
2465K ± 10K

T_{THAF} = 2470K ± 11K

Single-shot

Temperature, K

2435 2445 2455 2465 2475 2485 2495 2505

24 20 16 12 8 4 0
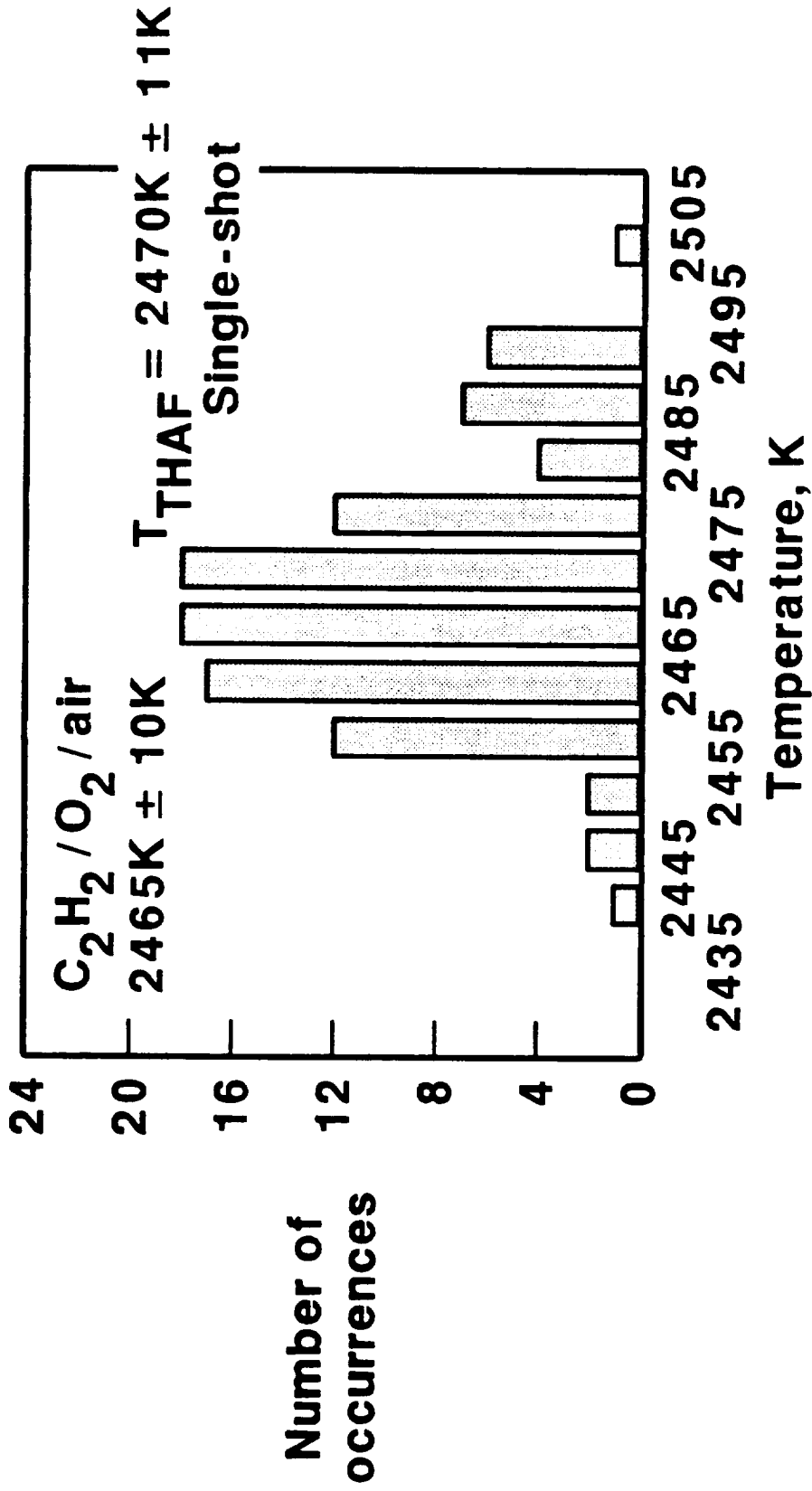
Ref: M.L. Elder, et al., Appl. Spect. 38, 113 (1984)

PANEL 29

353

2—D LASER IMAGING

Two—dimensional array detector

Field lens

Trap

Burner/Nozzle

Cylindrical lens

Laser beam
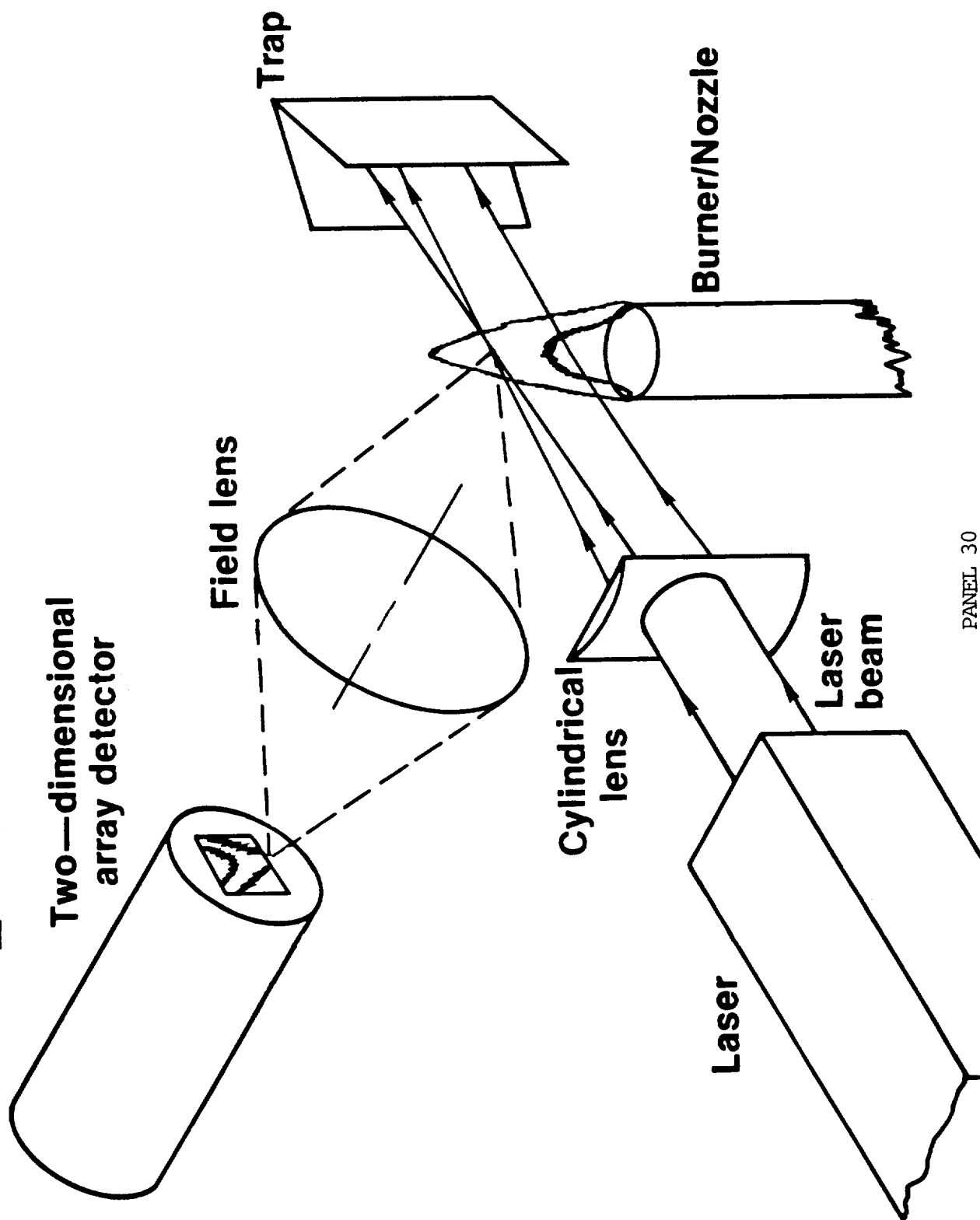
Laser

2-D IMAGING

MOTIVATION

- Laser based
- Field mapping
  - Spatial correlations
  - Phenomenological insight
- High repetition rates
  - Temporal correlations

PANEL 31

processes which are occurring. Such insight is often very difficult to glean from a series of statistically-uncorrelated single point measurements. Two dimensional imaging today can be done at very high repetition rates as lasers and cameras push into the hundreds of Hertz range. Such disadvantages as computer storage capabilities and computational speeds are rapidly diminishing with advances in the computer state of the art.

As summarized in Panel 32, all of the scattering processes previously considered can be potentially used for 2-D laser imaging. Mie scattering, i.e., the elastic scattering of light from particles, and laser-induced fluorescence have actually seen the most utilization in this regard due to the strength of the respective processes. Rayleigh scattering is fairly strong but its utility is restricted to total density measurements in particle-free situations as discussed earlier. Raman scattering, due to its weakness, is very difficult to implement in atmospheric pressure, two-dimensional situations unless one has very powerful one-of-a kind pulsed lasers [Ref. 15].

Imaging techniques have actually seen the most use for species concentrations measurements although they can be implemented to make temperature measurements as well. In our laboratory we have used linear Rayleigh imaging in a turbulent flow to measure flame thicknesses. In this particular application, Rayleigh scattering from along a line of laser light was imaged onto a linear diode array to observe the density variation through the flame front. Since the Mach number was low and since the composition dependence of the total Rayleigh cross section was also very small, temperature could be obtained from the density measurement through the perfect

SCATTERING PROCESSES FOR IMAGING

- **Mie Scattering**

  Seeding required

  Fractional concentration measurement

- **Rayleigh Scattering**

  Total density measurement

  Temperature from gas law, $M \ll 1$

- **Raman Scattering**

  Very weak

  Temperature, species mapping difficult
  in atmospheric pressure flames

- **Fluorescence**

  Species mapping (limited)

  Seeding possibly required

  Temperature measurements awkward

  Velocity mapping possible

PANEL 32

357

gas law. Panel 33 shows one such measurement example obtained with a single 10^{-8} sec laser pulse. Fluorescence has seen the most use for two-dimensional flame temperature mapping and most work to date has employed two line fluorescence approaches to perform the two dimensional temperature measurements [Ref. 16]. However such approaches require not only two lasers but also two detectors and one has to register very carefully the two spatial fields in order to get accurate temperature measurements. Thus this approach is quite cumbersome and is not easy to implement. The simplest approach demonstrated to date involves seeding the flame with an inert constituent at constant mole fraction. By picking the correct transition in the molecular seed, one can achieve a fluorescence intensity which displays a peak behavior relative to temperature as shown in Panel 34 by the $Q_1(22)$ transition in NO. Upon illuminating a flame or field whose temperature is to be measured, the area of maximum fluorescence intensity then corresponds to the temperature at which the peak in the fluorescence occurs. The temperature at other points in the field can then be deduced from this peak temperature by moving sequentially away from this self-calibration point as it were. An example of using this approach is shown in the temperature contours obtained in a rod stabilized flame shown in the right hand portion of Panel 34. For this technique to work, the seed must be chemically inert and must be uniformly dispersed throughout the entire medium.

Panel 35 presents a summary of the various spatially precise laser diagnostics that have been considered here for species and temperature measurements in the gas phase. Rayleigh scattering, because it is not species

358

RAYLEIGH IMAGING IN A TURBULENT FLAME

Single 10^{-8} sec pulse; CH_4—air

PANEL 33

359
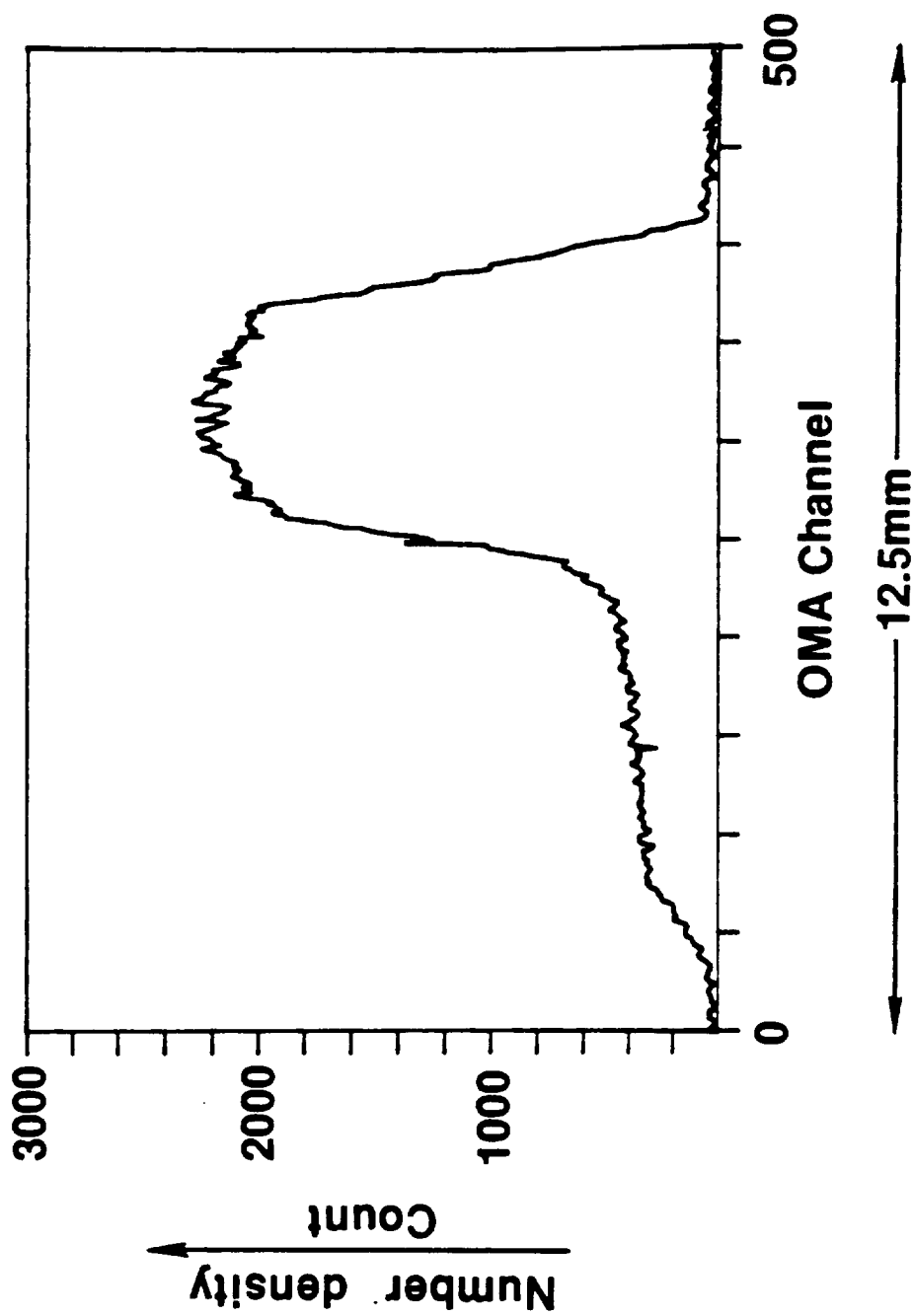
TWO-DIMENSIONAL LIFS
TEMPERATURE IMAGING IN FLAMES

NO seeded at constant mole fraction

Concept

Contours
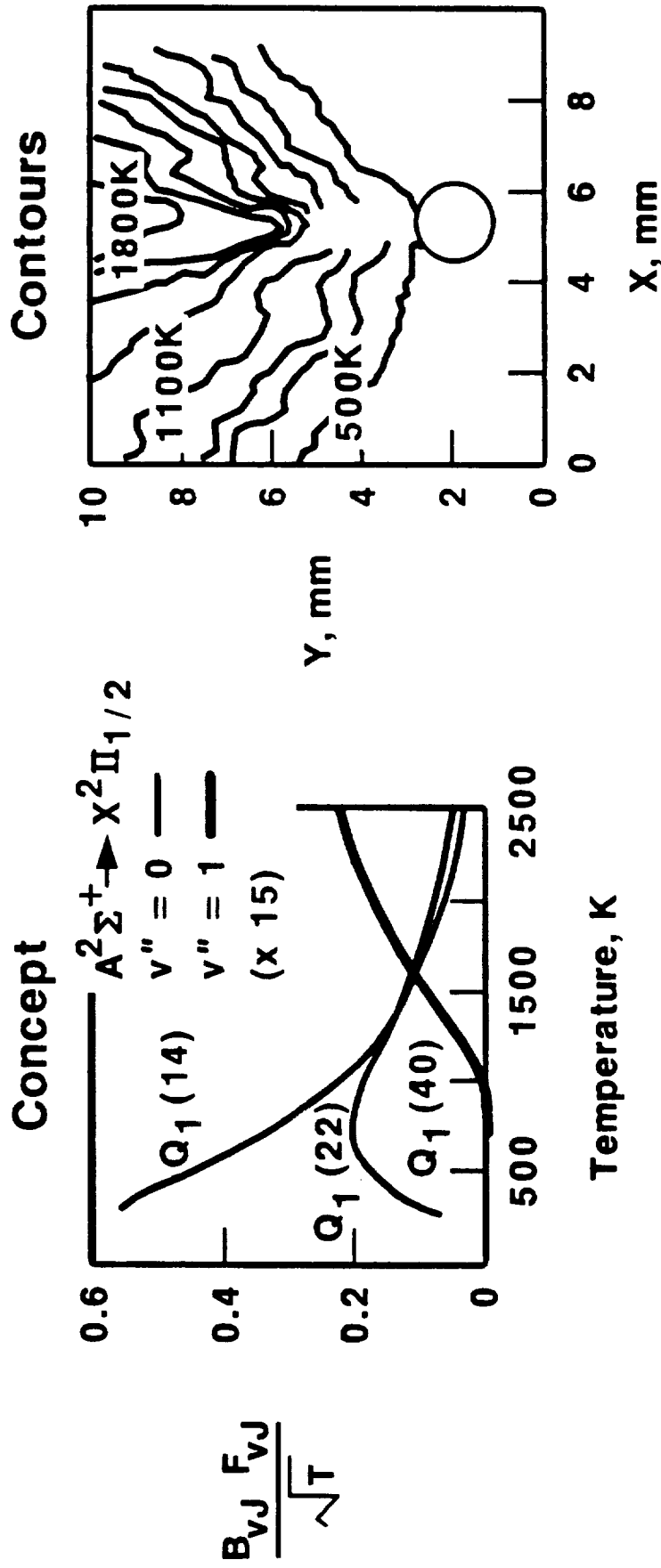
Ref: J.M. Seltzman, et al., Optics Letters 10, 439 (1985)

SPATIALLY-PRECISE LASER COMBUSTION DIAGNOSTICS
Summary

- Rayleigh scattering
  - Total number density, temperature (gas law)
  - Applicable only to particle-free situations

- Spontaneous Raman scattering
  - Thermometry, major species (>0.1%) measurements
  - Restricted to relatively clean flames and flows

- Laser induced fluorescence
  - Flame radicals, atomic species
  - Thermometry

- CARS
  - Thermometry, major species
  - Broadly applicable

PANEL 35

361

specific, can only be used to measure the total number density from which temperature can be derived if one has a constant pressure situation. Furthermore Rayleigh scattering is applicable only to particle free situations. However it is extremely strong and can be a very powerful technique with carefully chosen flames. Spontaneous Raman scattering is species specific. However, it is extremely weak technique and therefore is capable of measuring only the major species in combustion systems. Furthermore its utilization is restricted to flames that are relatively clean, that is whose luminosity levels are not too high and whose soot particle loadings are relatively low. Also due to its weakness it is very difficult to implement in two-dimensional imaging situations. Laser-induced fluorescence is an extremely sensitive technique for looking at flame radicals and atomic species, and because of its strength, lends itself readily to two-dimensional imaging. However its utilization for thermometry is generally somewhat cumbersome and, therefore, it is generally not the thermometric method of choice. CARS is capable of temperature and major species concentrations measurements in combustion systems. Because of its signal strength and coherence, it is a technique that is broadly applicable to many practical combustion systems and devices. CARS can also be implemented in a linear imaging mode but has not seen widespread attention in this regard.

I

References

1. A. C. Eckbreth, P. A. Bonczyk and J. F. Verdieck: Prog. Energy Combust. Sci. $\underline{5}$, 253 (1979).

2. A. C. Eckbreth: Proceedings 18th Symposium (International) on Combustion, p. 1471, The Combustion Institute, Pittsburgh, PA, 1981.

3. A. C. Eckbreth: AIAA Paper No. 86-0138 (1986); to be published in the J. Propulsion and Power (1987).

4. A. C. Eckbreth: <u>Laser Diagnostics for Combustion Temperature and Species</u>, Abacus Press, Kent U.K., 1987.

5. J. A. Shirley: pp. 603-617, NASA Conference Publication 2372 (1985).

6. A. C. Eckbreth and J. W. Davis: Appl. Opt. $\underline{16}$, 804 (1977).

7. J. A. Shirley: pp. 107-123, NASA Conference Publication 2436 (1986).

8. A. C. Eckbreth and T. J. Anderson: SPIE Paper 742-07 (1987).

9. A. C. Eckbreth: SPIE Proceedings $\underline{621}$, 116 (1986).

10. L. R. Boedeker and G. M. Dobbs: Comb. Sci. Tech. $\underline{46}$, 301 (1985).

11. A. C. Eckbreth, G. M. Dobbs, J. H. Stufflebeam and P. A. Tellex: Appl. Opt. $\underline{23}$, 1328 (1984).

12. G. Zizak, N. Omenetto and J. D. Winefordner: Opt. Eng. $\underline{23}$, 749 (1984).

13. R. Cattolica: Appl. Opt. $\underline{20}$, 1156 (1981).

14. R. K. Hanson, Proceedings 21st Symposium on Combustion, The Combustion Institute, Pittsburgh, PA, 1987, in press.

15. M. B. Long, D. C. Fourguette, M. C. Escoda and C. B. Layne: Opt. Lett. $\underline{8}$, 244 (1983).

16. R. J. Cattolica and D. A. Stephenson: pp. 714-721 in J. R. Bowen, N. Manson, A. K. Oppenheim and R. I. Soloukhin, Eds.: <u>Dynamics of Flames and Reactive Systems</u>, AIAA, New York, 1984.

I

RADIOMETRIC IMAGING

INFRARED RADIOMETRIC TECHNIQUE IN TEMPERATURE MEASUREMENT

by S. Glazer *
R. Madding **

ABSTRACT

One class of commercially available imaging infrared radiometers using cooled detectors is sensitive to radiation over the 3-12 micron wavelength band. Spectral filters can tailor instrument sensitivity to specific regions where the target exhibits optimum radiance. The broadband spectral response coupled with real time two-dimensional imaging and emittance/background temperature corrections make the instruments useful for remote measurement of surface temperatures from -20C to +1500C. Commonly used radiometric techniques and assumptions are discussed, and performance specifications for a typical modern commercial instrument are presented. The potential usefulness of an imaging infrared radiometer in space laboratories is highlighted through examples of research, nondestructive evaluation, safety, and routine maintenance applications. Future improvements in instrument design and application of the radiometric technique are discussed.

* Member of the Technical Staff, Applied Technologies Section, Jet Propulsion Laboratory, Pasadena, Calif.

**Manager of Applied Technology, Inframetrics, Inc., Bedford, Ma.

PRECEDING PAGE BLANK NOT FILMED

INTRODUCTION

The purpose of this presentation is to discuss the broadband infrared radiometric temperature measurement technique taken by that class of commercially available imaging infrared radiometers using cooled detectors and sensitive in the 3-12 micron wavelength band. These instruments are well suited for quantitative noncontact measurement of surface temperatures as low as -20C. This relatively low temperature capability, coupled with high spatial and thermal resolution, plus near real time scanning to be speeds, make these modern commercial instruments highly useful in a laboratory environment. One such modern infrared imaging radiometer, the Inframetrics 600 system, combines the above capabilities with a built-in temperature reference, the ability to make corrections for target emittance and background radiance, plus the ability to do extensive post processing. The specifications and capabilities of this instrument make it representative of the commercial state-of-the-art of quantitative infrared thermal imaging systems. The capabilities of modern systems suggest possible uses for infrared radiometers as standard instrumentation in space laboratories. Potential applications in Spacelab might include routine nondestructive evaluation, or maintenance/safety checks of laboratory equipment , and research uses in medical, biological, and microgravity science experiments.

COMMERCIAL INFRARED IMAGING RADIOMETERS

The most sensitive commercial infrared radiometric systems typically use detectors cooled to cryogenic temperatures to improve the specific detectivity. Instruments requiring fast response (on the order of microseconds), such as fast scanning or imaging systems, often use photon detectors, as opposed to thermal detectors. Two commonly used detector materials are InSb (indium-antiminide), and HgCdTe (mercury-cadmium-telluride). These detectors typically exhibit spectral sensitivity over at least a portion of the 3-12 micron wavelength band. Within this range, the 5-8 micron band is often avoided due to strong spectral atmospheric attenuation, principally from water vapor and carbon dioxide, while the subbands of 3-5 and 8-12 microns are commonly used. As described by the Wien displacement law, the shift to shorter wavelengths of the peak spectral photon radiance with increasing temperature results in higher temperature sensitivity in the 8-12 micron wavelength band for targets below approximately 400C . At higher temperatures, the 3-5 micron wavelength spectral band offers more sensitivity. By comparison, pyrometers which operate with detectors sensitive in very narrow spectral regions at much shorter wavelengths are better suited to accurate measurement of much higher temperatures, with 400C-800C often representing the low end of

I

the range.

For opaque targets, knowledge of the target emittance and background radiance is required for accurate calculation of the target temperature from the radiosity measurement. Inaccuracy in the calculated target temperature resulting from errors in its assumed emittance increases with decreasing emittance. For targets not fully opaque in the instrument spectral measurement band, additional knowledge of the transmittance is required. Further, signal attenuation due to optical components and absorbing media must be known. The broadband infrared detector response may often be exploited through spectral filtering to reduce the importance of the above effects on temperature measurement accuracy. Selective spectral filtering may be used, for example, to operate in a spectral region where the target exhibits optimal radiance (high emittance and/or low transmittance). It may also be employed to avoid spectral ranges where atmospheric attenuation is high. Where the transmittance through the optical train is dependant on intervening window temperatures, selective spectral filtering might first be used to view the windows where they are known to be opaque and possibly of high emittance. Then, the detector may again be filtered to operate where the window transmittance is high and well characterized as a function of its (known) temperature.

Near real time imaging systems operating, for example, at video rates of 30 frames per second, offer large advantages over nonimaging systems. Rapid observation of steady state and transient temperature gradients over large surfaces may prove highly useful in many applications. Also, the temperature of moving targets within the instrument field of view (FOV) may be observed without the need for active tracking.

PERFORMANCE CRITERIA

Understanding of a few common radiometer performance criteria is essential in evaluation of an instruments' capabilities, and when comparisons are made between several systems. Criteria discussed here are only intended to quantify the most basic thermal and spatial resolution capabilities.

Thermal Resolution Criteria: Two key thermal resolution criteria are the Noise Equivalent Temperature Difference (NETD), and the Minimum Detectable Temperature Difference (MDTD). The NETD is defined as the temperature difference where the change in signal output equals the rms system noise. This is a quantity which can be measured, and is independant of output device, observer, and imaging capabilities. The MDTD is the NETD for an imaging system, and takes into account the reduction of system noise due to the frame integration of the human eye during its 0.2 second persistence period. Typically, the noise is reduced by the square root of the number of frames integrated. For an imaging

369

system operating at video rates of 30 Hz, approximately 6 frames
are integrated by the human eye, resulting in an MDTD slightly
less than half the system NETD.

Spatial Resolution: Important spatial resolution criteria include
the Instantaneous Field of View (IFOV), and the Modulation
Transfer Function (MTF). The IFOV is the solid angle subtended
by the detector, and must not be confused with the overall Field
of View (FOV) of the imager. Obviously, the IFOV represents the
smallest target size which may be uniquely resolved by the
detector. The MTF is defined as the system response to a
sinusoidally varying input radiance pattern, plotted as a
function of spatial frequency (ie., cycles/milliradian). The MTF
is a function of the IFOV, scan rate, detector spectral range,
and detector/instrument time constant. For a given system, the
transient response of the detector/instrument to an instantaneous
step change in input radiance determines the time required to
attain, say, 95% of the steady state output response owing to the
step change. At a fixed scan rate, then, this can be translated
into the minimum target size, in terms of the detector IFOV,
required to reach the nearly steady output signal. At video scan
rates, with a typical HgCdTe detector of approximately 0.001 inch
square, a convenient "rule of thumb" is that a target must
subtend a minimum of five IFOV's for accurate, repeatable,
quantitative measurements to be made. It should be noted that
merely slowing or even stopping the scan does not reduce the
minimum target size requirement to one IFOV. Diffraction through
the system optics also contributes to the transient response to a
step change in the radiance pattern. Since the magnitude of the
diffraction blur increases with longer wavelengths, this
component of the minimum target size requirement is necessarily
larger for longer wavelength infrared systems than for the
typically short wavelength pyrometric instruments.

INFRAMETRICS 600 IMAGING INFRARED RADIOMETER SYSTEM

Performance Characteristics/Operational Capabilities: Introduced
in 1985/1986, the Inframetrics 600 imaging infrared radiometer
system is considered representative of a commercial state-of-the-
art instrument. Other manufacturers, such as AGA, and Hughes,
also produce a similar class of equipment, but with somewhat
different operating characteristics. Ownership of an
Inframetrics 600 system by the Applied Technologies Section of
the Jet Propulsion Laboratory and resultant familiarity with it
leads to representation of its operating characteristics in Table
1 as typical of a commercial state-of-the-art instrument.

Radiometric Equations for Temperature Calculation: Figure 1
schematically illustrates a scanner unit observing a target
through an optical window within a chamber. A general
formulation of the radiometric equation which may be written for

370

TABLE 1. INFRAMETRICS 600 IMAGING INFRARED RADIOMETER SYSTEM
KEY OPERATING CHARACTERISTICS

Spectral Sensitivity   3-5, 8-12, or 3-12 microns

Detector Type   HgCdTe

Detector Operating Temperature 77K (liquid nitrogen cooled)

NETD   0.2C @ 30C (8-12 microns)

MDTD   0.1C @ 30C (8-12 microns)

Integrated NETD   0.05C @ 30C (8-12 microns)

Accuracy   Larger of +/- 2% of (T-25C) or
                                     1C, for T<400C
                                Larger of +/- 5% of (T-25C) or
                                     2C, for T>400C

Output   RS-170 Video(30 Hz frame rate)

FOV   15 deg. vert. x 20 deg. horiz.

IFOV   2 mrad. x 2 mrad.
                                     (~0.1 mm x 0.1 mm,
                                        w/6 in. close up lens)

Chopper Temperature   Updated every 0.5 sec.

Calibration   I(T) stored in PROM for all
                                     installed filters, over
                                     the range of -20C<T<1500C

Radiometric Equation   Solved in real time for target
                                     temp. using window
                                     window transmittance,
                                     target emittance,
                                     background temp., and
                                     chopper temp.

371

TABLE 1. (CONTINUED)


Dynamic Range   8 bits, or 48 db w/16 frame
                                       integration option

Temperature Ranges   5, 10, 20, 50, 100, 200, 500,
                                       1000, 2000C

Internal Filters   Any of 4 selectable on command

Display Modes   Black/white, false color,
                                       point readout, isotherms,
                                       horiz. line scan, fast
                                       (125 microsec.) line scan

Post Processing   Extensive IBM PC/AT based
                                       system, average up to 256
                                       frames, statistical data,
                                       mult. display & parameter
                                       change options

Scanner Size/Weight   8 in. x 5 in. x 5 in., 6.5 lbs

Modes/Functions   Programmable through RS-232
                                       computer interface

C-5

FIGURE 1

RADIOMETRIC EQNS. FOR GRAY, DIFFUSE TARGET IN A UNIFORM TEMP. ENVIRONMENT:
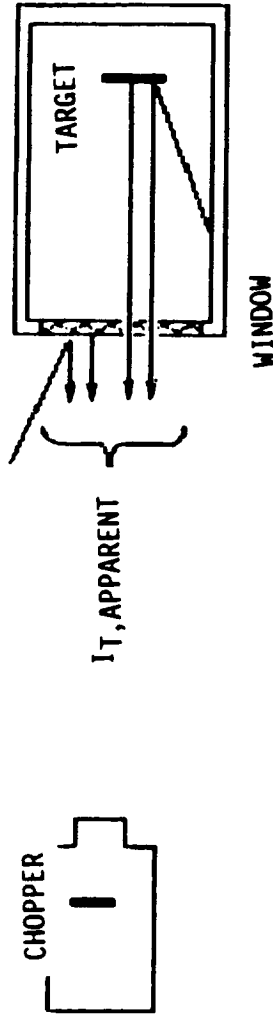
$$I_{T,APPARENT} - I_C = \tau_W\{\varepsilon_T I_T + (1-\varepsilon_T)I_{TB}\} + \varepsilon_W I_W + (1-\varepsilon_W-\tau_W)I_{WB} - I_C \quad (1)$$

$$(\Delta I_{T,MEASURED})$$

WHERE:

$I = I(T) = $ INSTRUMENT RESPONSE TO BLACKBODY RADIANCE,

$\varepsilon = $ EMITTANCE, $\tau = $ TRANSMITTANCE, $T = $ TEMPERATURE

SUBSCRIPTS:

$T = $ TARGET, $W = $ WINDOW, $C = $ CHOPPER, $B = $ BACKGROUND

IF $T_W = T_{WB} = T_C$, THEN EQN. (1) REDUCES TO:

$$\Delta I_{T,MEASURED} = \tau_W\{\varepsilon_T I_T + (1-\varepsilon_T)I_{TB} - I_C\} \quad (2)$$

the target temperature is shown on that figure as equation (1). Key assumptions and simplifications used in this particular formulation include:

- the target surface is gray and diffuse, and its graybody emittance over the spectral measurement range of the instrument is known;

- the target is opaque;

- the target meets the minimum 5 IFOV size requirement;

- the entire surroundings (background) temperature is uniform and known;

- the window is diffuse, contains no internal fresnel reflections, and its transmittance, emittance, and temperature are known;

- the temperature outside the window, reflecting into the scanner, is uniform and known;

- the chopper is at approximately the same temperature as its immediate enclosed environment within the scanner, and is known.

The requirement for diffuse target and window may be relaxed if the radiance of the appropriate background directionally reflecting from those surfaces is known. As shown on Figure 1, under the further assumption that the window (and all other camera optics), the external window surroundings, and the chopper are all at the same temperature, equation 1 may be simplified and rewritten as shown in equation (2). Since the instrument response I(T) is assumed only a function of temperature, and is known from the system calibration curve, the target temperature may be solved if only the window transmittance, target emittance, and target background temperature is known. The Inframetrics 600 system continuously solves equation (2) over the entire scene for the target temperature, and displays the calculated temperatures on its display in real time. A useful feature of the instrument is its ability to record all necessary setting parameters along with the data on video tape, permitting further analysis by its minicomputer based post processor system in real time or off-line. This permits solution of more detailed equations if required.

POTENTIAL APPLICATIONS IN A SPACE LABORATORY ENVIRONMENT

Many potential applications exist for a broadband infrared radiometer in a space laboratory environment. This section includes a brief listing of some research applications, as well as non-destructive evaluation (NDE) and routine station maintenance functions. Thermographic results of some similar earthbased applications are included in the Figures.

Research Applications:

.   Microgravity research experiments involving convective fluid flow;

.   Sample temperature measurement in containerless processing experiments;

.   Selective gas species identification through tunable wavelength active laser scanning. Several types of fluid mixing experiments could concievably be supported. Related work is being carried out by T. McRae at Lawrence Livermore National Laboratory;

.   Medical experiments involving body or biological tissue temperature measurements. Several routine medical diagnostic uses for infrared radiometry already have been identified (see Figure 2);

.   Non-contact temperature measurement of large structures/antennae, both deployable and fixed, for thermal modelling verification, and direct use in structural analysis and deflection prediction. Figure 3 illustrates an infrared examination of the Deep Space Net Echo antenna at Goldstone, Calif.;

Non-Destructive Evaluation, Station Maintenance Applications:

.   Thermal evaluation of electronic circuit boards. Ground based thermographic inspection of circuit boards is known to be a powerful diagnostic tool. Figure 4 illustrates a single hot chip on an electronics board;

.   Examination of solar cells and panel assemblies. Initial work performed at the Jet Propulsion Laboratory in support of the Flat Plate Solar Array (FSA) project confirmed the usefulness of infrared inspection of large photovoltaic assemblies for identification of damaged or severely back biased cells. Figure 5 illustrates a single back biased hot cell in a large photovoltaic panel;

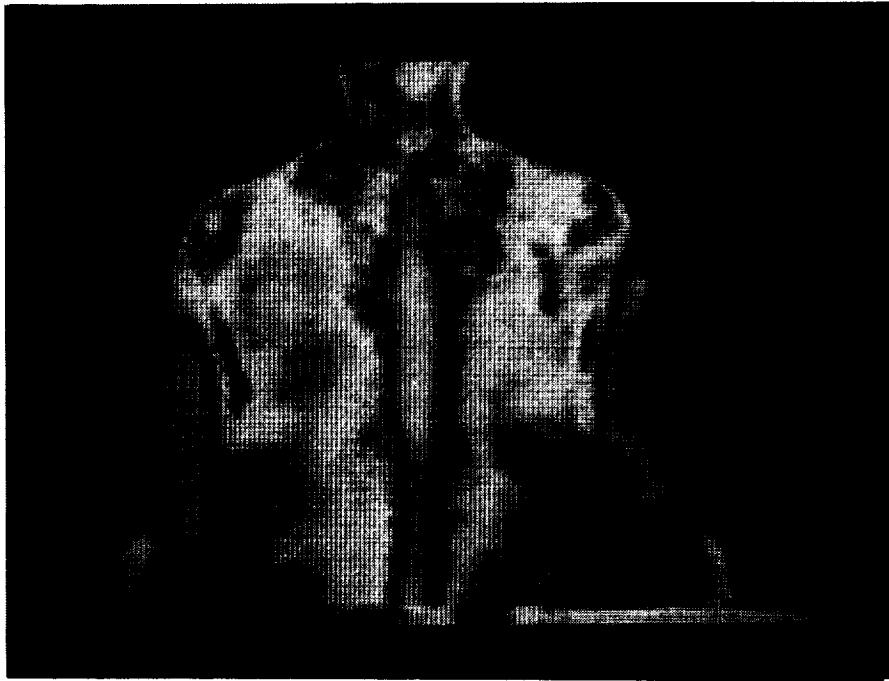.   Composite panel crack detection, or delamination
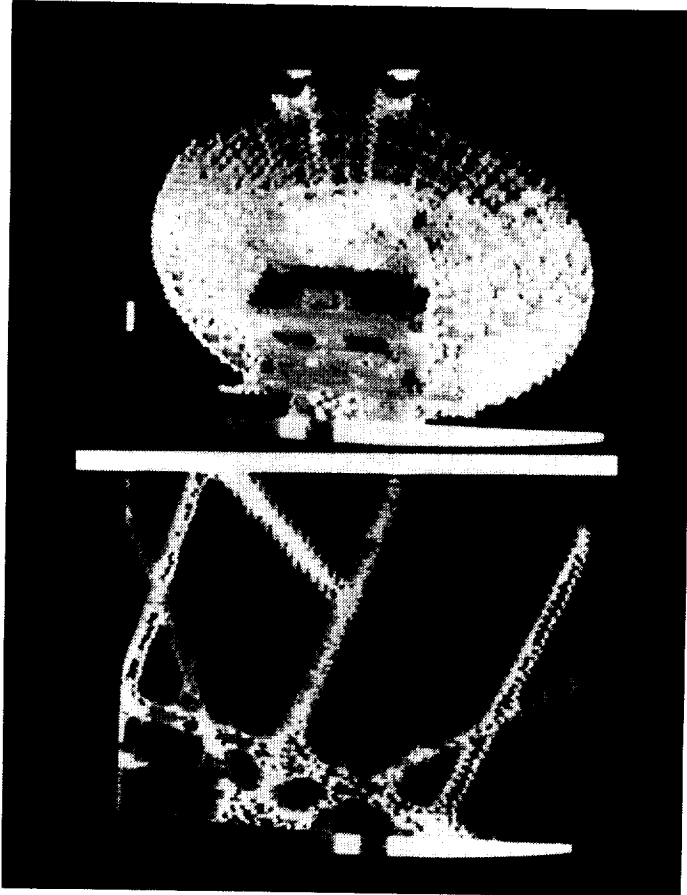
Figure 2. Medical Applications of Thermal Imaging

Figure 3. Thermal Image of Deep Space Net Echo Antenna at
Goldstone, Calif.
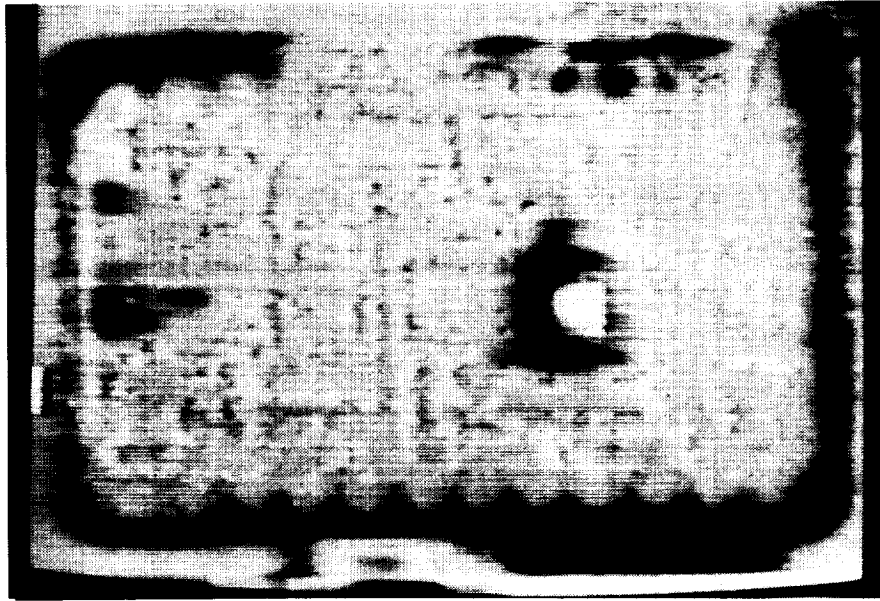
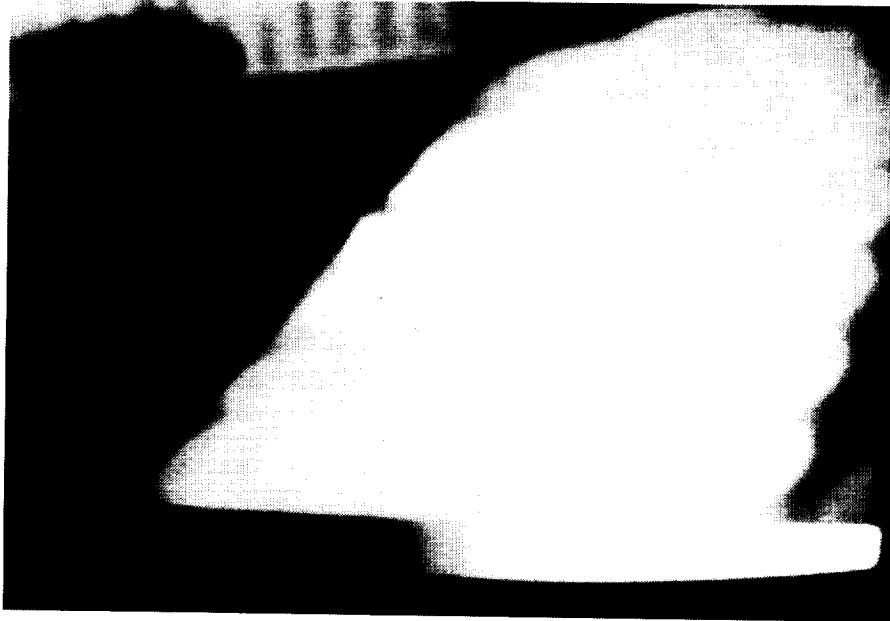Figure 4. Non-Destructive Infrared Evaluation of Printed Circuit Board

Figure 5. Infrared Examination of Photovoltaic Panel, with Hot (Back Biased) Cell

identification in composite or built-up structures. Figure 6 shows delamination in one of several heaters applied to the retro-propulsion module of the Galileo spacecraft. Actual local debonding of the film heater from the structure was confirmed. The heater was subsequently removed and rebonded;

. Thermal inspection of insulated panels, including multi-layer insulation blankets, to assist in thermal control;

. Infrared inspection of external surfaces, for the purpose of evaluating changes in emittance, and subsequent degradation of other thermal properties. Infrared radiometric equipment can be used to solve for target emittance under certain conditions;

. Thermal inspection of tanks containing liquids, to verify liquid/ullage levels. Figure 7 illustrates how the large heat capacity of liquefied natural gas in a tank translates to a large temperature difference during a transient heating event;

. spectral analysis of thruster plumes, and evaluation of contaminant spread to external surfaces.

FUTURE TRENDS IN INFRARED INSTRUMENTS/TEMPERATURE MEASUREMENT ALGORITHMS

Advances are being made in a number of areas relating to infrared instrument design and analysis algorithms. Practical results of these efforts promise simpler, more accurate, and more reliable instruments and data analysis. Some of the trends which would enhance the capabilities of instruments which may someday be qualified for spaceflight include:

. thermoelectric and closed cycle detector cooling. The use of stored cryogen for detector cooling is impractical for prolonged missions. Development of reliable closed cycle coolers will permit extended unattended operation, without mass or volume penalty associated with stored cryogens. AGA Corp. has already introduced a thermoelectric cooler in one of its commercially available radiometers.

. multielement (non-mechanical scanning) detector arrays. Although presently available in certain applications, high cost and difficulties in dynamic detector balancing and stability with time prevent their widespread use today.

. infrared optical fibers transparent in the 8-12 micron wavelength band. The availability of such fibers might provide weight and reliability improvements over a large
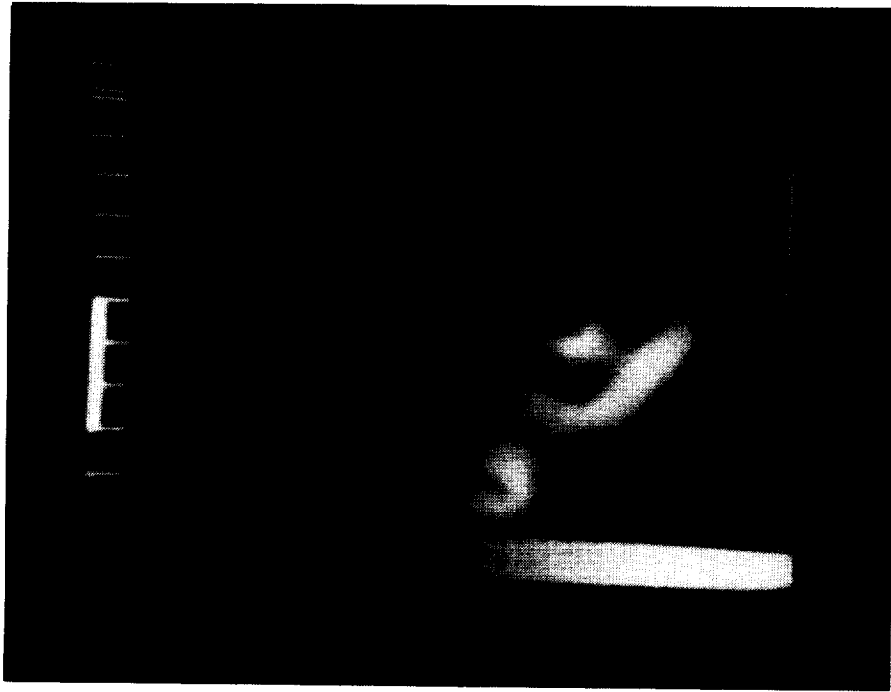
Figure 6.   Non-Destructive Infrared Evaluation of Film
           Heater on Galileo Spacecraft, Showing Delamination
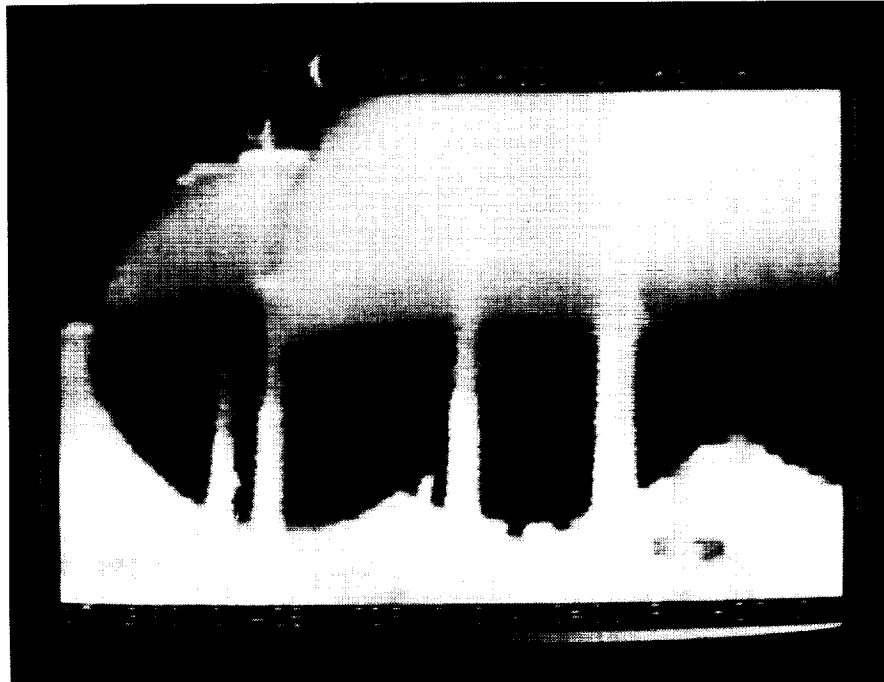
Figure 7. Thermal Image Showing Liquid Levels within LNG Tanks

382

number of distributed conventional temperature sensors
required in the Spacelab or aboard the Space Station. They
may also permit more extensive use in areas where non-
contact sensors are desireable, such as in certain
electronics assemblies.

development of simple methods for spatial emittance
measurement in specific situations. Techniques have already
been developed for emittance mapping of electronic circuit
boards under carefully controlled conditions during ground
testing. The concurrent use of these two dimensional
emittance maps with radiosity data promises to greatly
enhance data accuracy.

REAL TIME THERMAL IMAGING OF HIGH TEMPERATURE SEMICONDUCTOR MELTS

Michael J. Wargo

Massachusetts Institute of Technology

Cambridge, MA 02139

ABSTRACT

A real time thermal imaging system with temperature resolution better than +/- 1 degree centigrade and spatial resolution of better than 0.5 mm has been developed. It has been applied to the analysis of melt surface thermal field distributions in both Czochralski and liquid encapsulated Czochralski (LEC) growth configurations. The melt is viewed in near normal incidence by a high resolution (512x512) charge coupled device (CCD) camera to which is attached a very narrow bandpass filter (1 nm width centered on 632 nm). The resulting image is digitized (8 bit/pixel) and processed using a pipelined pixel processor operating at an effective 40 million operations per second thus permitting real time high frequency spatial and temporal filtering of the high temperature scene. The dual ported nature of the digital storage units allows the parallel processing of the optical intensity data by off-loading the task to the main CPU, floating point accelerator and array processor. In this way, graphics overlays are generated which display concurrently processed data with no performance penalty on image processing.

A multi-pixel averaging algorithm has been developed which permits localized, low noise sensing of temperature variations at any location in the hot zone as a function of time. This signal is being used to implement initial elements of a feedforward growth control scheme which is aimed at reducing thermal disturbances to the melt caused by the batch nature of the growth process. The effect of magnetic melt stabilization (with axial fields of up to 5 kgauss) on radial melt temperature distributions has been measured using this technique. Presently, the system is capable of measuring only relative temperature differences. Problems associated with residual internal reflections and non-optimized optical path geometry are discussed.

Introduction and Background

The growth of semiconductor single crystals by the Czochralski crystal pulling technique and, in particular, the growth of compound semiconductors like GaAs using the liquid encapsulated Czochralski (LEC) technique, requires precise control of the thermal field within the melt and growing crystal. The spatial temperature distribution in the melt is established by the hot zone, crystal and environmental thermal boundary conditions. In conventional growth systems, a single-input-single-output (SISO) closed loop proportional, integral and derivative (PID) controller is used to maintain and/or change a single temperature to accomplish the task of controlling the temperature distribution in the melt. Thermocouples or single color pyromters are generally used as the sensors for this purpose. As shown in figure 1, the location of the single point temperature sensor is typically well

Conventional Control Points

Heater

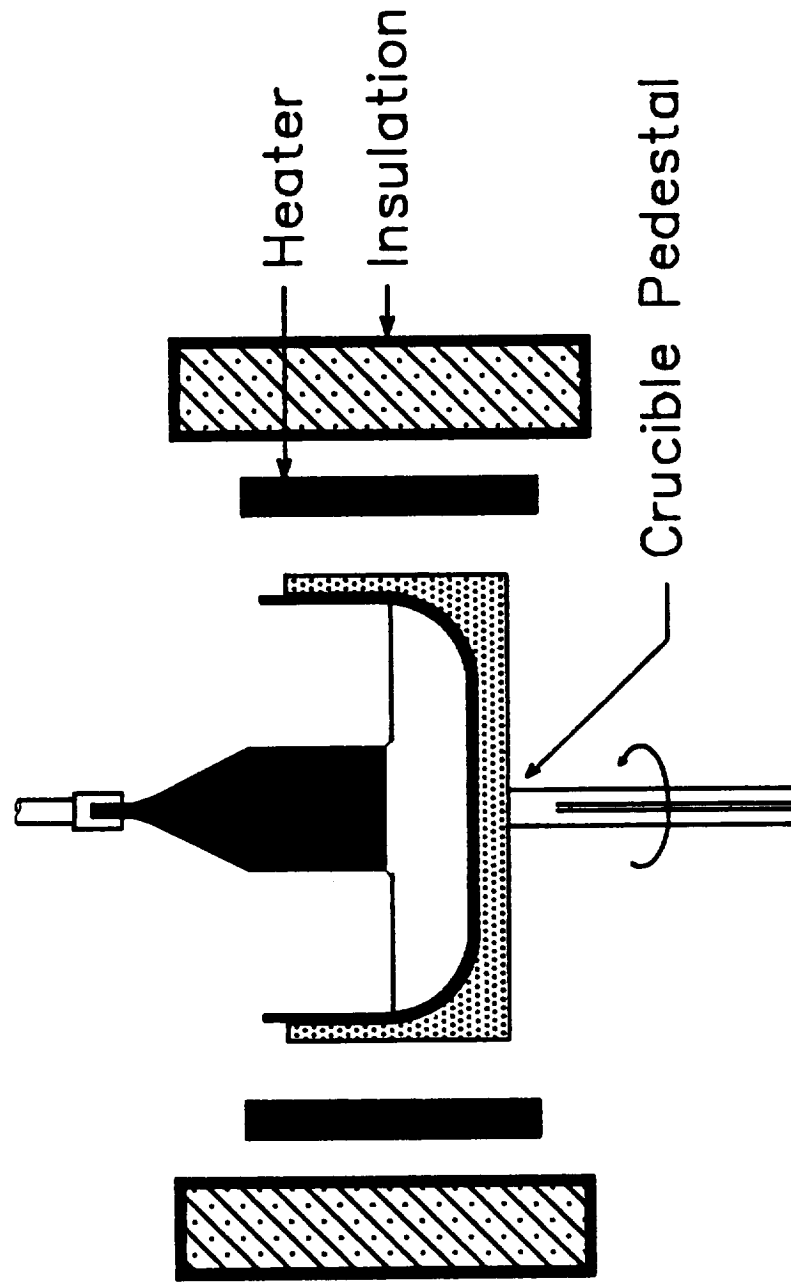**Insulation**

Crucible Pedestal

Figure 1 Locations of temperature sensors for control in conventional Czochralski and Liquid Encapsulated Czochralski (LEC) growth configurations. Typical sensors include thermocouples and optical pyrometers.

removed from the area of measurement interest: the melt/crystal interface. The sensor's placement is determined empirically. Passive means are also used to influence the temperature distribution in the melt and growing crystal. These include choice of the axial position of the crucible within the hot zone and heat shields to modify the heat transfer to and from the crystal/melt system.

The non-axisymmetric nature of the melt surface temperature distribution is known to cause periodic fluctuations in the microscopic rate of growth during rotational pulling [1]. The commensurate variation in electronic materials properties (e.g. carrier concentration) contributes to the inability of solid state semiconductor matrices to perform near their theoretical limits. Turbulent convection is present in large Czochralski melts due to unavoidable radial and axial temperature gradients. The effects of the random melt temperature fluctuations associated with turbulence are exhibited in the grown crystal as chaotic variations in dopant concentration superimposed on the periodic rotational variations discussed above. Application of a magnetic field to the melt has been shown to eliminate melt turbulence and its related effects on growth and segregation [2]. However, the application of the field has also been observed to change the magnitude of the radial temperature gradient [3]. Since the radial temperature gradient controls to a major extent the sensitivity of the crystal diameter to overall changes in hot zone temperature, the quantitative evaluation of the melt surface thermal field is critical to the development of an improved control scheme for the crystal growth process. To this end, a real time thermal imaging system has been developed. In addition, the imager has been used as an advanced sensor to control the temperature of the hot zone from positions nearer the critical phase transformation boundary.

Theoretical Basis for Image Interpretation

Wien's approximation [eq. 1] to Planck's radiation law is used to establish a relationship between changes in optical intensity (I), temperature (T) and wavelength (λ).

$$I(\lambda,T) = C_1\epsilon(\lambda,T)/\lambda^5 \left[\exp(-C_2/\lambda T)\right] \tag{1}$$

C_1 and C_2 are constants, 3.7403×10^{-4} watt μm^2 and 1.438×10^4 $\mu m°K$ respectively and ϵ is the emmisivity of the melt. In the first development phase, experiments were conducted to determine a direct relationship between intensity and temperature. (The thermal imager was calibrated using two methods. See section on temperature control by thermal imaging.) Work is presently in progress to quantitatively determine the input/output characteristics of the CCD camera used for the image acquisition. (See next section.) Once this is accomplished, the optical path will then be included in the calibration scheme so that the absolute intensity will be measured during an experiment. In this way, a direct, quantifiable relationship will exist between the measured intensity and the absolute temperature.

I

Hardware Configuration and System Architecture

The operation of the thermal imager is based on the same theoretical principles as single color optical pyrometry. The high termperature scene (the encapsulated GaAs melt) is viewed in near normal incidence by a high resolution (512 x 512 pixels) low noise (-60 dB) charge coupled device (CCD) camera (RCA). In this way, an array of 1/4 million discrete optical pyrometers are available to characterize the scene with a spatial resolution of better than 0.5 mm. A very narrow band pass filter (1 nm width, centered at 633 nm) is placed between the scene and the camera to obtain a monochromatic image. The transmission wavelength of the filter was chosen to match the peak in the spectral sensitivity of the CCD element while maintaining a steep slope on the I vs T curve of the emitting surface (the melt).

A schematic of the thermal imaging architecture and a preliminary control structure is shown in figure 2. The major components include the growth system (modified Hamco CG-800) with axial superconducting magnet (5 Kgauss, American Magnetics), the CCD camera and narrow bandpass filter, the image processing subsystems (Recognition Technology, Inc.) with high resolution analog RGB monitor and the host computer with integral high speed data acquisition and control capability (Masscomp MC-5500).

The camera generates information at 30 frames/second using a standard RS-170 configuration. Adjustment of gain and dc offset of the CCD camera's analog output is accomplished in the analog to digital subsystem. This permits operation at high gain for maximum sensitivity. At this time, the signal is pre-processed with user defineable look up tables (LUT) to correct for inherent non-linearities within the camera and digitized to 8 bits (256 gray levels). Image processing functions are carried out in the pipelined pixel processor. (For an in-depth description, see next section.) Other principle tasks include image storage and transfer within the digital storage units. A unique capability of the system is the dual ported nature of the digital storage units. Image memory appears as extended system memory on the host. As a result, image data can be accessed simultaneously by the pipelined pixel processor and the host CPU. In this way, parallel processing of the information can be accomplished with no performance penalty. Real time graphics overlays and linear convolutions are produced in this manner. Two of the digital storage units are configured as a 16 bit pair to hold high precision intermediate results produced during certain image processing calculations (e.g. 2-d convolutions and temporal averaging, see next section). A third 1024 x 1024 image memory unit is configured as four contiguous 512 x 512 frame stores.

The processed images (in real time) are sent back through the A/D subsystem where a second LUT is used to false color the outgoing monochrome signal. The LUT is defined to map low intensities to blue and high intensities to red with a linear interpolation of the complete 8 bit dynamic range. In

Thermal Imaging Architecture With
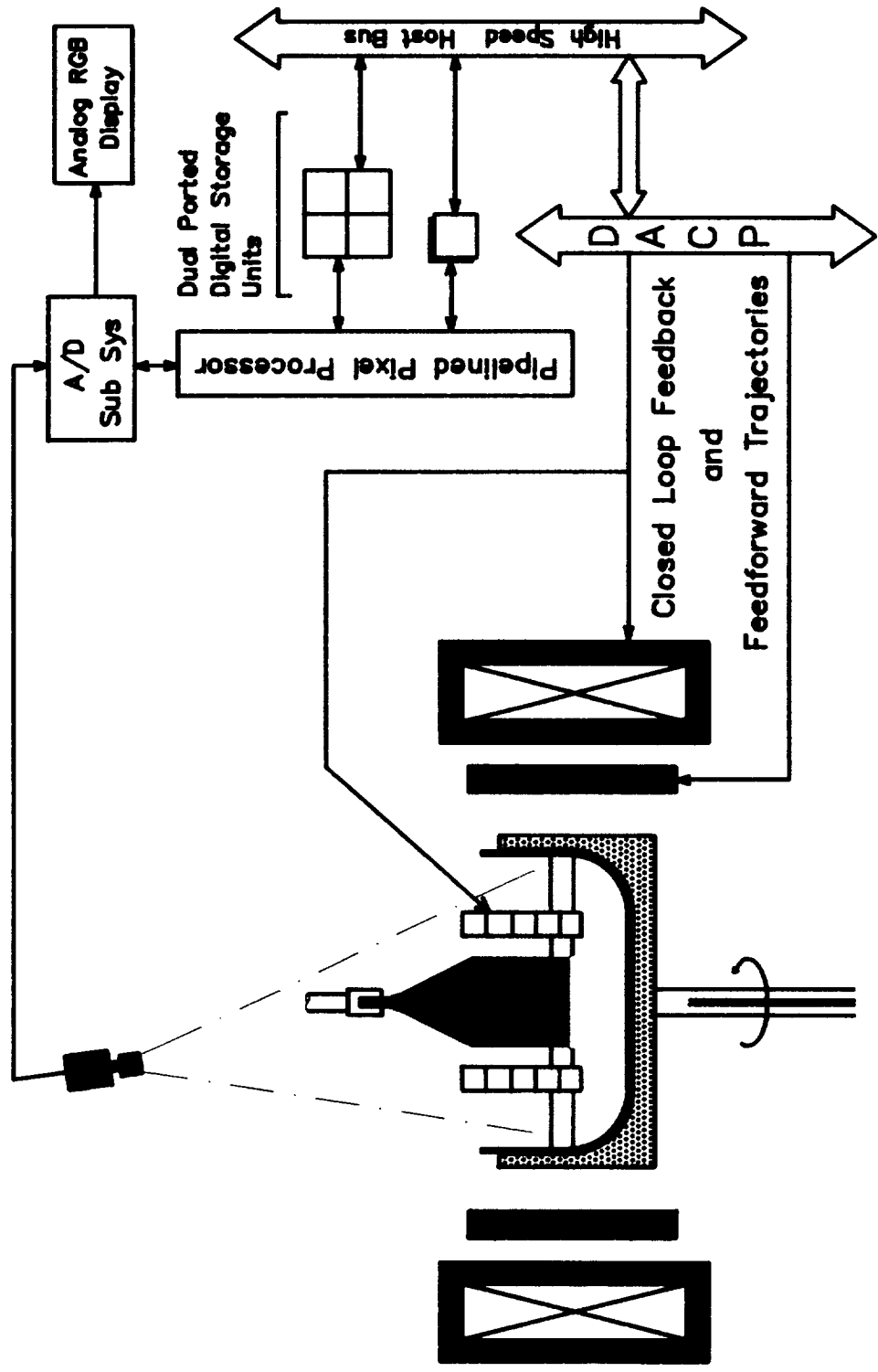
Preliminary Control Structure

Figure 2 Thermal imaging architecture and preliminary control structure for LEC growth of GaAs. The use of closed loop feedback and feedforward trajectories are discussed in detail in reference 4. Non-traditional control elements include the heat exchange system (HES) around the growing crystal and the superconducting magnet around the furnace.

this way, a complete spectrum between blue and red corresponds to intensities from 0 to 255 gray levels. The output is displayed (with graphics overlays) on a high resolution RGB monitor.

Thermal information is selectively extracted from the thermal image and passed, via the host, to the Data Acquisition and Control Processor (DACP). In this mode, the raw thermal data is scaled and offset to conform to the required output characteristics (e.g. a platinum/platinum10% rhodium thermocouple) and sent from a digital to analog (D/A) converter to the crystal puller to be used for temperature control. Figure 2 also indicates alternate strategies for systems control from the thermal imager. Development is currently in progress to adjust, by computer, the magnitude of the axial magnetic field for closed loop control of the radial temperature gradient in the melt based on a line scan of the surface temperature field obtained from the thermal imager. In like manner, the thermal field within the growing crystal will be controlled through a heat exchange system (HES) mounted coaxially about the growing crystal.

Thermal Imaging of High Temperature Semiconductor Melts

The thermal imaging geometry is illustrated in figure 3. The CCD camera is, by necessity, mounted off-axis and non-normal to the melt surface. The crystal pull shaft is on the rotational axis and the camera axis is located 3.5 inches from it inclined at 5° to the normal. As a result, internal reflections from the melt surface are reduced but not totally eliminated. The high temperature scene comprises the melt, crucible, heater elements, crystal and pull shaft. However, the only portion of the scene which provides optical information that is readily convertible to temperature is that which is emitted from the surface of the melt.

A raw (unprocessed, single frame) thermal image of a conventional LEC GaAs melt just prior to seeding is shown in figure 4. False color representation of the high temperature scene depicts high melt temperatures as red and lower temperatures as progressively bluer. The horizontal line crossing the encapsulated melt represents a linear array of picture elements (pixels) from which temperature data is extracted, processed and displayed in real time. This data is shown in the curved line above the displayed horizontal pixel array. It has been processed by a linear convolution to remove high spatial components. This processing was offloaded from the pipelined pixel processor to the main CPU to maintain real time performance. The gray level scale on the ordinate corresponds directly to temperature. (Calibration of the gray scale is discussed below.) Thus, the slope of the line indicates the magnitude of the radial temperature gradient. Shown in the image are the bubbles inevitably present just following the melting of the charge. It is clear that the bubbles mask any temperature information in that region of the image. However, continuous temporal averaging of consecutive images (with exponential de-emphasis of previous frames) can be used to 'eliminate' the effect of
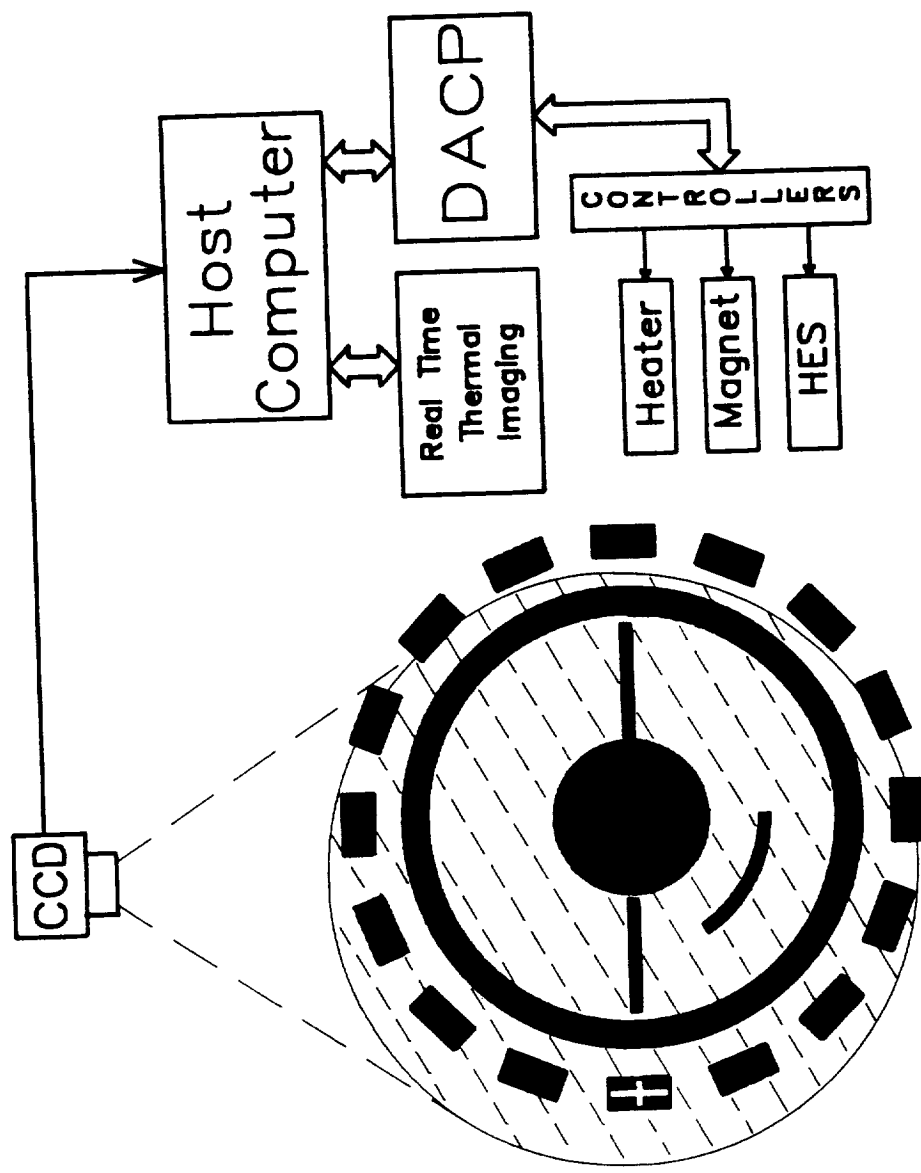
389

Figure 3

Geometry of thermal imaging system. Alternative temperature sensing locations and geometries are indicated. At present the line scan across the melt and crystal and the single point (cross-hair at heater element) have been implemented. Only the single point approach is currently used for control.

these spatial perturbations (figure 5). The temporal averaging facility operates in real time and the number of frames averaged is user selectable.

Figure 6 is a thermal image taken during the initial stages of GaAs growth. The bright disk just below the seed shaft is the growing crystal. It appears bright (red, in false color) due to the higher emissivity of the solid compared to the melt as well as its reflecting the high temperature information coming from the crucible wall. The intensity does not, in this case, unambiguously reflect the temperature of the crystal. With more quantitative information about the emissive nature of the crucible and crystal this temperature distribution could also be determined. Even so, the abrupt discontinuity of the optical intensity observed on crossing the melt/crystal boundary provides useful information concerning the diameter of the growing crystal and can, in principle, be used as a feedback signal for diameter control. This measurement has significant advantages compared to the differential weight which is used in conventional LEC growh systems for ADC (automatic diameter control) [4].

Figure 7 shows the same growth conditions but with the application of a 2000 gauss axial magnetic field. Comparison of the displayed data with figure 6 (no field) indicates the increase in radial temperature gradient caused by the magnetic field. The magnetic field reduces the convective component of heat transfer in the melt. Since the heat lost from the crystal is not influenced by the magnetic field, the temperature distribution in the crystal is not expected to be modified. Thus, an increased radial temperature gradient in the melt is required to bring, by conduction alone, the same amount of heat to the crystal/melt interface. Based on a measured gray level to temperature correspondence of 0.5°C/gray level (see section on systems calibration), the radial temperature gradient in the absence of the field was less than 5°C/cm whereas the temperature gradient with melt stabilization of 2000 gauss was in excess of 10°C/cm.

High spatial frequency noise in a thermal image can be eliminated on a full frame basis. Such a two dimensional convolution is performed in n frame times where n is the the number of non-zero elements in the convolution kernal (typically 8 of 9 in a 3 x 3 matrix). Thus, a complete convolution is accomplished in 8 frame times or 8/30 second. This technique is illustrated in figures 8 and 9. Figure 8 is a single frame thermal image. Isotherms, corresponding to constant intensity contours, are revealed by highlighting selected gray levels. Note the diffuse nature of the isotherm representation. In figure 9, the convolved image illustrates a reduction in high spatial frequency noise. Isotherms are now depicted in a more coherent form.

The foregoing thermal imaging capabilities are characterized by a view of the scene and display of the data at a single point in time (though it may have been time averaged). Another approach, found to be useful for systems control purposes, is to acquire and display intensity (temperature) data as a continuous function of time. Figure 10 shows the result of a pixel averaging alogorithm

which takes intensity data from an n x m array of pixels (in this case, 3 x 3), arithmetically averages it and displays the results in real time overlayed on the thermal image.

System Calibration

Two techniques were employed to calibrate the thermal imager. Both permit relative but not absolute determination of the temperature; i.e. only temperature changes are measureable quantitatively. In the first approach, a magnetically stabilized melt was imaged at three different temperatures separated by 10°C (figure 11). (These temperature changes were accomplished using a conventional temperature control scheme where the sensing thermocouple is in close proximity to the heater.) In each image, the same three isotherms, 20 gray levels apart, are highlighted. At temperature, T, all three isotherms are visible; it is hottest at the crucible wall, coldest at the center of the melt. At T+10°C, the innermost (coldest) isotherm has all but disappeared and its previous position (at T) has been taken by the second (middle) isotherm. This near replacement of isotherms is repeated once more at T+20°C. Now the third isotherm (originally near the crucible wall) is in approximately the same position as that of the first isotherm at temperature, T. This indicates that, over this temperature range, approximately 20 gray levels correspond to 10°C. Or, the sensitivity of the thermal imager is given as 0.5°C per gray level. The second calibration was conducted without a melt in the crucible but with a thermocouple present to directly measure temperature changes at one location. Using the algorithm described above for measuring the optical intensity at a point, the output of the thermal imager was amplified, scaled, processed by a digital to analog converter and directly compared to the response of the thermocouple. The pixel array chosen was 9x9. The results (figure 12) show that there is a direct relationship between the changes measured by the thermocouple and the signal produced by the thermal imager. While the output of the thermal imager is represented in the figure in volts, it corresponds to the same value for calibration of the system as the first method: 20 gray levels for every 10°C.

Temperature Control by Thermal Imaging

As previously indicated, conventional temperature control schemes in LEC growth configuration (figure 1) are based on sensor locations which are well removed from the critical area of interest. Using the thermal imager as an advanced single point temperature sensor, it was possible to control the temperature of the growth system from a more advantageous position within the crucible. The intensity (temperature) information from the imager was re-scaled (gain and d.c. offset) so that the output of the D/A converter, after processing by a 1000:1 voltage divider, corresponded directly to that of a Pt/Pt-10%Rh thermocouple. In this way, the signal could be fed to the conventional, analog PID controller which had previously been used to control a thermocouple placed near a heater ele-

I

ment. Figure 13 shows the results of 5°C control changes made with the analog controller. The output of the thermocouple located within the crucible and the old control thermocouple (at the heater) were recorded. In both cases, the change in output corresponds to the temperature changes made at the controller indicating that the signal from the thermal imager successfully tracked and measured the temperature response of the system. The ringing (decaying, oscillatory) component of the temperature response recorded by the thermocouples reflects the non-optimized PID parameters of the analog controller. These values were left unchanged from those previously determined for the thermocouple sensing the heater temperature. Considerably improved control performance would be achieved with the retuning of the PID settings.

Discussion

Three fundamental assumptions are made which permit, in LEC growth configuration, the interpretation of the output of the thermal imager as temperature information. First, to eliminate any effect of internal reflections, the high temperature scene is viewed in normal incidence. Second, the emissivity of the melt does not change over the temperature range of interest. And, third, the characteristics of the optical path are time independent. It is important to recognize how closely these assumptions are adhered to in the present experimental configuration as well as what effect any deviation from them has on the interpretation of the images. Finally, approaches to reducing or eliminating these effects are considered.

As indicated in figure 2, the camera is mounted inclined about 5° to the normal. The effect of this deviation from normal incidence is most evident during observation of melts. Isotherms appear to be shifted from a centro-symmetric position. However, when an empty graphite crucible (with roughened surface) is imaged, no effect of the non-normal incidence is observed; isotherms are concentric about the center of the crucible. This indicates that high temperature information from the crucible walls is being reflected from the melt surface to the thermal imager. Work is currently in progress to negate this effect with a correction technique that subtracts from the live image a reference image containing information characteristic of the reflection.

There is currently no indication that the emissivity of the melt changes significantly over the temperature range encountered during a typical growth emperiment. However, an effective change does occur if, for example, the perturbations associated with bubbles are considered. In this case, the temporal averaging algorithms are being modified to be included in the systems control module of the computer code. This will eliminate the radical transients measured by the imager as a result of bubbles crossing control point.

One significant change that does occur over the course of a growth run is the characteristics of the optical path. During this time: 1. The window through which the imager views the melt gradu-

ally becomes covered with material which has condensed from volatile melt constituents that are not totally contained by the liquid encapsulant. 2. The optical transparency of the encapsulant changes as its chemistry is modified by the disolution of melt and dopant components. Two approaches to this problem are being pursued. In a manner similar to that discussed above to deal with the internal reflection problem, image subtraction can correct for changes in the optical path as long as these changes are reproducible and well characterized. It is preferable, however, to eliminate both the clouding effect as well as the window coating by development of alternative encapsulants which do not suffer from the limitations encountered with the use of the conventional encapsulant, boric oxide. Work is in progress in this area.

Summary

A high resolution thermal imaging system which operates in real time has been developed. It has been used to characterize the radial temperature distributions in high temperature semiconductor melts. This system also operates as an advanced non-contact temperature sensor and has been used to actively control the temperature of a low pressure LEC GaAs crystal puller. High performance spatial and temporal filtering algorithms have been applied to reduce high spatial frequency noise inherent in both the process and the measurement. This technique is potentially well suited to thermal characterization and control of other materials processing technologies. The non-contact aspect of the design makes it attractive to those applications where non-invasive measurement of temperature is required.

Acknowledgements

References

1. K. Morizane, A.F. Witt and H.C. Gatos, J. Electrochem. Soc. 114 (7) 738 (1967).
    A.F. Witt and H.C. Gatos, J. Electrochem. Soc. 115 (1) 70 (1968).

2. A.F. Witt, C.J. Herman and H.C. Gatos, J. Materials Science 5 822 (1970).
    K. Hoshikawa , Jap. J. Appl. Phys. 21 (9) L545 (1982).
    K. Hoshikawa, H. Kohda and H. Hirata, Jap. J. Appl. Phys. 23 (1) L37 (1984).

I

3. M. J. Wargo and A. F. in preparation for J. Crystal Growth.

4. M. A. Gevelber, M. J. Wargo and G. Stephanopoulos, accepted for publication in J. Crystal Growth.
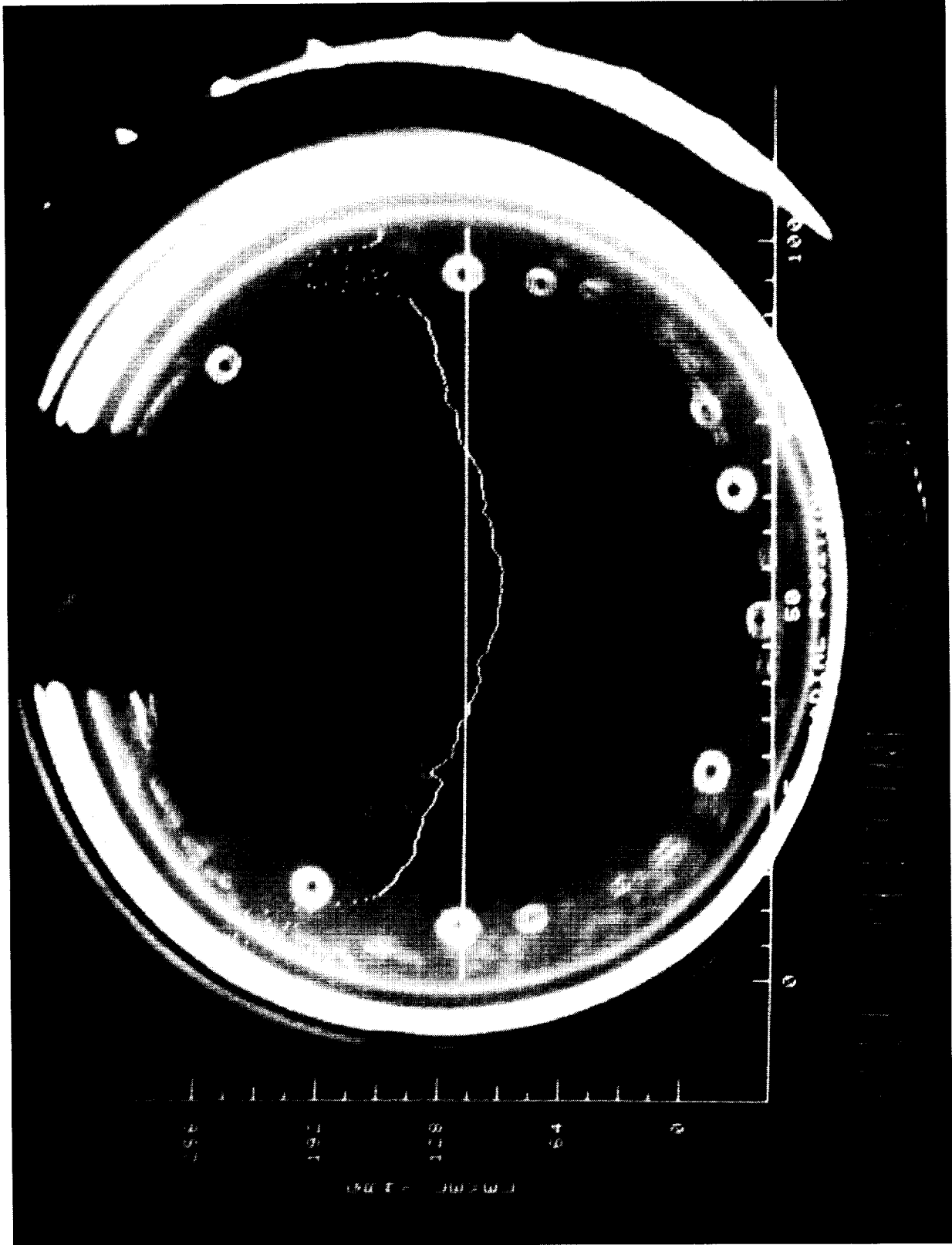
Thermal image of an encapsulated GaAs melt. No processing has been done on the image. However, the data plotted in the graphic overlay has been subjected to a linear convolution to remove high spatial frequency noise.
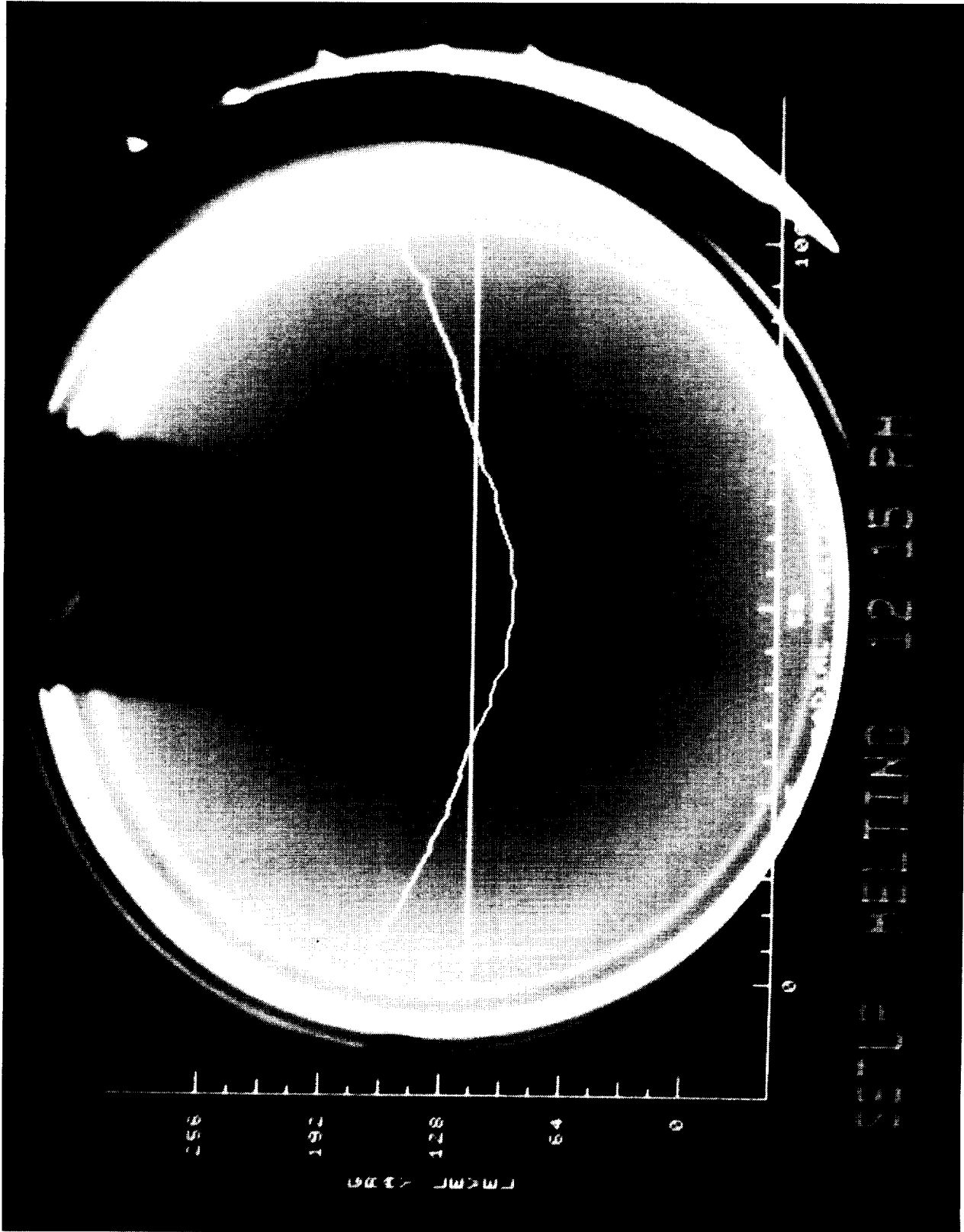
Figure 4

Figure 5   Thermal image of an encapsulated GaAs melt. Temporal averaging has been used to 'elimi-
nate' the effect of the bubbles.
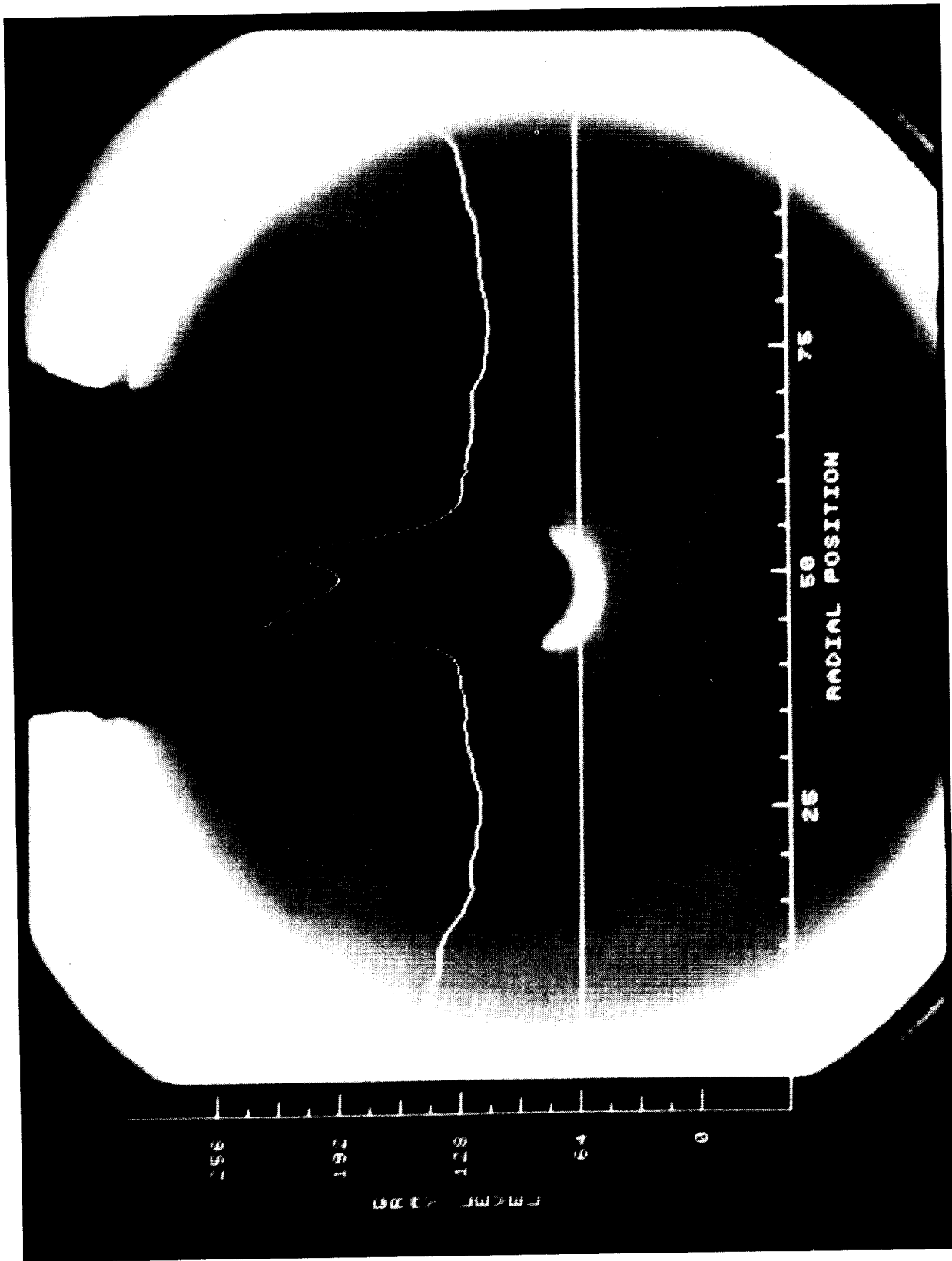
Figure 6 Thermal image of an encapsulated GaAs melt taken during the seeding process. No magnetic field is applied. Note the low radial temperature gradient indicated by the limited gray scale range of the intensity distribution across the melt.
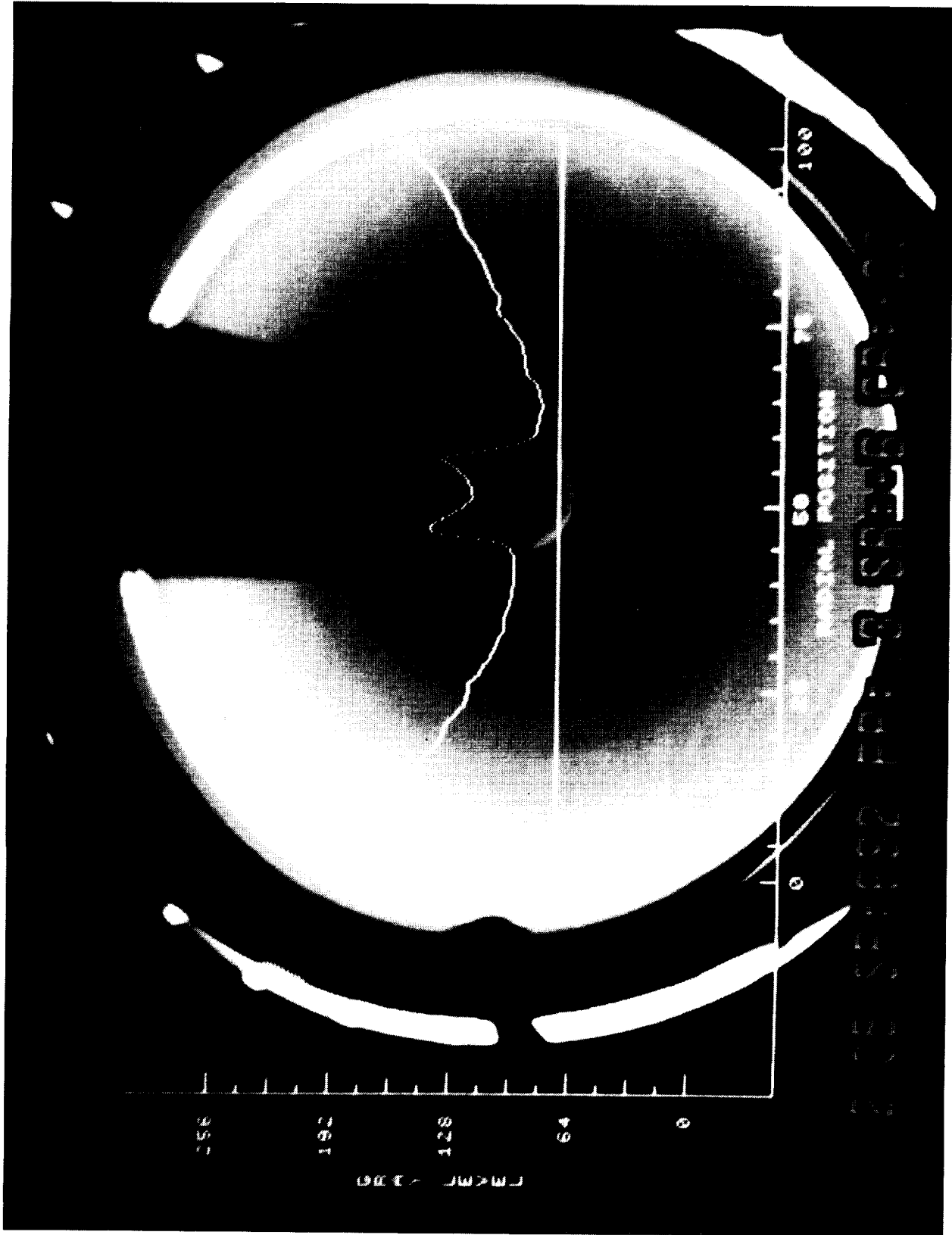
Thermal image of an encapsulated GaAs melt with an applied magnetic field of 2000 gauss. All growth conditions are the same as figure 6 except for the presence of the field. The radial temperature gradient is substantially increased.
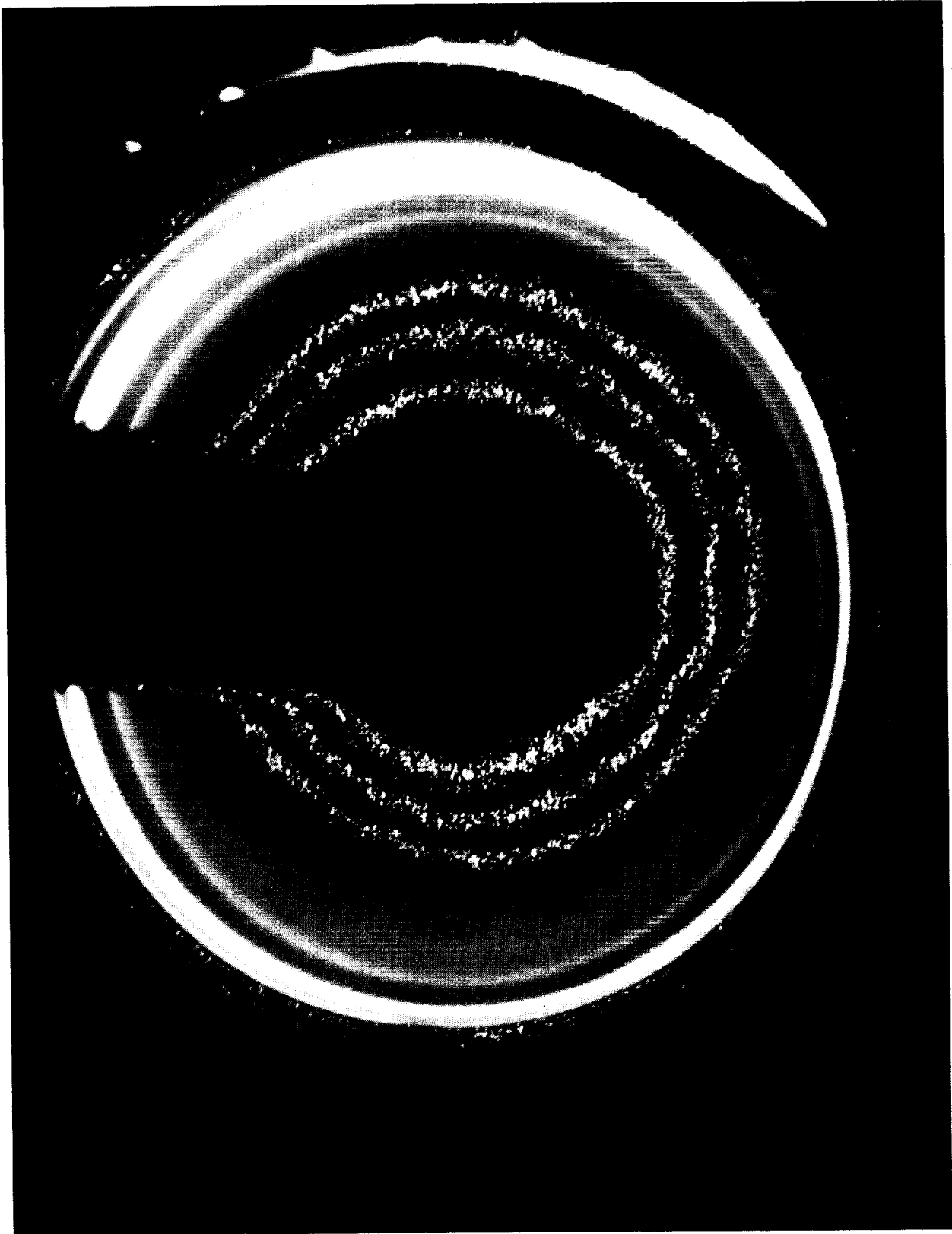
Figure 7

Figure 8 Isotherm representation on an encapsulated GaAs melt: 3000 gauss. No image processing has been applied to reduce high frequency spatial noise. Note the spatially diffuse nature of the isotherms.

400
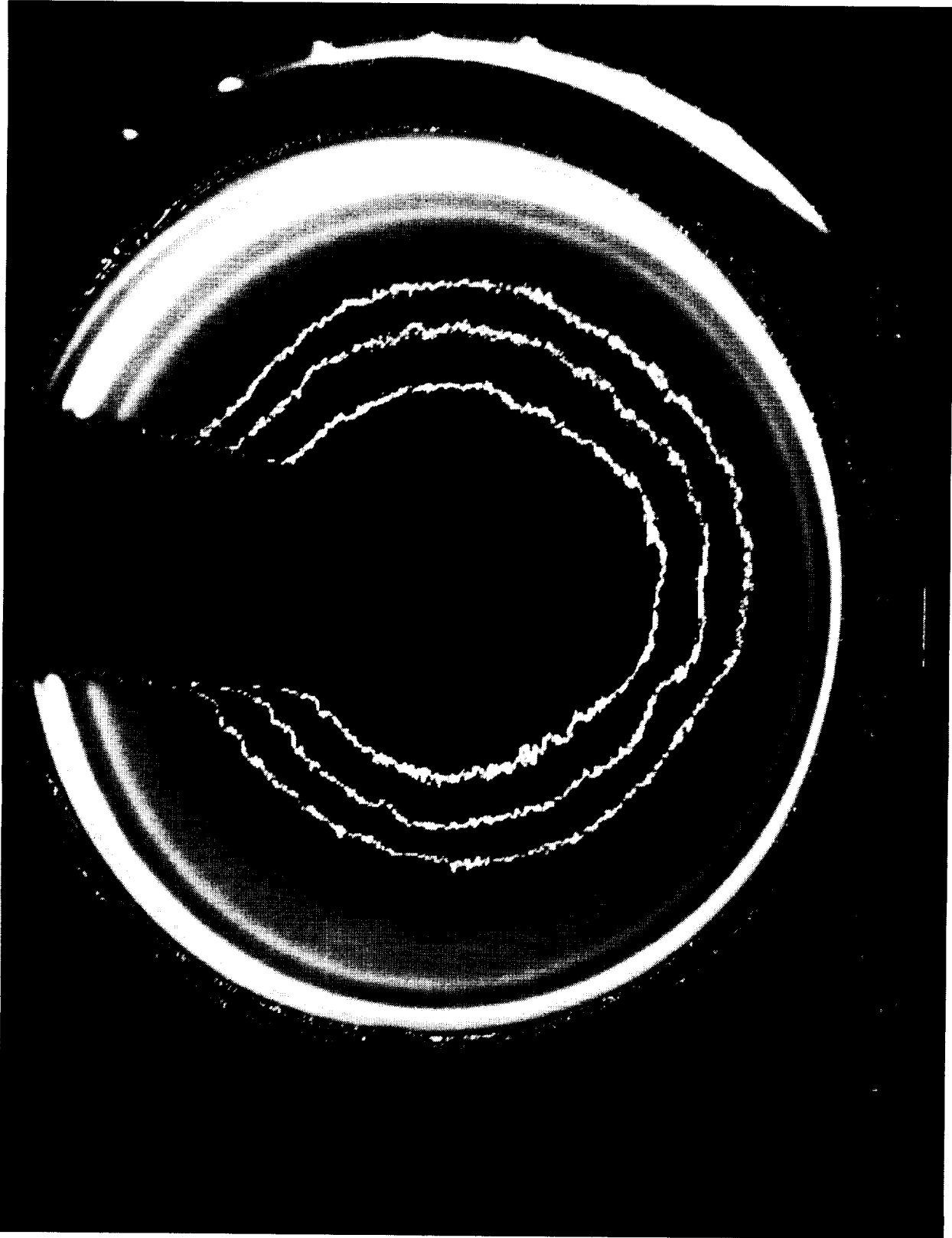
Figure 9   Isotherm representation after application of a two dimensional low pass filtering convolution
utilizing a 3 x 3 convolution kernal. Note the reduction in high spatial frequency noise resulting
in a more coherent representation of the isotherms.
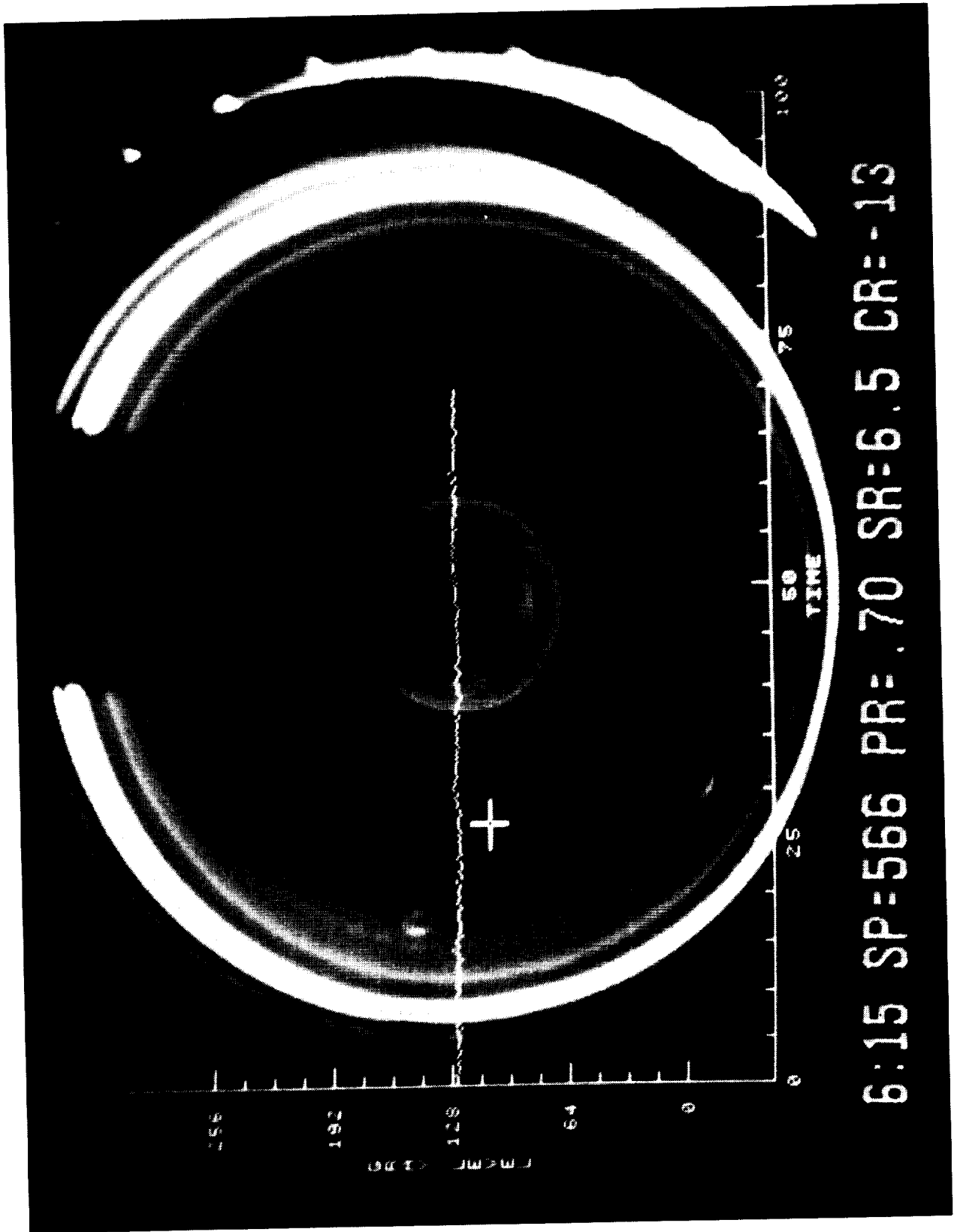
Figure 10   Thermal image of an encapsulated GaAs melt with graphic display of the output of a multi-pixel averaging algorithm. The optical intensity (temperature) data is taken from a single point (defined by the cross-hair) and displayed in real time.

402

1000 Gauss

1. T = T
2. T = T + 10
3. T = T + 20
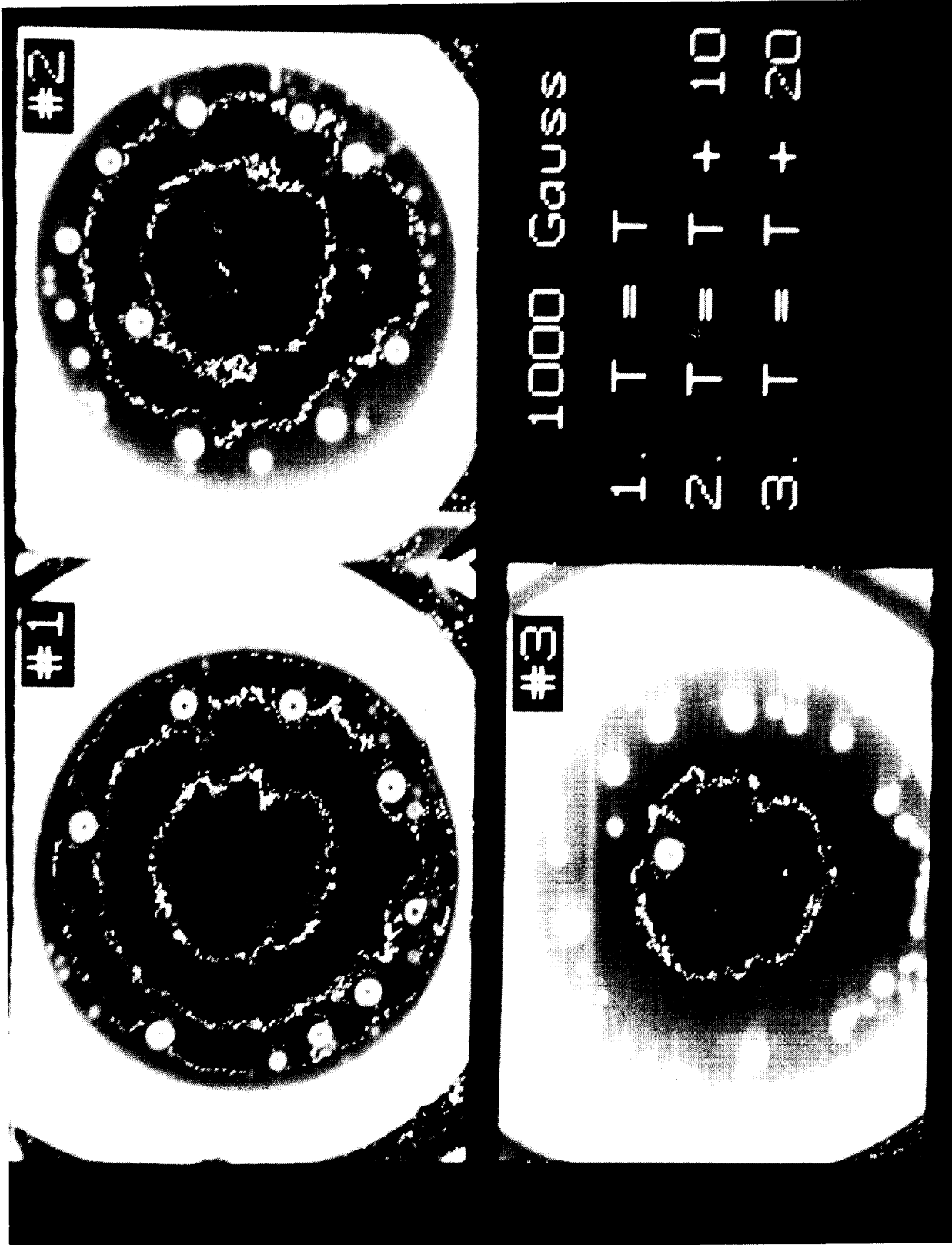
Figure 11   Calibration of the thermal imager. Three thermal images are depicted where the temperature increases in 10°C increments between them. The isotherms shown in each image are at the same gray levels. See text.

Temperature (PID) Control by Thermal Imager (9X9 pixel avg)

Figure 13

Temperature control of an LEC GaAs puller using the thermal imager as an advanced sensor. Temperature changes are 5°C. The plot on the left is the output of a thermocouple located in the crucible. The plot on the right is the output of the thermocouple used for conventional control located at the heater (Note change in scale). The ringing in the control response is due to non-optimized PID parameters used with the conventional controller which was driven by the imager. See text.

Temperature Control by T/C at Heater

Figure 12

Calibration of the thermal imager. The plot on the left is the output of a thermocouple located in the crucible. The plot on the right depicts the output of the thermal imager scaled to permit plotting on the same instrument. Results are the same as for the technique illustrated in figure 11. See text.

Clinical Applications of Computerized Thermography

Michael Anbar

Professor and Chairman, Department of Biophysical Sciences
School of Medicine, SUNY, Buffalo, NY, 14214

Abstract

Computerized, or "digital", thermography is a new, rapidly growing diagnostic imaging modality. It has superceded contact thermography and analog imaging thermograpphy which do not allow effective quantitation. Medical applications of digital thermography can be classified in two groups -- static and dynamic imaging. They can also be classified into macro thermogra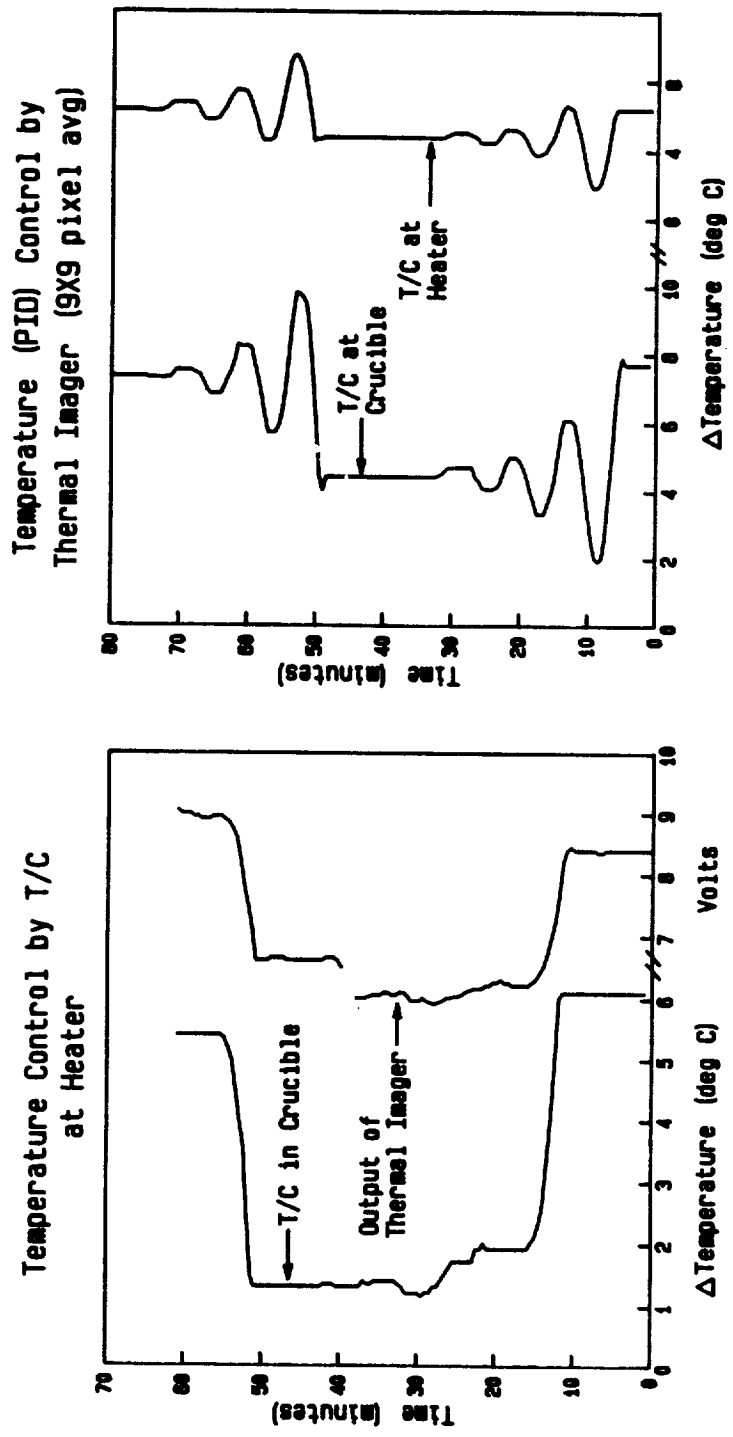phy (resolution>1mm) and micro thermography (resolution<100um). Both modalities allow a thermal resolution of 0.1 centigrade. The diagnostic power of images produced by any of these modalities can be augmented by the use of digital image enhancement and image recognition procedures. Computerized thermography has been applied in neurology, cardiovascular and plastic surgery, rehabilitation and sports medicine, psychiatry, dermatology, and ophthalmology. Examples of these applications will be shown and their scope and limitations will be discussed.

CLINICAL APPLICATIONS OF COMPUTERIZED THERMOGRAPHY

Michael Anbar
Department of Biophysical Sciences
School of Medicine, SUNY, Buffalo, NY, 14214

Clinical thermography is a relatively new diagnostic modality that has just recently gained acceptance by the medical community at large. In fact, the first comprehensive book on thermography appeared just a few months ago.[1] This paper presents a brief review of clinical thermography -- recording and displaying images that depict the distribution of temperature on the skin surface of patients. It describes the current status of computerized, remote sensing thermographic instrumentation, emphasizing the most recent developments. It then reviews some of the widely used clinical applications of thermology, which is the systematic interpretation of clinical thermograms, pointing out new applications currently explored. Finally, it attempts to assess the overall role and place of thermology in medicine, pointing out the need for fundamental thermological research.

INTRODUCTION

The assessment of local skin temperature as an indicator of pathology is as old as medicine and the correlation between local "hot spots" and local infections may have been discovered by the prehistorical cave men; even animals may sense the elevated temperature of local "hot spots" due to infection and then lick them. From the perspective of the written history of medicine, the associating of hot infected areas with disease appears already in Egyptian scriptures more than 2000 years before Hippocrates, who tried to classify diseases by their pyretic characteristics.[2]

Skin temperature is determined by subcutaneous blood supply, by the metabolic rate of subcutaneous tissue, by the rate of evaporation of subcutaneous moisture (including diaphoresis), and by the cooling rate of the surface. The latter may be conductive (to a touching body), convective (to the surrounding air) or radiative.

Skin temperature can be measured by contact with the measuring device (e.g, a hand, a mercury thermometer, a thermocouple, a liquid crystal layer), assuming the establishment of thermal equilibrium between the measured skin and the measuring body, and presuming that the contact does not affect the physiological behavior of the examined area. These limitations, as well as the lack of sensitivity, precision and accuracy, of measurement of the distribution of skin temperature by physical contact, made this approach unfit for meaningful clinical diagnosis.

Assessment of skin temperature through its intrinsic radiative losses (black body radiation) are much more meaningful because of the extremely fast rate of thermo-radiative equilibrium, because skin is non reflective in the wavelength range of 9 to 11 microns (the range of maximal black body emission at body temperature), and because of the negligible effect of IR sensors (since also they are non reflective black bodies) on the emisivity of the monitored surface. Since the black body radiation of the skin at body temperature peaks at about 10 microns, the assessment of skin temperature had to await the advent of an appropriate detector (photoresistive HgCdTe) coupled with a reflective optical scanner. Moreover, the quantitative measurement of skin temperature requires not only continual real-time calibration of the temperature sensor and distortion-free optics, but also the development of computerized image processing. Thus, it is not surprising that quantitative thermal mapping of the skin was achieved just a few years ago.

CURRENT STATE OF THERMOGRAPHIC INSTRUMENTATION

Today, the state of the art in clinical thermography comprises scanning cameras with high resolution (<1 milliradian, allowing surface resolution of <0.1mm at 30 cm from the camera), with a temperature resolution of <0.05C, and temperature measurement accuracy of <0.1C. A combination of rapidly rotating mirrors reflects each spot of the observed object onto the infrared thermoresistive detector, which is maintained at low temperature. The optics of most commercial machines do not permit imaging at a short distance from the camera (<15 cm), but this limitation has now been overcome by recent R&D.

The scanning speed of the best cameras used in medical diagnosis is about 30 frames per second. The time limitation is, in part, due to the relatively slow response time of the detector, and in part determined by the speed of the reflective optical scanner. The voltage across the detector is a function of its temperature, this voltage can be converted into a digital signal or stored in analog form and digitized later. The 12 bit A/D conversion currently used in clinical thermography exceeds the precision thermology requires. The resolution of the digitized image depends on the amount of memory available on the dedicated microcomputer. It has reached now 640x512 and might soon improve to 1024x1024 pixels. No single commercial machine has the combination of all the features described above (speed and resolution), but this is likely to change within the next year or two.

IMAGE PROCESSING AND DISPLAY

Image averaging and subtarction, as well as obtaining the maximal, minimal and average (absolute) temperatures of any specified area on the image, are routine in most commercial digital machines. More sophisticated image handling techniques, such as relating thermographically significant features to

specific anatomic markers, as well as other pattern recognition algorithms, are currently being developed. These will enable to derive quantitative, diagnostically meaningful information, especially regarding temporal changes characteristically associated with certain pathologies or their treatment.

Thermographic diagnostic images are generally displayed on a CRT as contour maps, where each isothermal area is displayed in the same shade of grey or in the same pseudocolor. Most machines display 16 shades (on a monochrome display) or 8 to 64 colors. The baseline temperature (lowest temperature in a given image) can be selected in the range of interest (generally 20 to 40C), and one can select the temperature range (1 to 20C) to be displayed. Thus each of the 16 shades or colors can represent 0.1 to 1C. From the clinical standpoint temperature differences smaller than 1C are currently of little diagnostic value, and since the temperature range of most diagnostically interesting images is less than 10C, as few as 8 shades or psuedocolors can provide all the information necessary for the current clinical uses of thermography. The use of more shades, or colors, may reveal new, diagnostically useful, thermographic features, but their manifestation will require substantially better control of the thermal environment of the examined organ than practiced in current clinical thermography.

CLINICAL APPLICATIONS OF THERMOLOGY

Clinical thermology is essentially the science of studying local changes in skin temperature which appear on thermograms and are not due to environmental cooling or heating. As stated above, changes in local skin temperature are, generically speaking, a function of subcutaneous blood supply, and under special circumstances also of subcutaneous metabolic rate. Subcutaneous blood supply depends on (1) the patency of the arteries bringing blood into the region, (2) the rate of blood flow in these (which depends on cardiac output), (3) the extent of subcutaneous vascularization, and (4) the vasodilation or constriction of the subcutaneous arterioles. Generally, blood acts as a cutaneous heating fluid, but in cases of local hypermetabolism it may act as a coolent. The patency of arterioles is controlled by the autonomous nervous system, while that of the major arteries is primarily determined by their anatomy. In addition, thermograms may show major subcutanous veins.

Thermography reveals abnormalities in the local heating or cooling. Pathological thermological changes can, therefore, be due to (1) occlusion of arteries, (2) impaired innervation of arterioles (resulting in either excessive vasoconstriction or vasodilation, depending on the interaction between the sympathetic and parasympathetic systems and the location of the interference), (3) local interstitial fluid retention (edema) that exerts hydrostatic pressure on the arterioles and may, therefore, change both the residence time of blood in the affected region and the heat exchange with the skin, (4) a

mechanically damaged capillary bed, (5) increased local vascularization, (6) local hypermetabolism or (7) local hypometabolism that are not compensated by increased circulation (cooling or heating respectively). For a review of mechanisms of local thermal aberrations from different points of view see [3].

The latter situations are accentuated by positive feedback due to the positive temperature coefficient of tissue metabolism -- inadequate cooling will result in a faster metabolism and, therefore, in an even more extensive local heat generation, while inadequate heating of a hypometabolic region might result in a local "run away" cooling effect. The situation is further complicated by the fact that inadequate temporary blood supply to a region might result in hypoxia and subseuqent glycolysis, which generates more local heat than normal aerobic metabolism.

Each of these thermographically demonsrtable pathological changes can have concrete clinical application in the diagnosis and management of different disorders. The limitations of length of this paper allow us to give just a few examples of clinical situations where the pathological changes, generically described above, are applied in different medical specialties. We will try to include references to leading recent contributions, however, for certain applications, which are currently under development, we will not be able to cite references.

1. Neurology.

Damage to the spinal cord due to osteoporotic compression or trauma may result in impaired nerve signal transmission to the arterioles in the back or the extremities, generally resulting in an assymetric temperature distribution.[4-7] Often the pattern of abnormal temperature distribution overlaps the pattern of tactile sensation or the perception of pain in the affected region.[8-10] Thermography has also been shown to be useful in the diagnosis of migraine and other types of headache.[11] The relation between temperature distribution and pain led to the popularized reference to thermography as a method to "visualize pain"; this is conceptually wrong, since pain is a mental perception and thermography measures in this case only changes in the blood flow rate through the subcutaneus capillary bed. This methodolody that indicates spinal cord lesions, is likewise applicable to any peripheral nerve that interfaces with arteriols. In certain situations the diagnosis may be confirmed by repeated thermography in the presence of electrical stimulation or drug blockage of nerves.

A different area in neurology that lends itself to thermologic diagnostic quantitation is the transient CNS stimulation of the systemic sympathetic nervous system, which results in blushing or in turning pale. Likewise, it has been shown that excessive orthostatic hypotension might be diagnosed by a transient facial blushing. Unlike the nervous system studies described above, the latter type of diagnosis calls for the

interpretation of sequences of images ("dynamic thermography").
The latter findings may make thermology an interesting tool in
space medicine to study remotely and continuously the behavior of
the autonomous nervous system under reduced gravity.

2. Surgery.

Clinically significant occlusion of one of the carotid
arteries often results in assymetrical blood supply to the upper
face, particularly around the eyes.[12] Thermography might,
therefore, be used as a rapid and inexpensive screening test for
early detection of incipient stroke or progressive hypoxia of the
brain. Other diagnostic applications in this field include the
localization of occlusive venous trombosis in the legs and of
impaired capillary bed circulation in the foot associated with
diabetes mellitus.

A new use for real time high-resolution thermography is
during open heart surgery, especially in bypass operations.
Since the heart is cooled down during the procedure, the patency
of the grafted vessels and the success of the anastomosis can be
assessed by introduction of a slightly warmer infusate. Using
short focal length high resolution thermography it might be
possible to determine the success of arteioplasty and of
anastomosis of different parts of the gastrointestinal tract and
thus avoid the risks of injection of contrast agents to a
recently traumatized region. Also plastic surgery starts to apply
thermography to objectively assess healing of grafts.

3. Orthopedic surgery and physiotherapy.

One of the classical uses of thermology is the assessment of
the severity of inflamation of joints. This application has been
extented to include the postoperative follow up of the recovery
of joints.[13] In current studies the progress of recovery
following arthroscopic surgery of the knee is evaluated
thermologically to determine the efficacy of postoperative
physiotherapy. The control of postoperative edema of joints is
studied comparing impedence plethysmography and thermography.

4. Emergency and trauma medicine

Thermography has been used and abused in legal medicine to
document persistent soft tissue injuries following trauma (mainly
of motor vehicle accidents). Thermology may, however, be more
useful to the victims of such accidents and make a substantial
contribution to emergency medicine. Correctly staging of the
level of injury may be critical in such cases. A rapid
themographic inspection of a traumatized patient may readily
detect subcutanous hemorage and acute soft tissue injury, and
reveal even injuries to deep lying blood vessels that supply
blood to different regions of the skin. Also spinal injuries may

be detected faster and earlier than by other means. Thermography may also help in the management of burn patients, patients with frost bites, patients with acute phlebitis or lymphatitis, patients with heat stroke, or poisoned individuals, all of whom are known to manifest pathological local or general changes in skin temperature. Essentially what would be indicative is gross assymetries in the thermographic images as well as gross deviations from the skin temperature distribution of normal subjects. An open question that may exist in such situations is whether a thermographic abnormality is related to the injury or did exist beforehand. Knowledge of normal thermophysiology combined with a repeated scan after a short while may help to differentiate between these alternatives.

5. Dermatology.

Thermological applications to dermatology have been made possible only recently with the advent of a short focal length camera. With a resolution of <0.1 mm and a thermal resolution of <0.1C the temperatures of skin lessions can be assessed and one can differentiate between vascularized or hypermetabolic lessions and hypometabolic non-vascularized ones. Research aimed at differentiating between malignant and non malignant vascularized lessions is in progress.

A special subject combining dermatology and immunology is the quantitative assessment of skin sensitivity to chemicals, by measuring the local temperature of the skin at predetermined times following a given topical exposure. This application is an extention of using themography to obtain a permanent quantitative record of allergy response following the subcutaneous injection of an antigen.

6. Oncolgy.

Thermography has gained substantial disrepute following claims that using contact area measurement methods (liquid crystals) it is an effective screening method for the detection of breast cancer.[14] The rationale was based on the fact that carcinoma of the breast is a vascularized hypermetabolic lesion, the temperature of which is proportional to its malignancy. The early success of easy detection of shallow malignant lesions was followed by the disapointing results with deeply situated malignant lumps that could be detected by other imaging modalities. It is not completely clear whether the lack of sensitivity is intrinsic in the methodology, whether it was caused by limitations of the instrumentation used in several pilot studies, or was due to lack of standardization and experience of the operators.[15] In any case, the American Cancer Society, the National Cancer Institute and the American college of Radiology have expressed serious doubts regarding claims on the efficacy of thermography as a screening technique for cancer of the breast.

On the other hand, there have been several recent reports
that strongly suggest that this diagnostic method is more
efficatious than is now generally believed.[15-17] It has been
pointed out that using higher resolution of imaging, standardized
preparation of the patients, and global pattern analysis of the
images are prerequisits of an effective screening test.[15] Even
contact thermography is claimed to produce reliable results if
better controlled procedures are applied,[18] and the sensitivity
of diagnosis improves when inflammed malignancy is assessed.[19]
We must conclude that this application of thermography warrants a
new and independent reevaluation.

7. Space medicine.

Thermography might offer unique information by remote
monitoring of human circulation and temperature control
physiology in a micro-gravity environment. Assessment of the
reactions of the autonomous nervous system has been referred to
above. In addition, using a light-weight telescopic IR camera,
one might continuously and unobtrusively monitor the
hydrostatically induced changes in cerebral blood flow during
acceleration and deceleration of the space vehicle. Other uses of
thermography might include the rapid detection of diaphoresis and
possibly of fatigue by monitoing the faces of space travelers.

CONCLUSIONS AND PROJECTIONS

For unfortunate historical reasons, thermography became
known as a technique used by lawyers and physical therapists
rather than by clinicians. This and the possible oversale of
thermography as a screening method for breast cancer, explain the
fact that only this year has thermography been considered by the
AMA for approval as an effective diagnostic procedure in
neurology. This unhappy history will probably be soon forgotten
with the growing number of high quality demonstration studies now
in progress. Also the instrumentation that was just a few years
ago marginally adequate for objective, quantitative diagnosis,
has been substantially improved. New and significantly more
versatile and more accurate thermographic imaging systems are
being currently developed and will become part of the arsenal of
clinical imaging in the next year or two.

As has been described in this brief review, computerized
thermography is a new and rapidly emerging clinical technology
that offers novel, objective and quantitative, diagnostic
information to a growing number of medical specialties.
Thermology stands out among other diagnostic imaging modalities
by its completely non invasive nature which allows its repeated
or continuous application with no side effects. Like computerized
tomography, magnetic resonance imaging or digital radiography,
thermography records an image (in this case a raster of the
absolute temperature of each pixel of a projected plane

perpendicular to the camera) that can be processed at will to later extract substantial diagnostic information. Although generically all that thermography represents is blood flow rates and the rate of local tissue metabolism, this information, which is diagnostically important in a large variety of clinical situations, is not duplicated by any other imaging modality. There is, in fact, less redundancy between thermographic diagnostic information and that of other imaging modalities, than among many of the other imaging methods.

Where does thermography fit in clinical practice? Will we train a new breed of thermological specialists, probably as a subspecialty of diagnostic imaging? Or, will thermographs become one of the many tools of the neurologist (like the EEG or EMG), or of the orthopedic or plastic surgeon (like the surgical laser)? The relatively low cost of computerized thermographic systems, the "user friendliness" of their software, and the fact that thermography is _free_ from any side effects, will probably make this imaging technique part of the equipment arsenal of any specialty that can benefit from it; the experience with ultrasonic imaging, where for instance, sonocardiographic imaging became a routine cardiological tool while fetal imaging is routinely done in obtetrics, encourages us to make this prediction.

What is still missing is more information on the precise mechanisms of the physiological distribution and control of skin temperature on different parts of the human body. Such information will lead to a better understanding of pathological states. This information will probably be forthcoming soon with the general acceptance of thermology as an effective diagnostic method and with the advent of additional diagnostic applications.

NOTE: This review is based on a paper recently submitted by the author to the International Journal of Technology Assessment in Health Care.

REFERENCES

[1]   Abernathy, M. & Uematsu, S., (Eds), Medical Thermology, American Academy of Thermology, Washington, DC, 1986

[2]   Bar-Sela, A. The history of temperature recording from antiquity to the present. In REF #2 pp 1-5.

[3]   Hamilton, B. An overview of proposed mechanisms underlying thermal dysfunction. In REF #2 pp 6-18.

[4]   Maultsby, J. A. et al. Electronic thermography: A valuable aid in evaluating and treating symptomatic spinal pathology. In REF #2 pp 165-169.

[5] Perelman, R. B. & Adler, D. A comparison of lumboscleral thermograms with CT scans. In REF #2 pp 127-133.

[6] Ignacio, D. R., Pavot, A., Azer R.I. & Jackson, H. Thermography and decompensated shoulder syndrome. In REF #2 pp 120-123.

[7] Adatto, K. N. et al. Thermography and computed tomography in evaluation of lumbar disc disease, In REF #2 pp 170-174.

[8] Brelsford, K. L. & Uematsu, S. Thermographic presentation of cutaneous sensory and vasomotor activity in the injured peripheral nerve. J. Neurosurg. 1985, 62, 711-715.

[9] Uematsu, S. Thermal imaging of cutanous sensory segment in patients with peripheral nerve injury, J. Neurosurg. 1985, 62, 716-720.

[10] Uematsu, S. Thermographic sensory examination, In REF #2 pp 73-78.

[11] Rapoport, A. M., Sheftell, F. D. & Altemus, M. Correlation of facial thermograms and headache diagnosis, In REF #2 pp 56-61.

[12] Abernathy, M., Chang, L., Nichols R. & Brandt, M. M. Stroke detection by noninvasive testing, In REF #2 pp 26-49.

[13] Urricio Jr., J. V. Thermography in the evaluation of causalgia, In REF #2 pp 134-137.

[14] Gershon-Cohen, J., Haberman J. & Brueschke, E. E. Medical thermography: A summary of current status. Radiol. Clin North Am. 1965, 3, 403-431.

[15] Haberman, J. The phenix is rising - An overview of breast cancer thermography in the United States, REF #2 pp 218-233.

[16] Pochaczevsky, R. & Capace, N. R. Thermographic evaluation of the remaining breast after contralateral mastectomy or lumpectomy, in REF #2 pp 240-245.

[17] Karpman, H. L. & Jay, E. B. Computerized breast thermography, in REF #2 pp 256-262.

[18] Gautherie, M., Haehnel, P. & Walter, J. Improvement of thermographic findings on minimal breast cancer based on the use of advanced liquid crystal technology and computer-assisted protocols of interpretation, in REF #2 pp 263-276.

[19] Farrell, C., Perez-Mesa, C. & Blackwell, C. Thermographic findings in inflammatory breast cancer, in REF #2 pp 277-280.

AUTHORS

Noncontact Temperature Measurement Workshop

April 30 - May 1, 1988

Dr. James Allen
MS 183-410
Jet Propulsion Laboratory
4800 Oak Road Drive
Pasadena, CA 91109
818-354-3046

Professor Michael Anbar
University of New York
Dept. of Biophysical Science
School of Medicine
Buffalo, NY 14214
716-831-2328

Dr. Ared Cezairliyan
National Bureau of Standards
Thermophysis Division
Gaithersburg, MD 20899
301-975-5931

Professor Robert H. Doremus
Rennnsselaer Polytechnic Institute
Materials Engineering Dept
Troy, NY 12181
518-266-6709

Dr. Alan Eckbreth
MS 90
United Technologies Research Center
Silver Lane
East Hartford, CT 06108
203-727-7269

Dr. Michael E. Frish
PSI
Dascomb Research Park
P.O. Box 3100
Andover, MA 01810-7100
614-475-9030

Dr. Stuart D. Glazer
MS 157-102
Jet Propulsion Laboratory
4800 Oak Road Drive
Pasadena, CA 91109
818-354-2372

Dr. Sandor Lehoczky
Mail Code ES 72
Marshall Space Flight Center
MSFC, AL 35812
205-544-7759

Dr. Don McSparron
National Bureau of Standards
B306, Bldg 220
Radiometric Physics Division
Gaithersburg, MD 20899
301-975-2321

Dr. Paul Nordine
Midwestern Research Institute
425 Volker Blvd
Kansas City, MO 64110
816-753-7600

Professor Gene D. Nutter
University of Wisconsin
Instrumentation Systems Center
1500 Johnson Drive
Madison, WI 53706
608-263-1678

Professor Paul D. Ronney
Princeton University
Dept. Mechanical and Aerospace
    Engineering
Princeton, NJ 08544
609-452-5278

Mr. Kurt Sacksteder
Mail Code 501-8
Lewis Research Center
National Aeronautics and Space
    Administration
Cleveland, OH 44135
216-433-2857

Mr. Jack Salzmann
Mail Code 500-217
Lewis Research Center
National Aeronautics and Space
    Administration
Cleveland, OH 44135
216-433-2868

Dr. Robert Snyder
Mail Code ES73
Marshall Space Flight Center
MSFC, AL 35812
205-544-7805

Professor Erik Spjut
Masachusetts Institute Technology
Dept. Material Science & Engineering
Room 8-301
Cambridge, MA 02139
617-253-0252

Dr. Alex Stein
Quartum Logics
610 Sandering Court
Secaucus, MA 02072
201-866-9284

Dr. Riccardo Vanzetti
Vanzetti Systems, Inc.
111 Island Street
Stoughton, MA 02072
617-828-4650

Dr. Michael Wargo
Massachusetts Institute Technology
Room 13-4057
Cambridge, MA 02139
617-253-3295

WORKSHOP ATTENDEES

NONCONTACT TEMPERATURE MEASUREMENT WORKSHOP ATTENDEES

March 30 - April 1, 1987

Dr. James Allen
Mail Stop 183-401
Jet Propulsion Laboratory
4800 Oak Grove Drive
Pasadena, CA 91109

Professor Michael Anbar
University of New York
Department of Biophysical Science
School of Medicine
Buffalo, NY 14214

Dr. Martin B. Barmatz
Mail Stop 183-401
Jet Propulsion Laboratory
4800 Oak Grove Drive
Pasadena, CA 91109

Mr. Richard Bradfield
Bionetics Corporation
955 L'Enfant Plaza, S.W.
Suite 1500
Washington, D.C. 20024

Mr.Alfred M. Buonchristiani
Mail Stop 468
Langley Research Center
Hampton, VA 23665-5225

Dr. Charles E. Byvik
Mail Stop 468
Langley Research Center
Hampton, VA 23665-5225

Dr. Ared Cezairliyan
National Bureau of Standards
Thermophysis Division
Gaithersburg, MD 20899

Dr. Roger Crouch
Code EN
NASA Headquarters
Washington, D.C. 20546

PRECEDING PAGE BLANK NOT FILMED

Professor Robert H. Doremus
Rensselaer Polytechnic Department
Materials Engineering Department
Troy, NY 12181

Dr. Alan A. Eckbreth
Mail Stop 90
United Technologies Research Center
Silver Lane
East Hartford, CT 06108

Dr. Dan D. Elleman
Mail Stop 183-401
Jet Propulsion Laboratory
4800 Oak Grove Drive
Pasadena, CA 91109

Dr. Val Fogle
PSI
Dascomb Research Park
Andover, MA 01810-7100

Dr. Michael E. Frish
PSI
Dascomb Research Park
P.O. Box 3100
Andover, MA 01810-7100

Dr. Stuart D. Glazer
Mail Stop 157-102
Jet Propulsion Laboratory
4800 Oak Grove Drive
Pasadena, CA 91109

Paul S. Greenberg
Mail Stop 500-217
Lewis Research Center
National Aeronautics and Space
        Administration
Cleveland, OH 44135

Mr. Warren Hodges
Code EN
NASA Headquarters
Washington, D.C. 20546

424

Cpt. Brian C. Hoekstra
NASA Center
107 Peyton Hall
Clarkson University
Potsdam, NY 13676

Mr. William Hofmeister
Vanderbilt University
Dept. Mechanical & Materials Engineering
Nashville, TN 37235

Mr. Ira Kasindorf
Quantum Logics
610 Sandering Court
Secaucus, NJ 07094

Mrs. Mary Kicza
Code EN
NASA Headquarters
Washington, D.C. 20546

Mr. Richard Klass
Vanzette Systems, Inc
111 Island Street
Stoughton, MA 02072

Dr. Norbert Kreidl
1433 Canyon Road
Santa Fe, NM 87501

Dr. Mark Lee
Code EN
NASA Headquarters
Washington, D.C. 20546

Dr. Alex Lehoczky
MS ES72
Marshall Space Flight Center
MSFC, AL 35812

Dr. Don W. Lewis
MS 157-205
Jet Propulsion Laboratory
4800 Oak Grove Drive
Pasadena, CA 91109

Dr. Donald McSparron
National Bureau of Standards
B306, Building 220
Radiometric Physics Division
Gaithersburg, MD 20899

Mr. Robert Madding
c/o Stuart Glazer
MS 157-102
Jet Propulsion Laboratory
4800 Oak Grove Drive
Pasadena, CA 91109

Dennis Merkley
Intersonics Inc
425 Huel Unit 11A
Northbrook, IL 60062

Tripty Mookherji
MS 52
Advance Space Program Center
Cumming Research Park
Teledyne Brown Engineering
Huntsville, AL 35807

Andrew D. Morrison
MS 125-112
Jet Propulsion Laboratory
4800 Oak Grove Drive
Pasadena, CA 91109

Dr. Dennis Morrison
Code SD4
Johnson Space Center
Houston, TX 77058

Dr. Robert Naumann
Mail code ES71
Marshall Space Flight Center
MSFC, AL 35812

Dr. Paul Nordine
Midwestern Research Institute
425 Volker Blvd
Kansas City, MO 64110

Professor Gene D. Nutter
University of Wisconsin
Instrumentation Systems Division
1500 Johnson Drive
Madison, WI 53706

Dr. William A. Oran
Code CC
NASA Headquarters
Washington, D.C. 20546

Richard J. Parker
MS 500-205
Lewis Research Center
National Aeronautics and Space
        Administration
Cleveland, OH 44135

Mr. Martin Phillips
Quantum Logics
610 Sandering Court
Secaucus, NJ 07094

Dr. Nancy Pilpch
MS 77-1
Lewis Research Center
National Aeronautics and Space
        Administration
Cleveland, OH 44135

Mr. Michael Price
Code EN
NASA Headquarters
Washington, D.C. 20546

Mr. Charles Ray
Intersonics, Inc
425 Huel Unit 11A
Northbrook, IL 60062

Michael Richardson
EX3
Johnson space Center
Houston, TX 77058

Michael Robinson
Mail code ES74
Marshall Space Flight Center
MSFC, AL 35812

Professor Paul D. Ronney
Princeton University
Dept. Mechanical & Aerospace Engineering
Princeton, NJ 08544

Mr. Kurt Sacksteder
Mail Code 501-8
Lewis Research Center
National Aeronautics and Space
    Administration
Cleveland, OH 44135

Mr. Jack Salzman
Mail Code 500-217
Lewis Research Center
National Aeronautics and Space
    Administration
Cleveland, OH 44135

Dr. Gilbert Santoro
MS 500-205
Lewis Research Center
National Aeronautics and Space
    Administration
Cleveland, OH 44135

Katy Schmoll
Code E
NASA Headquarters
Washington, D.C. 20546

Mr. Wilson Smith
University of Alabama, Birmingham
UAB Station
Box THT 79
Birmingham AL 35294

Dr. Robert Snyder
ES 73
Marshall Space Flight Center
MSFC, AL 35812

Professor Eric Spjut
Massachusetts Institute of Technology
Dept. Materials Science & Engineering
Room 8-301
Cambridge, MA 02139

Dr. Alex Stein
Quartum Logics
610 Sandering Court
Secaucus, NJ 07094

Dr. Riccardo Vanzetti
Vanzetti systems, Inc
111 Island Street
Stoughton, MA 02072

Dr. Taylor W. Wang
Mail Code 183-401
Jet Propulsion Laboratory
4800 Oak Grove Drive
Pasadena, CA 91109

Mr. Michael Wargo
Massachusetts Institute of Technology
Room 13-4057
Cambridge, MA 02139

Mr. John Williams
Center for Space & Advanced Technology
500 Blvd South
Suite 104
Huntsville, AL 35802

Dr. Gary Workman
University of Alabama in Huntsville
Research Institute
Box 212
Huntsville, AL 35899

Mr. Don Wrublik
NASA, Swales Associates
5050 Ponder Mill Road
Beltsville, MD 20705

David Yoel
Boeing Aerospace Company
MS 83-23
P.O. Box 3999
Seattle, WA 98124

Report Documentation Page

1. Report No. NASA CP-2503	2. Government Accession No.	3. Recipient's Catalog No.
4. Title and Subtitle Noncontact Temperature Measurement		**5. Report Date** March 1988
		6. Performing Organization Code EN
7. Author(s) Mark C. Lee, Editor		**8. Performing Organization Report No.**
		10. Work Unit No.
9. Performing Organization Name and Address Microgravity Science and Applications NASA Office of Space Science and Applications		**11. Contract or Grant No.**
		13. Type of Report and Period Covered Conference Publication
12. Sponsoring Agency Name and Address National Aeronautics and Space Administration Washington, DC 20546		
		14. Sponsoring Agency Code

15. Supplementary Notes

16. Abstract

This document contains the proceedings of a workshop held April 30 – May 1, 1987 at NASA Headquarters, Washington, D.C.

Noncontact Temperature Measurement Instrument has been identified as one of the eight Advanced Technology Development (ATD) areas to support the effort of the Microgravity Science and Applications Division in developing six Space Station Flight Experiment Facilities. This two-day workshop was an opportunity for all six disciplines to present their requirements on noncontact temperature measurement; equally important, the state of the art technology for noncontact measurement for each discipline was reviewed and assessed. A preliminary survey of this report reveals that at least three categories of experiments demand immediate attention: those involving levitated samples and samples falling in a drop tube, crystal growth processes, and gaseous and fluid flow. This document represents an initial effort to identify critical technology required in the Space Station area. Additional areas in which noncontact temperature measurement is important will certainly become apparent as the task progresses.

17. Key Words (Suggested by Author(s)) noncontact temperature measurement laser pyrometer thermoimaging blackbody radiation	18. Distribution Statement Unclassified – Unlimited Subject Category 29

19. Security Classif. (of this report) Unclassified	20. Security Classif. (of this page) Unclassified	21. No. of pages 438	22. Price A19